Reconstructing past mean ocean temperature using noble-gas ratios in the EDC ice core

Inaugural dissertation

of the Faculty of Science,
University of Bern

presented by

Markus Grimmer

from Bern BE

Supervisor of the doctoral thesis:

Prof. Dr. Hubertus Fischer

Dr. Daniel Baggenstos

Climate and Environmental Physics

Physics Institute of the University of Bern

Reconstructing past mean ocean temperature using noble-gas ratios in the EDC ice core

Inaugural dissertation

of the Faculty of Science,
University of Bern

presented by

Markus Grimmer
from Bern BE

Supervisor of the doctoral thesis:

Prof. Dr. Hubertus Fischer
Dr. Daniel Baggenstos

Climate and Environmental Physics
Physics Institute of the University of Bern

Accepted by the Faculty of Science.

The Dean:
Bern, 29. November 2023 Prof. Dr. Marco Herwegh

Nüt!
Eifach nüt!
Mir chunt eifach nüt i sinn, was i söu schribe.

U we mir nüt z'sinn chunt,
cha i ou nüt schribe,
nid äs gedicht,
nid ä strophe,
nid ä riem,
nid ä satz,
nid äs wort,
ja nid ä mau ä buechstabä.

U we i nüt cha schribe,
cha i ou nüt abgä,
ou nüt vorläsä,
u de stani vor äm publikum u cha nüt sägä,
nüt,
ussert vilecht: Nüt!
Eifach nüt!
Mir isch eifach nüt z'sinn cho!
Nüt!
Nid ä buechstabä,
nid äs wort,
nid ä satz,
nid ä riem,
nid ä strophe,
u ersch rächt nid äs gedicht!

U au das wüu mir nüt z'sinn chunt!

U anstatt am schluss itz nüt z'säga,
säg i doch no öppis:
Äs isch de glich ***nid nüt****!*

Poem in response to some homework in 8th grade. Probably the best text I have written thus far and oddly fitting for the writing process of this thesis.

Loose translation:
Nothing! / Simply nothing! / I simply cannot think of anything to write.
And when I cannot think of anything, / I cannot write anything, / no poem, / no verse, / no rhyme, / no sentence, / no word, / not even a single letter.
And if I cannot write anything, / I cannot hand in anything, / nor present anything, / and then I will stand in front of the public and cannot say anything, / nothing, / maybe except for: Nothing! / Simply nothing! / I simply could not think of anything! / Nothing! / No letter, / no word, / no sentence, / no rhyme, / no verse, / and certainly no poem!
And all because I cannot think of anything!
And instead of not saying anything in the end, / I will say this: / This is not nothing after all!

Summary

Throughout the Quaternary, Earth's climate system has repeatedly undergone major reorganisations. Glacial terminations, the transitions of the climate system from its cold glacial to its warmer interglacial state, represent the largest natural reorganisations in this period. As the climate shifts from glacial to interglacial state, the planet takes up vast amounts of energy. This energy is largely split up between Earth's two dominant surface energy reservoirs on glacial–interglacial timescale: the ocean and the latent heat used to melt continental ice sheets. The extent of continental ice sheets can be inferred from sea level reconstructions, whereas the energy stored in the ocean is described by the ocean heat content, which through the heat capacity of water is directly linked to mean ocean temperature (MOT). Thus, global sea level and MOT are the two key metrics for determining Earth's energy imbalance during the Quaternary.

Ratios of noble gases and N2 trapped in polar ice cores are a novel proxy for MOT. Since noble gases are inert, their atmospheric abundances on glacial-interglacial timescale are solely dependent on their well understood temperature-dependent solubilities in ocean water. As the atmosphere is well-mixed, a single ice core sample is sufficient to obtain a snapshot of the global ocean's noble gas content, and, through the temperature-dependent solubilities, its heat content. Thanks to high precision mass spectrometry, the 1σ uncertainty for reconstructing MOT in Bern is on the order of 0.3 °C. Consequently, MOT has proven to be a novel powerful proxy for the past climate.

The aims of this PhD-project were twofold. The first aim was to further improve the analytical procedure used to reconstruct MOT here at the University of Bern. This was achieved by improving the extraction system's capacity for capturing drilling fluid, which caused problems in previous measurement campaigns; by increasing the analytical precision for measuring noble-gas ratios through introducing new mass spectrometry corrections and updating established ones; and by establishing a fully data-based correction routine for firn fractionation processes, thereby reducing systematic uncertainties of the routine. The second aim was to produce a new MOT dataset, making use of the improved procedure. This was achieved by measuring 72 EPICA Dome C ice core samples, which span Terminations II, III, and IV, and their subsequent interglacials. This new dataset greatly expands on the existing MOT data and for the first time allows for studying the past four glacial–interglacial transitions and their subsequent interglacials from an OHC perspective. The dataset reveals consistent influence of ocean overturning circulation on the evolution of deglacial and early interglacial MOT evolution.

Contents

1. Introduction

Earth’s energy imbalance is one of the most fundamental metrics to gauge the planet’s climate state. It describes the balance between the amount of energy Earth receives at the top of its atmosphere in form of solar radiation, and the amount of energy it loses to space by reflecting shortwave radiation and emitting longwave radiation. Under a stable climate, incoming and outgoing energy are in balance, such that Earth’s energy imbalance equals 0. However, climate drivers, such as greenhouse gases or aerosols, in combination with climate feedbacks can tip this balance in either direction (Intergovernmental Panel on Climate Change, 2021). The resulting energy imbalance leads to a net warming or cooling.

It is unequivocal that human activities have heated our climate (Intergovernmental Panel on Climate Change, 2021). This warming and associated changes in the climate system are rapid, intensifying, and unprecedented in at least the last 2,000 years (Neukom et al., 2019). Until today, the burning of fossil fuels and land-use changes have led to an increase in global mean surface temperature of approximately 1.2 °C since 1850 (Intergovernmental Panel on Climate Change, 2021). In 2015, 196 parties of the UN Climate Change Conference have pledged to limit this warming to well-below 2 °C above pre-industrial levels and ideally to below 1.5 °C by the end of this century. However, current policies of governments worldwide are insufficient as they are projected to lead to 2.4 to 2.8 °C warming by 2100 (Boehm et al., 2022).

Observations suggest that Earth’s current energy imbalance is about 0.74 ± 0.22 W m^{-2} (Marti et al., 2022), which are fully attributable to the anthropogenic emission of greenhouse gases (von Schuckmann et al., 2020). This is in good agreement with the value obtained by climate models in the framework of CMIP6 of 1.1 ± 0.8 W m^{-2} (Wild, 2020). About 90 % of this surplus of energy is stored in Earth’s dominant fast exchanging energy reservoir, the global ocean (Intergovernmental Panel on Climate Change, 2021; von Schuckmann et al., 2020). Consequently, OHC has increased between 1958 and 2019 by 378.4 ± 64.5 ZJ, which translates to 6.20 ± 0.98 ZJ yr^{-1} (Cheng et al., 2022). Large parts of this energy uptake have occurred in the last twenty to thirty years as warming rates have been increasing over time (Loeb et al., 2021). Considering its long overturning timescale and large thermal energy capacity, the ocean responds only gradually to this energy imbalance, with particularly slow response in the deep ocean. OHC will thus likely continue to increase for many centuries to come (Cheng et al., 2022; Intergovernmental Panel on Climate Change, 2021).

1.1. Mean ocean temperature

Through the heat capacity of water, this increase in OHC is directly linked to an increase in the global mean ocean temperature (MOT). It thereby contributes to the observed rise in global sea level through thermal expansion (World Climate Research Programme, 2018) and reduces the ocean’s capacity to act as a carbon sink (Gruber, 2011). Warmer MOT also influence ocean circulation (e.g., Caesar et al., 2018; Shi et al., 2018) and the hydrological cycle (Held and Soden, 2006), lead to an increase in the frequency, intensity, and extent of marine heatwaves, thus affecting marine wildlife (Frölicher et al., 2018), and contribute to increased melting of sea ice and ice sheets (Pritchard et al., 2012) with potentially irreversible consequences (Armstrong McKay et al., 2022). The close to 400 ZJ of excess energy taken up until today translate into a MOT warming of about 0.1 °C.

In the last decades, there has been considerable progress in measuring the current change in OHC. The first estimates of OHC were produced during the International Geophysical Year in 1957/1958, during which large amounts of hydrographic data were collected (Cheng et al., 2022). However, the major revolution in ocean temperature monitoring happened in 1999, when the first autonomous profiling floats were deployed in the scope of the Argo program. The freely drifting Argo floats monitor temperature, salinity, and more recently also a suite of biogeochemical variables (Riser et al., 2016). A typical float records a temperature and salinity profile every ~10 days by ascending from 2,000 m depth to the surface within about 6 hours. After transmitting the data at the surface, the float redescends to a depth of 1,000 m, where it drifts for about 9 days, before descending further to 2,000 m and subsequently starting the next profile. With close to 4,000 operational floats today, data coverage is better than 70% for the global ocean area (Meyssignac et al., 2019). Nowadays, Argo floats also push into monitoring seasonal sea-ice zones and marginal seas while increasing data coverage in critical regions (Jayne et al., 2017; Riser et al., 2016). This near-global uniform coverage by Argo floats, thus, yields highly credible data products of the heat content of the upper 2,000 m of the global ocean.

However, OHC estimates from the deep ocean remain highly uncertain, as conventional Argo floats only monitor the upper 2,000 m of the ocean. Although most of the anthropogenic warming signal is expected to not have penetrated below 2,000 m depth yet, recent studies suggest that the abyssal ocean also might contribute significantly as a heat sink (e.g., Storto et al., 2022). To extend the data product from Argo floats to the deep part of the ocean, a new generation of floats called Deep Argo has been in development since 2012 with first deployments in 2015 (Riser et al., 2016). Deep Argo aims to systematically sample the global ocean down to a depth of 6,000 m, for which a total of 1,228 floats should be deployed in the future (https://argo.ucsd.edu/expansion/deep-argo-mission/). As of July 2023, only 193 of these Deep Argo floats were operational.

1.2. Archives of past ocean temperature

Major reorganisations of Earth's climate system have occurred in the past, albeit at a slower pace than today's anthropogenic warming. Glacial terminations, the transitions of the climate system from its cold glacial to its warmer interglacial state, represent the largest such reorganisations in the Quaternary, i.e., the last 2.6 million years (Myr). Terminations are the consequence of gradual changes in orbital forcing and nonlinear internal feedback mechanisms connected to changes in greenhouse gas concentrations and planetary albedo (Rothlisberger et al., 2008; Wolff et al., 2009). As the climate shifts from glacial to interglacial state, the planet takes up vast amounts of energy. This energy is largely split up between Earth's two dominant surface energy reservoirs on glacial–interglacial timescale: the ocean and the latent heat used to melt continental ice sheets (Baggenstos et al., 2019). The extent of continental ice sheets can be inferred from sea level reconstructions, whereas the energy stored in the ocean is given by the OHC and thus MOT. Thus, global sea level and MOT are the two key metrics for determining Earth's energy imbalance during the Quaternary.

Within the Quaternary, the warm interglacial periods and the terminations leading up to them are of particular interest. Human society evolved within the current interglacial, the Holocene, and fossil fuel burning and anthropogenic land-use change have ensured that we will live in a warm climate state for millennia to come (Berger and Loutre, 2002). However, although we have a good understanding of the current climate, we do not understand in detail how this climate state came to be (Past Interglacials Working Group of PAGES, 2016). To better understand how past and current climate evolved, and to further constrain projections of future climate change under anthropogenic warming, we require a better mechanistic understanding of the climate system. This mechanistic understanding is mostly gained from climate models, for which paleo data is invaluable as it constrains boundary conditions and acts as a testbed for model simulations (e.g., Otto-Bliesner et al., 2017). Of particular interest are periods during which the climate system showed nonlinear behaviour, which may happen on very different timescales; from abrupt events lasting but a few years to decades, such as methane pulses, over millennial-scale variability, such as Dansgaard-Oeschger events (D/O-events), to orbitally-paced glacial–interglacial transitions. Furthermore, past climate can serve as a potential analogue for certain aspects of the current and near-future climate. In view of anthropogenic climate change, especially the warmest amongst the interglacial periods have attracted scientific interest, that is, Marine Isotope Stages (MIS) 11c, 9e, 7e, and 5e, and out of these particularly the Last Interglacial (LIG), MIS 5e (Past Interglacials Working Group of PAGES, 2016). We here follow the suggestion of the former PAGES working group PIGS for numbering marine isotope stages and substages (Past Interglacials Working Group of PAGES, 2016). OHC is of great interest to the modelling community for all these periods, as it constrains one of the two major energy fluxes in the climate system on glacial–interglacial timescale (e.g., Obase et al., 2021).

1.2.1. The ocean

Due to its volume, the deep ocean dominates global OHC. Consequently, today's MOT of ~3.5 °C (Pawlowicz, 2013) is much closer to the average deep ocean temperature (DOT) of about 1.4 °C (Orsi et al., 2001) than to the current average sea surface temperature (SST) of ~17.5 °C (Birkel, 2023). The abyssal ocean is predominantly filled with water that originated from the continental margins of Antarctica, where Antarctic Bottom Water (AABW) forms in localised areas of deep convection under Antarctic ice shelves (Thompson et al., 2018) and openings in the sea ice, so-called polynyas (Gordon, 2014). The second significant contribution to deep water formation stems from the Nordic Seas (Greenland, Iceland, and Norwegian Seas) and the Labrador Sea, where deep convection of cold surface water eventually leads to the formation of North Atlantic Deep Water (NADW). Today, AABW makes up about 65% of the total deep water, with the rest filled by NADW (Johnson, 2008). AABW is colder and less saline than NADW, making it the densest water mass in the main basins of the global ocean. Hence, AABW covers much of the global ocean floor, except for parts of the North Atlantic.

Despite a comparable volume flux (in Sverdrup) of meridional overturning circulation associated with NADW and AABW (Orsi et al., 2001), the larger volume of AABW leads to a longer global mean residence time of AABW compared to NADW (Johnson, 2008), that is, more time elapses between the downward advection and the resurfacing to the ocean surface-mixed layer. Deep ocean residence times vary from a few centuries in the deep North Atlantic, over half a millennium in the Southern Ocean, to around 1.5 kyr in the North Pacific (DeVries and Holzer, 2019; Matsumoto, 2007). Glacial residence times are assumed to be longer still (Skinner et al., 2017), implying weakened overturning circulation and a more stratified ocean.

However, proxy evidence on glacial overturning circulation and water mass distribution is conflicting (Lynch-Stieglitz, 2017), with some pointing towards a shoaling and weakening of the Atlantic Meridional Overturning Circulation (AMOC), i.e., the NADW branch (Curry and Oppo, 2005), others suggesting a shoaled but more vigorous glacial AMOC (Lippold et al., 2012), and again others find little to no change compared to modern (Du et al., 2020; Pöppelmeier et al., 2020) and, thus, stable glacial AMOC (Böhm et al., 2015).

Changes in ocean overturning, stratification, as well as biological productivity play a key role in shaping Earth's climate through their control on the uptake, export, and storage of carbon (e.g., Sabine et al., 2004; Sigman et al., 2010) and heat (Pedro et al., 2018) in the deep ocean, and through their significant contribution to poleward heat transport (Ganachaud and Wunsch, 2000). At the same time, the effectiveness of deepwater formation, and connected thereto the geometry of abyssal water masses, is controlled by a variety of factors that are themselves subject to the climate, such as freshwater forcing or the position and strength of westerly wind belts (Barker et al., 2015; Glasscock et al., 2020; Weber et al., 2007). Ocean circulation and water mass distribution thereby are both slave and master of climate change.

A tight coupling between ocean circulation and climate has long been suggested (Ruddiman and McIntyre, 1981; Stommel, 1961). Observations of millennial-scale climate oscillations, which have been recorded as rapid changes in Greenland ice core proxy records (Dansgaard et al., 1993; Severinghaus and Brook, 1999), i.e., D-O events, but are associated with more gradual changes in Antarctic records (Johnsen et al., 1972), have given rise to the thermal bipolar seesaw hypothesis. This hypothesis states that under weak AMOC conditions, heat export to the northern high latitudes by the surface branch of AMOC is reduced and instead most of the heat remains in the South Atlantic (Stocker and Johnsen, 2003). There it leads to gradual accumulation of heat in a southern reservoir, which was initially suggested to be the Southern Ocean (Stocker and Johnsen, 2003), but more recent findings instead point towards a warming of the global ocean interior north of the ACC (Pedro et al., 2018). This gradual increase in southern hemisphere heat is then archived in Antarctic ice core records. Furthermore, the accumulation of heat in the ocean interior was suggested to have a net effect on global OHC in several climate models (Galbraith et al., 2016; Pedro et al., 2018) as it more than compensates the reduction in North Atlantic SST, which is supported by proxy evidence (Bereiter et al., 2018b; Shackleton et al., 2020). Upon AMOC reinvigoration, the heat flux to the northern hemisphere is restrengthened, leading to rapid warming in the North Atlantic region known as D-O events, whereas the ocean interior and Antarctica gradually cool again.

1.2.2. Reconstructing past ocean temperatures

Considering the prominent role of the deep ocean, past evolution of OHC may be approximated by reconstructions of global DOT. Although various proxies for the reconstruction of past ocean temperature exist, obtaining a globally representative record proves to be a major challenge. Ocean temperature proxies are mostly based on remains of marine biota found in marine sediments. Changes in their living environment are mirrored in the shells of surface-dwelling (planktonic) and sediment-dwelling (benthic) foraminifera, or the lipids produced by haptophyte algae and Thaumarchaeota. Under favourable circumstances, these remains are preserved in the sediment and, thus, provide proxy evidence for local climatic conditions. Sea sediment proxies for DOT involve the relative abundance of the heavy oxygen isotope ^{18}O, the ratio of Mg/Ca, or the clumped carbon and oxygen isotope in foraminiferal calcite ($CaCO_3$) tests. For SST, additional proxies are available, such as the relative unsaturation of alkenones produced by haptophyte algae and the ratio of glycerol dialkyl glycerol tetraethers (GDGTs) from Thaumarchaeota (Lawrence and Woodard, 2017).

The oxygen isotopic composition of foraminiferal $CaCO_3$ tests ($\delta^{18}O_C$) found in marine sediment cores is considered a valuable proxy record for both eustatic sea level (ESL) and local temperature (e.g., Emiliani, 1955; Lisiecki and Raymo, 2005; Shackleton, 1967). Benthic and planktonic foraminifera build their $CaCO_3$ shells from the surrounding seawater. The oxygen isotopic composition of $CaCO_3$ depends on the temperature in which the mineral precipitated but also varies with $\delta^{18}O$ of the sea water ($\delta^{18}O_{SW}$) in which it formed. This $\delta^{18}O_{SW}$ in turn is a function of global $\delta^{18}O_{SW}$, the main control of which is the size of continental ice sheets and, thus, ESL, but local temperature plays a role as well (Emiliani, 1955; Shackleton, 1967). Thus, local hydrography affects $\delta^{18}O_C$, which may be overcome through careful site selection (Elderfield et al., 2012), or by stacking multiple sediment records (e.g., Hoffman et al., 2017; Shakun et al., 2015). However, to disentangle the two main imprints on $\delta^{18}O_C$, sea level and local temperature, an independent measure of one of these two controlling factors is required.

A popular approach to isolate $\delta^{18}O_{SW}$ from $\delta^{18}O_C$ is to use measurements of Mg/Ca in shells of planktonic and benthic foraminifera. Foraminiferal Mg/Ca shows an exponential dependency on temperature, a consequence of both thermodynamics and biology (Lea et al., 1999; Nürnberg et al., 1996). Various calibration curves exist for linking Mg/Ca to local sea surface temperature (Tierney et al., 2019). These calibrations are complicated by other, secondary environmental controls of Mg/Ca, such as bottom water calcite saturation, salinity, and pH (Lea et al., 1999; Nürnberg et al., 1996; Regenberg et al., 2014). These non-thermal influences on Mg/Ca paleo-thermometry are most critical for relatively cold temperatures (Stirpe et al., 2021), at which sensitivity of the thermometer is already reduced due to its exponential temperature relationship and, by consequence, precision is rather low with 1σ uncertainties of 1 to 1.5 °C (Rohling et al., 2022). Here and throughout this thesis, analytical uncertainties are given as one standard deviation (1σ) unless stated otherwise. In recent years, some first records have been published that use the temperature-dependent clumping of the heavy C and O isotopes in calcite Δ_{47} (e.g., Rodríguez-Sanz et al., 2017). The method shows great promise, as it yields absolute water temperature estimates that do not show species-specific signals, nor are they affected by seawater pH, DIC, or the carbonate saturation state (Huntington and Petersen, 2023). However, they are currently still limited by their precision (1–1.5 °C) and rather large sample size requirements (Rohling et al., 2022).

For SST, additional proxies exist. The $U_{37}^{K'}$ index describes the relative abundance of two- and three-times unsaturated alkenones produced by surface-dwelling haptophyte algae. The production of unsaturated alkenones of these algae changes in response to local temperature conditions. Again, secondary non-thermal influences exist. Light and nutrient stress, degradation, or lateral advection of alkenones (due to long residence times) can all have an influence on the alkenone-temperature calibration curve (Rühlemann and Butzin, 2006; Tierney and Tingley, 2018). Further concerns exist regarding the seasonality of the alkenone production, as production is affected by temperature, nutrient availability, stratification, and competition, and thus varies strongly throughout the year (Rosell-Melé and Prahl, 2013). Furthermore, temperature sensitivity might be nonlinear at both ends of the calibration range (Tierney and Tingley, 2018).

Over the past decades, various DOT records were created based on different combinations of the marine sediment proxies presented above. Often, these are temperature records on a local, regional, or basin-wide scale. Some of them inferred the bottom water temperature by measuring Mg/Ca in benthic foraminifera (e.g., Martin et al., 2002), whereas others attempted to disentangle sea-level and temperature influence on $\delta^{18}O_C$ through comparison of different $\delta^{18}O_C$ records (e.g., Duplessy et al., 1980); by linear or more statistically-driven scaling of the sea level influence inferred from different sea level proxies (e.g., Bates et al., 2014; Chappell and Shackleton, 1986; Cutler et al., 2003; Siddall et al., 2010; Waelbroeck et al., 2002); through direct measurement of $\delta^{18}O_{SW}$ in pore fluids (Adkins and Schrag, 2001; Schrag et al., 1996); or through coupled ice sheet-ocean temperature inverse modelling (Bintanja et al., 2005). Most of these studies found glacial–interglacial DOT differences of 2–4 °C for the different ocean basins, or in the case of Bintanja et al., 2005, for global DOT.

More recently, several global estimates of DOT have been published. Elderfield et al., 2012 used a combination of $\delta^{18}O_C$ and Mg/Ca from Ocean Drilling Program site 1123, located at the Chatham Rise. This site to the east of New Zealand receives water from the Deep Western Boundary Current, which accounts for more than half of the deep-water flux of the major ocean basins (Elderfield et al., 2012). Thus, the record should be representative for large parts of the deep ocean. A different approach was chosen by Rohling et al., 2014, who used a planktonic $\delta^{18}O_C$ stack from the eastern Mediterranean to reconstruct relative sea-level changes at Gibraltar and then infer ESL changes over the last 5.3 Myr. The ESL estimate is converted into estimates of $\delta^{18}O_{SW}$ on the basis of scaling factors obtained from pore fluid measurements (Adkins et al., 2002; Schrag et al., 1996), which they then used in combination with the LR04 benthic stack (Lisiecki and Raymo, 2005) to derive DOT. Later, they refined their reconstruction through process-based modelling of the different parameters affecting measured $\delta^{18}O_C$ (Rohling et al., 2021). Shakun et al., 2015 again used the approach of disentangling the temperature imprint on $\delta^{18}O_C$ with Mg/Ca. They did so for a total of 49 sites, from which they derived an estimate for the planktonic $\delta^{18}O_{SW}$ evolution. Unlike Rohling et al., 2014, their approach does not extrapolate Mediterranean $\delta^{18}O_C$ to $\delta^{18}O_{SW}$ but instead assumes that $\delta^{18}O_{SW}$ as reconstructed from the planktonic $\delta^{18}O_C$ stack equals $\delta^{18}O_{SW}$ changes in the deep ocean. They then used the same approach as Rohling et al., 2014 and subtracted this reconstructed sea level component from the LR04 benthic stack to obtain an 800-thousand-year (800 kyr) DOT record. An extensive overview of DOT reconstructions based on benthic $\delta^{18}O_C$, as well as sea level reconstructions, can be found in the recent review article of Rohling et al., 2022. The three global reconstructions of DOT mentioned in this paragraph are plotted for Terminations I-IV in Figure 1.1.

In summary, marine sediment cores provide valuable proxy records from which local to regional SST and DOT in many, but not all, ocean areas can be deduced. Although their proxy information is only representative for the coring site, reconstructions of global SST and DOT can be obtained through careful site selection (Elderfield et al., 2012) or stacking of records (Rohling et al., 2014; Shakun et al., 2015; Hoffman et al., 2017). However, such a stack requires a globally representative set of cores that have to be rigorously cross-dated, which is not an easy task, particularly for the pre-^{14}C period. Moreover, marine sediment records can be affected by complex biogeochemical processes and sea level changes. They also may be limited in precision, especially for the cold deep ocean (Chandler and Langebroek, 2023).

Furthermore, they can be affected by post-depositional effects such as partial dissolution, bioturbation, or precipitation of calcite (e.g., Stirpe et al., 2021).

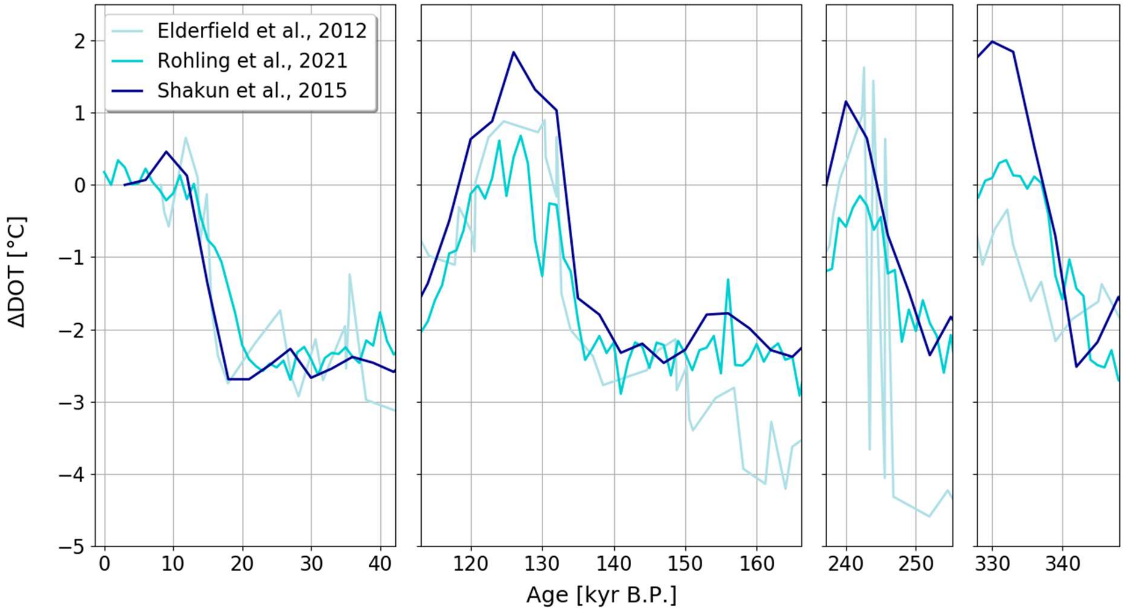

Figure 1.1.: Reconstructions of global ocean temperature during the last four glacial terminations based on marine sediment proxies. The record from Elderfield et al., 2012 shows higher variance, as it is retrieved from one core only. The records of Shakun et al., 2015 and Rohling et al., 2021 are both based on the LR04 benthic stack but use a different $\delta^{18}O_{SW}$ and different scaling of $\delta^{18}O_{SW}$ to sea level.

1.3. The temperature-solubility relationship

Many of the challenges of reconstructing past ocean temperature based on marine sediment cores are connected to the biogeochemistry involved in the various steps from marine organism to proxy record. Species-specific temperature responses, complex dependencies on calcite saturation and pH, and post-depositional disturbance of the sediment are but a few complications added by biogeochemical processes. These complications can be avoided if we consider a purely physical proxy for ocean temperature instead: the concentration of noble gases dissolved in ocean water.

The underlying idea of noble gas thermometry is as follows: gases dissolve in water, and the amount that dissolves depends on the water temperature (Figure 1.2.). Given a water parcel's gas content, its temperature can directly be inferred based on this temperature-solubility relationship, assuming the water parcel is at equilibrium, i.e., saturated. Considering that there are no essential heat sources or sinks in the ocean interior (Ritz et al., 2011), ocean heat and gas exchange only take place at the ocean-atmosphere interface. Consequently, the gas content of an ocean water parcel is intimately linked to its heat content, bar some minor mixing of water masses in the ocean interior, and the gas content of the global ocean is a direct measure of MOT. However, determining the gas content of all ocean water parcels is not straight-forward, as no continuous archive of old ocean water exists. The alternative approach is to determine the amount of gas stored in all reservoirs that interact with the ocean reservoir on relevant timescales. The oceanic component can then be inferred by subtracting the contributions of these reservoirs from the total stock. However, for most gases, this approach is unfeasible, as they are reactive and, thus, involved in many complex biogeochemical cycles, such that too many different reservoirs would have to be considered.

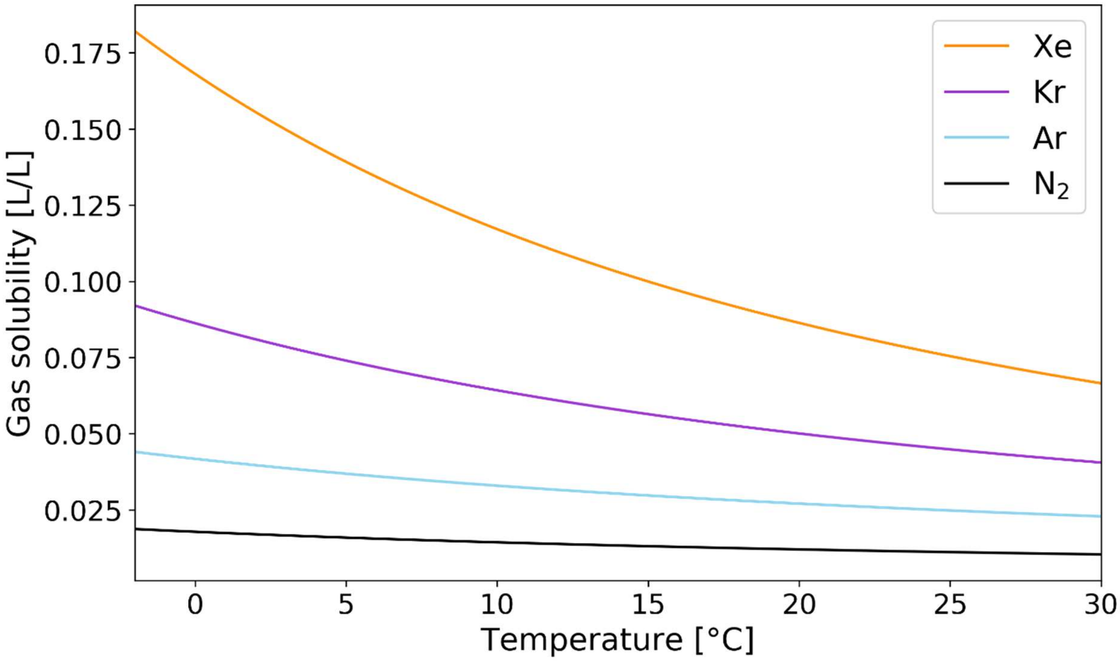

Figure 1.2.: Temperature-dependent solubilities of xenon (Xe), krypton (Kr), argon (Ar), and molecular nitrogen (N_2) in ocean water. Solubility equations are from Jenkins et al., 2019 (Xe, Kr, Ar) and Hamme and Emerson, 2004 (N_2).

This is where noble gases and their "boring" characteristic of inertness stand out. Noble gases are not involved in biogeochemical processes, and, thus, do not have any major sources or sinks in the ocean–atmosphere system. Consequently, the sum of their oceanic and atmospheric inventories can be assumed constant over glacial–interglacial timescale. So, for the special case of the heavy noble gases Ar, Kr, and Xe, the oceanic concentration can directly be deduced from the atmospheric composition (apart from a small and slow geological degassing component for ^{40}Ar produced during ^{40}K decay; Bender et al., 2008). The light noble gases He and Ne are both products of radioactive decays and their abundance in the atmosphere-ocean system is, thus, not constant. Furthermore, their high diffusivities cause them to not be preserved quantitatively in ice cores. The heavy noble gas Ra, on the other hand, is radioactive with a half-life time of less than 4 days. Neither of these three noble gases are thus suitable for our purpose. However, in addition to Ar, Kr, and Xe, molecular nitrogen also fulfils the condition of the atmospheric composition being representative of the oceanic concentration. Although not a noble gas, fluxes of nitrogen into and out of the atmosphere-ocean system due to nitrification and denitrification are negligible on glacial–interglacial timescale in comparison to the size of the atmospheric and oceanic inventories. The mean atmospheric residence time of N_2 is estimated to about 14 Myr (Schlesinger and Bernhardt, 2013). For our purpose, we will thus consider molecular nitrogen as a noble gas and use it in combination with Ar, Kr, and Xe for the reconstruction of past MOT.

The major challenge of measuring noble gases in ice cores is their extremely low atmospheric abundance. Both Kr and Xe are present only in trace gas amounts of 1.10 ppm and 87 ppb, respectively, in Earth's atmosphere (Table 1.1.). To reconstruct changes in MOT, we need to measure changes in their atmospheric abundance. Only about 2.5% and 4.8% of Kr and Xe, respectively, is found in the global ocean (Table 1.1.; Figure 1.2.). Consequently, even major changes in oceanic temperature only lead to a minor signal in the atmospheric noble gas content. The largest change in MOT over a glacial termination of about 3 °C (Figures 1.1.; 1.3.) entails a decrease in the oceanic Xe reservoir of about 6%, which translates to an increase in the atmospheric Xe concentration of a mere 3‰. Additionally, measured elemental ratios require corrections for fractionation processes in the firn column, which can be quantified using measurements of the isotopic composition of the same noble gases with precisions on the per meg level, as explained in detail in Chapter 3. Consequently, high precision mass spectrometry is needed to precisely measure such miniscule changes in low abundance gases (see Chapter 2). Due to these miniscule changes in elemental and isotopic ratios on the order of permille or even per meg (parts per million), gas ratios are typically expressed in δ-notation. The δ-value of a sample, δ_{SA}, is given as follows:

$$\delta_{SA} = \left(\frac{R_{SA}}{R_{STD}} - 1\right) \cdot 1{,}000‰ \qquad (1.1.)$$

The gas ratio of a sample R_{SA} is thus expressed relative to that of a standard R_{STD} and then typically in units of permille or per meg (in which case the multiplication would be by a factor of 10^6 per meg).

It should be noted that the MOT metric is distinctly different from reconstructions of average SST. Although the temperature and the noble gas content of a water parcel are set at the ocean surface, these water parcels are then advected down into the ocean interior. Both the temperature and noble gas content of the water parcel are conserved as the parcel moves through the ocean interior. Thus, the atmospheric noble gas content is representative of the noble gas content of all water parcels and thereby integrates over water masses of different ventilation ages. MOT may therefore be thought of as an integrated SST signal, biased towards the deep-water forming high latitudes, with contributions from the last ~2,000 years (e.g., Matsumoto, 2007). Nonetheless, any change in MOT is instantaneously captured by this noble gas thermometer. The only temporal lag is given by the time it takes for air-sea gas exchange to occur, which for noble gases in on timescale of hours to days (Seltzer et al., 2019), and for the signal to then mix within the atmosphere, which takes about one year (Orsi, 2013). These small temporal lags considered, all we require to reconstruct past MOT is a proxy archive from which we can reconstruct the past atmospheric noble gas composition, which is representative of the noble gas content of the whole ocean and is thus proportional to the global OHC at the time of the sample age. This is exactly what ice cores allow us to do.

Gas	**N_2**	**Ar**	**Kr**	**Xe**
Natural abundance [%]	78.08	0.934	$1.1 \cdot 10^{-4}$	$8.7 \cdot 10^{-6}$
% Ocean	0.6	1.3	2.5	4.8

Table 1.1.: Natural abundances of the gases used for noble gas thermometry, N_2, Ar, Kr, and Xe, and their approximate partitioning between the atmosphere and the ocean. Although atmospheric Kr concentration has been revised to 1.099 ± 0.009 ppm almost 20 years ago (Aoki and Makide, 2005), many publications still use a value of 1.14 ppm.

1.4. Ice cores

Polar ice sheets from Greenland and Antarctica offer an invaluable archive for the reconstruction of past climate and in particular past atmospheric composition. In the absence of seasonal melting and major wind-drift, snow fall events on top of a polar ice sheet are stratigraphically ordered. The snow itself contains information on the evolution of regional temperature and the hydrological cycle through changes in its water isotopic composition. Additionally, various aerosol species are deposited on the ice sheet, where they are incorporated into the ice matrix and act as a proxy for past climate in their source region and for atmospheric transport patterns. Finally, polar ice contains atmospheric air. In the 50–120 m of consolidating snow on top of an ice sheet, the so-called firn layer, atmospheric air resides in small air pockets that are connected to one another and to the atmosphere through an interwoven network of tiny ducts (Schwander and Stauffer, 1984). As new layers of snow accumulate at the surface, the older layers are gradually pushed to greater depths. With increasing hydrostatic pressure, snow crystalline structure transforms through sintering and creep, the snow is compacted, and eventually turns into ice. In the compacting snow, the ducts between air pockets gradually get smaller and fewer, with sintering, creep, grain growth, and minimisation of the surface free energy of the pores (by decreasing surface curvature of the pores) representing competing processes that slowly reduce porosity (Schwander, 1989). Eventually, at the bottom of the firn column, in the lock-in zone, all pockets are cut off, thus isolating individual samples of firn air in bubbles. These gas inclusions in polar ice thereby offer not just proxy information but a direct insight into the composition of the past atmosphere. Unlike for proxies from other climate archives, no biological transfer function is required to reconstruct past atmospheric gas concentrations from ice cores. However, physical processes do alter the composition of air in the firn, such that the air measured in an ice sample is somewhat different from the past atmosphere, as will be discussed in detail in Chapter 3.

As new snow accumulates on top of the ice sheet, the ice matrix and the air inclusions therein are pushed further down, causing them to undergo transformations. With depth, hydrostatic pressure increases, which to first order also controls bubble pressure (Gow, 1968; Langway, 1958). Once the bubble pressure reaches the dissociation pressure of air hydrates, mostly given by that of N_2 and O_2 multiplied by their abundances, bubbles start to disintegrate and form air hydrates (clathrates; Miller, 1969; Shoji and Langway, 1982). This transformation takes place over a depth interval of several hundreds of meters, the bubble to clathrate transition zone (BCTZ). Depending on site temperature and accumulation rate, the BCTZ typically falls somewhere between 500 m and 1,500 m below the surface (Uchida et al., 2014 and references therein). At Dome C, it roughly spans from 600 m to 1,200 m. In this BCTZ, differences in permeation coefficients and dissociation pressures lead to differences in composition of gas already in the clathrate phase and the gas left behind in the bubbles (Ikeda et al., 1999; Ikeda-Fukazawa et al., 2001; Kobashi et al., 2008). The slowly permeating heavy noble gases (in particular Xe) may thus be enriched in bubbles and depleted in the clathrate phase within the BCTZ (Haeberli et al., 2021). Also, as an SI-clathrate forming gas, Xe might be excluded from the SII-clathrates formed by the other atmospheric gases, and instead be found dissolved in the ice after bubble dissociation (Haeberli et al., 2021).

The upper part of the BCTZ is characterised by relatively more brittle ice than the rest of the core directly after core retrieval. The ice in this section is especially vulnerable to the rapid decompression during hoisting of the core to the surface and after core retrieval as the high bubble pressure exceeds the tensile strength of the surrounding ice matrix (Neff, 2014). This is aggravated as the core also experiences significant temperature stress after being hoisted to the surface. Cracks occur more frequently in ice retrieved from this depth range, which in turn may be subject to gas loss. In case of gas loss, the different air composition in bubbles and clathrates in the BCTZ may bring about fractionation in noble-gas ratios. Below the BCTZ, the air is again representative of the initial firn composition, albeit slightly smoothed due to gradual diffusion of gases through the ice lattice (Lüthi et al., 2010). This smoothing is further helped by the thinning of layers towards the bottom of the ice sheet, which is accelerated by increasing in situ temperature, hence higher diffusion constants, towards the bottom. Due to this temperature increase, drilling also becomes considerably more challenging, and retrieved ice cores are generally of considerably poorer ice quality with an increased number of cracks and breaks and potentially affected by gas loss. Again, this gas loss may fractionate noble-gas ratios due to the potential exclusion of Xe from clathrates. Haeberli et al., 2021 attribute discrepancies between MOT derived from different noble-gas ratios that they found in most of their samples from the BCTZ and many from the bottom-most part of the EDC ice core precisely to such (mainly Xe) fractionating gas loss. Samples analysed during this PhD-project are all from the clathrated part of the EDC ice core, above the more heavily fractured bottom-most meters.

In a single archive, polar ice offers a large variety of direct data and proxy information on past climate evolution. However, although all this information can be gained from the same climate archive, its interpretation is somewhat complicated by different age scales for the air inclusions on the one hand, and the ice and impurity proxies on the other hand. About 90% of pores are occluded only in the bottommost 10% of the firn column (Schwander, 1996). Depending on the accumulation rate, the ice at this depth is between ~100 to several thousand years old, whereas air may diffuse down from the atmosphere usually within decades (e.g., Kaspers et al., 2004; Severinghaus et al., 1998; Spahni et al., 2003). Consequently, the trapped air in an ice core is always younger than its surrounding ice matrix. This ice age-gas age difference, called Δage, varies in time as it is a function of accumulation rate and temperature (Buizert, 2021). For the EPICA Dome C (EDC) ice core, which was used for the MOT reconstructions in this PhD-project, Δage is on the order of 1,000–2,000 years during warm, somewhat wetter interglacial periods, and about 3,000–4,000 years during cold and dry glacial periods (Bazin et al., 2013; Veres et al., 2013).

Furthermore, the slow bubble enclosure process as well as the diffusive gas transport in firn, which leads to gradual mixing with older air masses, causes the gas at the bottom of the firn column to consist of atmospheric air of a wide age range, from some decades up to millennia (Nehrbass-Ahles et al., 2020). The firn air trapped inside a polar ice sample is thus best described by a log-normal distribution tailing towards older ages (Köhler et al., 2011; Spahni et al., 2003). We expect older mean ages and a wider gas age distribution at the bottom of the firn column at colder sites with deep firn columns (Kaspers et al., 2004; Nehrbass-Ahles et al., 2020). For the EDC ice core, the empirical relationship linking gas age distribution to Δage suggested by Nehrbass-Ahles et al., 2020 (which is based on the method of Fourteau et al., 2017) yields a mean age of about 100–250 years, considerably reducing earlier estimates (Köhler et al., 2011). About 60–100 years may be attributed to the diffusive transport in the firn column (Kaspers et al., 2004; Sturges et al., 2001). As these values are for CO_2, we would expect somewhat older mean ages and wider gas age distributions for Kr and Xe, which have lower diffusivities and smaller concentration gradients in time than CO_2, leading to a slower diffusive mixing process.

Temporal resolution and age span of an ice core are given by a variety of factors, such as site temperature, accumulation rate, bedrock topography and associated glacier flow, and local geothermal heat flux. The relatively high temperatures and accumulation rates in Greenland allow for annual resolution of the last 60 kyr and high temporal resolution throughout the Greenland records (Svensson et al., 2008), although the gas-age distribution mentioned above leads to a smoothing of the gas records. However, Greenlandic ice cores "only" continuously cover the period back to the LIG, some 123 kyr into the past (North Greenland Ice Core Project members, 2004), although some older ice was found in folded sections of different ice cores (Landais, 2003; NEEM community members, 2013). Similarly high temporal resolutions can be gained from high accumulation sites in coastal regions and the western part of Antarctica (Sigl et al., 2016).

The plateau region of the East Antarctic Ice Sheet, on the other hand, features the coldest and driest conditions on the planet, and thereby offers ideal conditions for old ice. The currently oldest continuous ice core record, the EPICA Dome C ice core, contains the climate history of the past ~800 kyr (EPICA community members, 2004). Major efforts are currently being undertaken by the international ice core community to expand this record to include the

Mid-Pleistocene transition (~0.9–1.2 Myr) and possibly cover the last 1.5 Myr. As of the 2022/23 summer season, the European effort, the Beyond EPICA – Oldest Ice project, has drilled to ~800 m depth and is hoping to reach the bottom by the end of the 2024/25 season, where ~1.5 Myr old ice is expected (Chung et al., 2023). Australia, China, Japan, Russia, South Korea, and the U.S.A. also intend to drill ice older than 1 Myr within the next decade (see Silva, 2021 for an in-depth overview). Even older, albeit discontinuous ice exists in blue ice areas, in which ancient stagnant ice outcrops (Higgins et al., 2015; Yan et al., 2019). The large age span of east Antarctic ice cores comes at the disadvantage of reduced temporal resolution. The low accumulation rate leads to thin annual snow layers, which are further thinned by hydrostatic pressure as they are pushed towards the bottom of the ice sheet (e.g., Chung et al., 2023), although the thinning is somewhat smaller than at high accumulation sites. Additionally, for gas inclusions, the gradual bubble enclosure and molecular diffusion in the firn column lead to wide gas age distributions and, thus, lower temporal resolution at colder sites with deep firn columns (Nehrbass-Ahles et al., 2020). Also, in the strongly thinned deep part of the ice sheet, diffusion processes can become relevant (Lüthi et al., 2010). The bottom-most meters at the Beyond EPICA – Oldest Ice drilling site is expected to contain some 15–20 kyr per meter (Chung et al., 2023). The very deep, old part of east Antarctic ice cores, thus, typically only allows for reconstructions on the centennial to millennial timescale. Nonetheless, when compared to other proxy records, ice cores can offer supreme temporal resolution over the entire 800 kyr and potentially soon 1.5 Myr that they cover.

Thanks to a variety of dating techniques, age control of ice core records is good. At high accumulation sites, large parts of the core can be dated using annual layer counting (Sigl et al., 2016; Svensson et al., 2008). Chronologies for low accumulation sites, on the other hand, rely on ice flow and accumulation models that are constrained by different age markers (Bouchet et al., 2023). These constraints include radionuclides such as ^{10}Be, ^{40}Ar, or ^{81}Kr, or gas proxies that evolve synchronously with the well-understood orbital parameters, such as $\delta^{18}O_{atm}$, $\delta O_2/N_2$, or total air content. Additionally, links to other chronologies can be made using stratigraphic links provided for example by aligning volcanic ash layers or abrupt changes in CH_4, or by matching of $\delta^{18}O_{atm}$ (Extier et al., 2018) or radionuclides (Adolphi et al., 2018) to $\delta^{18}O_{calcite}$ and the U/Th series of absolutely dated speleothems, respectively. Furthermore, to determine Δage, an estimate of past firn column depth is required, which is typically gained from $\delta^{15}N_2$. For the EDC ice core, multiple chronologies have been in use over the last ~20 years. The original EDC2 (EPICA community members, 2004) and soon after EDC3 (Parrenin et al., 2007) chronologies were replaced by the AICC2012, a chronology that links the chronologies of the EDC, NGRIP, TALDICE, EDML, and Vostok ice cores (Bazin et al., 2013; Veres et al., 2013). More recently, Extier et al., 2018 have presented a further update to the EDC chronology and Bouchet et al., 2023 published the AICC2023, an improved version of the AICC2012. For ease of comparison to other published records, ages are consistently expressed on the AICC2012 chronology in this PhD-thesis. AICC2012 has an average chronological uncertainty of 2.5 kyr, somewhat higher than the 1.8 kyr of the new AICC2023 (Bazin et al., 2013; Bouchet et al., 2023; Veres et al., 2013).

1.5. MOT records from noble-gas ratios in ice cores

Ice cores offer a continuous record of the atmospheric composition for the past ~800 kyr in high temporal resolution and with good age control. By studying past atmospheric noble-gas ratios, we can reconstruct past OHC, a fundamental metric of the climate system. Indeed, noble-gas ratios in ice cores have been measured for close to thirty years by now (Craig and Wiens, 1996; Severinghaus et al., 2003). However, although the solubility influence on these ratios was recognised by these early studies, their focus lay on constraining firn fractionation processes and gas loss effects. The potential of atmospheric noble-gas ratios for OHC reconstruction was pointed out by Ralph Keeling (Scripps Institution of Oceanography) as acknowledged by Craig and Wiens, 1996, but noble-gas ratios as MOT proxies were only realised for the first time by Headly and Severinghaus, 2007. Building on the analytical approach of Sowers et al., 1989 and Severinghaus et al., 2003, they measured $\delta Kr/N_2$ in 63 ice core samples from GISP 2. Their derived Holocene-Last Glacial Maximum (LGM) MOT difference of 2.7 ± 0.6 °C is in line with other ocean temperature reconstructions (see Section 1.2.2.). The analytical method they used is described in further details in the PhD-thesis of Headly (Headly, 2008).

Since then, progress has been made through advances in analytical technique (Bereiter et al., 2018a; Häberli, 2019; see Chapter 2 for more details) and proxy understanding (Pöppelmeier et al., 2023; Ritz et al., 2011). Interest in past MOT was further increased as the key role of OHC for Earth's energy imbalance on glacial–interglacial timescale was realised (Baggenstos et al., 2019). This link has recently been utilised also with datasets of benthic $\delta^{18}O_C$ (Shackleton et al., 2023). At the same time, interpretation of MOT records is complicated by inconsistencies between MOT reconstructions from different noble-gas ratios and from different ice cores. These inconsistencies point towards a yet incomplete understanding of firn fractionation processes (Shackleton, 2019; see Chapter 3 for details). Although they for now prevent us from interpreting reconstructed absolute MOT, relative MOT changes appear to be unaffected.

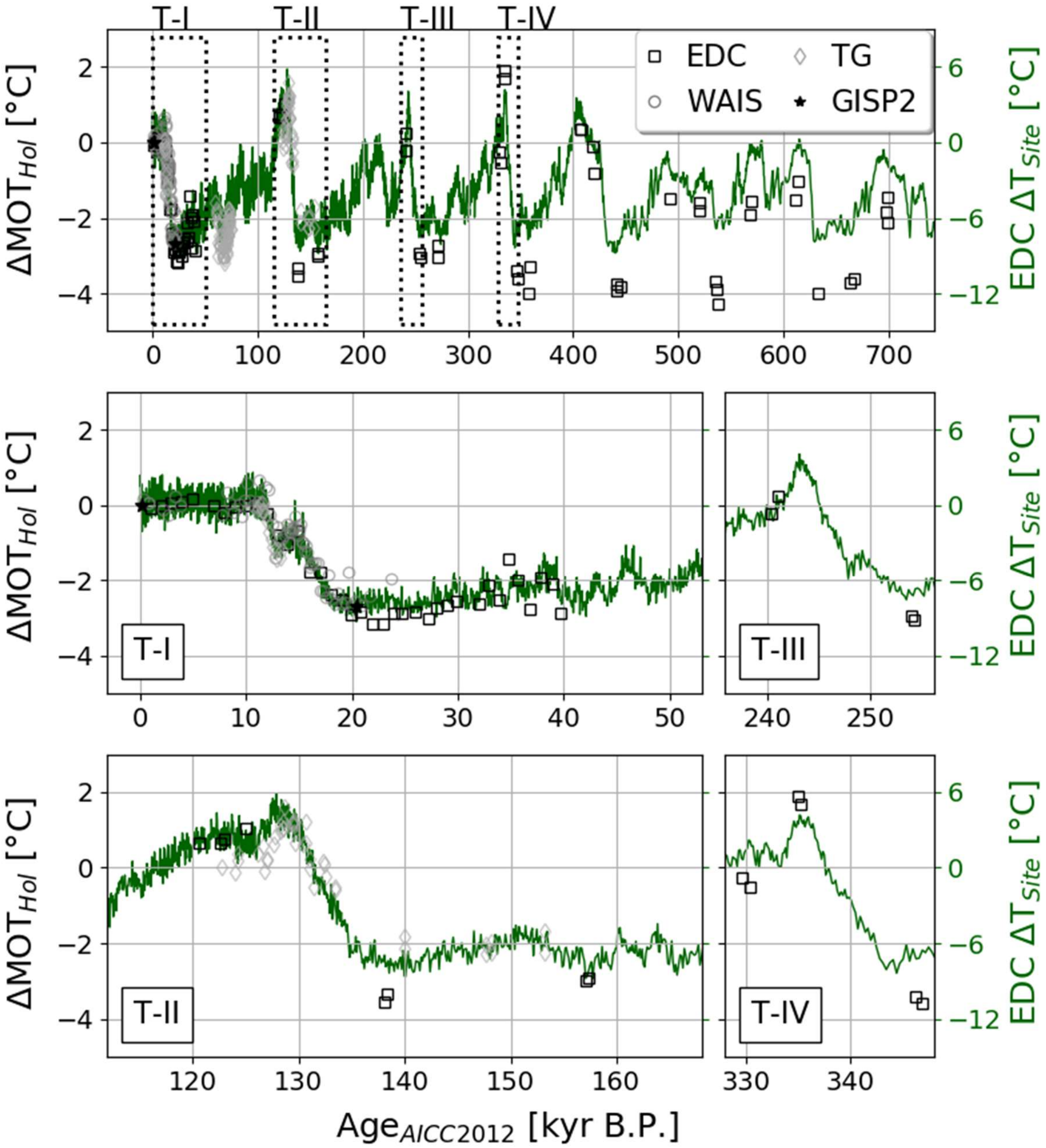

Figure 1.3.: Overview of published MOT datasets. EDC data is from Baggenstos et al., 2019 and from Haeberli et al., 2021; TG data are from Shackleton et al., 2021; 2020; 2019; WAIS data is from Bereiter et al., 2018b; and GISP2 data is from Headly and Severinghaus, 2007. Shown is the mean of the MOT values derived from the three noble-gas ratios, except for the snapshot data of Haeberli et al., 2021, where only δKr/N$_2$-derived MOT is plotted, as δXe/N$_2$ and δXe/Kr data were suspected to be affected by gas loss. All datasets are plotted relative to the MOT Holocene (0–10 kyr) mean value of the respective ice core. Terminations II-IV were studied in detail during this PhD-project and are thus shown in greater detail. Before this PhD-project, no high-resolution MOT record existed for these three terminations. For orientation, we also show EDC site temperature anomalies (Landais et al., 2021).

In recent years, some first high-resolution MOT records were published, using ice from WAIS Divide, Taylor Glacier, and EDC (Figure 1.3.). Most of these records focus on the MOT evolution across Termination I (Baggenstos et al., 2019; Bereiter et al., 2018b; Shackleton et al., 2019), but there also exists data for Marine Isotope Stage 4 (Shackleton et al., 2021) and the LIG (Shackleton et al., 2020). These records also helped to constrain the role of MOT in past sea level high-stands and deep ocean carbon storage, and support mechanistic links between variations in the AMOC strength and MOT suggested by modelling studies (Galbraith et al., 2016; Pedro et al., 2018). Furthermore, snapshots of glacial and interglacial MOT across the past 700 kyr (Haeberli et al., 2021) and of some ~2 Myr old samples from the Allan Hills blue ice area (Yan et al., 2019) give insights on the glacial–interglacial MOT amplitude for different periods of the Quaternary.

However, highly resolved MOT records still only exist for a few select periods. To further our mechanistic understanding of controls on MOT evolution and to find potential past analogues for future climate under anthropogenic climate warming, glacial terminations and their subsequent interglacials are of particular interest. To date, MOT reconstructions of glacial terminations prior to Termination I are still missing. Also, no high-resolution interglacial MOT data exists for interglacial periods prior to the LIG. Within this PhD-project, we measured noble-gas ratios in ice core samples across Termination II, III, and IV, and their subsequent interglacial periods. Together with published Termination I data (Baggenstos et al., 2019), the EDC MOT record now spans the last four glacial terminations and subsequent interglacials and sheds light on the OHC component of Earth's energy imbalance during these major transitions and warm states of the global climate and the role of AMOC therein.

1.6. Aims of this PhD-project and structure of the thesis

The aims of this PhD-project were twofold. The first part of the project was focused on optimising the analytical method with the overall goals of limiting drill fluid influence and improving reproducibility. When measuring their MOT snapshot dataset, Haeberli et al., 2021 found several of their samples to be affected by drilling fluid contamination. To tackle this problem, we decided to increase the surface area in the existing liquid nitrogen (LN_2) trap, thus increasing the extraction system's capacity for retaining drilling fluid and, thus, removing it from the sample air. Consequently, only three out of the 72 samples measured during this PhD-project were slightly affected by drilling fluid contamination, compared to a total of 13 affected samples in the dataset of Haeberli et al., 2021. Reproducibility of measured gas ratios could be markedly improved, especially for ratios measured on the Delta V isotope ratio mass spectrometer. This was achieved by minimising changes in measurement conditions by using only a small set of sample tubes and by limiting the duration of the measurement period. Reproducibility was further improved by limiting mass spectrometer instabilities by careful choice of source parameters and subsequent signal monitoring. Furthermore, the formerly applied corrections for non-linearity effects during mass spectrometer measurements were found to not remove all mass spectrometer artefacts. Thus, mass spectrometer corrections were adjusted accordingly and now allow for more accurate MOT reconstructions. Finally, an update to the extraction unit software ensures that future measurement periods can rely on a stable software. These optimisations of the analytical method are described in detail in Chapter 2.

In the second half of this PhD-project, the benefits of the improved reproducibility could then be utilised to pursue the project's main goal: to produce a MOT dataset for Terminations II-IV and their subsequent interglacials. This was done by measuring noble gas elemental and isotopic ratios in 72 EDC samples. To transform ice core noble-gas ratios into a reconstruction of past MOT, we need to correct the measured ratios for various fractionation processes that occur in the firn column. This is done using the isotopic ratios measured alongside the elemental noble-gas ratios. The derived past atmospheric noble-gas ratios are then translated to MOT using an atmosphere-ocean box model. The firn fractionation processes, their corrections, and the box model are described in detail in Chapter 3. Chapter 3 also looks more closely into the inconsistencies between reconstructed absolute MOT derived from different noble-gas ratios.

With this Termination I-IV MOT dataset, we aim to gain a more comprehensive picture of glacial–interglacial MOT changes and study MOT intensity and variability in past interglacial periods. Furthermore, the influence of AMOC variability on OHC should be studied, especially during the onsets of MIS 9e and MIS 5e, during which AMOC resumption led to overshoots in CO_2, CH_4, and Antarctic temperature (Bereiter et al., 2015; Loulergue et al., 2008; Parrenin et al., 2013). Chapter 4 gives an interpretation of our new MOT dataset.

In parallel to optimising the analytical method, we worked on publishing a dataset consisting of 86 EDC noble gas samples that had been measured by Häberli, 2019. The aim of the study was to constrain glacial–interglacial MOT amplitudes across the past 700 kyr. Our analysis of the dataset showed that peak glacial MOT conditions were consistently about 3.3 ± 0.8 °C (this comprises both stochastic and systematic uncertainty) colder than the Holocene, although a small trend towards even colder MOT might be visible for glacial periods prior to MIS 10. The data also shows substantially colder interglacial MOT during the lukewarm interglacials prior to the Mid-Brunhes Event 450 kyr ago. Consequently, glacial–interglacial MOT amplitudes were strongly reduced during that period. Furthermore, the snapshot data hints at considerable overshoots in MOT at the onset of MIS 5e and MIS 9e, probably in response to a resumption of the AMOC. The paper was published in Climate of the Past (Haeberli et al., 2021) and is reproduced in Chapter 5 of this thesis.

In addition to writing this thesis, the last few months of the project were also used to prepare the laboratory for future measurement periods. This involved replacing most of the connections of the extraction unit and the mass spectrometers. The first measurement period after completion of this PhD is aimed to reconstruct MOT evolution during MIS 8, which for the first time will allow us to study MOT variability throughout an entire glacial–interglacial cycle (MIS 9e to MIS 7e). Additionally, in collaboration with the British Antarctic Survey, we plan to measure 24 samples across D/O-events 7 and 8 using the new Skytrain ice core (Hoffmann et al., 2022; Mulvaney et al., 2023), and thus further our understanding of the role of MOT during fast-paced millennial-scale climate variability. Data from different ice cores and at different temporal resolution will hopefully also help us to improve our understanding of the influence of firn fractionation processes on noble-gas ratios in ice cores. This understanding will also be improved by analysing firn air samples from the 2022/23 year-round firn air sampling campaign at Dome Concordia, which was initiated by the University of Bern and carried out in collaboration with LSCE in Paris. Moreover, firn air sampling of the entire firn column at Little Dome C was initiated by LSCE and samples collected in the summer season 2022/23 will also be measured at the University of Bern. A more extensive outlook about further MOT datasets of interest and planned future measurements to better constrain firn fractionation corrections is given in Chapter 6. Finally, the appendix offers measurement protocols and an overview of all samples measured during this PhD-project.

References

Adkins, J.F., McIntyre, K., Schrag, D.P., 2002. The Salinity, Temperature, and δ18O of the Glacial Deep Ocean. Science 298, 1769–1773. https://doi.org/10.1126/science.1076252

Adkins, J.F., Schrag, D.P., 2001. Pore fluid constraints on deep ocean temperature and salinity during the Last Glacial Maximum. Geophys. Res. Lett. 28, 771–774. https://doi.org/10.1029/2000GL011597

Adolphi, F., Bronk Ramsey, C., Erhardt, T., Edwards, R.L., Cheng, H., Turney, C.S.M., Cooper, A., Svensson, A., Rasmussen, S.O., Fischer, H., Muscheler, R., 2018. Connecting the Greenland ice-core and U⁄Th timescales via cosmogenic radionuclides: testing the synchroneity of Dansgaard–Oeschger events. Clim. Past 14, 1755–1781. https://doi.org/10.5194/cp-14-1755-2018

Aoki, N., Makide, Y., 2005. The Concentration of Krypton in the Atmosphere—Its Revision after Half a Century—. Chem. Lett. 34, 1396–1397. https://doi.org/10.1246/cl.2005.1396

Armstrong McKay, D.I., Staal, A., Abrams, J.F., Winkelmann, R., Sakschewski, B., Loriani, S., Fetzer, I., Cornell, S.E., Rockström, J., Lenton, T.M., 2022. Exceeding 1.5°C global warming could trigger multiple climate tipping points. Science 377, eabn7950. https://doi.org/10.1126/science.abn7950

Baggenstos, D., Häberli, M., Schmitt, J., Shackleton, S.A., Birner, B., Severinghaus, J.P., Kellerhals, T., Fischer, H., 2019. Earth's radiative imbalance from the Last Glacial Maximum to the present. Proc. Natl. Acad. Sci. 116, 14881–14886. https://doi.org/10.1073/pnas.1905447116

Barker, S., Chen, J., Gong, X., Jonkers, L., Knorr, G., Thornalley, D., 2015. Icebergs not the trigger for North Atlantic cold events. Nature 520, 333–336. https://doi.org/10.1038/nature14330

Bates, S.L., Siddall, M., Waelbroeck, C., 2014. Hydrographic variations in deep ocean temperature over the mid-Pleistocene transition. Quat. Sci. Rev. 88, 147–158. https://doi.org/10.1016/j.quascirev.2014.01.020

Bazin, L., Landais, A., Lemieux-Dudon, B., Toyé Mahamadou Kele, H., Veres, D., Parrenin, F., Martinerie, P., Ritz, C., Capron, E., Lipenkov, V., Loutre, M.-F., Raynaud, D., Vinther, B., Svensson, A., Rasmussen, S.O., Severi, M., Blunier, T., Leuenberger, M., Fischer, H., Masson-Delmotte, V., Chappellaz, J., Wolff, E., 2013. An optimized multi-proxy, multi-site Antarctic ice and gas orbital chronology (AICC2012): 120–800 ka. Clim. Past 9, 1715–1731. https://doi.org/10.5194/cp-9-1715-2013

Bender, M.L., Barnett, B., Dreyfus, G., Jouzel, J., Porcelli, D., 2008. The contemporary degassing rate of 40Ar from the solid Earth. Proc. Natl. Acad. Sci. 105, 8232–8237. https://doi.org/10.1073/pnas.0711679105

Bereiter, B., Eggleston, S., Schmitt, J., Nehrbass-Ahles, C., Stocker, T.F., Fischer, H., Kipfstuhl, S., Chappellaz, J., 2015. Revision of the EPICA Dome C CO $_2$ record from 800 to 600 kyr before present: Analytical bias in the EDC CO2 record. Geophys. Res. Lett. 42, 542–549. https://doi.org/10.1002/2014GL061957

Bereiter, B., Kawamura, K., Severinghaus, J.P., 2018a. New methods for measuring atmospheric heavy noble gas isotope and elemental ratios in ice core samples. Rapid Commun. Mass Spectrom. 32, 801–814. https://doi.org/10.1002/rcm.8099

Bereiter, B., Shackleton, S., Baggenstos, D., Kawamura, K., Severinghaus, J., 2018b. Mean global ocean temperatures during the last glacial transition. Nature 553, 39–44. https://doi.org/10.1038/nature25152

Berger, A., Loutre, M.F., 2002. An Exceptionally Long Interglacial Ahead? Science 297, 1287–1288. https://doi.org/10.1126/science.1076120

Bintanja, R., Van De Wal, R.S.W., Oerlemans, J., 2005. Modelled atmospheric temperatures and global sea levels over the past million years. Nature 437, 125–128. https://doi.org/10.1038/nature03975

Birkel, S.D., 2023. Climate Reanalyzer [WWW Document]. Mon. Reanalysis Time Ser. URL https://climatereanalyzer.org/research_tools/monthly_tseries/ (accessed 8.29.23).

Boehm, S., Jeffery, L., Levin, K., Hecke, J., Schumer, C., Fyson, C., Majid, A., Jaeger, J., Nilsson, A., Naimoli, S., Thwaites, J., Cassidy, E., Waite, R., Wilson, R., Castellanos, S., Singh, N., Lee, A., Geiges, A., 2022. State of Climate Action 2022. World Resour. Inst. https://doi.org/10.46830/wrirpt.22.00028

Böhm, E., Lippold, J., Gutjahr, M., Frank, M., Blaser, P., Antz, B., Fohlmeister, J., Frank, N., Andersen, M.B., Deininger, M., 2015. Strong and deep Atlantic meridional overturning circulation during the last glacial cycle. Nature 517, 73–76. https://doi.org/10.1038/nature14059

Bouchet, M., Landais, A., Grisart, A., Parrenin, F., Prié, F., Jacob, R., Fourré, E., Capron, E., Raynaud, D., Lipenkov, V.Y., Loutre, M.-F., Extier, T., Svensson, A., Legrain, E., Martinerie, P., Leuenberger, M., Jiang, W., Ritterbusch, F., Lu, Z.-T., Yang, G.-M., 2023. The AICC2023 chronological framework and associated timescale for the EPICA Dome C ice core (preprint). Ice Dynamics/Ice Cores/Milankovitch. https://doi.org/10.5194/egusphere-2023-1081

Buizert, C., 2021. The Ice Core Gas Age-Ice Age Difference as a Proxy for Surface Temperature. Geophys. Res. Lett. 48, e2021GL094241. https://doi.org/10.1029/2021GL094241

Caesar, L., Rahmstorf, S., Robinson, A., Feulner, G., Saba, V., 2018. Observed fingerprint of a weakening Atlantic Ocean overturning circulation. Nature 556, 191–196. https://doi.org/10.1038/s41586-018-0006-5

Chandler, D.M., Langebroek, P.M., 2023. Glacial-interglacial Circumpolar Deep Water temperatures during the last 800,000 years: estimates from a synthesis of bottom water temperature reconstructions.

Chappell, J., Shackleton, N.J., 1986. Oxygen isotopes and sea level. Nature 324, 137–140. https://doi.org/10.1038/324137a0

Cheng, L., Von Schuckmann, K., Abraham, J.P., Trenberth, K.E., Mann, M.E., Zanna, L., England, M.H., Zika, J.D., Fasullo, J.T., Yu, Y., Pan, Y., Zhu, J., Newsom, E.R., Bronselaer, B., Lin, X., 2022. Past and future ocean warming. Nat. Rev. Earth Environ. 3, 776–794. https://doi.org/10.1038/s43017-022-00345-1

Chung, A., Parrenin, F., Steinhage, D., Mulvaney, R., Martín, C., Cavitte, M.G.P., Lilien, D.A., Helm, V., Taylor, D., Gogineni, P., Ritz, C., Frezzotti, M., O'Neill, C., Miller, H., Dahl-Jensen, D., Eisen, O., 2023. Stagnant ice and age modelling in the Dome C region, Antarctica. The Cryosphere 17, 3461–3483. https://doi.org/10.5194/tc-17-3461-2023

Craig, H., Wiens, R.C., 1996. Gravitational Enrichment of ^{84} Kr/ ^{36} Ar Ratios in Polar Ice Caps: A Measure of Firn Thickness and Accumulation Temperature. Science 271, 1708–1710. https://doi.org/10.1126/science.271.5256.1708

Curry, W.B., Oppo, D.W., 2005. Glacial water mass geometry and the distribution of δ13C of ΣCO2 in the western Atlantic Ocean. Paleoceanography 20. https://doi.org/10.1029/2004PA001021

Cutler, K.B., Edwards, R.L., Taylor, F.W., Cheng, H., Adkins, J., Gallup, C.D., Cutler, P.M., Burr, G.S., Bloom, A.L., 2003. Rapid sea-level fall and deep-ocean temperature change since the last interglacial period. Earth Planet. Sci. Lett. 206, 253–271. https://doi.org/10.1016/S0012-821X(02)01107-X

Dansgaard, W., Johnsen, S.J., Clausen, H.B., Dahl-Jensen, D., Gundestrup, N.S., Hammer, C.U., Hvidberg, C.S., Steffensen, J.P., Sveinbjörnsdottir, A.E., Jouzel, J., Bond, G., 1993. Evidence for general instability of past climate from a 250-kyr ice-core record. Nature 364, 218–220. https://doi.org/10.1038/364218a0

DeVries, T., Holzer, M., 2019. Radiocarbon and Helium Isotope Constraints on Deep Ocean Ventilation and Mantle-3He Sources. J. Geophys. Res. Oceans 124, 3036–3057. https://doi.org/10.1029/2018JC014716

Du, J., Haley, B.A., Mix, A.C., 2020. Evolution of the Global Overturning Circulation since the Last Glacial Maximum based on marine authigenic neodymium isotopes. Quat. Sci. Rev. 241, 106396. https://doi.org/10.1016/j.quascirev.2020.106396

Duplessy, J.-C., Moyes, J., Pujol, C., 1980. Deep water formation in the North Atlantic Ocean during the last ice age. Nature 286, 479–482. https://doi.org/10.1038/286479a0

Elderfield, H., Ferretti, P., Greaves, M., Crowhurst, S., McCave, I.N., Hodell, D., Piotrowski, A.M., 2012. Evolution of Ocean Temperature and Ice Volume Through the Mid-Pleistocene Climate Transition. Science 337, 704–709. https://doi.org/10.1126/science.1221294

Emiliani, C., 1955. Pleistocene Temperatures. J. Geol. 63, 538–578.

EPICA community members, 2004. Eight glacial cycles from an Antarctic ice core. Nature 429, 623–628. https://doi.org/10.1038/nature02599

Extier, T., Landais, A., Bréant, C., Prié, F., Bazin, L., Dreyfus, G., Roche, D.M., Leuenberger, M., 2018. On the use of δ18Oatm for ice core dating. Quat. Sci. Rev. 185, 244–257. https://doi.org/10.1016/j.quascirev.2018.02.008

Fourteau, K., Faïn, X., Martinerie, P., Landais, A., Ekaykin, A.A., Lipenkov, V.Y., Chappellaz, J., 2017. Analytical constraints on layered gas trapping and smoothing of atmospheric variability in ice under low-accumulation conditions. Clim. Past 13, 1815–1830. https://doi.org/10.5194/cp-13-1815-2017

Frölicher, T.L., Fischer, E.M., Gruber, N., 2018. Marine heatwaves under global warming. Nature 560, 360–364. https://doi.org/10.1038/s41586-018-0383-9

Galbraith, E.D., Merlis, T.M., Palter, J.B., 2016. Destabilization of glacial climate by the radiative impact of Atlantic Meridional Overturning Circulation disruptions: RADIATIVE IMPACT OF AMOC DISRUPTIONS. Geophys. Res. Lett. 43, 8214–8221. https://doi.org/10.1002/2016GL069846

Ganachaud, A., Wunsch, C., 2000. Improved estimates of global ocean circulation, heat transport and mixing from hydrographic data. Nature 408, 453–457. https://doi.org/10.1038/35044048

Glasscock, S.K., Hayes, C.T., Redmond, N., Rohde, E., 2020. Changes in Antarctic Bottom Water Formation During Interglacial Periods. Paleoceanogr. Paleoclimatology. https://doi.org/10.1029/2020PA003867

Gordon, A.L., 2014. Southern Ocean polynya. Nat. Clim. Change 4, 249–250. https://doi.org/10.1038/nclimate2179

Gow, A.J., 1968. Bubbles and Bubble Pressures in Antarctic Glacier Ice. J. Glaciol. 7, 167–182. https://doi.org/10.3189/S0022143000030975

Gruber, N., 2011. Warming up, turning sour, losing breath: ocean biogeochemistry under global change. Philos. Trans. R. Soc. Math. Phys. Eng. Sci. 369, 1980–1996. https://doi.org/10.1098/rsta.2011.0003

Häberli, M., 2019. Noble-gas ratios in polar ice cores: a new proxy to infer the mean ocean temperature over the last 700 ka (Diss.). University of Bern, Bern.

Haeberli, M., Baggenstos, D., Schmitt, J., Grimmer, M., Michel, A., Kellerhals, T., Fischer, H., 2021. Snapshots of mean ocean temperature over the last 700 000 years using noble gases in the EPICA Dome C ice core. Clim. Past 17, 843–867. https://doi.org/10.5194/cp-17-843-2021

Hamme, R.C., Emerson, S.R., 2004. The solubility of neon, nitrogen and argon in distilled water and seawater. Deep-Sea Res. 1 11, 1517–1528.

Headly, M.A., 2008. Krypton and xenon in air trapped in polar ice cores: Paleo-atmospheric measurements for estimating past mean ocean temperature and summer snowmelt frequency (diss.). University of California, San Diego.

Headly, M.A., Severinghaus, J.P., 2007. A method to measure Kr/N $_2$ ratios in air bubbles trapped in ice cores and its application in reconstructing past mean ocean temperature. J. Geophys. Res. 112, D19105. https://doi.org/10.1029/2006JD008317

Held, I.M., Soden, B.J., 2006. Robust Responses of the Hydrological Cycle to Global Warming. J. Clim. 19, 5686–5699. https://doi.org/10.1175/JCLI3990.1

Higgins, J.A., Kurbatov, A.V., Spaulding, N.E., Brook, E., Introne, D.S., Chimiak, L.M., Yan, Y., Mayewski, P.A., Bender, M.L., 2015. Atmospheric composition 1 million years ago from blue ice in the Allan Hills, Antarctica. Proc. Natl. Acad. Sci. 112, 6887–6891. https://doi.org/10.1073/pnas.1420232112

Hoffman, J.S., Clark, P.U., Parnell, A.C., He, F., 2017. Regional and global sea-surface temperatures during the last interglaciation. Science 355, 276–279. https://doi.org/10.1126/science.aai8464

Hoffmann, H.M., Grieman, M.M., King, A.C.F., Epifanio, J.A., Martin, K., Vladimirova, D., Pryer, H.V., Doyle, E., Schmidt, A., Humby, J.D., Rowell, I.F., Nehrbass-Ahles, C., Thomas, E.R., Mulvaney, R., Wolff, E.W., 2022. The ST22 chronology for the Skytrain Ice Rise ice core – Part 1: A stratigraphic chronology of the last 2000 years. Clim. Past 18, 1831–1847. https://doi.org/10.5194/cp-18-1831-2022

Huntington, K.W., Petersen, S.V., 2023. Frontiers of Carbonate Clumped Isotope Thermometry. Annu. Rev. Earth Planet. Sci. 51, annurev-earth-031621-085949. https://doi.org/10.1146/annurev-earth-031621-085949

Ikeda, T., Fukazawa, H., Mae, S., Pepin, L., Duval, P., Champagnon, B., Lipenkov, V.Ya., Hondoh, T., 1999. Extreme fractionation of gases caused by formation of clathrate hydrates in Vostok Antarctic Ice. Geophys. Res. Lett. 26, 91–94. https://doi.org/10.1029/1998GL900220

Ikeda-Fukazawa, T., Hondoh, T., Fukumura, T., Fukazawa, H., Mae, S., 2001. Variation in N2/O2 ratio of occluded air in Dome Fuji antarctic ice. J. Geophys. Res. 106, 17799–17810. https://doi.org/10.1029/2000JD000104

Intergovernmental Panel on Climate Change, 2021. Climate Change 2021 – The Physical Science Basis: Working Group I Contribution to the Sixth Assessment Report of the Intergovernmental Panel on Climate Change, 1st ed. Cambridge University Press. https://doi.org/10.1017/9781009157896

Jayne, S., Roemmich, D., Zilberman, N., Riser, S., Johnson, K., Johnson, G., Piotrowicz, S., 2017. The Argo Program: Present and Future. Oceanography 30, 18–28. https://doi.org/10.5670/oceanog.2017.213

Jenkins, W.J., Lott, D.E., Cahill, K.L., 2019. A determination of atmospheric helium, neon, argon, krypton, and xenon solubility concentrations in water and seawater. Mar. Chem. 211, 94–107. https://doi.org/10.1016/j.marchem.2019.03.007

Johnsen, S.J., Dansgaard, W., Clausen, H.B., Langway, C.C., 1972. Oxygen Isotope Profiles through the Antarctic and Greenland Ice Sheets. Nature 235, 429–434. https://doi.org/10.1038/235429a0

Johnson, G.C., 2008. Quantifying Antarctic Bottom Water and North Atlantic Deep Water volumes. J. Geophys. Res. Oceans 113. https://doi.org/10.1029/2007JC004477

Kaspers, K.A., van de Wal, R.S.W., van den Broeke, M.R., Schwander, J., van Lipzig, N.P.M., Brenninkmeijer, C. a. M., 2004. Model calculations of the age of firn air across the Antarctic continent. Atmospheric Chem. Phys. 4, 1365–1380. https://doi.org/10.5194/acp-4-1365-2004

Kobashi, T., Severinghaus, J.P., Kawamura, K., 2008. Argon and nitrogen isotopes of trapped air in the GISP2 ice core during the Holocene epoch (0–11,500 B.P.): Methodology and implications for gas loss processes. Geochim. Cosmochim. Acta 72, 4675–4686. https://doi.org/10.1016/j.gca.2008.07.006

Köhler, P., Knorr, G., Buiron, D., Lourantou, A., Chappellaz, J., 2011. Abrupt rise in atmospheric CO_2 at the onset of the Bølling/Allerød: in-situ ice core data versus true atmospheric signals. Clim. Past 7, 473–486. https://doi.org/10.5194/cp-7-473-2011

Landais, A., 2003. A tentative reconstruction of the last interglacial and glacial inception in Greenland based on new gas measurements in the Greenland Ice Core Project (GRIP) ice core. J. Geophys. Res. 108, 4563. https://doi.org/10.1029/2002JD003147

Landais, A., Stenni, B., Masson-Delmotte, V., Jouzel, J., Cauquoin, A., Fourré, E., Minster, B., Selmo, E., Extier, T., Werner, M., Vimeux, F., Uemura, R., Crotti, I., Grisart, A., 2021. Interglacial Antarctic–Southern Ocean climate decoupling due to moisture source area shifts. Nat. Geosci. 14, 918–923. https://doi.org/10.1038/s41561-021-00856-4

Langway, C.C., 1958. Bubble pressures in Greenland glacier ice. Presented at the Union Géodésique et Géophysique Internationale. Association Internationale d'Hydrologie Scientifique. Symposium de Chamonix, 16–24 sept. 1958, pp. 336–349.

Lawrence, K.T., Woodard, S.C., 2017. Past sea surface temperatures as measured by different proxies-A cautionary tale from the late Pliocene: Exploring the Consistency of PaleoSSTs. Paleoceanography 32, 318–324. https://doi.org/10.1002/2017PA003101

Lea, D.W., Mashiotta, T.A., Spero, H.J., 1999. Controls on magnesium and strontium uptake in planktonic foraminifera determined by live culturing. Geochim. Cosmochim. Acta 63, 2369–2379. https://doi.org/10.1016/S0016-7037(99)00197-0

Lippold, J., Luo, Y., Francois, R., Allen, S.E., Gherardi, J., Pichat, S., Hickey, B., Schulz, H., 2012. Strength and geometry of the glacial Atlantic Meridional Overturning Circulation. Nat. Geosci. 5, 813–816. https://doi.org/10.1038/ngeo1608

Lisiecki, L.E., Raymo, M.E., 2005. A Pliocene-Pleistocene stack of 57 globally distributed benthic δ^{18}O records: PLIOCENE-PLEISTOCENE BENTHIC STACK. Paleoceanography 20, n/a-n/a. https://doi.org/10.1029/2004PA001071

Loeb, N.G., Johnson, G.C., Thorsen, T.J., Lyman, J.M., Rose, F.G., Kato, S., 2021. Satellite and Ocean Data Reveal Marked Increase in Earth's Heating Rate. Geophys. Res. Lett. 48, e2021GL093047. https://doi.org/10.1029/2021GL093047

Loulergue, L., Schilt, A., Spahni, R., Masson-Delmotte, V., Blunier, T., Lemieux, B., Barnola, J.-M., Raynaud, D., Stocker, T.F., Chappellaz, J., 2008. Orbital and millennial-scale features of atmospheric CH4 over the past 800,000 years. Nature 453, 383–386. https://doi.org/10.1038/nature06950

Lüthi, D., Bereiter, B., Stauffer, B., Winkler, R., Schwander, J., Kindler, P., Leuenberger, M., Kipfstuhl, S., Capron, E., Landais, A., Fischer, H., Stocker, T.F., 2010. CO2 and O2/N2 variations in and just below the bubble–clathrate transformation zone of Antarctic ice cores. Earth Planet. Sci. Lett. 297, 226–233. https://doi.org/10.1016/j.epsl.2010.06.023

Lynch-Stieglitz, J., 2017. The Atlantic Meridional Overturning Circulation and Abrupt Climate Change. Annu. Rev. Mar. Sci. 9, 83–104. https://doi.org/10.1146/annurev-marine-010816-060415

Marti, F., Blazquez, A., Meyssignac, B., Ablain, M., Barnoud, A., Fraudeau, R., Jugier, R., Chenal, J., Larnicol, G., Pfeffer, J., Restano, M., Benveniste, J., 2022. Monitoring the ocean heat content change and the Earth energy imbalance from space altimetry and space gravimetry. Earth Syst. Sci. Data 14, 229–249. https://doi.org/10.5194/essd-14-229-2022

Martin, P.A., Lea, D.W., Rosenthal, Y., Shackleton, N.J., Sarnthein, M., Papenfuss, T., 2002. Quaternary deep sea temperature histories derived from benthic foraminiferal Mg/Ca. Earth Planet. Sci. Lett. 198, 193–209. https://doi.org/10.1016/S0012-821X(02)00472-7

Matsumoto, K., 2007. Radiocarbon-based circulation age of the world oceans. J. Geophys. Res. 112, C09004. https://doi.org/10.1029/2007JC004095

Meyssignac, B., Boyer, T., Zhao, Z., Hakuba, M.Z., Landerer, F.W., Stammer, D., Köhl, A., Kato, S., L'Ecuyer, T., Ablain, M., Abraham, J.P., Blazquez, A., Cazenave, A., Church, J.A., Cowley, R., Cheng, L., Domingues, C.M., Giglio, D., Gouretski, V., Ishii, M., Johnson, G.C., Killick, R.E., Legler, D., Llovel, W., Lyman, J., Palmer, M.D., Piotrowicz, S., Purkey, S.G., Roemmich, D., Roca, R., Savita, A., Schuckmann, K.V., Speich, S., Stephens, G., Wang, G., Wijffels, S.E., Zilberman, N., 2019. Measuring Global Ocean Heat Content to Estimate the Earth Energy Imbalance. Front. Mar. Sci. 6, 432. https://doi.org/10.3389/fmars.2019.00432

Miller, S.L., 1969. Clathrate Hydrates of Air in Antarctic Ice. Science 165, 489–490. https://doi.org/10.1126/science.165.3892.489

Mulvaney, R., Wolff, E.W., Grieman, M.M., Hoffmann, H.H., Humby, J.D., Nehrbass-Ahles, C., Rhodes, R.H., Rowell, I.F., Parrenin, F., Schmidely, L., Fischer, H., Stocker, T.F., Christl, M., Muscheler, R., Landais, A., Prié, F., 2023. The ST22 chronology for the Skytrain Ice Rise ice core – Part 2: An age model to the last interglacial and disturbed deep stratigraphy. Clim. Past 19, 851–864. https://doi.org/10.5194/cp-19-851-2023

NEEM community members, 2013. Eemian interglacial reconstructed from a Greenland folded ice core. Nature 493, 489–494. https://doi.org/10.1038/nature11789

Neff, P.D., 2014. A review of the brittle ice zone in polar ice cores. Ann. Glaciol. 55, 72–82. https://doi.org/10.3189/2014AoG68A023

Nehrbass-Ahles, C., Shin, J., Schmitt, J., Bereiter, B., Joos, F., Schilt, A., Schmidely, L., Silva, L., Teste, G., Grilli, R., Chappellaz, J., Hodell, D., Fischer, H., Stocker, T.F., 2020. Abrupt CO2 release to the atmosphere under glacial and early interglacial climate conditions 7.

Neukom, R., Steiger, N., Gómez-Navarro, J.J., Wang, J., Werner, J.P., 2019. No evidence for globally coherent warm and cold periods over the preindustrial Common Era. Nature 571, 550–554. https://doi.org/10.1038/s41586-019-1401-2

North Greenland Ice Core Project members, 2004. High-resolution record of Northern Hemisphere climate extending into the last interglacial period. Nature 431, 147–151. https://doi.org/10.1038/nature02805

Nürnberg, D., Buma, J., Hemleben, C., 1996. Assessing the reliability of magnesium in foraminiferal calcite as a proxy for water mass temperatures. Geochim. Cosmochim. Acta 60, 803–814. https://doi.org/10.1016/0016-7037(95)00446-7

Obase, T., Abe-Ouchi, A., Saito, F., 2021. Abrupt climate changes in the last two deglaciations simulated with different Northern ice sheet discharge and insolation. Sci. Rep. 11, 22359. https://doi.org/10.1038/s41598-021-01651-2

Orsi, A., 2013. Temperature reconstruction at the West Antarctic Ice Sheet Divide, for the last millennium, from the combination of borehole temperature and inert gas isotope measurements. University of California, San Diego.

Orsi, A.H., Jacobs, S.S., Gordon, A.L., Visbeck, M., 2001. Cooling and ventilating the Abyssal Ocean. Geophys. Res. Lett. 28, 2923–2926. https://doi.org/10.1029/2001GL012830

Otto-Bliesner, B.L., Braconnot, P., Harrison, S.P., Lunt, D.J., Abe-Ouchi, A., Albani, S., Bartlein, P.J., Capron, E., Carlson, A.E., Dutton, A., Fischer, H., Goelzer, H., Govin, A., Haywood, A., Joos, F., LeGrande, A.N., Lipscomb, W.H., Lohmann, G., Mahowald, N., Nehrbass-Ahles, C., Pausata, F.S.R., Peterschmitt, J.-Y., Phipps, S.J., Renssen, H., Zhang, Q., 2017. The PMIP4 contribution to CMIP6 – Part 2: Two interglacials, scientific objective and experimental design for Holocene and Last Interglacial simulations. Geosci. Model Dev. 10, 3979–4003. https://doi.org/10.5194/gmd-10-3979-2017

Parrenin, F., Jouzel, J., Kawamura, K., Lemieux-Dudon, B., Loulergue, L., Masson-Delmotte, V., Narcisi, B., Raisbeck, G., Raynaud, D., Ruth, U., Schwander, J., Severi, M., Spahni, R., Steffensen, J.P., Svensson, A., Udisti, R., Waelbroeck, C., Wolff, E., 2007. The EDC3 chronology for the EPICA Dome C ice core. Clim Past 13.

Parrenin, F., Masson-Delmotte, V., Köhler, P., Raynaud, D., Paillard, D., Schwander, J., Barbante, C., Landais, A., Wegner, A., Jouzel, J., 2013. Synchronous Change of Atmospheric CO $_2$ and Antarctic Temperature During the Last Deglacial Warming. Science 339, 1060–1063. https://doi.org/10.1126/science.1226368

Past Interglacials Working Group of PAGES, 2016. Interglacials of the last 800,000 years. Rev. Geophys. 54, 162–219. https://doi.org/10.1002/2015RG000482

Pawlowicz, R., 2013. Key Physical Variables in the Ocean: Temperature, Salinity, and Density | Learn Science at Scitable [WWW Document]. URL https://www.nature.com/scitable/knowledge/library/key-physical-variables-in-the-ocean-temperature-102805293/ (accessed 8.18.23).

Pedro, J.B., Jochum, M., Buizert, C., He, F., Barker, S., Rasmussen, S.O., 2018. Beyond the bipolar seesaw: Toward a process understanding of interhemispheric coupling. Quat. Sci. Rev. 192, 27–46. https://doi.org/10.1016/j.quascirev.2018.05.005

Pöppelmeier, F., Baggenstos, D., Grimmer, M., Liu, Z., Schmitt, J., Fischer, H., Stocker, T.F., 2023. The Effect of Past Saturation Changes on Noble Gas Reconstructions of Mean Ocean Temperature. Geophys. Res. Lett. 50, e2022GL102055. https://doi.org/10.1029/2022GL102055

Pöppelmeier, F., Blaser, P., Gutjahr, M., Jaccard, S.L., Frank, M., Max, L., Lippold, J., 2020. Northern-sourced water dominated the Atlantic Ocean during the Last Glacial Maximum. Geology 48, 826–829. https://doi.org/10.1130/G47628.1

Pritchard, H.D., Ligtenberg, S.R.M., Fricker, H.A., Vaughan, D.G., Van Den Broeke, M.R., Padman, L., 2012. Antarctic ice-sheet loss driven by basal melting of ice shelves. Nature 484, 502–505. https://doi.org/10.1038/nature10968

Regenberg, M., Regenberg, A., Garbe-Schönberg, D., Lea, D.W., 2014. Global dissolution effects on planktonic foraminiferal Mg/Ca ratios controlled by the calcite-saturation state of bottom waters. Paleoceanography 29, 127–142. https://doi.org/10.1002/2013PA002492

Riser, S.C., Freeland, H.J., Roemmich, D., Wijffels, S., Troisi, A., Belbéoch, M., Gilbert, D., Xu, J., Pouliquen, S., Thresher, A., Le Traon, P.-Y., Maze, G., Klein, B., Ravichandran, M., Grant, F., Poulain, P.-M., Suga, T., Lim, B., Sterl, A., Sutton, P., Mork, K.-A., Vélez-Belchí, P.J., Ansorge, I., King, B., Turton, J., Baringer, M., Jayne, S.R., 2016. Fifteen years of ocean observations with the global Argo array. Nat. Clim. Change 6, 145–153. https://doi.org/10.1038/nclimate2872

Ritz, S.P., Stocker, T.F., Severinghaus, J.P., 2011. Noble gases as proxies of mean ocean temperature: sensitivity studies using a climate model of reduced complexity. Quat. Sci. Rev. 30, 3728–3741. https://doi.org/10.1016/j.quascirev.2011.09.021

Rodríguez-Sanz, L., Bernasconi, S.M., Marino, G., Heslop, D., Müller, I.A., Fernandez, A., Grant, K.M., Rohling, E.J., 2017. Penultimate deglacial warming across the Mediterranean Sea revealed by clumped isotopes in foraminifera. Sci. Rep. 7, 16572. https://doi.org/10.1038/s41598-017-16528-6

Rohling, E.J., Foster, G.L., Gernon, T.M., Grant, K.M., Heslop, D., Hibbert, F.D., Roberts, A.P., Yu, J., 2022. Comparison and Synthesis of Sea-Level and Deep-Sea Temperature Variations Over the Past 40 Million Years. Rev. Geophys. 60. https://doi.org/10.1029/2022RG000775

Rohling, E.J., Foster, G.L., Grant, K.M., Marino, G., Roberts, A.P., Tamisiea, M.E., Williams, F., 2014. Sea-level and deep-sea-temperature variability over the past 5.3 million years. Nature 508, 477–482. https://doi.org/10.1038/nature13230

Rohling, E.J., Yu, J., Heslop, D., Foster, G.L., Opdyke, B., Roberts, A.P., 2021. Sea level and deep-sea temperature reconstructions suggest quasi-stable states and critical transitions over the past 40 million years. Sci. Adv. 7, eabf5326. https://doi.org/10.1126/sciadv.abf5326

Rosell-Melé, A., Prahl, F.G., 2013. Seasonality of U K ′ 37 temperature estimates as inferred from sediment trap data. Quat. Sci. Rev. 72, 128–136. https://doi.org/10.1016/j.quascirev.2013.04.017

Rothlisberger, R., Mudelsee, M., Bigler, M., de Angelis, M., Fischer, H., Hansson, M., Lambert, F., Masson-Delmotte, V., Sime, L., Udisti, R., Wolff, E.W., 2008. The Southern Hemisphere at glacial terminations: insights from the Dome C ice core. Clim Past.

Ruddiman, W.F., McIntyre, A., 1981. The mode and mechanism of the last deglaciation: Oceanic evidence. Quat. Res. 16, 125–134. https://doi.org/10.1016/0033-5894(81)90040-5

Rühlemann, C., Butzin, M., 2006. Alkenone temperature anomalies in the Brazil-Malvinas Confluence area caused by lateral advection of suspended particulate material: ALKENONE TEMPERATURE ANOMALIES. Geochem. Geophys. Geosystems 7, n/a-n/a. https://doi.org/10.1029/2006GC001251

Sabine, C.L., Feely, R.A., Gruber, N., Key, R.M., Lee, K., Bullister, J.L., Wanninkhof, R., Wong, C.S., Wallace, D.W.R., Tilbrook, B., Millero, F.J., Peng, T.-H., Kozyr, A., Ono, T., Rios, A.F., 2004. The Oceanic Sink for Anthropogenic CO $_2$. Science 305, 367–371. https://doi.org/10.1126/science.1097403

Schlesinger, W.H., Bernhardt, E.S., 2013. Biogeochemistry. An Analysis of Global Change, 3rd ed. Academic Press, Waltham, MA, USA.

Schrag, D.P., Hampt, G., Murray, D.W., 1996. Pore Fluid Constraints on the Temperature and Oxygen Isotopic Composition of the Glacial Ocean. Science 272, 1930–1932. https://doi.org/10.1126/science.272.5270.1930

Schwander, J., 1996. Gas diffusion in firn, in: Chemical Exchange between the Atmosphere and Polar Snow, NATO ASI Series. Series I: Global Environmental Change. Springer-Verlag, Berlin, Heidelberg and New York, pp. 527–540.

Schwander, J., 1989. The transformation of snow to ice and the occlusion of gases. Environ. Rec. Glaciers Ice Sheets 53–67. https://doi.org/10.48350/161003

Schwander, J., Stauffer, B., 1984. Age difference between polar ice and the air trapped in its bubbles. Nature 311, 45–47. https://doi.org/10.1038/311045a0

Seltzer, A.M., Ng, J., Severinghaus, J.P., 2019. Precise determination of Ar, Kr and Xe isotopic fractionation due to diffusion and dissolution in fresh water. Earth Planet. Sci. Lett. 514, 156–165. https://doi.org/10.1016/j.epsl.2019.03.008

Severinghaus, J.P., Brook, E.J., 1999. Abrupt Climate Change at the End of the Last Glacial Period Inferred from Trapped Air in Polar Ice. Science 286, 930–934. https://doi.org/10.1126/science.286.5441.930

Severinghaus, J.P., Grachev, A., Luz, B., Caillon, N., 2003. A method for precise measurement of argon 40/36 and krypton/argon ratios in trapped air in polar ice with applications to past firn thickness and abrupt climate change in Greenland and at Siple Dome, Antarctica. Geochim. Cosmochim. Acta 67, 325–343. https://doi.org/10.1016/S0016-7037(02)00965-1

Severinghaus, J.P., Sowers, T., Brook, E.J., Alley, R.B., Bender, M.L., 1998. fractionated gases in polar ice 391, 6.

Shackleton, N., 1967. Oxygen Isotope Analyses and Pleistocene Temperatures Re-assessed. Nature 215, 15–17. https://doi.org/10.1038/215015a0

Shackleton, S., 2019. Tracking Past Changes in Ocean Heat Content with Atmospheric Noble Gases in Ice Cores. University of California, San Diego.

Shackleton, S., Baggenstos, D., Menking, J.A., Dyonisius, M.N., Bereiter, B., Bauska, T.K., Rhodes, R.H., Brook, E.J., Petrenko, V.V., McConnell, J.R., Kellerhals, T., Häberli, M., Schmitt, J., Fischer, H., Severinghaus, J.P., 2020. Global ocean heat content in the Last Interglacial. Nat. Geosci. 13, 77–81. https://doi.org/10.1038/s41561-019-0498-0

Shackleton, S., Bereiter, B., Baggenstos, D., Bauska, T.K., Brook, E.J., Marcott, S.A., Severinghaus, J.P., 2019. Is the Noble Gas-Based Rate of Ocean Warming During the Younger Dryas Overestimated? Geophys. Res. Lett. 2019GL082971. https://doi.org/10.1029/2019GL082971

Shackleton, S., Menking, J.A., Brook, E., Buizert, C., Dyonisius, M.N., Petrenko, V.V., Baggenstos, D., Severinghaus, J.P., 2021. Evolution of mean ocean temperature in Marine Isotope Stage 4. Clim. Past 17, 2273–2289. https://doi.org/10.5194/cp-17-2273-2021

Shackleton, S., Seltzer, A., Baggenstos, D., Lisiecki, L.E., 2023. Benthic δ18O records Earth's energy imbalance. Nat. Geosci. https://doi.org/10.1038/s41561-023-01250-y

Shakun, J.D., Lea, D.W., Lisiecki, L.E., Raymo, M.E., 2015. An 800-kyr record of global surface ocean δ 18 O and implications for ice volume-temperature coupling. Earth Planet. Sci. Lett. 426, 58–68. https://doi.org/10.1016/j.epsl.2015.05.042

Shi, J.-R., Xie, S.-P., Talley, L.D., 2018. Evolving Relative Importance of the Southern Ocean and North Atlantic in Anthropogenic Ocean Heat Uptake. J. Clim. 31, 7459–7479. https://doi.org/10.1175/JCLI-D-18-0170.1

Shoji, H., Langway, C.C., 1982. Air hydrate inclusions in fresh ice core. Nature 298, 548–550. https://doi.org/10.1038/298548a0

Siddall, M., Hönisch, B., Waelbroeck, C., Huybers, P., 2010. Changes in deep Pacific temperature during the mid-Pleistocene transition and Quaternary. Quat. Sci. Rev. 29, 170–181. https://doi.org/10.1016/j.quascirev.2009.05.011

Sigl, M., Fudge, T.J., Winstrup, M., Cole-Dai, J., Ferris, D., McConnell, J.R., Taylor, K.C., Welten, K.C., Woodruff, T.E., Adolphi, F., Bisiaux, M., Brook, E.J., Buizert, C., Caffee, M.W., Dunbar, N.W., Edwards, R., Geng, L., Iverson, N., Koffman, B., Layman, L., Maselli, O.J., McGwire, K., Muscheler, R., Nishiizumi, K., Pasteris, D.R., Rhodes, R.H., Sowers, T.A., 2016. The WAIS Divide deep ice core WD2014 chronology – Part 2: Annual-layer counting (0–31 ka BP). Clim. Past 12, 769–786. https://doi.org/10.5194/cp-12-769-2016

Sigman, D.M., Hain, M.P., Haug, G.H., 2010. The polar ocean and glacial cycles in atmospheric CO2 concentration. Nature 466, 47–55. https://doi.org/10.1038/nature09149

Skinner, L.C., Primeau, F., Freeman, E., de la Fuente, M., Goodwin, P.A., Gottschalk, J., Huang, E., McCave, I.N., Noble, T.L., Scrivner, A.E., 2017. Radiocarbon constraints on the glacial ocean circulation and its impact on atmospheric CO2. Nat. Commun. 8, 16010. https://doi.org/10.1038/ncomms16010

Sowers, T., Bender, M., Raynaud, D., 1989. Elemental and isotopic composition of occluded O2 and N2 in polar ice. J. Geophys. Res. Atmospheres 94, 5137–5150. https://doi.org/10.1029/JD094iD04p05137

Spahni, R., Schwander, J., Flückiger, J., Stauffer, B., Chappellaz, J., Raynaud, D., 2003. The attenuation of fast atmospheric CH_4 variations recorded in polar ice cores. Geophys. Res. Lett. 30, 1571. https://doi.org/10.1029/2003GL017093

Stirpe, C.R., Allen, K.A., Sikes, E.L., Zhou, X., Rosenthal, Y., Cruz-Uribe, A.M., Brooks, H.L., 2021. The Mg/Ca proxy for temperature: A Uvigerina core-top study in the Southwest Pacific. Geochim. Cosmochim. Acta 309, 299–312. https://doi.org/10.1016/j.gca.2021.06.015

Stocker, T.F., Johnsen, S.J., 2003. A minimum thermodynamic model for the bipolar seesaw: THERMAL BIPOLAR SEESAW. Paleoceanography 18, n/a-n/a. https://doi.org/10.1029/2003PA000920

Stommel, H., 1961. Thermohaline Convection with Two Stable Regimes of Flow. Tellus 13, 224–230. https://doi.org/10.1111/j.2153-3490.1961.tb00079.x

Storto, A., Cheng, L., Yang, C., 2022. Revisiting the 2003–18 Deep Ocean Warming through Multiplatform Analysis of the Global Energy Budget. J. Clim. 35, 4701–4717. https://doi.org/10.1175/JCLI-D-21-0726.1

Sturges, W.T., McIntyre, H.P., Penkett, S.A., Chappellaz, J., Barnola, J.-M., Mulvaney, R., Atlas, E., Stroud, V., 2001. Methyl bromide, other brominated methanes, and methyl iodide in polar firn air. J. Geophys. Res. Atmospheres 106, 1595–1606. https://doi.org/10.1029/2000JD900511

Svensson, A., Andersen, K.K., Bigler, M., Clausen, H.B., Dahl-Jensen, D., Davies, S.M., Johnsen, S.J., Muscheler, R., Parrenin, F., Rasmussen, S.O., Röthlisberger, R., Seierstad, I., Steffensen, J.P., Vinther, B.M., 2008. A 60 000 year Greenland stratigraphic ice core chronology. Clim. Past 4, 47–57. https://doi.org/10.5194/cp-4-47-2008

Thompson, A.F., Stewart, A.L., Spence, P., Heywood, K.J., 2018. The Antarctic Slope Current in a Changing Climate. Rev. Geophys. 56, 741–770. https://doi.org/10.1029/2018RG000624

Tierney, J.E., Malevich, S.B., Gray, W., Vetter, L., Thirumalai, K., 2019. Bayesian Calibration of the Mg/Ca Paleothermometer in Planktic Foraminifera. Paleoceanogr. Paleoclimatology 2005–2030.

Tierney, J.E., Tingley, M.P., 2018. BAYSPLINE: A New Calibration for the Alkenone Paleothermometer. Paleoceanogr. Paleoclimatology 33, 281–301. https://doi.org/10.1002/2017PA003201

Uchida, T., Yasuda, K., Oto, Y., Shen, R., Ohmura, R., 2014. Natural supersaturation conditions needed for nucleation of air-clathrate hydrates in deep ice sheets. J. Glaciol. 60, 1111–1116. https://doi.org/10.3189/2014JoG13J232

Veres, D., Bazin, L., Landais, A., Toyé Mahamadou Kele, H., Lemieux-Dudon, B., Parrenin, F., Martinerie, P., Blayo, E., Blunier, T., Capron, E., Chappellaz, J., Rasmussen, S.O., Severi, M., Svensson, A., Vinther, B., Wolff, E.W., 2013. The Antarctic ice core chronology (AICC2012): an optimized multi-parameter and multi-site dating approach for the last 120 thousand years. Clim. Past 9, 1733–1748. https://doi.org/10.5194/cp-9-1733-2013

von Schuckmann, K., Cheng, L., Palmer, M.D., Hansen, J., Tassone, C., Aich, V., Adusumilli, S., Beltrami, H., Boyer, T., Cuesta-Valero, F.J., Desbruyères, D., Domingues, C., García-García, A., Gentine, P., Gilson, J., Gorfer, M., Haimberger, L., Ishii, M., Johnson, G.C., Killick, R., King, B.A., Kirchengast, G., Kolodziejczyk, N., Lyman, J., Marzeion, B., Mayer, M., Monier, M., Monselesan, D.P., Purkey, S., Roemmich, D., Schweiger, A., Seneviratne, S.I., Shepherd, A., Slater, D.A., Steiner, A.K., Straneo, F., Timmermans, M.-L., Wijffels, S.E., 2020. Heat stored in the Earth system: where does the energy go? Earth Syst. Sci. Data 12, 2013–2041. https://doi.org/10.5194/essd-12-2013-2020

Waelbroeck, C., Labeyrie, L., Michel, E., Duplessy, J.C., McManus, J.F., Lambeck, K., Balbon, E., Labracherie, M., 2002. Sea-level and deep water temperature changes derived from benthic foraminifera isotopic records. Quat. Sci. Rev. 21, 295–305. https://doi.org/10.1016/S0277-3791(01)00101-9

Weber, S.L., Drijfhout, S.S., Abe-Ouchi, A., Crucifix, M., Eby, M., Ganopolski, A., Murakami, S., Otto-Bliesner, B., Peltier, W.R., 2007. The modern and glacial overturning circulation in the Atlantic ocean in PMIP coupled model simulations. Clim. Past 3, 51–64. https://doi.org/10.5194/cp-3-51-2007

Wild, M., 2020. The global energy balance as represented in CMIP6 climate models. Clim. Dyn. 55, 553–577. https://doi.org/10.1007/s00382-020-05282-7

Wolff, E.W., Fischer, H., Röthlisberger, R., 2009. Glacial terminations as southern warmings without northern control. Nat. Geosci. 2, 206–209. https://doi.org/10.1038/ngeo442

World Climate Research Programme, 2018. Regional Sea-level Changes and Coastal Impacts, in: WCRP Publication. New York.

Yan, Y., Bender, M.L., Brook, E.J., Clifford, H.M., Kemeny, P.C., Kurbatov, A.V., Mackay, S., Mayewski, P.A., Ng, J., Severinghaus, J.P., Higgins, J.A., 2019. Two-million-year-old snapshots of atmospheric gases from Antarctic ice. Nature 574, 663–666. https://doi.org/10.1038/s41586-019-1692-3

2. Methods: From polar ice to noble-gas ratios

Reconstructing past mean ocean temperature (MOT) from a piece of polar ice consists of three major steps. First, the ancient air stored in the ice is extracted quantitatively and subsequently analysed for its noble gas elemental and isotopic composition. Second, the measured elemental ratios are converted into past atmospheric gas concentrations, which requires isotope-informed corrections for various firn fractionation effects. And third, the atmospheric ratios obtained are translated into past MOT using an ocean box model. While the path from measured noble-gas concentrations to MOT will be discussed in Chapter 3, this second chapter aims to answer the question of how to get from a piece of polar ice to elemental and isotopic gas ratios. The laboratory setup and procedures necessary for this task will be discussed in five sections:

- The introduction section talks about the main challenge we face in the laboratory when working with (heavy) atmospheric noble gases: their low abundance. The section then gives a brief overview of past efforts to overcome this challenge at the Scripps Institution of Oceanography in San Diego, USA, and here at the University of Bern.
- Section 2.2. gives an overview of the hardware and software of the extraction system and describes the procedure that is followed to extract the ancient gas from the ice. This includes gas extraction, thermal equilibration, splitting of the gas sample in two aliquots, removal of CO_2 and potential drilling fluid by a liquid nitrogen trap, and removal of reactive gases in a getter oven. This section also discusses why and how the liquid nitrogen trap was modified in the early phase of this PhD-project to reduce drilling fluid contamination.
- Next, Section 2.3. focuses on the analysis of the extracted gas samples, for which two isotope ratio mass spectrometers (IRMS) are used. The section presents the mass spectrometer configurations used in Bern and gives an overview of mass spectrometer non-linearities and how corrections to the raw data are made.
- Section 2.4. explains the standards and reference gas used for noble gas thermometry here in Bern. Noble gas measurements follow the concept of identical treatment. Ice samples and reference gas are passed through the same extraction line and treated as similarly as possible to minimize the effect of potential fractionating effects during extraction and subsequent mass spectrometer analysis. We use a Dual Inlet system for the mass spectrometer analysis, which allows for timely sample and standard gas

comparison. The section provides an estimate of the analytical uncertainty of the various measured ratios, which are given by the reproducibility of outside air measurements.

- Finally, Section 2.5. provides the reader with the measurement protocols for sample preparation, gas extraction, reference gas and working standard sampling, and analyses on the two IRMS.

2.1. Introduction

The main challenge of measuring atmospheric noble-gas ratios is their low atmospheric abundance. Except for Ar, which makes up about 0.934% of Earth's atmosphere, noble gases are found in trace amounts only (Table 1.1.). This is further complicated by the fact that we are interested not in these concentrations per se, but in their very small deviations caused by changes in MOT. Moreover, we also require information on changes in the isotopic ratios of these heavy noble gases, which are needed to correct firn fractionation effects (see Chapter 3 for more detail). The lighter noble gases He and Ne would be more abundant in the atmosphere but are unfortunately not an option, as both diffuse through the ice lattice too easily and are quantitatively lost from ice core samples after drilling. Thus, to reach a satisfactory resolution, noble-gas based reconstruction of MOT requires a combination of large ice samples and high-precision mass spectrometry.

In their pioneering work in the field of noble gas thermometry, Headly and Severinghaus, 2007 measured 50–60 g pieces of GISP2 ice, which contain roughly 4 cm^3 sample air at standard temperature and pressure (STP), to determine the Last Glacial Maximum (LGM) MOT. Improving on the analytical approach developed by Sowers et al., 1989 and Severinghaus et al., 2003, Headly and Severinghaus were able to determine the Holocene–LGM MOT difference. Due to their limited sample size, they had to stretch the 4 cm^3 STP sample air with pure N_2 to measure noble-gas ratios using dynamic mass spectrometry. The small sample size also meant that ion currents and thus analytical precision were low. Hence, they required 63 $\delta Kr/N_2$ measurements (33 for the Holocene, 30 for the LGM) to obtain a value of 2.7 ± 0.6 °C for the Holocene–LGM MOT difference. This is in line with other, mostly marine sediment based, ocean temperature reconstructions (e.g., Barker et al., 2005; Elderfield et al., 2012; Shakun et al., 2015), also in terms of achieved precision. However, the high number of samples required rendered this original methodology unsuitable for obtaining a high-resolution MOT record.

Since 2007, advances in sample preparation, gas extraction, and mass spectrometry have led to considerable improvements in noble gas thermometry. One of the most important changes is the use of considerably larger sample sizes nowadays. Working with larger samples allows us to achieve higher precision than Headly and Severinghaus from just one sample per depth interval instead of 30 and avoids the addition of artificial N_2 to the sample. The amount of ice needed depends on the ice's total air content (TAC). TAC is primarily a function of atmospheric pressure and thus of the altitude of the drilling site, although local wind speed, insulation, temperature, and accumulation also have a minor influence on TAC (Eicher et al., 2016). For EDC, roughly 550–600 g of ice are required for one data point, which corresponds to approximately 50–55 mL STP. These larger samples enabled the inclusion of Xe in the measurement routine, which allows for cross-validation of the $\delta Kr/N_2$ based MOT reconstructions and to perform more comprehensive data-based corrections of the fractionation processes in the firn. This includes the correction of kinetic fractionation, an additional firn fractionation effect (see Chapter 3 for more detail). The larger sample size and thus higher ion currents also allow for the correction of additional non-linearities during mass spectrometer analysis (see Section 2.3.3.). Making use of these advances, recent publications on MOT were able to reduce uncertainties to 0.24–0.4 °C (Baggenstos et al., 2019; Bereiter et al., 2018; Haeberli et al., 2021; Shackleton et al., 2021, 2020, 2019).

In Bern, work on noble gas thermometry started in 2009. In the framework of the ERC-funded MATRICs project, Thomas Kellerhals set up the methodology that – with some adjustments – is still in use today. The methodology in Bern was chosen slightly differently to the one used at Scripps and allows for measuring Xe isotopic ratios. Due to the low atmospheric abundance of Xe and consequently low ion counts, measuring Xe isotopic ratios requires considerable amounts of sample gas and thus comes at the cost of slightly reduced precision for other gas ratios. However, Xe isotopes give us further information on firn fractionating processes and are thus part of our correction routine (see Chapter 3). Thomas Kellerhals then went on to build the extraction line and set up the mass spectrometry system. Later, Daniel Baggenstos and Marcel Haeberli made several adjustments to the extraction system and to the method. This not only considerably improved the overall precision of the method, but also greatly increased the sample throughput from two to four samples per 5-day week. The first major dataset was produced as a joint effort of Marcel Haeberli and Daniel Baggenstos, resulting in two publications (Baggenstos et al. 2019, Haeberli et al. 2021). During their measurements, however, they encountered issues with drilling fluid contamination, which affected $\delta^{15}N_2$ values and elemental and isotopic ratios containing ^{82}Kr in 13 ice samples (Häberli, 2019).

In this PhD-project, some further modifications to the extraction system were made to prevent future drilling fluid influence. Additionally, the software used for the instrument control was overhauled. A considerable part of this PhD-project also went into IRMS analysis. This included learning how to best prevent signal instabilities and how to cope with the remaining ones, improving on the existing correction methods for non-linearities, and introducing a correction for the ^{40}Ar-beam tailing. Using this updated version of the extraction system and the mass spectrometry setup, a MOT dataset covering Terminations II, III, and IV and their subsequent interglacials could be measured during this PhD-project.

2.2. The extraction system

This section aims to give the reader a brief overview of the general functionality of the extraction system, its components, and the software used to control these components. A more detailed step-by-step protocol of the sample preparation and the noble gas extraction can be found in the annex.

2.2.1. Hardware

The noble gas extraction unit is the centre piece of our method. It is used to extract gas from polar ice samples, split the extracted gas into two aliquots in a non-fractionating manner, and remove different gases from these two aliquots. Figure 2.1. offers a schematic of the system and a list of its components is given in Table 2.1.

The extraction system is constantly kept under vacuum by a membrane pump for low vacuum and a turbo-molecular pump that achieves high vacuum (on the order of 10^{-8} mbar). Two manual valves (M_1 and M_2) control which of the two pumps is connected to the system. Both pumps are protected from water vapour by a liquid nitrogen trap.

Individual parts of the extraction line are separated by pneumatic valves (V). Additionally, four manual Nupro valves (N) are installed. N_1 and N_2 are located at the end of two flexible stainless-steel hoses, to each of which a stainless-steel dip tube (“finger”) can be connected via connections C_1 and C_2. These fingers can be sealed with a Nupro valve and serve as transport vessels to move gas samples between different parts of the system and the mass spectrometers. For this, the gas is frozen into these fingers by placing the fingers into a helium-exchange cryostat cooled to 15 K (10 K when melting an ice sample). The other two Nupro valves (N_3 and N_4) are used to control inflow from gas cylinders connected to C_7 and C_8. In total, the extraction system has eight external connections, seven of which are ¼” VCR threads. C_7 is an Ultra-Torr vacuum fitting. C_1-C_6 are frequently used during sample extraction. The temperature and pressure at different locations in the extraction system are constantly monitored. The two pressure gauges are located close to the sample vessel connection (P_1, pressure range of 10^{-2}–10^{2} mbar) and next to where the gas is frozen into the fingers (P_2, pressure range of 10^{-5}–10^{-1} mbar). For temperature control, six sensors are available, four of which are frequently used during a regular extraction procedure, namely those for the getter oven, the two water traps, and the equilibration box. The tubing itself consists of stainless steel with inner diameters of ⅛” (between V_{17} and V_{18}), ⅜” (between V_{18} and V_{13}, and between N_3 and N_4), ½” (between P_1, the two vacuum pumps, and the getter oven), and ¼” (all other). Additionally, stainless steel hoses are used for lines that need to be flexible, which are the line between V_{21} and V_{22} (⅝” stainless steel hose), and the lines between V_{11} and C_1 and between V_9 and C_2 (¼” stainless steel hose).

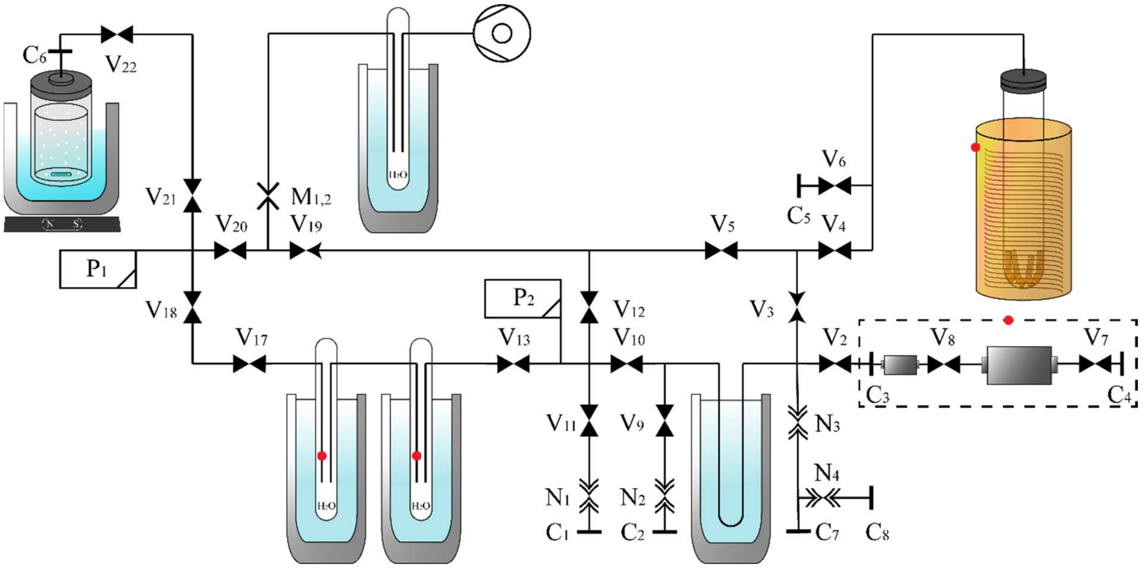

Figure 2.1.: Schematic of the extraction line in the “split” position. Pneumatic valves are abbreviated with V, manual valves with M, and Nupro valves with N. External connections (mostly VCR) are shown by a thick line and denominated with the letter C. The figure also schematically shows the positions of the extraction vessel, water traps, liquid nitrogen traps, vacuum pumps, getter oven, equilibration box (dashed box), the two equilibration volumes, the two pressure gauges (shown as flags denominated with a letter P), and the frequently used temperature sensors (red dots). For gettering, the two equilibration volumes need to be disconnected from C_3 and attached to C_5 instead.

Extraction system component	**Manufacturer and specifics**
Turbo-molecular pump	Pfeiffer Vacuum, HiCube 80 Classic, DN 40 ISO-KF, MVP 040
Membrane pump	Pfeiffer Vacuum, KNF, N 813.4 ANE
Helium exchange cryostat	Janis, Closed Cycle Refrigerator, CCS-500/204
Pneumatic valves	Fujikin, Metal diaphragm valves, FWBR-71
Nupro valves	Swagelok, Stainless Steel Bellows Sealed Valve, SS-4H-TW (N_1, N_2) and SS-4BG (N_3, N_4)
Manual valves	Pfeiffer Vacuum, AVC 016 SA
Pressure gauges	Pfeiffer Vacuum, Capacitance gauge, CMR 362 and CMR 365
Glass capillaries	CM Scientific, Round Borosilicate Glass Capillary, CV8010-100 and CV4055-100

Table 2.1.: Overview of extraction system components and their manufacturers and precise denominations. The getter oven and water traps were built by the workshop in house and are thus not listed here.

During the melt extraction, several additional components of the extraction system play an essential part. After the ice sample is melted, two sequential water traps (WT), located between V_{13} and V_{17}, are used to remove all water vapour from the sample air. The two traps are cooled to −95 °C and –90 °C, respectively. The dry air sample is then frozen into a finger placed in the cryostat. Next, the finger is removed from the cryostat and subsequently attached to C_4. There, the sample is expanded from the finger (inner volume of ~7 cm^3) into a small (~2 cm^3) and large (~50 cm^3) volume attached to C_3 and then brought into temperature equilibrium in an insulated metal box (12 cm x 16 cm x 100 cm). Two fans attached to the ceiling of this equilibration box ensure a stable temperature regime (fluctuations of <0.3 °C/h). After equilibration, the sample air is split into two aliquots. The smaller aliquot is dedicated for bulk air analysis on a Delta V IRMS, whereas the larger aliquot is used for analysing noble gas isotopic and elemental ratios on a MAT 253 IRMS. After splitting the sample into these two aliquots, the Delta V aliquot is passed through a liquid nitrogen trap located between V_2, V_3, V_9, and V_{10} to remove CO_2 and potential drilling fluid. The trap consists of a U-shaped ¼” stainless steel tubing, which is placed into a dewar filled with liquid nitrogen. To remove the hydrocarbon-based drilling fluid, the trap contains 74 glass capillaries of 0.55 mm outer diameter (OD) and 0.4 mm inner diameter (ID), and an additional 22 glass capillaries of 1 mm OD and 0.8 mm ID, which largely increases the available surface for adsorption of contaminants. After processing the Delta V aliquot and freezing it into a finger, the larger equilibration volume is connected via C_5 before the sample air is then admitted to the getter oven, which has been heated to roughly 900 °C.[1]. This oven consists of a 3 cm OD quartz glass tube that is sealed to the rest of the extraction system via a ConFlat-flange and can be inserted into the oven. Inside the quartz glass tube there are 4 Al/Zr strips of roughly 5 cm length each, which are replaced before each measurement. When heated, Zr/Al strips absorb all reactive gases, thus concentrating inert noble gases of the admitted MAT 253 aliquot. In a final step, the MAT 253 aliquot is frozen into a finger and the two aliquots are transported to the respective mass spectrometers for analysis.

The extraction system aims to mimic the concept of identical treatment, meaning that reference gas can also be fed into it, which then undergoes the same splitting and processing steps as an ice sample. The only difference between ice sample and reference air is how the sample is connected to the extraction system. As shown in Figure 2.1., the glass vessel containing the ice sample is connected via C_6, whereas the reference gas volume is connected via C_4. Tests performed by Thomas Kellerhals have shown no noticeable fractionation introduced by these different inlets.

2.2.2. Software

Pneumatic valves, water traps, and the getter oven are all controlled with custom-made software written in LabView (National Instruments). The getter oven temperature is regulated by the proportional-integral-derivative (PID) Virtual Instrument that comes with LabView 2020. The cooling of the water traps works in a similar way, in that the pumping speed of two liquid nitrogen (LN_2) nozzles (“Spuckis”) is controlled by the above-mentioned PID function. These Spuckis consist of a plastic tubing with a small resistor attached to one end (Schmitt, 2006) and have been successfully utilised in similar cooling systems (Schmitt et al., 2014). The end with the resistor is placed in a dewar filled with LN_2, while the other end feeds into an aluminium collar placed around the water trap. Whenever the water trap temperature rises above a threshold controlled by the PID function, the resistor is heated, producing a gentle stream of LN_2 droplets from the dewar, through the nozzle, into the aluminium collar (Schmitt, 2006). There, the LN_2 vaporises and thus cools the water trap. In addition to these forms of active temperature control, the software keeps track of temperature and pressure readings, which can be saved to disk on demand.

During this PhD, the control software was overhauled. With this overhaul, the software now runs considerably more stable. Additionally, the options to load extraction scripts and

---

[1] In practice, the getter oven is heated to a set temperature of 608 °C, measured by a temperature sensor placed just outside of the oven. This corresponds to roughly 900 °C in the oven interior.

write to a log file were added. The new version of the software also comes with some safety checks, which are designed to prevent accidental flooding of the system with lab air. Finally, changes to the visual design and adding documentation to both the front panel and the block diagram allow a new user easier access to the software.

2.2.3. Tackling drilling fluid contamination: the new LN_2 trap

Deep ice drilling operations typically make use of a drilling fluid to prevent hole closure (Talalay and Gundestrup 2002). For this, the drilling fluid needs to be of the same or slightly higher density than the surrounding ice. This is usually realised by using a low-density hydrocarbon fluid as a basis, which when mixed with densifiers attains suitable density and viscosity for deep ice drilling. Densifiers are needed to increase the density of the hydrocarbon fluid (usually around 800–850 kg/m^3) to that of glacial ice (around 920 kg/m^3). Such densifiers consist either of halogenated hydrocarbons or fluorocarbon (Talalay and Gundestrup, 2002). For EDC, a blend of dearomatized kerosene (Exxsol D30) and the fluorocarbon HCFC-141b (1,1-Dichlor-1-fluorethan, $C_2H_3Cl_2F$) was used (Augustin et al., 2007).

Haeberli et al., 2021 reported drilling fluid contamination of 13 EDC ice samples. For the most part, these were samples from the bubble-clathrate transition zone (BCTZ; at EDC between 600 and 1200 m depth, corresponding to a gas age of about 24–81 kyr) and the bottom-most part of the EDC ice core. Ice quality in these two depth ranges is typically poorer than that of other parts of the core as the ice is relatively more brittle. In the BCTZ, this brittleness is the consequence of the co-existence of bubbles and clathrates, whereas in the deepest part of the ice sheet, temperatures get close to the pressure melting point due to geothermal heating, making drilling extremely challenging (see Section 1.4.). Moreover, the ice experiences strong thermal stress as it is brought up to the surface, as the in-situ temperature at the bottom of the ice sheet is close to the pressure melting point, whereas the drilling fluid higher up in the bore hole is close to the surface temperature of about −55 °C. Both effects (drilling difficulty and thermal stress) favour the formation of (micro-)cracks and thus intrusion of drilling fluid into the ice. To avoid drilling fluid contamination as best as possible, the ice is decontaminated during sample preparation by shaving away at least 5 mm of all edges and by cutting out visible cracks. However, the drilling fluid that found its way into the sample interior has to be removed by the LN_2 trap. The LN_2 trap design used by Haeberli et al., 2021 was unable to do so for several samples from depth layers characterised by more brittle ice and even some samples of higher ice quality.

2.2.3.a. Impact of drilling fluid contamination on $\delta^{15}N_2$

Drilling fluid contamination of measured EDC samples mainly affected the Delta V aliquot, where it caused anomalously low $\delta^{40/36}Ar$ and anomalously high $\delta^{15}N_2$. This suggests that at least parts of the hydrocarbons manage to pass the LN_2 trap through which the Delta V aliquot is directed during sample extraction. Most probable candidates are the light hydrocarbons propane and ethane, as the mass spectrum of ethane shows peaks for mass-to-charge (m/z) ratios 28 and 29, while that of propane additionally encompasses m/z 36 and 40 (Linstrom and Mallard, 2023). Moreover, at −42.1 °C for propane and −88.5 °C for ethane, they have lower freezing temperatures than heavier hydrocarbons and are thus more likely to pass the trap (although still considerably higher than LN_2 at −196 °C). If remnants of these two hydrocarbons made it into the Delta V aliquot, isobaric interferences at the above-mentioned m/z ratios would be expected and thus could explain the observed anomalies in $\delta^{40/36}Ar$ and $\delta^{15}N_2$.

To test whether ethane and propane can indeed pass the LN_2 trap, we spiked our Delta V working standard with different amounts of pure ethane and pure propane and measured its effect on $\delta^{40/36}Ar$ and $\delta^{15}N_2$. This was done both with LN_2 added to the trap and without the trap being active. The results of the experiments with added ethane can be found in Figure 2.2, similar results were found with propane. Both propane and ethane clearly influence measured $\delta^{15}N_2$, as is evident from the samples for which the trap was not cooled to −196 °C. However, an active trap was always able to capture the added hydrocarbons. Even when relatively high amounts of ethane (100 ppm) or propane (10 ppm) were added to the working standard, $\delta^{15}N_2$ was indistinguishable from standard-vs.-standard measurements.

These results were somewhat unexpected, as Haeberli et al., 2021 clearly showed that some parts of the drilling fluid did make it past the LN_2 trap. Despite the LN_2 trap showing good performance in these initial tests, we thus speculated that in the presence of drilling fluid, small amounts of light alkanes contained therein might make it past the LN_2 trap. This might be due to some kind of competition behaviour between the main components of the EDC drilling fluid (pentane, hexane, and alkanes of higher order) and the small amounts of low-order alkanes of the drilling fluid, such as ethane and propane (Jochen Schmitt, personal communication). While the heavier hydrocarbons should all freeze out in the LN_2 trap, they might thereby block available surface area and cause some of the lighter hydrocarbons to not interact with the cold surface.

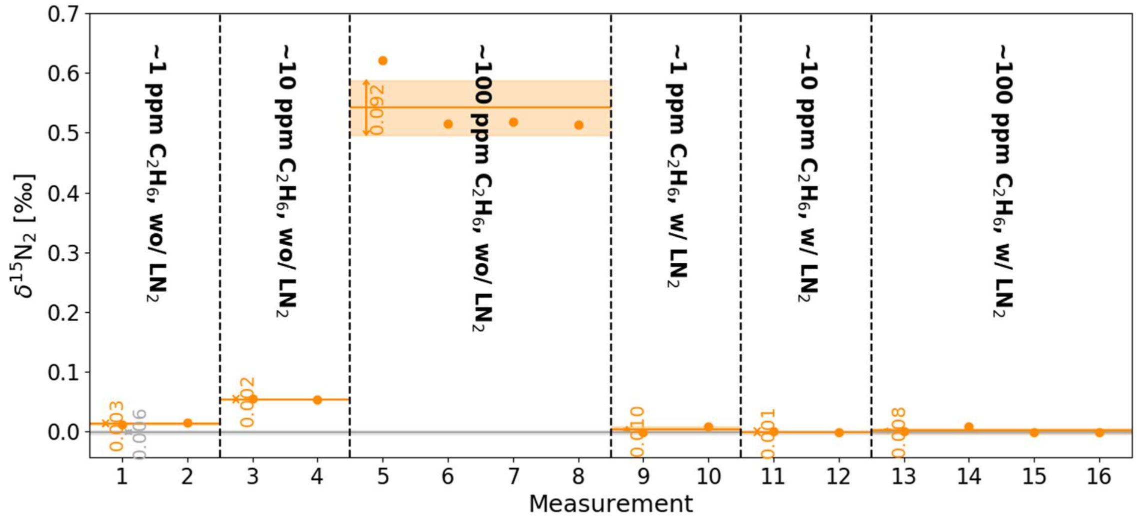

Figure 2.2.: Response in $\delta^{15}N_2$ to the addition of ethane to the Delta V working standard, which was then passed through the LN_2 trap with and without liquid nitrogen added to it. Orange points show measured values with orange lines and shaded areas indicating the mean and standard deviation for each set of measurements, respectively. The area shaded in grey shows the $\delta^{15}N_2$ range as expected from standard-vs.-standard measurements.

Thus, we decided to adjust the LN_2 trap and increase its internal surface area, while simultaneously somewhat reducing the gas flow. This was achieved by adding thin glass capillaries to the two sides of the original U-shaped stainless-steel LN_2 trap. Each of the two sides was filled with 37 glass capillaries of 10 cm length, 0.55 mm OD, and 0.4 mm ID, on top of which 11 glass capillaries of the same length and with 1 mm OD and 0.8 mm ID were placed. Adding these glass capillaries increased the trap surface area more than fourfold, while also reducing gas flow and thus increasing the likelihood that molecules interact with the cold surface and are trapped.

After these adjustments, the performance of the new LN_2 trap, equipped with glass capillaries, was compared against that of the original, the empty trap. Since even the original trap was able to filter out pure ethane and propane, the only way to do so was to measure an actual sample that was visibly contaminated by drilling fluid. We thus selected a piece from the very bottom of the EDC ice core, EDC 5714, which is a bag from 3142 m depth. The ice sample was prepared and analysed as described in Annex A.1. However, instead of gettering the larger equilibration volume to obtain a noble gas aliquot, all the extracted gas was used by splitting it into ten aliquots. Two of these aliquots were used to obtain a benchmark from the original trap, the other eight aliquots were run through the new trap.

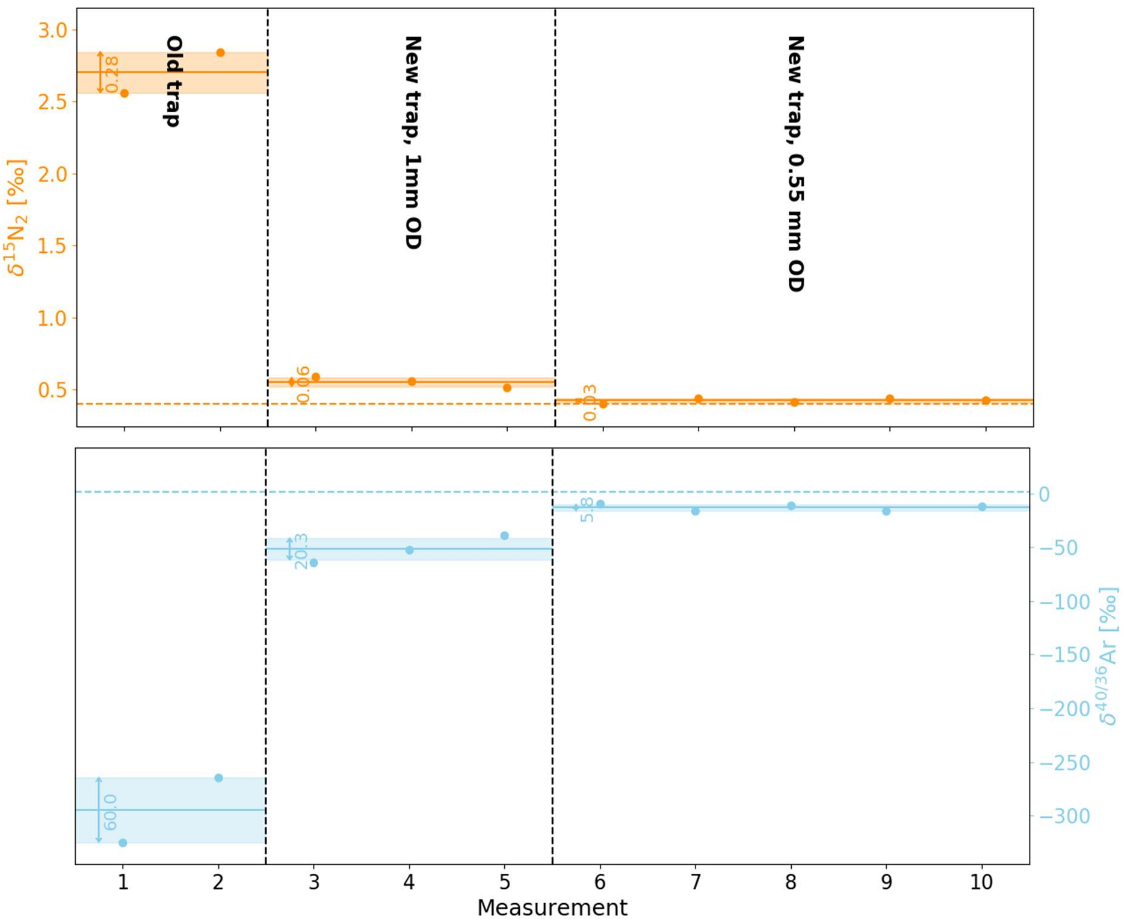

Figure 2.3.: Measured $\delta^{15}N_2$ (orange) and $\delta^{40/36}$Ar (blue) for EDC 5714 after passing the extracted gas through the old or one of two versions of the new LN_2 trap design, respectively. Points show measured values with drawn lines and shaded areas indicating the mean and standard deviation for each set of measurements, respectively. The dashed horizontal lines indicate the expected values, as suggested by extrapolating data from Dreyfus et al., 2010.

The measured $\delta^{15}N_2$ and $\delta^{40/36}$Ar for all ten aliquots can be found in Figure 2.3. A clear difference in the performance of the two traps is evident in both ratios. Published data from Dreyfus et al., 2010 suggest a $\delta^{15}N_2$ of about 0.40‰ for that depth, while for $\delta^{40/36}$Ar a value of around 1.6‰ is expected. The two samples that were passed through the old trap are offset the furthest from these expected values. The eight samples that saw the new trap design, on the other hand, have only slightly elevated $\delta^{15}N_2$. Similarly, $\delta^{40/36}$Ar is substantially less negative when using the trap with increased surface area. Thus, for both $\delta^{15}N_2$ and $\delta^{40/36}$Ar, increasing the surface area improves the trap's performance. This may also be seen when comparing the three data points of samples passed through a trap filled with 1 mm OD capillaries, which roughly doubled the surface area of the old trap, with the last five data points, for which the trap was filled with 0.55 mm OD capillaries, thus increasing the surface area approximately threefold. However, even with this later version of the trap, the measured $\delta^{15}N_2$ and $\delta^{40/36}Ar$ values were still outside the range expected from Dreyfus et al., 2010.

In conclusion, the updated liquid nitrogen trap can capture considerably more drilling fluid than the old design. However, the results also show that even with more than three times the surface area (i.e., a trap filled with 74 0.55 mm OD glass capillaries), small amounts of drilling fluid are able to pass the trap. It was thus decided to also add the 22 1 mm OD glass capillaries, thereby increasing the old trap's surface area more than fourfold. However, the trap should be stocked with more and thinner glass capillaries if more heavily contaminated ice samples are to be analysed in the future. As no such highly contaminated samples were analysed during this PhD, there was no need for additional glass capillaries. Indeed, only three samples measured during this PhD-project showed anomalous $\delta^{40/36}Ar$, and likely only one of them strong enough to also affect $\delta^{15}N_2$, further proving the functionality of the new LN_2 trap.

2.2.3.b. Drilling fluid contamination of ^{82}Kr

Haeberli et al., 2021 also found altered $\delta^{84/82}Kr$ and $\delta^{86/82}Kr$ ratios in some of their EDC sample aliquots analysed with the MAT 253, which coincided with the respective Delta V aliquots that showed anomalous $\delta^{15}N_2$ and $\delta^{40/36}Ar$. This was unexpected, as this larger noble gas aliquot undergoes a gettering process, where the gas is heated to about 900 °C. No hydrocarbon should be stable at these temperatures.

We can think of two theories, both rather improbable, for the observed interference at m/z 82.

- One possible explanation is that some component of the drilling fluid survives the gettering process. Potential candidates might be some HCFC components. However, no such component was found by an external lab (Martin Vollmer, Empa) in a gettered air sample. Another drilling fluid component which may cause m/z 82 interference would be some sort of fluorinated molecule (e.g., C_2HF_3), which might survive the gettering process or recombine afterwards (Jochen Schmitt, personal communication). All these options seem rather improbable, as none of these components should be stable at the temperatures encountered during the gettering process.
- Another potential cause for interference at m/z 82 would be some combination of two ^{40}Ar and two H atoms. This may be realised either through a ^{40}Ar dimer which could build an adduct with an H_2 molecule, or two ArH molecules that form a dimer. H_2 is formed during the gettering process, while H might be available in the mass spectrometer source as it is an ionisation product of CH_4 or C_2H_6 (Jochen Schmitt,

> personal communication). Drilling fluid contamination does lead to increased H_2 and CH_4 (C_2H_6) presence in the getter oven. Thus, for heavily contaminated samples, complete adsorption of hydrogen and methane molecules by the gettering material might not be possible. This way, enough hydrogen might be present in the mass spectrometer source to form one of the two forms of Ar-H dimers.

As we did not want to contaminate our getter oven with drilling fluid, no further experiments were run to test the first hypothesis. We did, however, perform several experiments to investigate the Ar-H dimer hypothesis. Firstly, different amounts of pure H_2 were added to the noble gas working standard, using the method described in Annex A.5. Indeed, for extremely high H_2 concentrations (addition of roughly 2.5% H_2), small anomalies in $\delta^{86/82}$Kr (and $\delta^{84/82}$Kr) were found, as shown in Figure 2.4. However, $\delta^{40/38}$Ar is also sensitive to large additions of H_2, which was not observed by Haeberli et al., 2021 for contaminated ice samples. The change in $\delta^{86/82}$Kr may be explained by both adduction of H_2 to an Ar-dimer or two ArH molecules forming a dimer, whereas the anomaly in $\delta^{40/38}$Ar can only be caused by adduction of H_2 to ^{36}Ar. This adduction does not take place if, instead of H_2, a molecule which produces H^+ ions (and no H_2) gets past the getter. Candidates for this would again be methane and ethane. In a second set of experiments, we therefore added different amounts of C_2H_6 to our MAT 253 working standard. However, no detectable effect on any of the ratios of interest was observed, even when adding as much as 1% of pure C_2H_6 (see Figure 2.4.).

In summary, the dimer hypothesis is not able to explain the ^{82}Kr anomalies observed for heavily contaminated samples. The other hypothesis, equally improbable, of some fluorinated molecule which might survive the gettering process or recombine afterwards, could not be tested, as we did not want to contaminate the getter vessel. This was not a big issue for this PhD-project, as no heavily contaminated samples were analysed. Indeed, only three EDC samples measured during this PhD-project showed anomalous ^{82}Kr. However, additional experiments regarding this m/z 82 interference may be advisable in case heavily contaminated ice samples should be analysed again in the future.

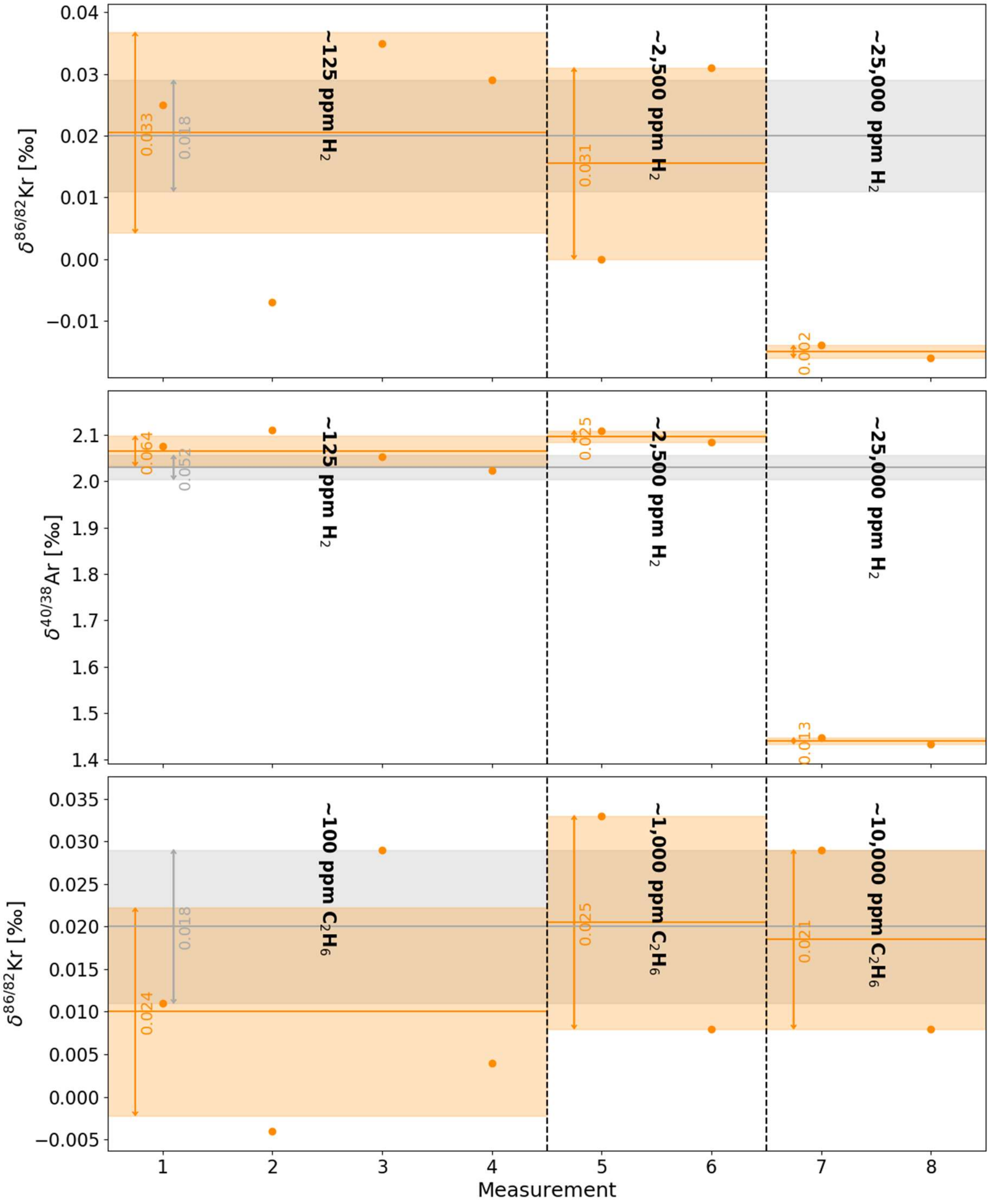

Figure 2.4.: The top and the middle panel show the response in δ$^{86/82}$Kr and δ$^{40/38}$Ar, respectively, to the addition of different amounts of H$_2$ to the MAT 253 working standard. In the bottom panel, the response in δ$^{86/82}$Kr to addition of various amounts of C$_2$H$_6$ is plotted. Orange points show measured values with orange lines and shaded areas indicating the mean and standard deviation for each set of measurements, respectively. The area shaded in grey shows the δ$^{86/82}$Kr and δ$^{40/38}$Ar range as expected from standard-vs.-standard measurements.

2.3. Mass spectrometry

We use two different isotope ratio mass spectrometers (IRMS) to analyse the two aliquots obtained during sample extraction: an MAT 253 IRMS and a Delta V Plus IRMS, both from Thermo Fisher Scientific. The two mass spectrometers are both equipped with a dual inlet system, which allows for direct comparison of the sample air against a standard, where sample and standard are dynamically introduced in an alternating fashion through the changeover valve. Introduction of the gas into the ion source via the changeover valve is done through crimped steel capillaries that ensure viscous flow from the standard or sample bellow into the mass spectrometer. We measure all our samples against our primary working standards I (WS I). These working standards are contained in 2 L stainless-steel cylinders that are sealed at their exit by two consecutive Nupro valves. The Nupro valves enclose a pipette volume of roughly 1.5 cm^3 and, thus, allow us to introduce an amount of standard gas similar in size to the amount of air in an ice sample. More detail on the system of standards used can be found in Section 2.4.

Although the Delta V aliquot and the MAT 253 aliquot are analysed for different elemental and isotopic ratios, the sample handling up until the mass spectrometer analysis is identical. First, the finger containing the sample is connected to the sample (left) side, of the respective mass spectrometer. This is done using a VCR connection for the MAT 253 and a VCR-to-Ultra-Torr connection for the Delta V. As the finger comes directly from the 10 K cryostat, it is left to get to room temperature for at least 3 hours. On the standard (right) side of the IRMS, the WS I cylinder is connected. The actual measurement procedure then starts by opening the first of the two Nupro valves of the WS1 cylinder. The aliquot of working standard in the pipette volume is left to equilibrate for 5 minutes, after which the first Nupro valve is closed again. When the 5 minutes are up, the sample and standard aliquots are expanded into their respective bellow, which beforehand were expanded to their maximum (40 ml). The aliquots are again left to equilibrate for 5 minutes, after which bellows are closed on the inlet side and subsequently opened to the mass spectrometer source. Then, sample and standard bellow openings are manually adjusted to roughly match signal intensities and the measurement routine is started. This measurement routine is different for the MAT 253 and the Delta V. The two routines are described in the following.

2.3.1. MAT 253 IRMS

We use an MAT 253 IRMS in dual inlet mode to determine noble gas elemental and isotopic ratios. The MAT 253 measures isotopes of Ar (^{36}Ar, ^{38}Ar, ^{40}Ar), Kr (^{82}Kr, ^{84}Kr, ^{86}Kr), and Xe (^{129}Xe, ^{132}Xe, ^{134}Xe, ^{136}Xe), from which isotopic and elemental ratios of these three noble gases are calculated. Although elemental ratios could be derived using all the above isotopes, only δ^{84}Kr/^{40}Ar, δ^{129}Xe/^{40}Ar, δ^{132}Xe/^{40}Ar, δ^{129}Xe/^{84}Kr, and δ^{132}Xe/^{84}Kr are used for MOT reconstruction. The measurement uses the cup configurations described in Table 2.2.

IRMS measurements are run in blocks. A block is characterised by its measurement parameters, the most important of which are the magnetic field strength, controlled by magnet current, the source parameters, and the recorded faraday cups and, thus, observed mass-to-charge ratios m/z. These measurement parameters cannot be adjusted during a block measurement, meaning that only a narrow range of masses can be analysed within a block. To measure other mass ranges, magnet current and source parameters are changed between blocks.

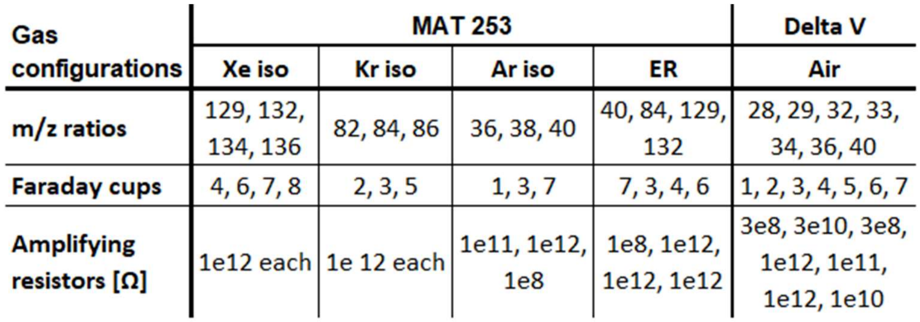

Gas configurations	MAT 253				Delta V
	Xe iso	Kr iso	Ar iso	ER	Air
m/z ratios	129, 132, 134, 136	82, 84, 86	36, 38, 40	40, 84, 129, 132	28, 29, 32, 33, 34, 36, 40
Faraday cups	4, 6, 7, 8	2, 3, 5	1, 3, 7	7, 3, 4, 6	1, 2, 3, 4, 5, 6, 7
Amplifying resistors [Ω]	1e12 each	1e 12 each	1e11, 1e12, 1e8	1e8, 1e12, 1e12, 1e12	3e8, 3e10, 3e8, 1e12, 1e11, 1e12, 1e10

Table 2.2.: Cup configurations used for the different isotopes measured during MAT 253 and Delta V measurement sequences. On the MAT 253, four different gas configurations, that is, different magnet currents and source parameters, are required to obtain isotopic ratios of the three noble gases and their elemental ratios (ER). On the Delta V, one gas configuration is sufficient to measure all required m/z. Adapted from Haeberli, 2019.

Each block is made up of a certain number of cycles of the changeover valve, which allows for timely measurements of gas from the standard side and sample side. A cycle starts with a standard side measurement, during which beam voltages measured in the different faraday cups are integrated for t_{int} seconds. Next, the changeover valve switches to the sample side and the system idles for t_{idle} seconds to permit the ion beam to stabilise, before the ion current of the gas from the sample side is measured. The changeover valve then switches back to the standard side and the cycle starts again. At the start of each block, standard and sample bellow pressures are adjusted such that beam intensities (ion currents) I_{adj} measured at a specified m/z ratio amu$_{adj}$ reach a preset value. At the end of each block, the standard side is measured once more, such that each sample measurement is bracketed by two standard measurements. This is done to account for the signal drop over time, i.e., to determine the recorded standard beam intensities at the time of the sample measurement.

A condensed overview of the MAT 253 noble gas routine can be found in Table 2.3. In detail, the measurement procedure starts with four measurement blocks of each Xe isotopic ratios and Kr isotopic ratios, followed by two blocks to determine the Ar isotopic ratios. Before each element's first block, a peak centre routine is run to centre the beams in the faraday cups. For Kr and Xe, each measurement consists of a 26 s recording of the beam voltages. For Ar, recording time is reduced to 16 s. All blocks consist of 25 cycles of the changeover valve. Beam intensity ratios and thereby isotopic ratios of each individual cycle are calculated directly in ISODAT, the software used to control both mass spectrometers. We then aggregate these 25 individual datapoints per block and ratio to determine the block average for each isotopic ratio. After a correction for pressure imbalance (see Section 2.3.3.a), the average and standard deviation of the block averages is taken for each gas configuration. Only then do we correct for the chemical slope and the bellow gas amount imbalance (see Sections 2.3.3.b, c).

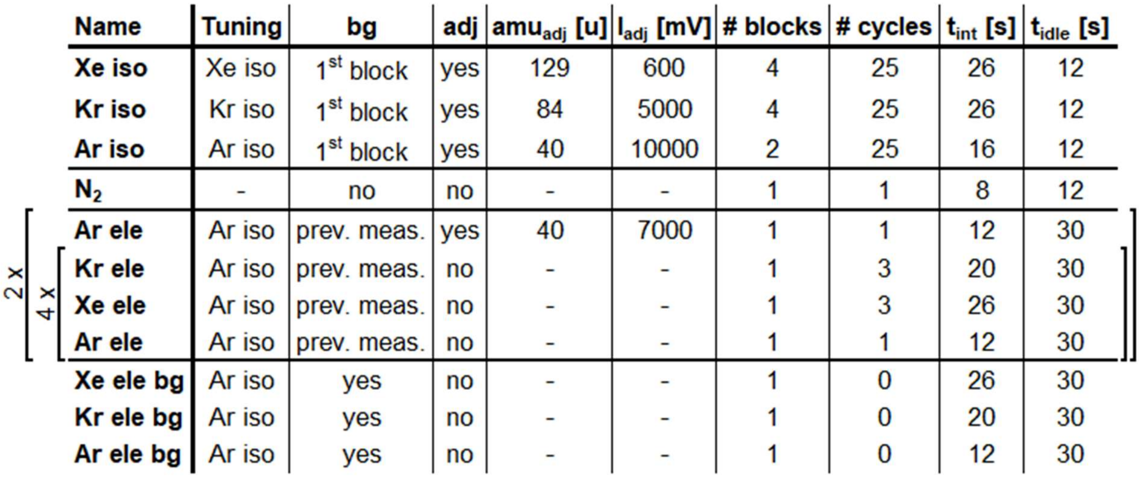

		Name	Tuning	bg	adj	amu$_{adj}$ [u]	I$_{adj}$ [mV]	# blocks	# cycles	t$_{int}$ [s]	t$_{idle}$ [s]
		Xe iso	Xe iso	1st block	yes	129	600	4	25	26	12
		Kr iso	Kr iso	1st block	yes	84	5000	4	25	26	12
		Ar iso	Ar iso	1st block	yes	40	10000	2	25	16	12
		N$_2$	-	no	no	-	-	1	1	8	12
2 x		**Ar ele**	Ar iso	prev. meas.	yes	40	7000	1	1	12	30
	4 x	**Kr ele**	Ar iso	prev. meas.	no	-	-	1	3	20	30
		Xe ele	Ar iso	prev. meas.	no	-	-	1	3	26	30
		Ar ele	Ar iso	prev. meas.	no	-	-	1	1	12	30
		Xe ele bg	Ar iso	yes	no	-	-	1	0	26	30
		Kr ele bg	Ar iso	yes	no	-	-	1	0	20	30
		Ar ele bg	Ar iso	yes	no	-	-	1	0	12	30

Table 2.3.: Measurement routine on the MAT 253. The following information are given for each type of measurement block: the source parameter tuning; whether and how background is corrected (bg; 1st block: bg measured at the beginning of the first block; prev. meas.: bg measured at the end of the previous measurement routine); whether the two sides are signal adjusted (adj); the m/z ratio used for signal adjustment; the intensity to which the signal is adjusted; the number of blocks; the number of cycles of the changeover valve; the integration time of one cycle; and the idling time between cycles.

After these first ten blocks, the abundance at m/z 28 is determined to check for N_2 remnants and thus make sure the gettering procedure has successfully removed all reactive gases from the noble gas aliquot. Slightly elevated sample m/z 28 was recorded for five samples measured during this PhD-project (see Annex A.6.). However, no anomalies in any of the isotopic or elemental ratios were found. After the N_2 block, we measure the elemental ratios using a peak jumping routine. Peak jumping means the sequential switching between the three magnet settings needed to measure Ar, Kr, and Xe. This is done in two sets, each of which consists of 13 individual blocks: four Ar-Kr-Xe triplets, followed by another Ar block to correct for the signal drop over time. These blocks consist of only one and three cycles of the changeover valve for Ar and for Kr and Xe, respectively. The same source parameters are used for all blocks, typically the one used for the Ar isotope blocks. After each magnet jump, an idle time of 30 s, plus the time needed to find the peak centre of about an additional minute, ensures that magnet hysteresis does not pose a problem. The timely measurement of Ar, Kr, and Xe beam intensities with the same source parameters allows for elemental ratios of these gases to be calculated. By applying a polynomial fit to the data obtained from the five Ar blocks, we derive the Ar beam intensity at the time of each Kr and Xe block. Knowing the Ar and Kr (Xe) signal intensity at the same point in time, we then can determine raw δKr/Ar (δXe/Ar) for each of the four triplets. Similarly, by fitting the Kr data and reading out the fitted values at the Xe block times, we calculate the raw δXe/Kr. The raw elemental ratios are then corrected for pressure imbalance. Finally, the resulting ratios of the two peak jumping sets are averaged and corrected for the bellow gas amount imbalance.

Ideally, the source parameters of a gas configuration are chosen such that they maximize signal linearity rather than signal intensity, i.e., such that they minimize the pressure-dependency (signal-intensity dependency) of calculated isotopic and elemental ratios. This reduces pressure imbalance sensitivity and thus the size of the pressure imbalance correction described in Section 2.3.3.a. To perform such a linearity focusing, we use a similar procedure to the one described by Orsi, 2013 for their MAT 252 IRMS at the Scripps Institute of Oceanography, San Diego. Other than at Scripps, we do adjust trap voltage and electron energy whenever we change the filament. As Orsi 2013 used a MAT 252 IRMS for her analyses, some of the tuning parameters are slightly different in our case, but the approach to linearity focusing remains the same in that the right choice of extraction voltage is decisive to reach a high linearity, as it controls space charge effects in the ion source. Typically, a higher extraction voltage results in better linearity. A more detailed description for the tuning of source parameters can be found in Annex A.4.2.

Even though the noble gas aliquot makes up roughly 97% of the total sample gas before gettering, the noble gas routine uses up almost all sample gas. The analysis is, thus, restricted by the available gas amount. One consequence of this restriction is that the correction factors for the pressure imbalance correction need to be determined in separate measurement runs. Another consequence concerns the source parameters, which typically cannot be focused for maximal linearity for all gas configurations. Instead, they must be chosen to maximise beam intensities and thus reduce gas consumption during measurement. This intensity tuning is done by running multiple ISODAT auto-focus routines, which adjust the voltages of the source deflection plates to maximize beam intensity. Usually, maximal signal strength is found at a relatively low extraction voltage (~35–40%). At such low extraction efficiency double ionisations become more likely. Low extraction voltage tunings are therefore prone to have poor linearity, i.e., high pressure imbalance sensitivities. It therefore usually takes multiple attempts to find an intensity tuning which features a reasonably low and constant pressure dependency of the signal ratios. What pressure imbalance sensitivities should be aimed for can be found in Table 2.5.

For a filament with high ionisation efficiency, intensity tuning is typically only necessary for the gas configuration used for Xe isotope blocks. Unfortunately, ionisation efficiency can vary substantially between filaments and usually multiple filaments have to be tested to find one with sufficient ionisation efficiency. Luckily, the filament used during the measurement campaign run in this PhD produced particularly high signal intensities, such that linearity focusing for the Kr, Ar and peak jumping tunings was possible. We found that careful filament placement is imperative (but no guarantee) for high signal intensities. Ideally, the filament is positioned as horizontally as possible at the very bottom of the box opening. Also, it is recommended to start measuring timely once a satisfactory set of source parameter settings has been found as filament degradation generally worsens linearity and signal intensity over time (see also Annex A.4.3.).

2.3.2. Delta V Plus IRMS

The second mass spectrometer used for MOT reconstruction is a Delta V Plus IRMS. This mass spectrometer is run in dual inlet mode, too, and provides $\delta^{15}N_2$, $\delta^{17}O_2$, $\delta^{18}O_2$, $\delta O_2/N_2$, $\delta^{40/36}Ar$, and $\delta^{40}Ar/N_2$. For this, m/z ratios 28, 29, 32, 33, 34, 36, and 40 are measured simultaneously, using the cup configuration found in Table 2.2. Since plenty of gas is available for this analysis of the most abundant air components, the source parameters are chosen in a manner to maximize linearity, rather than to maximize signal strength. Linearity tuning is described in Annex A.4.2.

From the ratios mentioned above, we are mainly interested in a precise determination of $\delta^{15}N_2$ and $\delta Ar/N_2$. $\delta Ar/N_2$ is essential to derive $\delta Xe/N_2$ and $\delta Kr/N_2$ from $\delta Xe/Ar$ and $\delta Kr/Ar$ measured on the MAT 253 IRMS. $\delta^{15}N_2$, on the other hand, is used for firn fractionation corrections. Still, the other ratios measured are more than just "nice to have". $\delta^{18}O_2$ as well as $\delta^{17}O_2$ are used for quality control by comparing them to existing records. Furthermore, they can inform us on the past oxygen cycle and are utilised to orbitally date ice cores. Similarly, $\delta O_2/N_2$ can be used for dating and furthermore acts as an indicator of gas loss. Finally, $\delta^{40/36}Ar$ was used by Haeberli et al., 2021 to detect samples with drilling fluid contamination. However, as $\delta^{40/36}Ar$ measured on the Delta V is less precise, we use $\delta^{40/36}Ar$ measured on the MAT 253 for firn fractionation corrections. Also, we find that the $\delta^{40/36}Ar$ measured on the Delta V is systematically offset from the value obtained by the MAT 253. This will be further explored in Section 2.3.3.b.

A measurement on the Delta V consists of eight identical blocks, which each consist of sixteen changeover valve cycles. Each of these cycles is made up of a 12 s recording of the beam voltages on the standard side, and another 12 s recording of the sample side. When switching between standard and sample side, the system is idle for 10 s to permit the beam to stabilise. Identical to the MAT 253 procedure, the standard side is measured once more at the end of each block, such that each sample measurement is bracketed by standard measurements. Individual ratios are then calculated as follows. First, we determine the block average over the sixteen individual measurements per block for each of the six ratios. After a correction for pressure imbalance and chemical slope (see Sections 2.3.3.a, b), the average and standard deviation of the eight block averages is taken.

After measuring these first eight blocks, the CO_2 abundance at m/z 44 is determined to make sure all CO_2 was removed by the LN_2 trap. This is critical as $\delta^{15}N_2$ could be affected by isobaric interference due to the CO fragment. For the samples measured during this PhD-project, m/z 44 signal intensity of sample and standard always closely matched, proving that CO_2 removal was successful for all samples of this measurement campaign (Annex A.6.). Because we are not limited by the gas amount on the Delta V, four additional blocks can be run, during which the sample bellow pressure is unbalanced from that of the standard side by roughly 10%, twice in each direction. This allows for a timely determination of the pressure imbalance sensitivity. So, unlike for the MAT 253 IRMS, no separate pressure imbalance measurements are necessary. A concise overview of the measurement procedure on the Delta V can be found in Table 2.4.

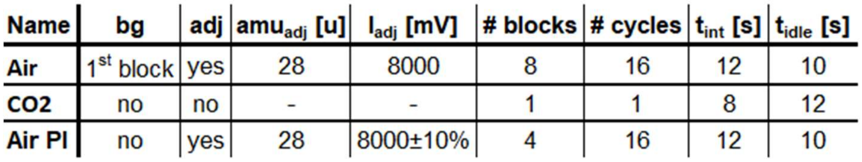

Name	bg	adj	amu_{adj} [u]	I_{adj} [mV]	# blocks	# cycles	t_{int} [s]	t_{idle} [s]
Air	1^{st} block	yes	28	8000	8	16	12	10
CO2	no	no	-	-	1	1	8	12
Air PI	no	yes	28	8000±10%	4	16	12	10

Table 2.4.: Measurement routine on the Delta V. The following information are given for each type of measurement block: whether and how background is corrected (bg; 1^{st} block: bg measured at the beginning of the first block); whether the two sides are signal adjusted adj); the m/z ratio used for signal adjustment; the intensity to which the signal is adjusted; the number of blocks; the number of cycles of the changeover valve; the integration time of one cycle; and the idling time between cycles. During the last four blocks, the sample signal is unbalanced from the standard signal by about 10% to determine pressure imbalance sensitivity.

2.3.3. Corrections

Dynamic dual inlet isotope ratio mass spectrometers use permanent magnets around the ionisation housing to get the ionising electrons to spiral. This greatly increases the chance of collision between the spiralling electrons and the sample gas, resulting in a considerably larger ion yield. Consequently, our two IRMS can achieve very high precision. However, this comes at the cost of linearity with measured ratios being affected by differences in source pressure or differences in chemical composition between sample and standard bellow.

Most linearity issues probably originate from the high ion (space charge) density in the ionisation housing. The positively charged ions are mutually repulsive, and the repulsion is bigger for higher ion density. As the ions are accelerated out of the source housing, a larger part of them will be caught at the exit slit when ion density is higher. We expect lighter ions to be preferentially excluded from the ion beam, as they are more easily deflected due to this space-charge effect (Jeffrey Severinghaus, pers. comm.). Furthermore, the high density of ions in the ionisation housing leads to formation of secondary ions, i.e., molecules that are ionised by other, already ionised molecules. Secondary ionisations are occurring only if the ion can provide enough energy to overcome the ionisation energy of the molecule. Consequently, heavy gases and non-noble gases with low first ionisation energies are more likely to be affected by secondary ionisations.

To minimize the effect of these non-linearities, sample and standard sides are signal matched typically at the start of each measurement block. However, the signal matching can only be as precise as the bellow stepping size allows. Additionally, small differences in the initial size of sample and standard aliquot will cause the mismatch to evolve as the bellow containing less gas will run empty faster. Furthermore, the signal matching can only be carried out for one of the faraday cups, which is problematic as we analyse gas mixtures with different chemical compositions. Consequently, various mass spectrometer corrections need to be applied to account for the varying measurement circumstances between individual measurements. These are the following four corrections, which will be discussed in further detail below:

- The **pressure imbalance correction**, which is applied to all ratios.
- The **chemical slope correction**, which is applied to Xe and Kr isotopic ratios on the MAT 253, and to $\delta^{15}N_2$, $\delta Ar/N_2$, and $\delta^{40/36}Ar$ on the DeltaV.
- The **bellow gas amount correction** is needed for all ratios measured on the MAT 253 except for Xe isotopic ratios.
- The **^{40}Ar-tail correction**, a correction for the effect of the ^{40}Ar-tail on the ^{38}Ar-beam measured on the MAT 253.

2.3.3.a. Pressure imbalance

The beam intensities in an IRMS are directly linked to the gas pressure in the source. As air is consumed and the source pressure decreases over the course of a measurement block, so do the recorded signal intensities. However, not all signal intensities decrease by the exact same rate, causing ratios between signal intensities to be pressure dependent. This pressure dependency is what we try to minimize when performing a linearity tuning of the IRMS source parameters. The pressure matching, or rather signal intensity matching, between sample side and standard side at the start of each block aims to minimize the size of the non-linearity. Still, a noticeable effect prevails as the pressure matching is not able to perfectly equilibrate the two sides.

We can correct for this non-linearity since the pressure dependency of the signal intensity ratios is approximately linear within a considerable pressure range. Thanks to the signal matching, this range is never exceeded during a measurement. Thus, by determining the pressure imbalance sensitivity (PIS), i.e., the slope of the linear relationship between source pressure mismatch and measured ratio, and by recording the pressure mismatch Δ_p for each measurement block, a correction to the raw ratio δ_{raw} can be applied:

$$\delta_{PI} = \delta_{raw} - PIS \cdot \Delta_p, \text{ where } \Delta_p = \left(\frac{\overline{I_{Sample}}}{\overline{I_{Standard}}} - 1\right) \cdot 10^3‰ \qquad (2.1.)$$

As shown in (2.1.), the pressure mismatch is estimated from the ratio between the block average beam intensities of the sample side and standard side, $\overline{I_{Sample}}$ and $\overline{I_{Standard}}$. This pressure imbalance correction is generally on the order of a few per meg up to some ten per meg for isotopic ratios but can reach hundred to several hundred per meg for $\delta^{40/36}$Ar measured on the Delta V, and elemental ratios measured on the MAT253. Typical values of PIS can be found in Table 2.5. The correction is described in more detail in Severinghaus et al., 2003.

Correction	**Ratios**							**Units**
MAT 253	**132/129**	**134/129**	**136/129**	**136/132**	**86/84**	**86/82**	**84/82**	
PIS	< 1	< 1.5	< 2	< 2	< 0.4	< 0.4	< 0.3	per meg/‰ PI
CS	< 1.5	< 3.5	< 3.5	< 3	< 1	< 1	< 1	per meg/‰ δXe/Ar (δKr/Ar)
BGA	-	-	-	-	~0.3	~0.3	~0.3	per meg/% Δ_{bellow}
MAT 253	**40/36$_{\mathrm{MAT}}$**	**40/38**	**84/40**	**129/40**	**132/40**	**129/84**	**132/84**	
PIS	< 1.5	~0.5*	< 5	< 3	< 3	< 3	< 3	per meg/‰ PI
BGA	~1	~0.5	~20	~20	~20	~3	~3	per meg/% Δ_{bellow}
Ar-tail	-	~0.5	-	-	-	-	-	per meg/‰ PI
Delta V	**29/28**	**34/32**	**33/32**	**32/28**	**40/28**	**40/36$_{\mathrm{Delta}}$**		
PIS	< 1	< 2	< 3	< 5	< 2	~15		per meg/‰ PI
CS	~1	-	-	-	~4	~20		per meg/‰ $\delta O_2/N_2$

Table 2.5.: Overview of the approximate size of mass spectrometer corrections factors during the 2022 measurement period. For correction factors that varied throughout the measurement period, upper limits were given, indicated with smaller-than signs. Factors that stayed roughly constant throughout the measurement period are denoted with a tilde. For unknown reasons, bellow gas amount factors in 2022 were considerably smaller than during previous measurement periods. The large PIS and CS for $\delta^{40/36}Ar_{Delta}$ are due to isobaric $^{18}O^{18}O$ interference (see main text). Pressure imbalances can reach up to about 8‰ on the Delta V, about 20‰ for Ar isotopes measured on the MAT 253, 30‰ for Kr isotopes and elemental ratios measured on the MAT 253, and up to 40‰ for Xe isotopes. For the chemical slope correction, $\delta O_2/N_2$ varies by up to 15‰, whereas δKr/Ar and δXe/Ar vary by up to about 30‰ and 60‰, respectively, largely due to the gravitational enrichment of heavier gas species in the firn column (see Chapter 3). For Δ_{bellow}, variations of up to 20% may occur for ice samples. PIS of $\delta^{40/38}Ar$ is for runs where an ^{40}Ar-tail correction was applied. Without correction, PIS is on the order of 7 per meg/‰ PI.

The above method in theory gives a clear recipe on how to correct for this source-pressure dependency of the measured ratios. In practise, the temporal evolution of PIS values also needs to be taken into consideration. While PIS are measured at the end of each Delta V measurement routine, we have too little gas to do the same for the MAT 253. Instead, the MAT 253 PIS are determined once a week in a separate routine. To then apply the correction to a sample measurement, PIS are interpolated to the time of measurement. Even though for the Delta V we measure PIS as part of each sample measurement, the PIS values used for pressure imbalance correction are also interpolation products of the individual PIS datapoints. This is done to reduce the effect of noise due to measurement uncertainty.

The temporal evolution of PIS can behave quite differently for different ratios. It also strongly depends on the state of the instrument, i.e., the filament and the source parameters. In the past, PIS was determined by linear regression through all PIS measurements performed during the lifetime of a filament. While this is appropriate for many ratios, the approach is not ideally suited for others, where sine-like oscillations dominate the temporal evolution of PIS. Figure 2.6. displays the extreme ends of the spectrum, with most temporal evolutions of PIS being somewhere between these two endmembers. Currently, the following three fits are used for determining the temporal evolutions of PIS:

- Linear regression: $y = ax + b$; (Figure 2.5.)
- Linear regression modulated by sine curve: $y = ax + b + c \cdot \sin(dx + e)$; (Figure 2.5.)
- Quadratic least-square fit: $y = ax^2 + bx + c$; ($\delta Ar/N_2$ and $\delta^{40/36}Ar$ in Figure 2.6.)

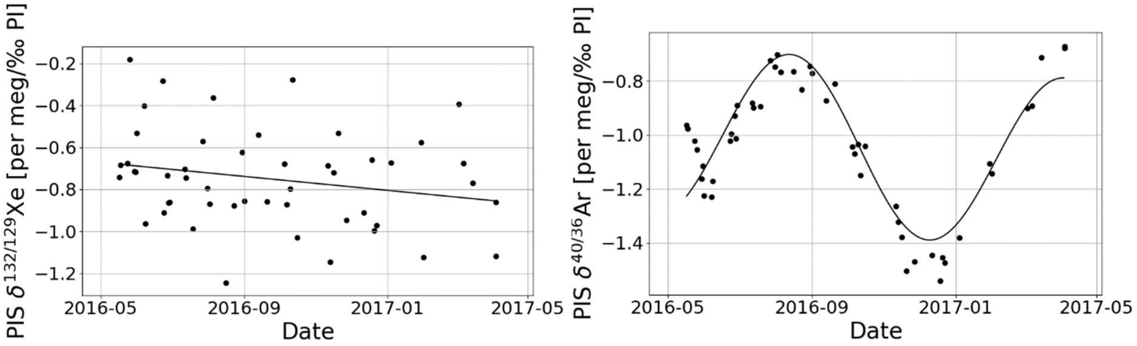

Figure 2.5.: Measured pressure imbalance sensitivities on the MAT 253 from May 2016 to April 2017 for $\delta^{132/129}$Xe and $\delta^{40/36}$Ar. Drawn lines represent the interpolation models for the temporal evolution of PIS that were chosen for performing the pressure imbalance correction.

Which fit is applied to what ratios and during what measurement period can be found in Table 2.6. The three models describe PIS evolutions of ratios measured on the Delta V reasonably well, as Delta V PIS values either barely change or do so in a close to linear/quadratic manner, with >90% of the variance being explained by the fit. This is not always the case for MAT 253 PIS. Particularly during the 2022 measurement period, MAT 253 PIS appeared to be quite variable on shorter timescales, such that none of the fits manages to explain more than 60% of the variance. To account for this higher degree of variability, PIS for a sample was set to be the average of the long-term PIS evolution, i.e., the fit through all PIS measurements, and the short-term PIS variability. This short-term variability was determined by linearly interpolating the PIS at the date of sample measurement from its two neighbouring PIS measurements. This approach led to a considerably better agreement between measured kinetic fractionation factors with literature values (Birner et al., 2018; Figure 2.8.; see Chapter 3 for more details on kinetic fractionation). More frequent MAT 253 PIS measurements should thus be performed during future measurement campaigns to better capture potential short-term variability of PIS.

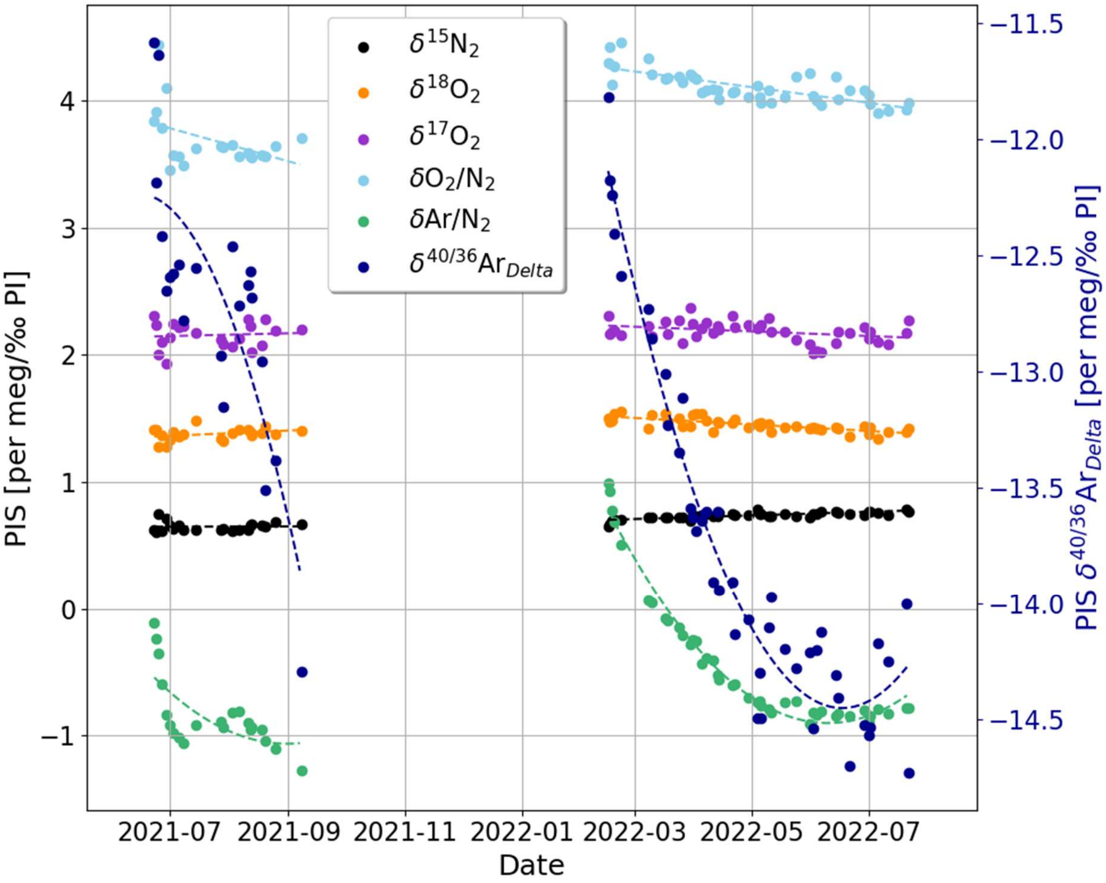

Figure 2.6.: Pressure imbalance sensitivities from June 2021 to July 2022 for all six ratios measured on the Delta V. The effect of a long measurement break on PIS is evident, pointing towards the necessity to determine separate temporal evolutions of PIS for each measurement period. Dashed lines indicate the chosen fits to individual PIS datapoints. In 2022, $\delta Ar/N_2$ and $\delta^{40/36}Ar$ appear to be best described by a second order polynomial rather than a linear slope.

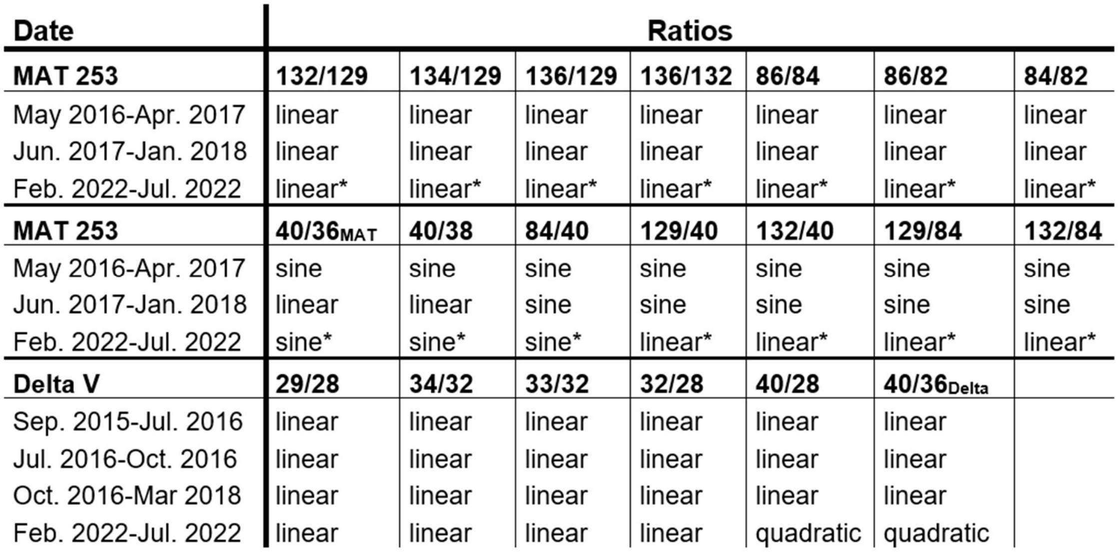

Date	**Ratios**						
MAT 253	**132/129**	**134/129**	**136/129**	**136/132**	**86/84**	**86/82**	**84/82**
May 2016-Apr. 2017	linear	linear	linear	linear	linear	linear	linear
Jun. 2017-Jan. 2018	linear	linear	linear	linear	linear	linear	linear
Feb. 2022-Jul. 2022	linear*	linear*	linear*	linear*	linear*	linear*	linear*
MAT 253	**$40/36_{\mathrm{MAT}}$**	**40/38**	**84/40**	**129/40**	**132/40**	**129/84**	**132/84**
May 2016-Apr. 2017	sine	sine	sine	sine	sine	sine	sine
Jun. 2017-Jan. 2018	linear	linear	sine	sine	sine	sine	sine
Feb. 2022-Jul. 2022	sine*	sine*	sine*	linear*	linear*	linear*	linear*
Delta V	**29/28**	**34/32**	**33/32**	**32/28**	**40/28**	**$40/36_{\mathrm{Delta}}$**	
Sep. 2015-Jul. 2016	linear	linear	linear	linear	linear	linear	
Jul. 2016-Oct. 2016	linear	linear	linear	linear	linear	linear	
Oct. 2016-Mar 2018	linear	linear	linear	linear	linear	linear	
Feb. 2022-Jul. 2022	linear	linear	linear	linear	quadratic	quadratic	

Table 2.6.: Overview of which of the three interpolation models is used to derive the temporal evolution of PIS during ice sample measurement periods. The three models are: linear, a linear regression; quadratic, a quadratic least-square fit; and sine, a linear regression modulated by a sine curve. During the 2022 measurement period, PIS was quite variable on short timescales. For that period, PIS for a sample was set to be the average of the long-term PIS evolution, i.e., the fit through all PIS measurements, and the short-term PIS variability, inferred from the two PIS measurements neighbouring the sample measurement.

2.3.3.b. Chemical slope

Things are further complicated when instead of a single gas species, a gas mixture is admitted to the mass spectrometer. As multiple gas species are measured at the same time, signal matching can only be applied to one of them. On the Delta V, signal matching is performed on m/z 28, as we are most interested in $\delta^{15}N_2$ and in $\delta Ar/N_2$. However, this means that beams with different m/z ratio will have to be measured out of pressure balance if sample and standard bellow do not contain the exact same gas mixture. Furthermore, the relative ionisation efficiency of a gas in a mixture is somewhat dependent on the mixture of the gas itself (Severinghaus et al., 2003). A second correction, thus, becomes necessary, which scales with the difference in chemical composition between standard and sample aliquot.

These two effects, the pressure imbalance and the change in ionisation efficiency due to differences in the chemical composition of sample and standard, are summarised as the chemical slope (CS) of a ratio. As the dominant gas species control the ionisation of a trace species in a sample, but not the other way round, the CS is controlled by the relative abundance of the dominant gas species. Thus, the CS can be determined by changing the relative abundance of the dominant gas species in the gas mixture, which we achieve by adding pure Ar for the MAT 253 and pure O_2 for the Delta V, and then recording the response of individual ratios as a function of the amount of gas added (Figure 2.7.). The CS effect is typically proportional to the change in composition of the sample over a wide range of the elemental ratio. We choose to add O_2 instead of N_2 to the Delta V standard as this allows us to determine the chemical slope for $\delta^{15}N_2$, while those of $\delta^{17}O_2$ and $\delta^{18}O_2$ are not as crucial to us. However, it might be worthwhile to also measure chemical slopes for oxygen isotope ratios by addition of pure N_2 instead of O_2 for future measurement campaigns. Once the CS has been determined, the chemical slope correction is applied to measured ratios as follows:

$$\delta_{PI,CS} = \delta_{PI} - CS \cdot \delta_{elemental\ ratio} \tag{2.2.}$$

We expect the largest chemical slope for ratios with large mass differences, i.e., $\delta Ar/N_2$, for which both the space-charge effect and ion-molecule interactions are more strongly pressure-dependent. Indeed, we find $\delta Ar/N_2$ to have a considerable chemical slope of several ten per meg. However, CS even reaches some hundred per meg for the $\delta^{40/36}Ar$ isotopic ratio measured on the Delta V. The reason for this unexpectedly large CS is explored in further detail when discussing the observed offset between $\delta^{40/36}Ar_{MAT}$ and $\delta^{40/36}Ar_{Delta}$ below. For other ratios, the chemical slope correction is generally on the order of a few per meg up to some ten per meg (Table 2.5.). The chemical slope is typically measured at the start and at the end of a measurement period as it stays roughly constant over the course of a few months. The value for CS is calculated as the average of all chemical slopes determined over the course of a measurement period.

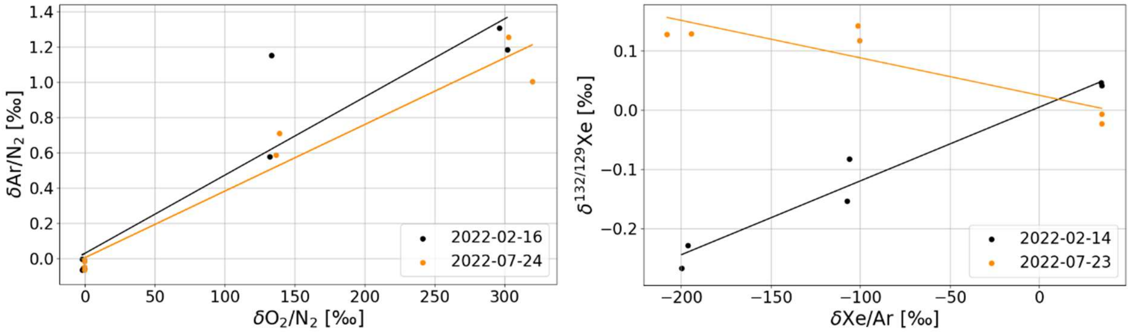

Figure 2.7.: Chemical slope of $\delta Ar/N_2$ and $\delta^{132/129}Xe$ over the course of the 2022 measurement period. Chemical slope is typically rather stable over such a timescale, as may be seen in the case of $\delta Ar/N_2$. Chemical slope correction is, thus, done using the average of the two chemical slopes displayed here. For the isotopic ratios of Xe and Kr, however, chemical slopes can be rather variable over time. The reason for this is further explored in the text.

Chemical slope on the MAT 253

The noble gas sample measured on the MAT 253 is essentially an Ar sample with trace gas amounts (~0.1‰) of Kr and Xe in it. Thus, essentially all collisions in the source will be with Ar. Consequently, we would expect no significant chemical slope effect on the MAT 253. However, when measuring a sample spiked with pure Ar against our working standard, a clear dependency of Xe and Kr isotopic ratios and δXe/Kr on the amount of added Ar is apparent.

For Xe and Kr isotopic ratios, the observed dependency is most likely due to the signal matching being performed on ^{129}Xe and ^{84}Kr, respectively, instead on doing so on ^{40}Ar. This is done for practical reasons, as otherwise repeated switching back and forth between the Xe and Kr gas configuration and the Ar gas configuration were necessary. However, not measuring with matched ^{40}Ar signals results in considerable pressure imbalance between sample side and standard side in case the two aliquots have different chemical compositions. The applied pressure imbalance correction infers the pressure imbalance from the measured Xe or Kr signal imbalance. It thereby does not consider the pressure imbalance induced by differences in the chemical composition. Consequently, the chemical slopes we find for Xe and Kr isotopic ratios are essentially scaled versions of PIS. Thus, the sole difference between chemical slope correction and pressure imbalance correction for Xe and Kr isotopic ratios is the measure for the pressure imbalance: difference in chemical composition or measured signal imbalance.

CS and PIS of Xe and Kr isotopic ratios essentially being the same is supported when comparing temporal evolutions of the two, which are highly similar throughout all measurement periods. It also explains why chemical slopes of Kr and Xe isotopic ratios appeared to be more variable than for other ratios (Figure 2.7.). Furthermore, kinetic fractionation factors measured during the 2022 measurement period agree considerably better with the literature values (Birner et al., 2018) when the temporal evolution of the chemical slope correction is inferred from PIS measurements (Figure 2.8.). Consequently, this is what we used to determine the size of the chemical slope correction for Kr and Xe isotopic ratios.

We do not yet fully understand what causes the chemical-slope-like dependency of δXe/Kr on Ar concentration. Prior to the MAT 253 peak jumping routine, sample and standard sides are signal adjusted on ^{40}Ar. Both sides are thus measured at the same source pressure but potentially at different Kr and Xe signal intensities. We find an increase in δXe/Kr by about 4 to 6 per meg per permille decrease in either δXe/Ar or δKr/Ar for all measurement periods. Considering that δXe/Ar of interglacial samples can be up to 50‰ different from our working standard, this dependency might have a significant effect on the resulting MOT of 0.2–0.3 °C. However, it is unclear whether the change in δXe/Kr is driven by δXe/Ar or δKr/Ar, such that applying a correction to ice samples, for which δXe/Ar is different from δKr/Ar, is not straightforward.

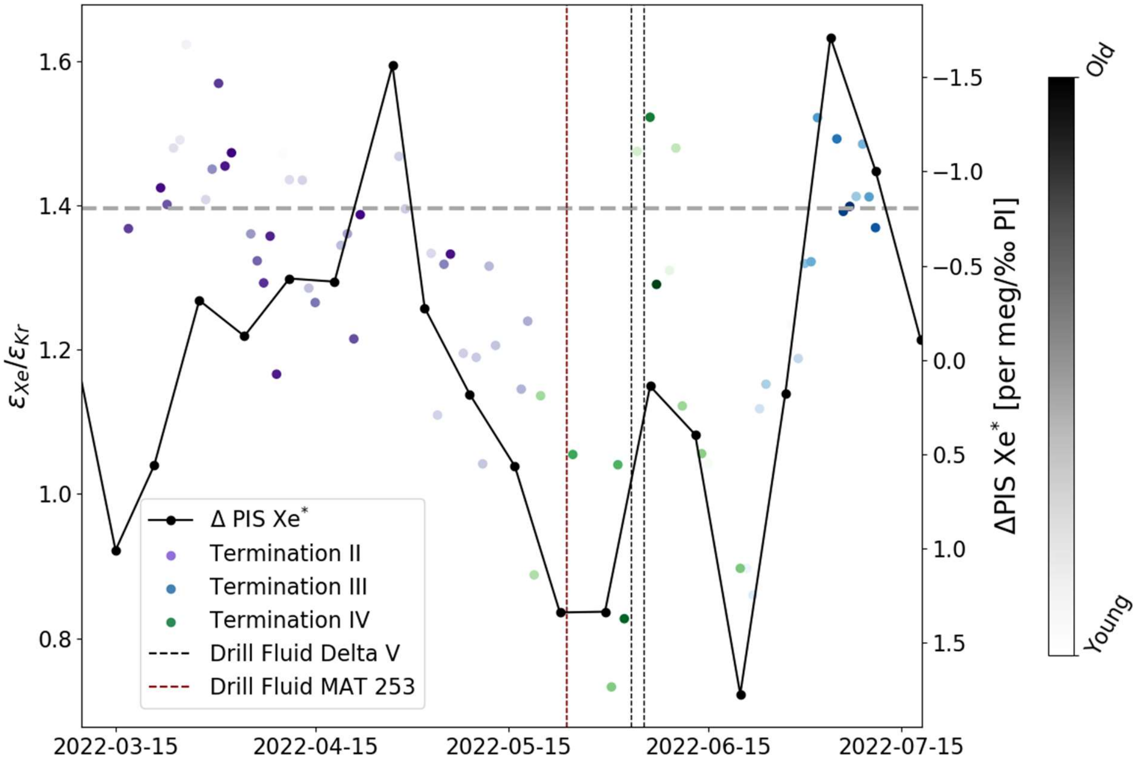

Figure 2.8.: Calculated $\varepsilon_{Xe}/\varepsilon_{Kr}$ from our measured isotopic ratios as a function of measurement date (see Chapter 3 for how this is done in detail). Colours of datapoints indicate the three different glacial Terminations measured in 2022, and the shading gives further indication of sample age within these Terminations. The theoretical value for $\varepsilon_{Xe}/\varepsilon_{Kr}$ of about 1.4 suggested by a 2D firn model (Birner et al., 2018) is shown as horizontal grey dashed line. Calculated $\varepsilon_{Xe}/\varepsilon_{Kr}$ strongly correlates with residuals of PIS for Xe isotopes, plotted as black dots connected with a black line. These residuals are calculated by taking the difference between the weekly measurements of PIS and the linear fit through these weekly PIS datapoints. The coloured datapoints are corrected for the chemical slope assuming such a linear temporal evolution of CS. However, the strong correlation with PIS residuals suggests that the temporal evolution of the chemical slope correction should follow that of the pressure imbalance correction instead. Vertical dashed lines in black indicate days on which samples with drilling fluid contamination as detected on the Delta V IRMS were measured. Dashed lines in red show samples with drilling fluid contamination detected on both IRMS. The affected samples themselves are not shown.

When measuring Xe and Kr signal intensities of a pure Ar sample, we found elevated intensities compared to what is expected from the operative background, i.e., compared to an empty bellow. The net effect, that is, the Kr or Xe signal intensity of the side containing pure

Ar minus the operative background, decreases exponentially with Ar signal intensity (ion source pressure; Figure 2.9.). This exponential decrease appears to be a combination of two effects: an exponential decrease of available Xe and Kr ions over time and a likely linear dependency of the effect on the Ar signal intensity. The net intensities of a gas species roughly scale with the isotopic abundances for this gas species, possibly with a slight enrichment of heavier isotopes. However, this abundance scaling breaks down when comparing different gas species: Xe signal intensities are approximately 2.5 higher than what would be expected from Kr signal intensities.

We believe that this phenomenon is caused by build-up of Xe and Kr (as well as Ar) on the surface of the mass spectrometer source housing or ion guiding plates. This happens either through adsorption to or incorporation in the surface layer of these parts. As the Ar beam hits the surface, it provides enough energy to release the adsorbed or incorporated Xe and Kr, which then finds its way to the respective cups. In such a process, we expect natural abundances to be roughly fulfilled. The fact that Xe is affected more strongly than Kr may be due to a higher readiness for adsorption/incorporation; assuming an incorporation process, we would expect the heavier Xe ions to be incorporated more readily. In our idealised experiment with pure Ar in one bellow and no gas in the other bellow, the Xe and Kr build-up is not replenished, leading to an exponential decrease over time. During an actual measurement, replenishment occurs constantly, and the effect should therefore stay constant over time.

We expect the effect to be negligible for isotopic ratios, as signal matching is done on ^{129}Xe and ^{84}Kr, respectively, meaning that the effect will roughly be equal for both sides. For elemental ratios, however, the effect does become relevant. Here, signal matching is performed on ^{40}Ar, and sample side and standard side will thus be measured at different Xe (Kr) signal intensities if the two aliquots differ in δXe/Ar (δKr/Ar). The relative importance of the effect will be larger on the side with lower δXe/Ar (δXe/Ar). It should be noted that differences in chemical composition between sample side and standard side might also lead to small differences in the build-up of Xe and Kr ions for the two sides. The Xe and Kr build-up of the side containing more Ar will be somewhat smaller, translating into slightly reduced desorption/sputtering for the other side, leading to a small degree of smoothing. However, this smoothing should be very minor, as the desorption/sputtering changes only little over the timespan of a changeover-valve cycle and differences in chemical composition between sample and standard are small.

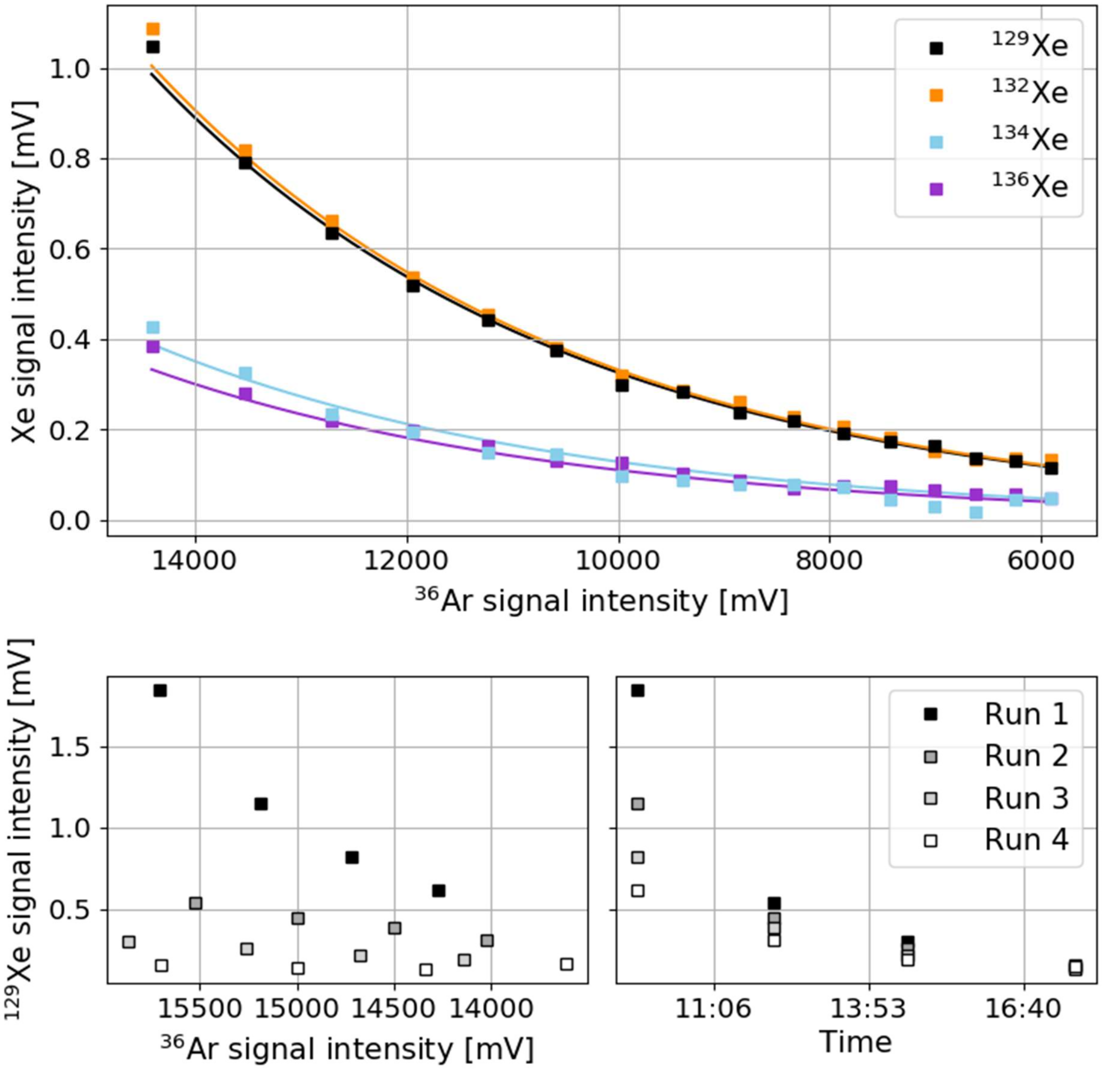

Figure 2.9.: The upper panel shows beam intensities for m/z 129 to 136 (Xe isotopes) measured on a pure Ar sample. The ratios between Xe signal intensities roughly match the ratios of Xe isotope natural abundances. As time progresses, the Xe signal intensities exponentially decrease. The exponential decay is a combined signal of two effects: a close to linear dependency of the Xe signal intensities on the Ar beam intensity, as shown in the bottom left panel; and an exponential decrease of the amount of Xe isotopes mobilised over time for a constant Ar beam intensity, shown in the bottom right panel. Lines in the upper panel indicate natural abundances of Xe isotopes relative to ^{129}*Xe. Shadings in the bottom panels distinguish between consecutive runs, at the start of which* ^{36}*Ar signal intensity was set to about 15.5V. Between runs, the Xe build-up was not replenished.*

When the Xe and Kr build-up is maximal, the effect reaches about 2 mV for ^{129}Xe and about 16.5 mV for ^{84}Kr. During peak jumping, ^{129}Xe and ^{84}Kr are measured at about 200 mV and 3000 mV signal intensity, respectively. For these signal intensities, the desorption/sputtering effect amounts to roughly 5.5 per meg change in δXe/Kr per permille change in Ar content. The exact size of the effect will be dependent on the source parameter settings. However, it is noteworthy that the effect is of similar size to the chemical slope found for δXe/Kr. For δXe/Ar, the effect from desorption/sputtering of Xe ions is almost twice as large as for δXe/Kr and might amount to an 0.35 °C overestimation of interglacial MOT based on this elemental ratio. Glacial MOT should be somewhat less elevated, about 0.25°C, due to the shallower firn column during glacial times and thus lower δXe/Ar of glacial samples. As the effect on Kr is about 2.5 times weaker than for Xe, δKr/Ar is affected less strongly than δXe/Ar. Due to the smaller temperature sensitivity of δKr/Ar, the effect still amounts to about 0.2 °C MOT overestimation during interglacial periods (~0.15 °C for glacial periods). For now, we refrain from applying a correction for this desorption/sputtering effect, as the underlying mechanism is not fully understood and as the expected effect on relative MOT is only small.

Mismatch between $\delta^{40/36}Ar_{MAT}$ and $\delta^{40/36}Ar_{Delta}$

The only ratio that is measured on both mass spectrometers is $\delta^{40/36}$Ar. The measurement on the MAT 253 is considerably more precise and is therefore the one used for MOT reconstruction, whereas the value obtained from the Delta V only serves to detect samples affected by drilling fluid. Somewhat concerningly, $\delta^{40/36}Ar_{MAT}$ and $\delta^{40/36}Ar_{Delta}$ rarely agree with one another within measurement uncertainty. As $\delta^{40/36}Ar_{MAT}$, unlike $\delta^{40/36}Ar_{Delta}$, is in good agreement with what we would expect it to be from N_2, Kr, and Xe isotopic ratios, $\delta^{40/36}Ar_{Delta}$ is the likely culprit for this discrepancy.

Closer inspection of the difference between $\delta^{40/36}Ar_{MAT}$ and $\delta^{40/36}Ar_{Delta}$ ($\Delta\delta^{40/36}$Ar) shows strong covariation between $\Delta\delta^{40/36}$Ar and $\delta O_2/N_2$ (Figure 2.10.) We believe isobaric interference of the clumped oxygen isotope $^{18}O^{18}O$ at m/z 36 to be the cause for this. Oxygen is not removed prior to sample analysis on the Delta V as we are interested in oxygen isotopic ratios and $\delta O_2/N_2$ of our ice samples. We currently do not correct for this interference. However, the chemical slope of oxygen on $\delta^{40/36}Ar_{Delta}$, which we measure as the change in $\delta^{40/36}Ar_{Delta}$ as a function of $\delta O_2/N_2$, has an $^{18}O^{18}O$ interference signal imprinted. Samples with higher $\delta O_2/N_2$, i.e., higher oxygen content, have a stronger isobaric interference of $^{18}O^{18}O$ on m/z 36, which affects the measured chemical slope. Consequently, the chemical slope of $\delta^{40/36}Ar_{Delta}$ is considerably larger and furthermore goes in opposite direction than the chemical slopes of oxygen on $\delta^{15}N_2$ and $\delta Ar/N_2$ (Table 2.5.). When correcting $\delta^{40/36}Ar_{Delta}$ of a sample for the chemical slope, the applied correction implicitly takes care of the $^{18}O^{18}O$ interference on m/z 36. However, this implicit correction is only correct when $\delta O_2/N_2$ is representative of $\delta^{36}O_2/^{36}Ar$. For ice samples, this relationship between $\delta O_2/N_2$ and $\delta^{36}O_2/^{36}Ar$

breaks down as differences in the expulsion of Ar and O_2 at bubble close-off cause $\delta O_2/N_2$ and $\delta Ar/N_2$ to vary independently. Furthermore, differences in gravitational fractionation strength leads to variations in $\delta^{40/36}Ar$ and $\delta^{18}O$, both of which then affect $\delta^{36}O_2/^{36}Ar$ and thus the strength of the $^{18}O^{18}O$ interference on m/z 36.

If same ionisation efficiencies for Ar and O_2 are assumed, the strength of the interference can be calculated as follows:

$$\Delta\delta^{40/36}Ar = \left(\frac{\left(\frac{A_{^{40}Ar}}{A_{^{36}Ar}}\right)_{Delta}}{\left(\frac{A_{^{40}Ar}}{A_{^{36}Ar}}\right)_{MAT}} - 1 \right) \cdot 10^3‰$$

$$= \left(\frac{\frac{A_{^{40}Ar_{Delta}}}{\left(A_{^{36}Ar_{Delta}} + A_{O_2} \cdot P_{^{18}O}{}^{2} \cdot \Delta\delta^{36}\mathrm{O_2}/^{36}\mathrm{Ar}\right)}}{\left(\frac{A_{^{40}Ar}}{A_{^{36}Ar}}\right)_{MAT}} - 1 \right) \cdot 10^3‰ \qquad (2.3.)$$

Here, A_x means the abundance of a gas or isotope x, $P_{^{18}O}$ is the natural abundance of ^{18}O in oxygen, and $\Delta\delta^{36}O_2/^{36}Ar$ is the difference between sample and standard $\delta^{36}O_2/^{36}Ar$. $\Delta\delta^{36}O_2/^{36}Ar$ itself is a function of $\delta^{40/36}Ar_{Delta}$, meaning that the above equation may only be solved iteratively. Using the above equation to correct both chemical slope measurements and ice sample measurements not only leads to the chemical slope of $\delta^{40/36}Ar_{Delta}$ to point in the same direction as those of $\delta^{15}N_2$ and $\delta Ar/N_2$, but also significantly improves the agreement between $\delta^{40/36}Ar_{Delta}$ and $\delta^{40/36}Ar_{MAT}$ (Figure 2.10.). However, even after applying this correction for $^{18}O^{18}O$ interference on m/z 36, $\Delta\delta^{40/36}Ar$ of samples measured in 2022 is still clearly different from 0. If the interference correction is expanded to outside air measurements, the discrepancy can be reduced by some 5 per meg. Yet, a small offset remains, which might be due to our incorrect assumption of equal ionisation efficiencies of Ar and O_2. Molecular oxygen has a considerably lower first ionisation energy than argon. The correction applied above is therefore likely a lower estimate. Furthermore, the effect of differences in ionisation efficiency on $\delta^{40/36}Ar_{Delta}$ should depend on the source parameters and was likely different for data from different measurement periods.

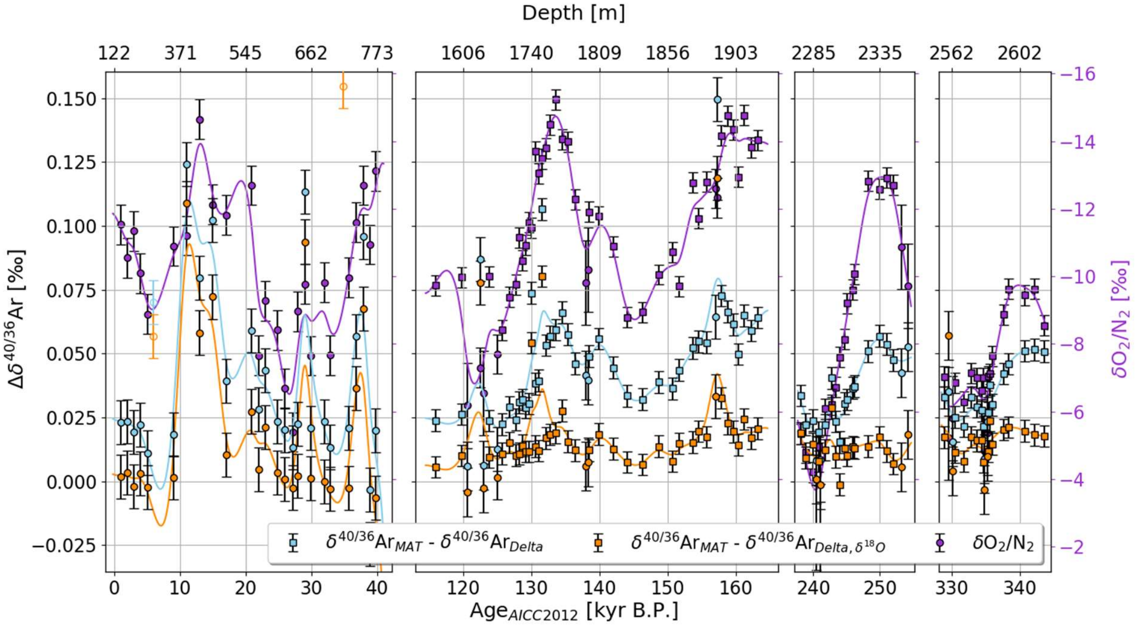

Figure 2.10.: Covariation between $\Delta\delta^{40/36}$Ar and $\delta O_2/N_2$. Blue markers show $\Delta\delta^{40/36}$Ar without correction for $^{18}O^{18}O$ interference, whilst data plotted in orange were corrected. Note that the y-axis is reversed for $\delta O_2/N_2$. Samples measured in the scope of this PhD thesis are given as squares, those measured during earlier periods are given as circles. Open symbols indicate data points that are affected by drilling fluid contamination. Lines show cubic smoothing splines with cutoff frequencies of 5 kyr.

2.3.3.c. Bellow gas amount correction

To minimize the pressure-dependency of the measured ratios, sample bellow and standard bellow are usually signal matched before each block. However, due to the initial difference in aliquot size, the bellow containing less gas will have to be compressed slightly more to achieve equal source pressure. The bellow containing less gas will deplete faster than the bellow containing more gas. Considering a measurement duration of more than nine hours for the MAT 253, this leads to sizable differences in leftover bellow gas amounts by the end of the routine, especially for samples that already start with a considerable gas amount imbalance. Thus, should any fractionation occur at the inlet capillaries, the gas remaining in the bellows will be gradually more fractionated in the opposite direction. This will affect the measured ratios even if both sides experience the same fractionation, as the accumulated fractionation product will have a stronger effect on the side containing less gas. Indeed, we find ratios measured towards the end of the MAT 253 routine to be correlated to the gas amount ratio of the two bellows.

We therefore introduce a bellow gas amount (BGA) correction, which we apply to the ratios measured at the end of the MAT 253 routine, i.e., the Kr and Ar isotopic ratios, and all the elemental ratios. To determine this correction, we perform a suite of measurements for which a range of differing gas amounts was admitted to the sample side and standard side bellows. The amounts are chosen such that the gas amount ratios between the two sides, Δ_{bellow}, cover somewhat more than the expected spectrum of ice sample and outside air measurements. We then calculate the difference between isotopic ratios obtained during a BGA measurement, $\delta_{\Delta_{bellow}}$, and those from a measurement with a gas amount ratio similar to what we expect from ice samples, $\delta_{\Delta_{bellow,\ ice\,sample}}$. For Kr isotopic ratios, the BGA correction factors are then determined through linear interpolation of these differences as a function of Δ_{bellow}. For Ar isotopic ratios and all elemental ratios, a quadratic fit is used instead.

$$\delta_{BGA}(\Delta_{bellow}) = \left(\delta_{\Delta_{bellow}} - \delta_{\Delta_{bellow,\ ice\,sample}}\right)$$

$$= \left(a \cdot \Delta_{bellow}{}^{2}\right) + b \cdot \Delta_{bellow} + c \qquad (2.4.)$$

The bellow gas amount ratio is defined as the ratio between the fraction of gas left in the sample bellow and the fraction left in the standard bellow after all isotope blocks are measured, i.e., at the end of the second Ar isotope block.

$$\Delta_{bellow} = \frac{f_{Sample}}{f_{Std}} = \frac{\Pi_i\left(1-\left(f_{block_i}\right)_{Sample}\right)}{\Pi_i\left(1-\left(f_{block_i}\right)_{Std}\right)} \qquad (2.5.)$$

To calculate the gas depletion within a measurement block i, f_{block_i}, we use the beam intensities of the most abundant isotopes, i.e., ^{132}Xe, ^{84}Kr, and ^{40}Ar in each of the respective gas configurations. For this, a linear relationship between signal intensity and bellow gas amount is assumed. The following equation shows this exemplary for ^{132}Xe.

$$f_{Xe} = \frac{{}^{132}Xe_{1st\ cycle} - {}^{132}Xe_{last\ cycle}}{{}^{132}Xe_{1s\ \ cycle}} \qquad (2.6.)$$

Finally, these BGA correction factors are applied to our mass spectrometry data:

$$\delta_{PI,CS,BGA} = \delta_{PI,CS} - \delta_{BGA}(\Delta_{bellow}) \qquad (2.7.)$$

Due to the nature of the fractionation, the BGA correction is largest for ratios measured towards the end of the measurement routine. It can be quite sizeable, especially for large Δ_{bellow}. The correction is on the order of a few per meg to some ten per meg for isotopic ratios but can reach up to about a hundred per meg for elemental ratios (Figure 2.11.). Xe isotopic ratios and ratios measured on the Delta V, on the other hand, are measured within the first three hours of the respective routine. The accumulation of the fractionation product therefore is too small to cause a noticeable bellow gas amount fractionation effect. Consequently, no correction is applied to these ratios.

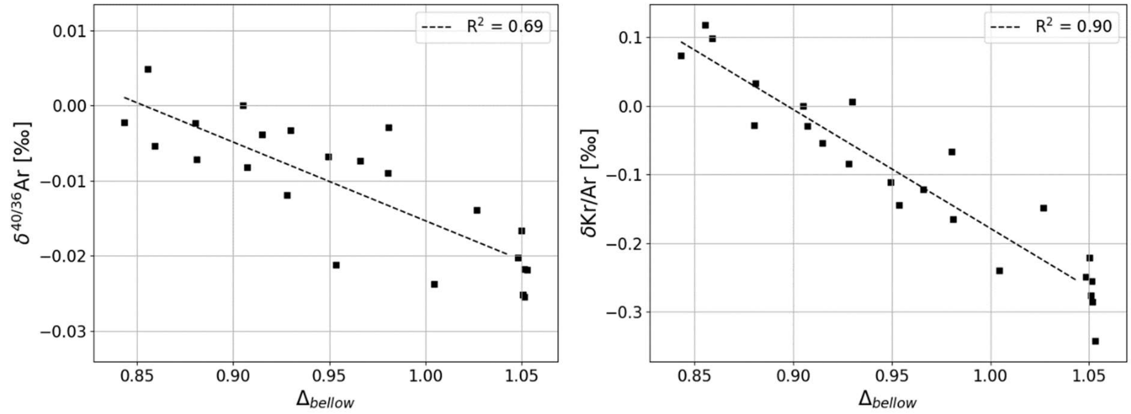

Figure 2.11.: Dependency of $\delta^{40/36}$Ar and δKr/Ar on bellow gas amount ratio for the 2022 measurement period.

Over the years, we found that the BGA correction is variable over time. This is unexpected, since our current understanding of the fractionation process would suggest a stable correction as long as the capillaries and crimps stay untouched. One way of creating a variable BGA correction might be if the fractionation that happens at the capillary were to be dependent on bellow pressure (Benjamin Birner, pers. comm.). The bellow pressure at which measurements are run does change between measurement periods because different filaments and source parameter settings require different source pressures to reach the set signal strength. We tested this hypothesis by measuring the BGA effect with the same source parameter settings but with different signal intensities. However, no clear relationship of signal intensity and bellow pressure could be established. Nonetheless, we suggest that some BGA measurements are run after each change of the filament or the source parameters to make sure the BGA parameters are unchanged.

2.3.3.d. ^{40}Ar-tail correction

After ionisation, not all ions are accelerated and focused to the exact same degree. This results in a bell-shaped ion beam with a small percentage drifting off far enough to end up in a cup of different m/z ratio than their own. For Ar, we typically find this to be the case for some tenths of a permille of ions. This can cause problems when measuring a less abundant ion in the presence of a highly abundant ion with similar m/z ratio. Such is the case when measuring ^{38}Ar with a natural abundance of about 0.06% in presence of ^{40}Ar, with 99.6% the predominant Ar species in our atmosphere. For 2022 source parameter settings, about 1% of the measured ^{38}Ar-beam intensity was caused by the lower tailing end of the ^{40}Ar-beam, leading to too low $\delta^{40/38}$Ar ratios. Since the beam shape is slightly pressure dependent, the effect the ^{40}Ar-tail has on ^{38}Ar is expected to be pressure dependent, too. This is exactly what we find when comparing $\delta^{40/38}$Ar* without ^{40}Ar-tail correction and $\delta^{40/38}$Ar* with ^{40}Ar-tail correction of standard-vs.-standard measurements performed in September of 2022 (Figure 2.12.). These measurements suggest a ~0.5 per meg increase in $\delta^{40/38}$Ar* per permille of pressure imbalance (0.5 per meg/‰ PI). The asterisk indicates that the ratios have been normalised to unit mass difference.

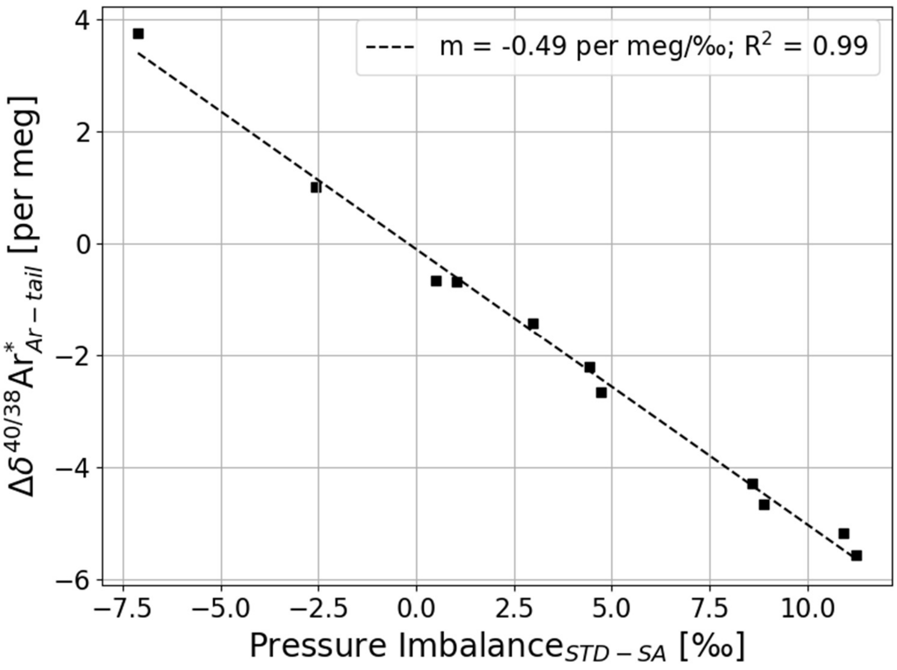

Figure 2.12.: Pressure dependency of $\Delta\delta^{40/38}Ar^{*}_{Ar\text{-}tail}$, i.e., the difference between $\delta^{40/38}Ar^{*}$ without and $\delta^{40/38}Ar^{*}$ with ^{40}Ar-tail correction. Both $\delta^{40/38}Ar^{*}$ have been corrected for the effect of "regular" pressure imbalance, chemical slope, and bellow gas amount ratio. Shown are standard-vs.-standard measurements performed in September 2022. The black dotted line gives the linear regression solution.

On first thought, one might expect the applied pressure imbalance correction to take care of this additional pressure imbalance signal dependency. After all, the here suggested ^{40}Ar-tail correction is nothing else than a second linear correction with the bellow pressure imbalance as predictor. The reason our pressure imbalance correction does not capture this secondary pressure imbalance signal lies in the way PIS is determined. To determine PIS as precisely as possible, we imbalance the bellow pressures by about 10% in both directions, which is an order of magnitude more than the expected pressure mismatch during a regular measurement. As the ion beam intensity curve is approximately bell-shaped, the tails should decay exponentially with distance from the centre. Within a narrow pressure imbalance range, this exponential decay can easily be approximated with a linear function, as seen in Figure 2.12. However, for larger ranges of pressure imbalance, the exponential shape of the tail has a noticeable effect, which cannot be captured by our two-point determination of PIS. Consequently, the slope of the applied pressure imbalance correction does not capture the full pressure imbalance effect. Since the pressure imbalance region of regular measurements is narrow, a second linear pressure imbalance correction can take care of this secondary pressure dependency. A ^{40}Ar-tail correction to the measured ^{38}Ar signal intensities is thus necessary.

To apply such an ^{40}Ar-tail correction, we extrapolate the influence of the ^{40}Ar-tail from the cup neighbouring the ^{38}Ar-cup to the ^{38}Ar-cup. This is currently done by multiplying the measured signal intensity on that neighbouring cup by an empirically determined factor of 0.9. This empirical correction has shown promising results in terms of reducing the standard deviation of $\delta^{40/38}$Ar within and between standard-vs-standard measurements. However, the ^{40}Ar-tail correction has only recently been established and other methods for the correction of the ^{40}Ar-tail may also be considered. One alternative might be to use the average of the signal intensities of the ^{38}Ar-cup's two neighbouring cups. This, however, would slightly overestimate the ^{40}Ar-tail influence on the measured ^{38}Ar-beam, as an exponential decay of the tail is expected.

The necessity of an ^{40}Ar-tail correction becomes evident when looking at $\delta^{40/36}$Ar* and $\delta^{40/38}$Ar* of ice samples measured during the three measurement periods between 2016 and 2022. Unlike for other gravitationally corrected isotopic ratios of the same element, $\delta^{40/38}$Ar* – $\delta^{40/36}$Ar* on average differs from the expected value of 0. This disagreement between the two isotope ratios could be indicative of a mass-fractionating gas-loss process taking place during bubble close-off. It is disputed whether mass-dependent fractionation of Ar during bubble close-off does happen with contradicting evidence presented in the literature (e.g., Battle et al., 2011; Buizert et al., 2023). As no correlation to the gas-loss indicator $\delta O_2/N_2$ is apparent, it seems likely that another process is at the cause of the offset. Closer inspection reveals a negative correlation of $\delta^{40/38}$Ar* – $\delta^{40/36}$Ar* with the mean pressure imbalance between the standard side and sample side during Ar isotope measurement blocks (Figure 2.13.). For samples measured in 2022, $\delta^{40/38}$Ar* – $\delta^{40/36}$Ar* is lower by about 0.4 per meg/‰ PI. This is in good agreement with the 5 per meg/% PI slope we find for the ^{40}Ar-tail correction of standard-vs-standard measurements. We thus suggest that the non-zero offset between $\delta^{40/38}$Ar* and $\delta^{40/36}$Ar* can be explained by the absence of an ^{40}Ar-tail correction during all three sample measurement periods.

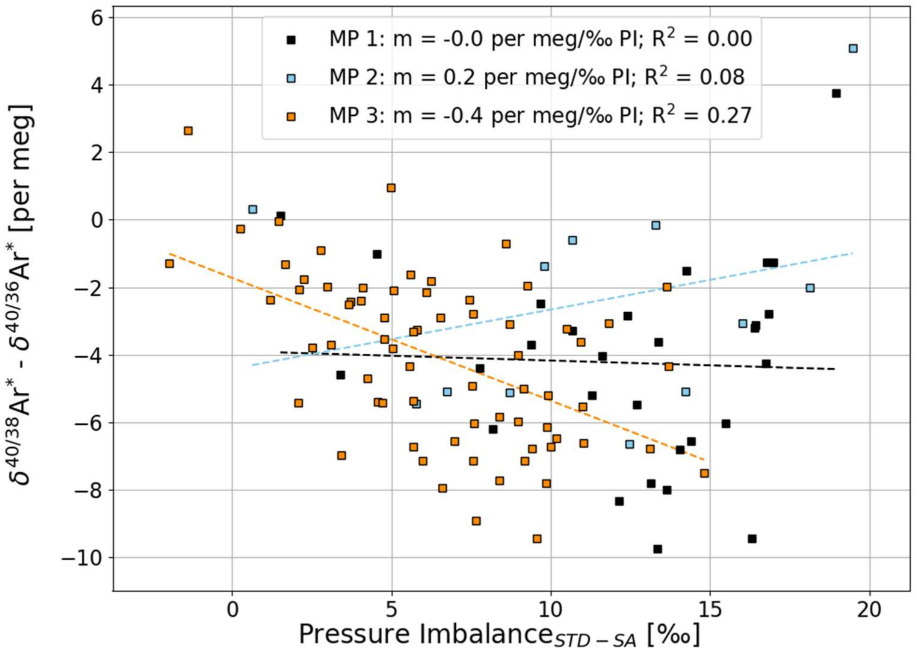

Figure 2.13.: Cross correlation plot of the pressure imbalance between standard side and sample side bellow during the Ar isotope measurement blocks and the difference between $\delta^{40/38}Ar^*$ *and* $\delta^{40/36}Ar^*$*. The three measurement periods (MP1: 2016-2017; MP2: 2017; MP3: 2022) are plotted in different colours. The dashed lines give the linear regression solutions.*

The correlation between $\delta^{40/38}\mathrm{Ar}^* - \delta^{40/36}\mathrm{Ar}^*$ and the associated pressure imbalance is statistically significant for samples measured in 2022 ($p < 0.001$), whereas there is only weak correlation for samples measured between 2016 and 2017. This is not surprising, as the older data was measured using different filaments and different source parameter settings, which would lead to different Ar-beam shapes. Figure 2.13 suggests that the ^{40}Ar-tail may have been less pressure-dependent during these earlier measurement periods. The lower correlation for measurements from 2016 and early 2017 may also in parts be due to slightly lower analytical precision.

Further support for the introduction of an ^{40}Ar-tail correction comes from the ^{40}Ar-dating slope, which we obtain as a "by-product" of our ice sample measurements. Atmospheric ^{40}Ar gradually increases over time due to radioactive decay of ^{40}K into ^{40}Ar in Earth's crust and upper mantle and the subsequent outgassing of ^{40}Ar therefrom. Past atmospheric ^{40}Ar content can thus be used as a dating tool for ice samples of unknown age. The rate of outgassing is believed to have stayed roughly constant within the past 800 kyr and the increase in atmospheric ^{40}Ar is therefore estimated to be linear (Bender et al., 2008). This ^{40}Ar-dating slope is calculated as the change in $\delta^{40/38}\mathrm{Ar} - 1.002\cdot\delta^{38/36}\mathrm{Ar}$ as a function of gas age. The factor of $1.002\cdot\delta^{38/36}\mathrm{Ar}$ serves as a correction for gravitational and thermal fractionation. As the ^{40}Ar-tail affects the ^{38}Ar-beam intensity, applying a correction for the ^{40}Ar-tail does have a noticeable effect on the steepness of the ^{40}Ar-dating slope, its uncertainty, and its y-intercept (Figure 2.14.). When applying such a correction to our data, using the parameters suggested by the regression lines in Figure 2.13., ^{40}Ar-dating slopes and y-intercepts of data measured by Häberli, 2019 and in the scope of this PhD-thesis get into better agreement with the published data from Bender et al., 2008. Also, the individual data points are on average slightly closer to the regression lines, leading to lower uncertainties in the regressions.

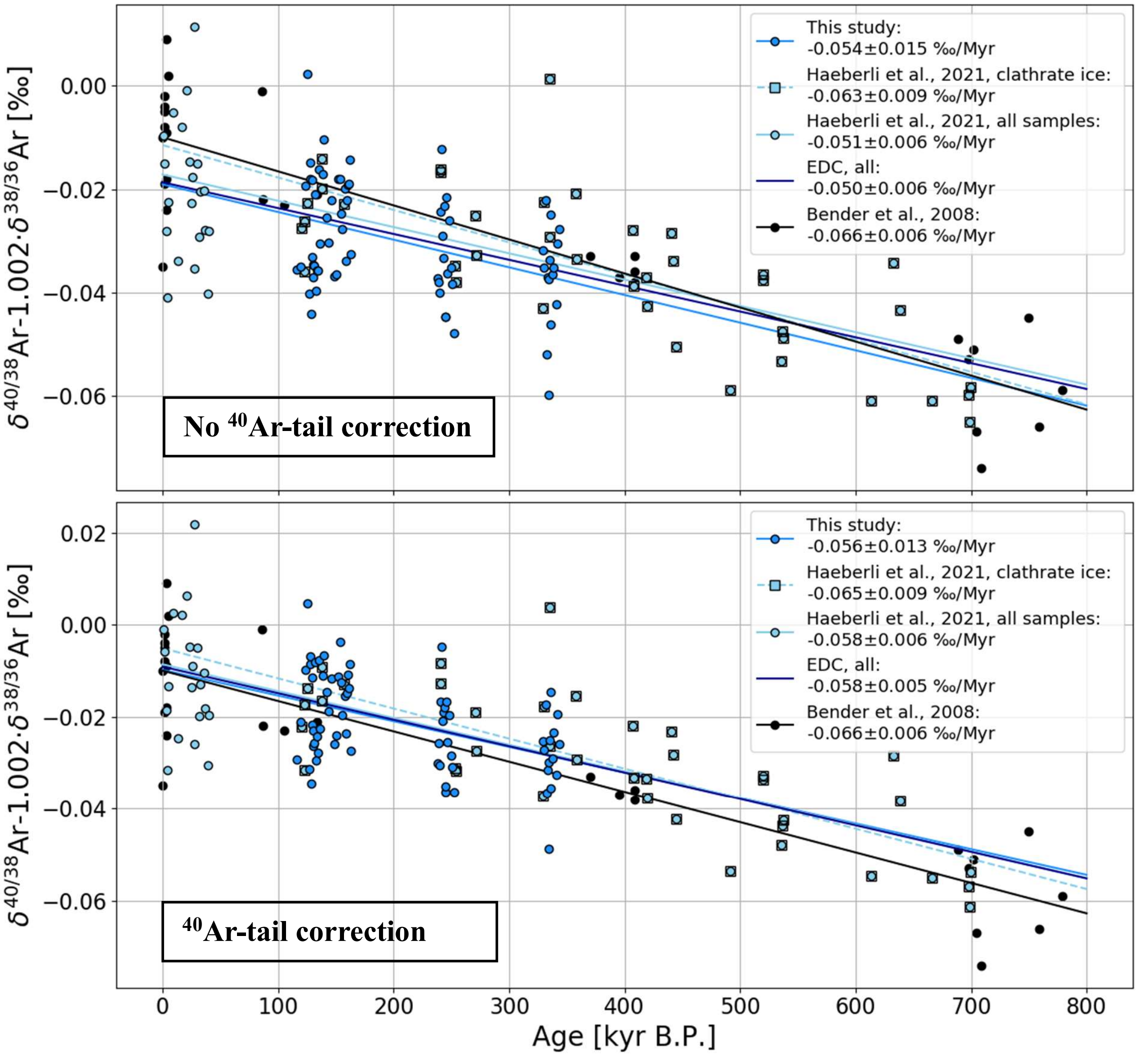

Figure 2.14.: Comparison of the ^{40}Ar-dating slopes derived from samples of various ice core measured by Bender et al., 2008, from EDC samples measured in Bern between 2016 and 2017 published in Haeberli et al., 2021, and from EDC samples measured in Bern in 2022. Drawn lines show the linear regressions to the different datasets, the dashed line indicates the linear regression for clathrate samples only. In the upper panel, samples from Bern have not been corrected for the ^{40}Ar-tail effect on ^{38}Ar, whereas in the lower panel, a correction to all Bern data has been applied, using the parameters suggested by the regression lines in Figure 2.13.

2.4. Set of standards

Both our mass spectrometers are equipped with a changeover-valve-based dual inlet system. This system allows for a direct and timely comparison of sample and standard. Measuring gas abundances relative to a standard is orders of magnitude more precise than if absolute abundances had to be determined. However, using this approach also demands for a trusted absolute standard. Here in Bern, a set of three standards is used: Bern outside air (BOA), our absolute standard; working standard I and working standard II (WS I and WS II) for everyday use; and Atemluft (AL), a second absolute standard as a control to ensure the stability of BOA. How those are utilised is schematically shown in Figure 2.15. and will be explained in more detail in the following.

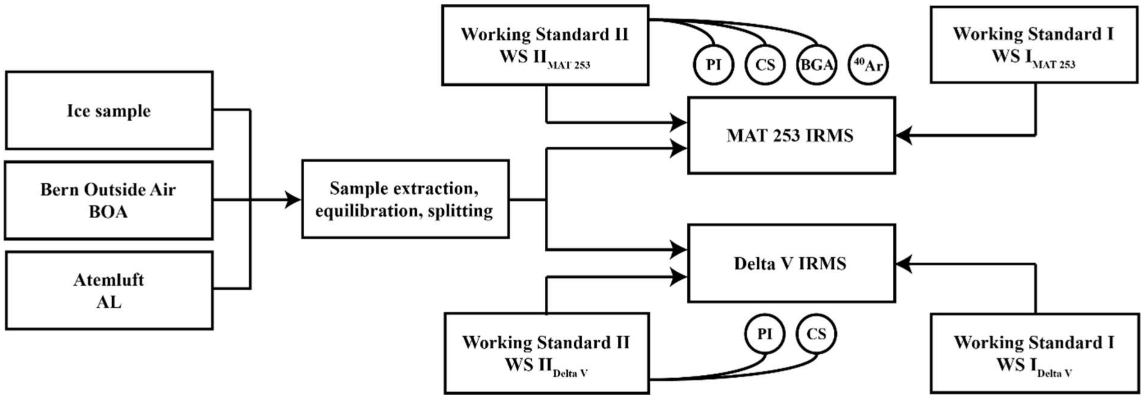

Figure 2.15.: Measurement flowchart indicating use of different standard gases in Bern. Outside air is our absolute standard against which we reference our ice sample measurements. For practicality, every sample is measured against WS I, whereas WS II is used to determine mass spectrometer corrections. Finally, Atemluft measurements ensure the long-term stability of outside air, even across working standard changes.

2.4.1. Bern outside air

We use the modern atmosphere as the ultimate reference for all our measurements. This absolute standard is chosen for multiple reasons. First and foremost, the atmospheric composition of heavy noble gases and nitrogen has essentially stayed constant since the onset of the Holocene. For nitrogen, the atmospheric reservoir is simply too large for even major changes in the nitrogen cycle to have a noticeable effect (Schlesinger and Bernhardt, 2013). The atmospheric noble-gas concentration, on the other hand, is controlled by air-sea exchange fluxes. These are affected by the seasonal cycle and the anthropogenic influence on the ocean temperature. The peak-to-peak seasonal cycle of $\delta Ar/N_2$ was measured to be between 0.006‰ and 0.026‰ (Ishidoya and Murayama, 2014 and studies therein), which is less than our measurement uncertainty (Tables 2.7.–2.9.). For $\delta Xe/N_2$, the ratio most sensible to ocean solubility changes, we expect about 5 times that amplitude, also less than our measurement uncertainty. The effect of anthropogenic warming on ocean temperature (thus far) is smaller than that of the seasonal cycle. Thus, even though small changes in the atmospheric abundances of these gases do occur, they are smaller than our measurement uncertainty, making outside air a reliable absolute standard. Second, the atmosphere is well-mixed with a mixing time of about one year. Thus, outside air is reproducible anywhere and can be used as an absolute standard worldwide. And third, there is no danger of ever running out of this absolute standard.

2.4.1.a. Sampling Bern outside air

To sample BOA, we proceed in almost identical fashion as described in Severinghaus et al., 2003 for air samples from the Scripps pier in La Jolla and adopted with minor modifications in many studies since (e.g., Bereiter et al., 2018; Haeberli et al., 2021; Headly and Severinghaus, 2007; Shackleton et al., 2021). In brief, the setup (Figure 2.16.) starts with a ¼" OD Dekabon polyethylene-aluminium composite tubing (Synflex 1300), which is sampling air from the atmosphere. This inlet tube is placed out of the sunlight to avoid thermal fractionation. A diaphragm vacuum pump (KNF Neuberger N 920 G) sucks the air into the tubing and through two sequential glass water traps cooled with ethanol to about −90 °C. Next comes the pump itself, followed by the outside air volume and a 5 L plastic flask. The plastic flask, together with the long tubing, is used as an air buffer tank and ensures a stable airflow. This airflow is controlled via a flowmeter that is placed downflow of the plastic flask. We aim for a constant airflow of around 4 L/min, which can be achieved through finely adjusting an in-line Nupro valve. Unlike Headly and Severinghaus, 2007, we do not use an additional pump that pulls air into a larger intake tube enclosing the actual sampling tube. Although this type of aspirated intake setup promises reduced fractionation at the intake (Blaine et al., 2005), we decided to stick with the simpler setup of having only the inlet tube sticking out into the atmosphere (as done by Severinghaus et al., 2003). This may be worth improving on in the future in order to avoid BOA sampling artefacts, as happened to a filling in June 2017 (Fig. 2.18.) Another small difference to the setup used by Headley and Severinghaus is the use of a 1-gallon (3.78 L) stainless-steel volume to sample the outside air into, instead of a series of 4 cm^3 volumes.

To sample outside air, the assembly is flushed at 4 L/min for at least 10 minutes to ensure a stable airflow and that the gas in the outside air volume was exchanged at least ten times. After these ten minutes, the pump is turned off. We then allow the air flow to cease for about three seconds and then simultaneously close the two Nupro valves that seal the outside air volume. A step-by-step description of the sampling procedure can be found in Annex A.3.1.

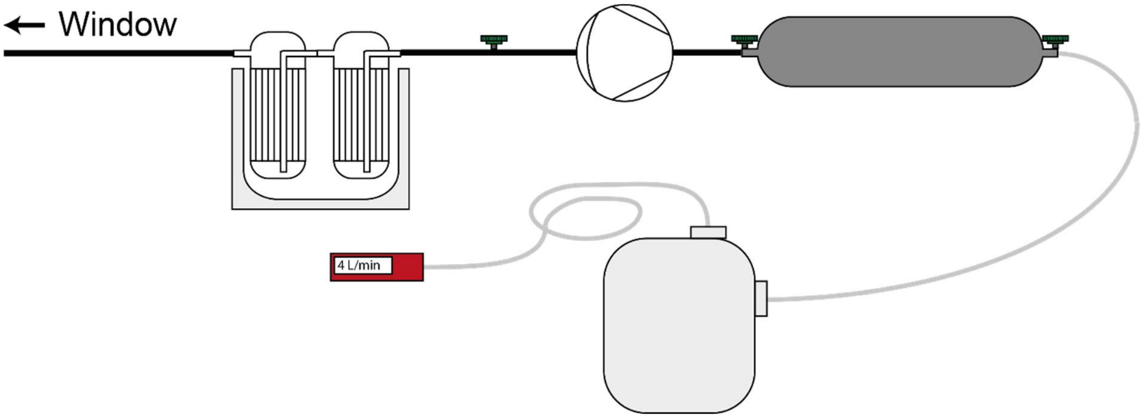

Figure 2.16.: The setup for sampling unfractionated atmospheric air used in Bern.

2.4.1.b. Measuring Bern outside air

From the 1-gallon outside air volume, between 13 and 15 BOA aliquots can be taken. To do so, the outside air volume is connected to the extraction system via C_4 (Figure 2.1.). Between the Nupro valve that seals the outside air flask and C_4 two different volumes can be placed: one of roughly 4 cm^3 and one of about 10 cm^3. Typically, the smaller volume is used for the first five to seven samples and the 10 cm^3 volume for the remaining samples. This ensures that for each sample, enough gas is available for the MAT 253 analysis of the noble gas aliquot. If instead the larger volume is used throughout, only 13 samples can be taken from one outside air filling.

The measurement procedure for an outside air sample mimics that of an actual ice sample as closely as possible, although it skips the initial steps an ice sample takes from the extraction vessel through the water traps. The effects of these steps were tested by Thomas Kellerhals by adding BOA through a capillary into the extraction vessel, who found no noticeable fractionation to occur. We thus directly start the BOA measurement procedure by connecting the outside air volume to the extraction system via C_4 as described above. After evacuating and leak testing the line leading to C_4, V_2 is closed and the Nupro valve sealing the outside air container is opened for about three seconds. This fills the volume placed between the Nupro valve and C_4 as well as the large and small equilibration volume. Thus, the first sample taken from a newly sampled outside air volume consists of about 56–62 mL STP atmospheric air. Next, the outside air sample is frozen into a finger cooled to 15 K in the cryostat. The finger with the sample air is then removed from the cryostat and, after disconnecting the outside air volume, connected to C_4 for overnight equilibration. All subsequent steps are analogous to those of an ice sample. The detailed outside air measurement procedure is described in Annex A.2.1.

2.4.1.c. Reproducibility of Bern outside air measurements

All our ice sample measurements are expressed relative to BOA, which thus acts as our absolute reference point. Additionally, we use BOA to determine the reproducibility of our ratios, as our method uses too much ice to allow for replicate ice measurements. The 1σ uncertainty of a ratio is given by the standard deviation of BOA measurements.

However, over the course of several years, BOA-vs-WS I values have slightly changed. Figure 2.17. shows this exemplary for $\delta Ar/N_2$ and $\delta^{40/36}Ar$ measured on the two IRMS. This change may be a consequence of a gradual shift in mass spectrometer baseline or extraction line baseline. However, they may more likely point towards a gradual accumulation of fractionation products in our WS I cylinder, as we find very similar trends in WS II-vs-WS I measurements as in BOA-vs-WS I. Some more drastic shifts in BOA-vs-WS I can be attributed to changes of the filament and hence altered (and potentially suboptimal) mass spectrometry corrections, changes of the working standard, or sampling artefacts of BOA. BOA datapoints that are clearly affected by fractionation during sampling, as is the case for $\delta Ar/N_2$ and $\delta^{40/36}Ar_{Delta}$ measured in early 2017, are removed from the record. A more gradual change of BOA-vs-WS I is more difficult to handle and requires strict selection criteria for BOA measurements.

When selecting BOA measurements for the three measurement periods, we aim to only choose BOA samples measured under the same mass spectrometer conditions as the ice samples. Filament, source parameter settings and corrections thus ideally should be the same. This is not always possible, as the Delta V filament had to be changed twice during the 2016–2017 measurement period. To ensure as similar mass spectrometer conditions as possible for BOA and ice samples, we only use BOA measurements performed from shortly before to shortly after the measurement period to reference our ice sample against. Also, we exclude outliers that are more than 2σ away from the average of BOA measurements considered for the respective measurement period. The means and 1σ uncertainties of the three sets of BOA measurements against which we reference our ice samples from the 2016-2017, 2017, and 2022 measurement periods can be found in Tables 2.7.–2.9.

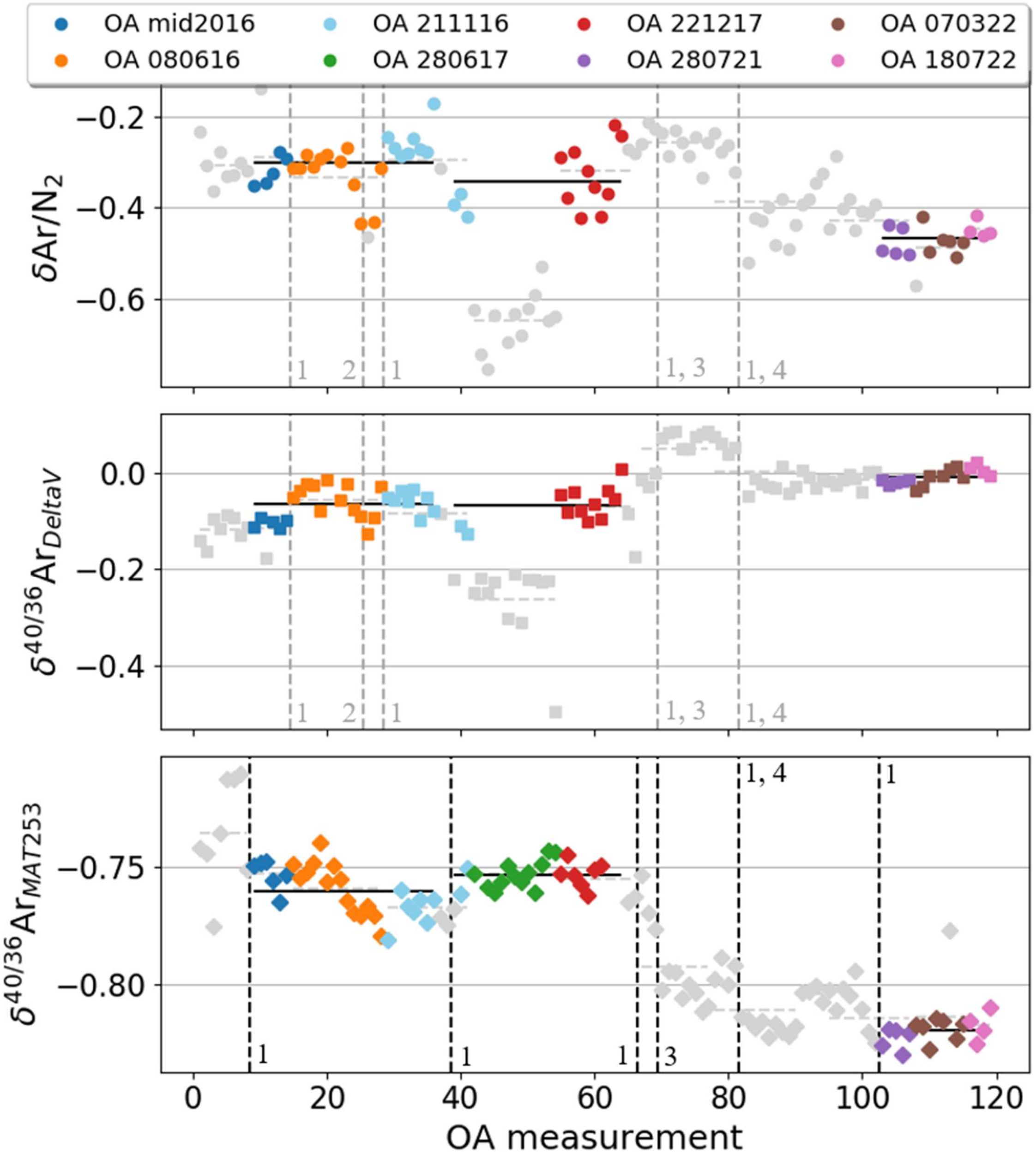

Figure 2.17.: Overview of BOA $\delta Ar/N_2$, $\delta^{40/36}Ar_{Delta}$, and $\delta^{40/36}Ar_{MAT}$, measured over the course of the last seven years. Datapoints in colour indicate samples considered for calculating the three reference values for the three measurement periods. These reference values are indicated as horizontal black lines. Datapoints in grey have not been considered for calculating reference values, either because they were measured at too big of a time difference to ice measurements; because they were affected by poor BOA sampling, such as $\delta Ar/N_2$ and $\delta^{40/36}Ar_{Delta}$ of OA 280617; or because they lie further than 2σ away from the reference value of the measurement period. Horizontal grey dashed lines indicate mean values of individual BOA fillings. Vertical lines in grey and black show major changes to the Delta V and MAT 253, respectively, where 1 indicates a filament change, 2 contamination due to oil pump collapse, 3 upgraded LN_2 trap, and 4 a change in working standards.

2016/2017	**$\delta_{BOA/WS}$**						
MAT 253	**132/129**	**134/129**	**136/129**	**136/132**	**86/84**	**86/82**	**84/82**
# of meas.	26	26	26	27	27	25	26
Mean [‰]	0.065	0.240	1.576	1.509	-0.066	-0.125	-0.062
1σ [‰]	0.016	0.031	0.033	0.038	0.012	0.016	0.014
MAT 253	**$40/36_{MAT}$**	**40/38**	**84/40**	**129/40**	**132/40**	**129/84**	**132/84**
# of meas.	27	26	25	27	26	26	26
Mean [‰]	-0.760	-0.185	-8.002	-2.920	-2.891	5.140	5.185
1σ [‰]	0.011	0.006	0.078	0.183	0.193	0.109	0.127
Delta V	**29/28**	**34/32**	**33/32**	**32/28**	**40/28**	**$40/36_{Delta}$**	
# of meas.	25	26	25	26	25	26	
Mean [‰]	0.005	0.028	0.006	0.218	-0.302	-0.065	
1σ [‰]	0.006	0.018	0.014	0.585	0.054	0.033	

Table 2.7.: Overview of BOA measurements used as reference for the 2016/2017 measurement period, during which 43 EDC ice samples were measured between June 3rd, 2016, and January 7th, 2017. The first BOA measurement considered was performed on May 15th, 2016, the last on January 29th, 2017. Given are the number of BOA measurements considered, their mean relative to the working standard $\delta_{BOA/WS}$, and their standard deviation for each ratio.

2017/2018	**$\delta_{BOA/WS}$**						
MAT 253	**132/129**	**134/129**	**136/129**	**136/132**	**86/84**	**86/82**	**84/82**
# of meas.	22	20	21	21	20	21	20
Mean [‰]	0.063	0.245	1.568	1.505	-0.060	-0.125	-0.062
1σ [‰]	0.030	0.039	0.032	0.030	0.012	0.021	0.015
MAT 253	**$40/36_{MAT}$**	**40/38**	**84/40**	**129/40**	**132/40**	**129/84**	**132/84**
# of meas.	21	21	21	21	20	21	21
Mean [‰]	-0.753	-0.184	-7.909	-2.740	-2.638	5.181	5.291
1σ [‰]	0.006	0.004	0.123	0.206	0.172	0.162	0.140
Delta V	**29/28**	**34/32**	**33/32**	**32/28**	**40/28**	**$40/36_{Delta}$**	
# of meas.	23	24	24	24	13	12	
Mean [‰]	0.003	0.037	0.018	-0.500	-0.344	-0.068	
1σ [‰]	0.007	0.032	0.022	1.274	0.069	0.038	

Table 2.8.: Overview of BOA measurements used as reference for the 2017/2018 measurement period, during which 44 EDC ice samples were measured between September 1st, 2017, and December 4th, 2017. The first BOA measurement considered was performed on June 26th, 2017, the last on March 23rd, 2018. Given are the number of BOA measurements considered, their mean relative to the working standard $\delta_{BOA/WS}$, and their standard deviation for each ratio. $\delta Ar/N_2$ and $\delta^{40/36}Ar_{Delta}$ measurements of filling OA 280617 were removed as they were clearly affected by fractionation during sampling.

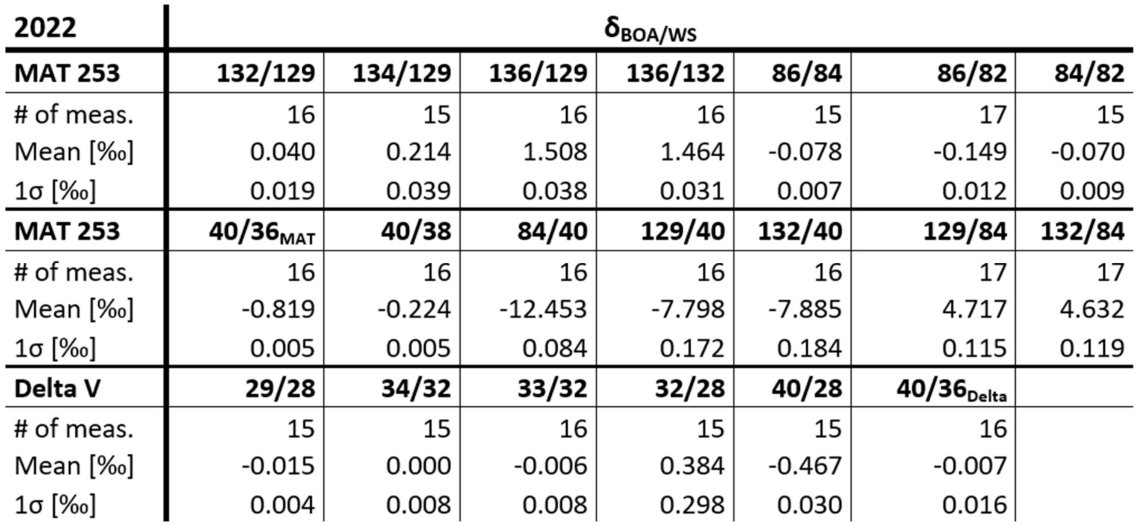

2022	$\delta_{BOA/WS}$						
MAT 253	**132/129**	**134/129**	**136/129**	**136/132**	**86/84**	**86/82**	**84/82**
# of meas.	16	15	16	16	15	17	15
Mean [‰]	0.040	0.214	1.508	1.464	-0.078	-0.149	-0.070
1σ [‰]	0.019	0.039	0.038	0.031	0.007	0.012	0.009
MAT 253	**$40/36_{MAT}$**	**40/38**	**84/40**	**129/40**	**132/40**	**129/84**	**132/84**
# of meas.	16	16	16	16	16	17	17
Mean [‰]	-0.819	-0.224	-12.453	-7.798	-7.885	4.717	4.632
1σ [‰]	0.005	0.005	0.084	0.172	0.184	0.115	0.119
Delta V	**29/28**	**34/32**	**33/32**	**32/28**	**40/28**	**$40/36_{Delta}$**	
# of meas.	15	15	16	15	15	16	
Mean [‰]	-0.015	0.000	-0.006	0.384	-0.467	-0.007	
1σ [‰]	0.004	0.008	0.008	0.298	0.030	0.016	

Table 2.9.: Overview of BOA measurements used as reference for the 2022 measurement period, during which 72 EDC ice samples were measured between March 17th, 2022, and July 11th, 2022. The first BOA measurement considered was performed on February 22nd, 2022, the last on July 22nd, 2022. Given are the number of BOA measurements considered, their mean relative to the working standard $\delta_{BOA/WS}$, and their standard deviation for each ratio.

2.4.2. Working standards

Although BOA serves as a good absolute standard, it is not very practical to work with on a daily basis. As we follow the principle of identical treatment, every aliquot of outside air needs to run through the entire extraction line. This is highly time-consuming: If every sample were to be directly measured against BOA, a sample throughput of two samples per week would be the upper limit. By using a set of working standards instead, the time for analysing an ice sample can be split in half.

We thus measure all our samples against our primary working standard, WS I. For the Delta V, WS I consists of an industrial air mixture called *Atemluft* from which we remove CO_2. For the WS I of the MAT 253, we use an industrial noble gas mixture, to which we mix a small amount of pure Ar. Both WS I are mixed to approximately match the respective sample air. How this is done in practice is described in Annex A.3.2. In addition to this main working standard, a secondary working standard, WS II, serves to assure the stability of WS I. WS II is also used for mass spectrometer tests, and for the determination of the various mass spectrometer correction factors. The two WS II are mixed almost identically to the respective WS I, the only difference being that for the MAT 253 WS II, no Ar is added. Both WS I and both WS II are contained in 2 L stainless-steel cylindrical cylinders, which each have a small pipette volume of roughly 1.5 cm^3 at their exit. This pipette volume is enclosed by two Nupro valves to allow to easily create non-fractionated gas aliquots with similar size as the ice samples. Via these pipette volumes, the working standard cylinders are connected to the respective mass spectrometer using an Ultra-Torr vacuum fitting.

Although these working standards are ideal for everyday use, their isotopic and elemental ratios are arbitrary and hard to replicate. Thus, for publication, we instead express all our ice sample data relative to our absolute standard, BOA. As both ice samples and outside air samples are measured against WS I, this can be done using the following equation. Here, $\delta_{SA/BOA}$ stands for a calculated sample ratio expressed relative to outside air, and $\delta_{SA/WS}$ ($\delta_{BOA/WS}$) is the measured ice sample ratio (outside air ratio) relative to WS I.

$$\delta_{SA/BOA} = \left(\frac{\frac{\delta_{SA/WS}}{1000‰}+1}{\frac{\delta_{BOA/WS}}{1000‰}+1} - 1 \right) \cdot 1000‰ \qquad (2.8.)$$

2.4.3. Atemluft

The industrial air mixture *Atemluft* (AL) is not only used to mix the Delta V working standards, but also serves as an additional absolute standard. As such, it ensures the long-term stability of outside air fillings, even across working standard changes. It comes into play when we need to tie a new set of working standards to previous measurements. Unfortunately, no successful AL measurements could be performed during the 2022 measurement period due to a leaky connection that could only be replaced after the completion of the measurement period.

The measurement procedure for AL is again aimed to mimic that of an ice sample. First, the AL connection line, which consists of a thin metal tubing attached to an arrangement of 0.2 mm OD fused silica capillaries, is connected to the extraction system via C_4 (Figure 2.1.). The connection line features an SGE valve to switch between flushing the line into the lab and admitting AL to the capillary attached to the extraction system. To ensure stable flow, the connection line is flushed for several hours before sampling, while the other capillary directed away from the SGE valve is already attached to the extraction system. After the extraction system and the connection line up to the SGE valve have been evacuated and leak tested, the valve is switched to admit AL to the extraction system pump for about ten minutes. This is done to again ensure stable flow in this new flow regime. Then, V_8 is closed, and AL is admitted to the large equilibration volume for 60 minutes with a gas flow of approximately 1 mL/min, yielding a similar sample size as obtained for ice samples and outside air samples. Next, V_7 is closed, and the sampled AL is frozen into a finger cooled to 15 K in the cryostat.

The finger with the sample air is then removed from the cryostat and, after disconnecting the outside air volume, connected to C_4 for overnight equilibration. All subsequent steps are analogous to those of an ice sample. The detailed AL measurement procedure is described in Annex A.2.2.

References

Augustin, L., Panichi, S., Frascati, F., 2007. EPICA Dome C 2 drilling operations: performances, difficulties, results. Ann. Glaciol. 47, 68–72. https://doi.org/10.3189/172756407786857767

Baggenstos, D., Häberli, M., Schmitt, J., Shackleton, S.A., Birner, B., Severinghaus, J.P., Kellerhals, T., Fischer, H., 2019. Earth's radiative imbalance from the Last Glacial Maximum to the present. Proc Natl Acad Sci USA 116, 14881–14886. https://doi.org/10.1073/pnas.1905447116

Barker, S., Cacho, I., Benway, H., Tachikawa, K., 2005. Planktonic foraminiferal Mg/Ca as a proxy for past oceanic temperatures: a methodological overview and data compilation for the Last Glacial Maximum. Quaternary Science Reviews 24, 821–834. https://doi.org/10.1016/j.quascirev.2004.07.016

Battle, M.O., Severinghaus, J.P., Sofen, E.D., Plotkin, D., Orsi, A.J., Aydin, M., Montzka, S.A., Sowers, T., Tans, P.P., 2011. Controls on the movement and composition of firn air at the West Antarctic Ice Sheet Divide. Atmos. Chem. Phys. 11, 11007–11021. https://doi.org/10.5194/acp-11-11007-2011

Bender, M.L., Barnett, B., Dreyfus, G., Jouzel, J., Porcelli, D., 2008. The contemporary degassing rate of 40Ar from the solid Earth. Proceedings of the National Academy of Sciences 105, 8232–8237. https://doi.org/10.1073/pnas.0711679105

Bereiter, B., Shackleton, S., Baggenstos, D., Kawamura, K., Severinghaus, J., 2018. Mean global ocean temperatures during the last glacial transition. Nature 553, 39–44. https://doi.org/10.1038/nature25152

Birner, B., Buizert, C., Wagner, T.J.W., Severinghaus, J.P., 2018. The influence of layering and barometric pumping on firn air transport in a 2-D model. The Cryosphere 12, 2021–2037. https://doi.org/10.5194/tc-12-2021-2018

Blaine, T.W., Keeling, R.F., Paplawsky, W.J., 2005. An improved inlet for precisely measuring the atmospheric Ar/N2 ratio. Atmos. Chem. Phys. Discuss. 5, 11899–11910.

Buizert, C., Shackleton, S., Severinghaus, J.P., Roberts, W.H.G., Seltzer, A., Bereiter, B., Kawamura, K., Baggenstos, D., Orsi, A.J., Oyabu, I., Birner, B., Morgan, J.D., Brook, E.J., Etheridge, D.M., Thornton, D., Bertler, N., Pyne, R.L., Mulvaney, R., Mosley-Thompson, E., Neff, P.D., Petrenko, V.V., 2023. The new Kr-86 excess ice core proxy for synoptic activity: West Antarctic storminess possibly linked to Intertropical Convergence Zone (ITCZ) movement through the last deglaciation. Clim. Past 19, 579–606. https://doi.org/10.5194/cp-19-579-2023

Dreyfus, G.B., Jouzel, J., Bender, M.L., Landais, A., Masson-Delmotte, V., Leuenberger, M., 2010. Firn processes and δ15N: potential for a gas-phase climate proxy. Quaternary Science Reviews 29, 28–42. https://doi.org/10.1016/j.quascirev.2009.10.012

Eicher, O., Baumgartner, M., Schilt, A., Schmitt, J., Schwander, J., Stocker, T.F., Fischer, H., 2016. Climatic and insolation control on the high-resolution total air content in the NGRIP ice core. Clim. Past 15.

Elderfield, H., Ferretti, P., Greaves, M., Crowhurst, S., McCave, I.N., Hodell, D., Piotrowski, A.M., 2012. Evolution of Ocean Temperature and Ice Volume Through the Mid-Pleistocene Climate Transition. Science 337, 704–709. https://doi.org/10.1126/science.1221294

Häberli, M., 2019. Noble-gas ratios in polar ice cores: a new proxy to infer the mean ocean temperature over the last 700 ka (Diss.). University of Bern, Bern.

Haeberli, M., Baggenstos, D., Schmitt, J., Grimmer, M., Michel, A., Kellerhals, T., Fischer, H., 2021. Snapshots of mean ocean temperature over the last 700 000 years using noble gases in the EPICA Dome C ice core. Clim. Past 17, 843–867. https://doi.org/10.5194/cp-17-843-2021

Headly, M.A., Severinghaus, J.P., 2007. A method to measure Kr/N $_2$ ratios in air bubbles trapped in ice cores and its application in reconstructing past mean ocean temperature. J. Geophys. Res. 112, D19105. https://doi.org/10.1029/2006JD008317

Ishidoya, S., Murayama, S., 2014. Development of a new high precision continuous measuring system for atmospheric O2/N2 and Ar/N2 and its application to the observation in Tsukuba, Japan. Tellus B: Chemical and Physical Meteorology 66, 22574. https://doi.org/10.3402/tellusb.v66.22574

Linstrom, P.J., Mallard, W.G., 2023. NIST Chemistry WebBook, NIST Standard Reference Database Number 69, National Institute of Standards and Technology. Gaithersburg MD, 20899, https://doi.org/10.18434/T4D303, (retrieved October 24, 2023).

Orsi, A., 2013. Temperature reconstruction at the West Antarctic Ice Sheet Divide, for the last millennium, from the combination of borehole temperature and inert gas isotope measurements. University of California, San Diego.

Schlesinger, W.H., Bernhardt, E.S., 2013. Biogeochemistry. An Analysis of Global Change, 3rd ed. Academic Press, Waltham, MA, USA.

Schmitt, J., 2006. A sublimation technique for high-precision δ13C on CO2 and CO2 mixing ratio from air trapped in deep ice cores. Universität Bremen, Bremerhaven.

Schmitt, J., Seth, B., Bock, M., Fischer, H., 2014. Online technique for isotope and mixing ratios of CH_4, N_2O, Xe and mixing ratios of organic trace gases on a single ice core sample. Atmospheric Measurement Techniques 7, 2645–2665. https://doi.org/10.5194/amt-7-2645-2014

Severinghaus, J.P., Grachev, A., Luz, B., Caillon, N., 2003. A method for precise measurement of argon 40/36 and krypton/argon ratios in trapped air in polar ice with applications to past firn thickness and abrupt climate change in Greenland and at Siple Dome, Antarctica. Geochimica et Cosmochimica Acta 67, 325–343. https://doi.org/10.1016/S0016-7037(02)00965-1

Shackleton, S., Baggenstos, D., Menking, J.A., Dyonisius, M.N., Bereiter, B., Bauska, T.K., Rhodes, R.H., Brook, E.J., Petrenko, V.V., McConnell, J.R., Kellerhals, T., Häberli, M., Schmitt, J., Fischer, H., Severinghaus, J.P., 2020. Global ocean heat content in the Last Interglacial. Nat. Geosci. 13, 77–81. https://doi.org/10.1038/s41561-019-0498-0

Shackleton, S., Bereiter, B., Baggenstos, D., Bauska, T.K., Brook, E.J., Marcott, S.A., Severinghaus, J.P., 2019. Is the Noble Gas‐Based Rate of Ocean Warming During the Younger Dryas Overestimated? Geophys. Res. Lett. 2019GL082971. https://doi.org/10.1029/2019GL082971

Shackleton, S., Menking, J.A., Brook, E., Buizert, C., Dyonisius, M.N., Petrenko, V.V., Baggenstos, D., Severinghaus, J.P., 2021. Evolution of mean ocean temperature in Marine Isotope Stage 4. Clim. Past 17, 2273–2289. https://doi.org/10.5194/cp-17-2273-2021

Shakun, J.D., Lea, D.W., Lisiecki, L.E., Raymo, M.E., 2015. An 800-kyr record of global surface ocean δ 18 O and implications for ice volume-temperature coupling. Earth and Planetary Science Letters 426, 58–68. https://doi.org/10.1016/j.epsl.2015.05.042

Sowers, T., Bender, M., Raynaud, D., 1989. Elemental and isotopic composition of occluded O2 and N2 in polar ice. Journal of Geophysical Research: Atmospheres 94, 5137–5150. https://doi.org/10.1029/JD094iD04p05137

Talalay, P.G., Gundestrup, N.S., 2002. Hole fluids for deep ice core drilling. Memoirs of National Institute of Polar Research Spec. Issue, 148–170.

3. From measured noble-gas ratios to MOT

By following the laboratory procedure and after applying various mass spectrometry corrections described in Chapter 2, we end up with a record of elemental and isotopic ratios of noble gases from the past. Measured elemental ratios of inert gases, i.e., δKr/N_2, δXe/N_2, and δXe/Kr for Terminations I–IV and their subsequent interglacials can be found in Figure 3.1. Samples from the warmer interglacial periods feature higher elemental ratios than those from glacial periods. However, ratios are enriched by up to 60‰ compared to today's atmosphere, against which they are referenced. Enrichments of this scale are clearly not caused by changes in MOT. This chapter will focus on how we can explain such strongly enriched δ-values, how we may correct them such that our data is representative of past atmospheric noble gas concentrations, and how the atmospheric noble gas concentration can then be translated into MOT. This will be done in five sections:

- First, Section 3.1. talks about how atmospheric gases are archived in ice. For this, we will have a closer look at the firn layer, that is, the porous layer of consolidating snow on top of polar ice sheets.
- Next, Section 3.2. focuses on how to translate measured noble-gas ratios into atmospheric ratios. The enriched elemental ratios found in Figure 3.1. are a consequence of several firn fractionation processes, for which corrections need to be applied to the measured ratios. There are various correction approaches, which will be presented in this section. At the end, we will argue to use an isotope-based approach, in which all corrections are based on measured noble gas isotopic ratios.
- Section 3.3. covers the last step of transforming atmospheric noble-gas ratios into MOT. Although ocean temperature is one of the deciding factors for setting the oceanic noble-gas content, it is not the only one. Temperature and salinity distribution within the ocean, ocean volume, and ocean saturation state all play a role. Section 3.3. briefly discusses how these factors affect oceanic noble-gas content, and thus MOT, and then presents the atmosphere-ocean box model we use to correct for them.
- Section 3.4. describes how we obtain a continuous MOT record for the last four glacial Terminations by interpolating between the discrete MOT datapoints using a cubic smoothing spline. The section furthermore explains how we use a Monte Carlo routine and bootstrapping to translate analytical noise into uncertainty of the MOT record.

- Finally, Section 3.5. explores the individual firn fractionation corrections introduced in Section 3.2. and their effect on the resulting MOT record in some more detail. Despite our best efforts to find an adequate correction routine in the previous sections, small offsets between the resulting MOT records obtained from the three noble-gas ratios remain. Also, the records are offset from their expected Holocene value. Similar issues are found in other MOT datasets and are likely reflecting our incomplete understanding of firn fractionation processes, leading to systematic biases in firn fractionation corrections. The last part of this section presents some hypotheses on what may cause these discrepancies and offsets.

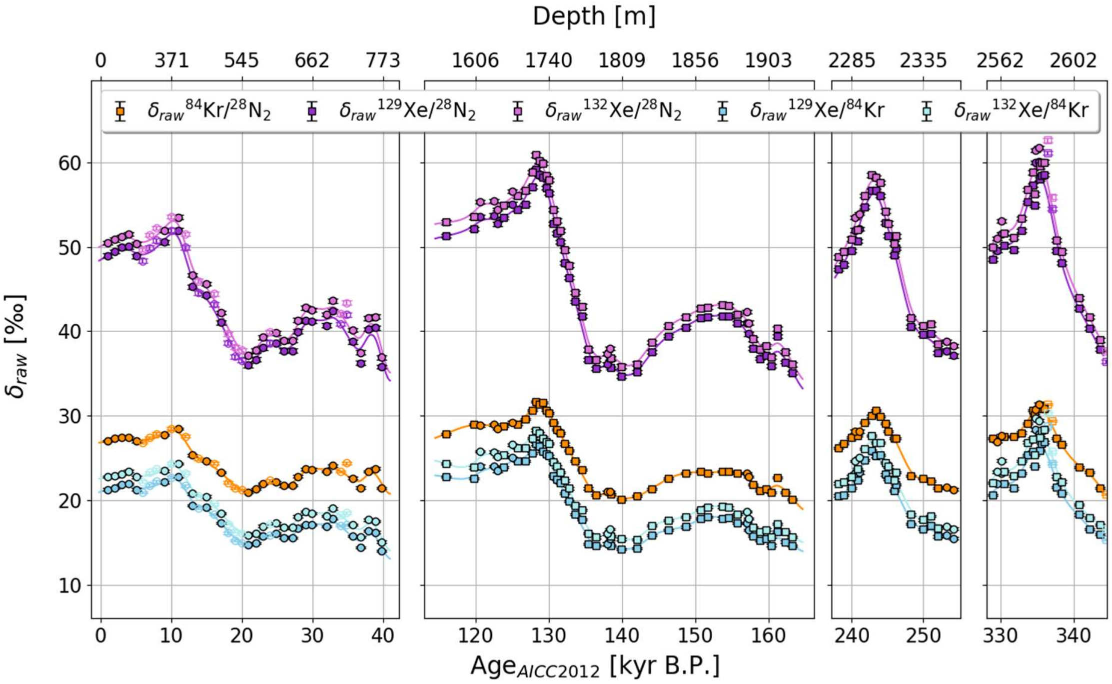

Figure 3.1.: Elemental ratios of inert gases in the EDC ice core for Terminations I–IV and their subsequent interglacials. The analytical uncertainties of the elemental ratios are on the order of 0.1‰ (Tables 2.7.–2.9.) and thus too small to be visible here. Samples measured in the scope of this PhD thesis are given as squares, those measured during earlier measurement periods are given as circles. Open symbols indicate datapoints that are affected by drilling fluid contamination. Drawn lines show cubic smoothing splines with cutoff frequencies of 5 kyr.

3.1. The firn layer

Consolidating snow on top of polar ice sheets forms a porous layer of about 50–120 m depth. Within this firn layer, a network of connected pores facilitates the movement of air from the surface, i.e., the atmosphere, all the way down to the bottom of the firn column. At Dome C, the low accumulation rate and cold temperature lead to a rather deep firn column of ~100 m (Kaspers et al., 2004; Sturges et al., 2001). As new snow falls on top of the ice sheet, the consolidated snow below recrystallizes and gets compacted as it is pushed downwards. With depth, the pressure from the layers above increases, capping more and more of the connecting channels. Eventually, the pores get occluded, entrapping the air inside them and preserving it as bubbles in the ice.

We can distinguish four different modes of gas transport in the firn column: molecular diffusion, convective mixing, dispersion, and advection (Birner et al., 2018; Buizert and Severinghaus, 2016). The small pore size in the firn largely prohibits convective mixing, and, thus, molecular diffusion is the dominant mode of air transport in the firn column (Schwander et al., 1988). In the absence of convective mixing, each gas component tends towards its own equilibration state, which is given by the barometric formula. Here, g means the local gravitational acceleration, R the universal gas constant, and T the average firn temperature (Schwander, 1996):

$$p_i(z) = p_i(0) \cdot \exp\left(\frac{m_i \cdot g \cdot z}{R \cdot T}\right) \qquad (3.1.)$$

The partial pressure p_i of gases with higher masses m_i will thus increase more strongly with increasing depth z than that of lighter gases. As about 90% of the pores get occluded in the bottommost 10% of the firn column (Schwander, 1996), this gravitational enrichment of heavy gases relative to lighter ones contributes the most to the total fractionation of firn air at bubble close-off relative to atmospheric air (Figure 3.2.; Craig et al., 1988; Schwander, 1989; Sowers et al., 1989), thus explaining most of the enrichment of elemental ratios displayed in Figure 3.1.

In addition to gravitational settling, molecular diffusion leads to a secondary fractionation process in the firn column that scales with the temperature difference between the top and the bottom of the firn column: thermal diffusion (Severinghaus et al., 1998). At the colder end of the firn column, the density of gas is slightly higher, leading to a somewhat elevated number of collisions between the gas particles compared to the warmer end of the column and thus a net flow towards the warmer end. Under a constant temperature gradient, a steady state between the temperature-induced current in one direction and back diffusion along the thereby created concentration gradient will be reached. The fractionation associated with this thermal diffusion process is mostly a function of mass but is also affected by the gas-air collisions and, thus, depends on the shape of the gas molecule. Thermal diffusion thereby generally leads to an enrichment of the heavier gas species or isotope at the colder end of the firn column.

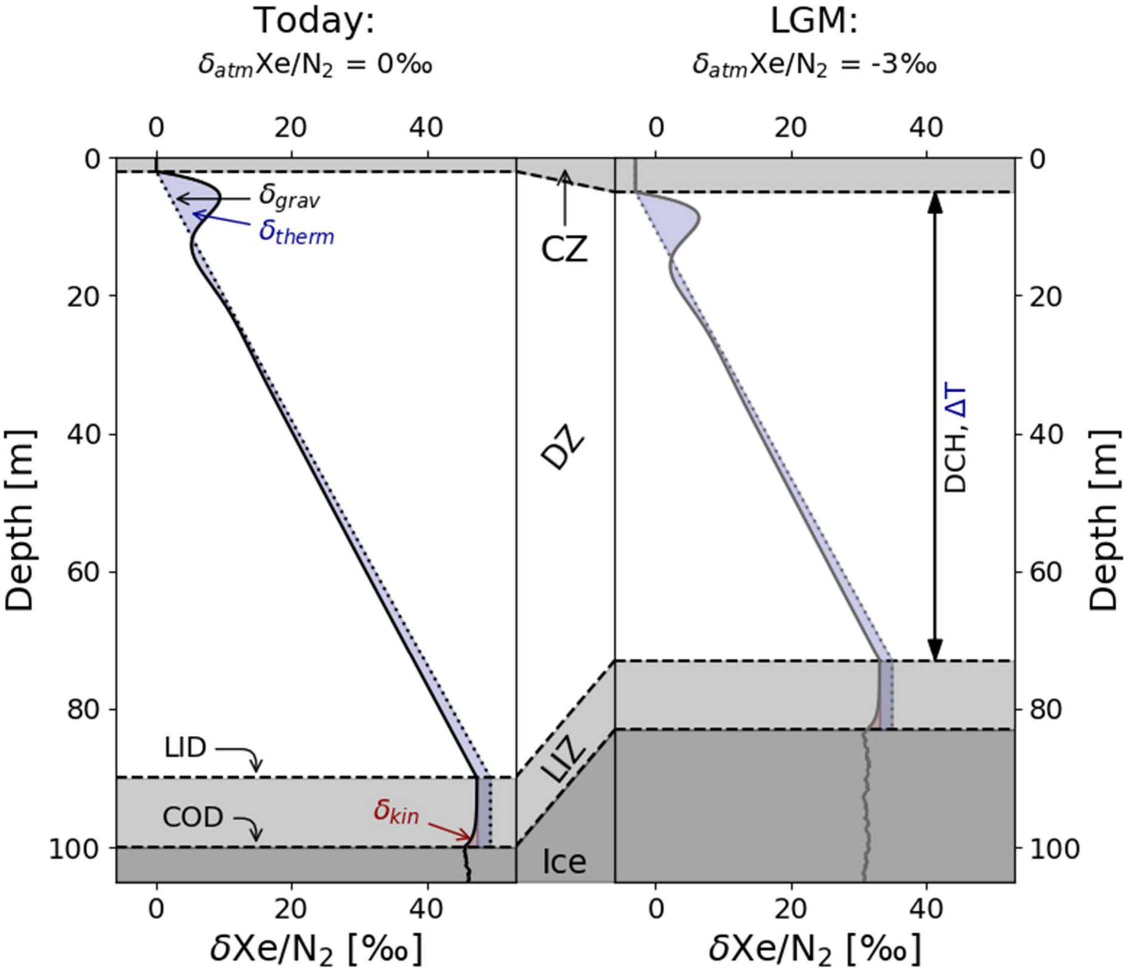

Figure 3.2.: Schematic drawing of the δXe/N$_2$-depth profile for a modern-like and an LGM-like firn column and atmospheric δXe/N$_2$. The dashed lines indicate the expected fractionation from gravitational enrichment alone, the drawn lines include thermal diffusion and kinetic fractionation. The difference between the two is shaded in blue. Additionally, characteristic firn column zones are indicated: the convective zone (CZ), where convective mixing hinders the development of a diffusive equilibrium and, hence, leads to some kinetic (disequilibrium) fractionation; the diffusive zone (DZ), where gas transport is dominated by molecular diffusion, leading to gravitational settling and thermal diffusion, the strength of which are given by the diffusive column height (DCH) and the top−bottom temperature difference ΔT, respectively; and the lock-in zone (LIZ), where molecular diffusion has ceased but dispersive mixing may still occur, causing kinetic fractionation. The lock-in depth (LID), the upper end of the LIZ, is typically defined as a sudden change in the slope of $\delta^{15}N_2$. Finally, the close-off depth (COD) marks the firn–ice transition, below which all pores are occluded and, thus, their gas content is not altered further.

Apart from molecular diffusion, convective mixing, dispersion, and advection also play an important role in firn air transport. Convection induced by high-frequency local pressure variations, so-called wind-pumping, or by buoyancy differences between the atmosphere and the firn column can lead to strong mixing in the near-surface layer of the firn column (Kawamura et al., 2013; Severinghaus et al., 2010). Similar bulk movement of air within the firn column occurs due to barometric pumping caused by surface pressure variability on longer timescales (Birner et al., 2018; Buizert et al., 2023). In response to synoptic pressure variations, air is repeatedly forced into and out of the firn column. In the highly tortuous deeper part of the firn column, dispersion is increased (Buizert and Severinghaus, 2016; Schwander et al., 1988), and barometric pumping thus leads to dispersive mixing of firn air. Further macroscopic air transport within the firn column is caused by downward advection of air in the firn column together with the surrounding ice matrix. As the pores are gradually getting smaller with increasing depth, the air contained therein is slowly expulsed, causing an upward airflow relative to the ice matrix (Buizert et al., 2013; Rommelaere et al., 1997), although the net flux is still downward. However, the resulting expulsion air flow is orders of magnitude smaller than that caused by synoptic pressure variations (Buizert and Severinghaus, 2016).

All three processes have a macroscopic air movement in common, which does not fractionate between gas species. Bulk air movement thereby mixes the air in the firn column, disturbs gravitational and thermal diffusive equilibrium, and partly undoes the associated diffusive fractionation. After being brought out of diffusive equilibrium, lighter gas species with typically larger diffusivities can more quickly return to their equilibrium state. Consequently, faster diffusing gases are closer to their diffusive equilibrium and, thus, more strongly fractionated relative to the atmosphere than gas species with lower diffusivities. Depending on the focus of the study, this fractionating effect has been coined either heavy isotope deficit (e.g., Baggenstos et al., 2019; Haeberli et al., 2021), or ^{86}Kr-excess (e.g., Buizert and Severinghaus, 2016; Buizert et al., 2023). Here, we stick to the term that describes the non-equilibrium process itself, kinetic fractionation.

The firn column can be split into three distinct zones (Figure 3.2.; Schwander, 1996; Sowers et al., 1992). In the uppermost meters of the firn, convective mixing dominates. In this convective zone or surface mixed layer (Birner et al., 2018), convection strongly hinders a diffusive equilibrium from establishing. However, for most deep ice cores sites, modern convective zones are small. This can be deduced from $\delta^{15}N_2$-based determinations of the firn column depth, which agree within 10 m to the “true” value obtained from density measurements (Bender et al., 2006). For EDC, the convective zone is estimated to be about 2–3 m (Landais et al., 2006; Severinghaus et al., 2010), which is in line with first results of recent seasonal firn pumping (see Section 3.5.2. for more information). The depth of this convective zone is strongly site-dependent as well as time-dependent, with accumulation rate and wind stress being the decisive factors. Substantial convective zones have only been observed at sites with extremely low accumulation rates or sites where extensive firn cracking facilitates wind intrusions (Kawamura et al., 2013, 2006; Severinghaus et al., 2010). The EDC convective zone might thus have been more extended during glacial periods, when accumulation rates were lower and wind pumping possibly stronger.

Below the convective zone lies the diffusive zone, throughout which molecular diffusion is the dominating mode of gas transport. This is the depth interval in which a diffusive equilibrium with associated fractionations establishes itself. Thus, it is the diffusive column height (DCH), and not the height of the entire firn column, that is decisive for the size of gravitational (and thermal) fractionation.

Diffusivity of the firn decreases towards the bottom of the firn. The gradual densification of the firn goes hand in hand with a decrease in porosity and an increase in tortuosity, thus, restricting diffusion (Schwander, 1988). At the bottom end of the firn column, where pores are gradually occluded and the firn-ice transition takes place, lies the lock-in zone (LIZ). The lock-in depth (LID) is usually defined as the depth at which a sudden change in the slope of the $\delta^{15}N_2$ profile, or the profiles of other trace gases, can be observed (Figure 3.2.). This change in slope is explained by a cessation of molecular diffusion, resulting in no further gravitational enrichment below the LID. Nonetheless, vertical transport continues throughout the LIZ (Buizert et al., 2012; Severinghaus et al., 2010). This vertical transport has been associated to mass-independent dispersive mixing caused by barometric pumping in combination with impermeable horizontal firn layers (Birner et al., 2018; Buizert and Severinghaus, 2016). The LIZ is about 5–10 m thick and delimited at the bottom by the close-off depth, below which all pores are occluded and thus no further alteration of their gas content occurs.

During the bubble close-off process, gases smaller than a threshold diameter of ~3.6 Å, such as O_2 and Ar, are preferentially excluded from the bubbles and conversely enriched in the still open pores above. The size-dependence has been hypothesised to be due to permeation of these gases through the thin ice lattice of recently closed bubbles (Huber et al., 2006a; Severinghaus and Battle, 2006). This process not only leads to size-dependent fractionation but also exhibits mass-dependent fractionation for $\delta^{18}O_2$ (Battle et al., 2011). For $\delta^{40/36}$Ar, on the other hand, the mass-dependence is less clear with the literature presenting somewhat contradictory results (Battle et al., 2011; Buizert et al., 2023; Kobashi et al., 2008). Ratios affected by close-off fractionation, i.e., $\delta O_2/N_2$, $\delta Ar/N_2$, and $\delta^{18}O_2$, are strongly correlated to local summer insolation. This may be a consequence of the summer insolation influencing snow morphology at the surface, which later affects the close-off process (Bender, 2002). These ratios are thus important tools for orbitally dating ice core records. However, the same close-off fractionation prohibits inferring MOT from ratios containing Ar, such that we need to build elemental ratios with N_2 instead.

There is an additional form of fractionating gas loss due to the relaxation of the ice directly after core retrieval or caused by long-term storage of the sample at temperatures above −50 °C (Oyabu et al., 2021). This post-coring gas loss is again size-fractionating and mass-fractionating for both oxygen and argon (Kobashi et al., 2008; Oyabu et al., 2021; Severinghaus et al., 2009), but may also affect other ratios (Haeberli et al., 2021). To test for post-coring gas loss of our samples, we compare the “gas-loss indicators” $\delta O_2/N_2$ and $\delta^{18}O_2$ with published data (Extier et al., 2018). Our record shows strong covariation with published $\delta O_2/N_2$ data, however, there appears to be a systematic offset for $\delta O_2/N_2$ of samples measured in 2022 (Figure 3.3.). Considering that the offset is roughly constant in time, and considering the good agreement of the $\delta^{18}O_2$ records, we ascribe the offset in $\delta O_2/N_2$ to not conditioning our stainless-steel sample tubes prior to the 2022 measurement period. We thus find no evidence of post-coring gas loss for our Termination I–IV samples.

In summary, gas ratios measured in ice cores can be related to the original atmospheric value using the following equation:

$$\delta_{meas} = \delta_{atm} + \delta_{grav} + \delta_{therm} + \delta_{kin} + \delta_{gas\ loss} \tag{3.2.}$$

The gravitational enrichment δ_{grav} caused by molecular diffusion accounts for most of the difference between the ratios measured at the bottom of the firn column δ_{meas}, and that of the overlying atmosphere δ_{atm}. Thermal diffusion δ_{therm}, as a secondary effect of molecular diffusion, also contributes to this difference. Disruptions of the diffusive equilibrium can be summarized in a single kinetic fractionation term δ_{kin}. These three fractionation types will be discussed in more detail in the upcoming section. Finally, gas loss fractionation $\delta_{gas\ loss}$ plays a role for ratios involving gas molecules smaller than ~3.6 Å and additionally may affect other ratios of samples from more brittle parts of the ice core or samples stored for extended time periods at suboptimal temperatures. To circumvent close-off fractionation, we use elemental noble-gas ratios with N_2 instead of Ar. The samples analysed during this PhD-project all stem from the non-brittle, clathrated section of the EDC ice core. Also, they were stored at −50 °C. Indeed, we do not find any signs of fractionating gas loss (Figure 3.3.).

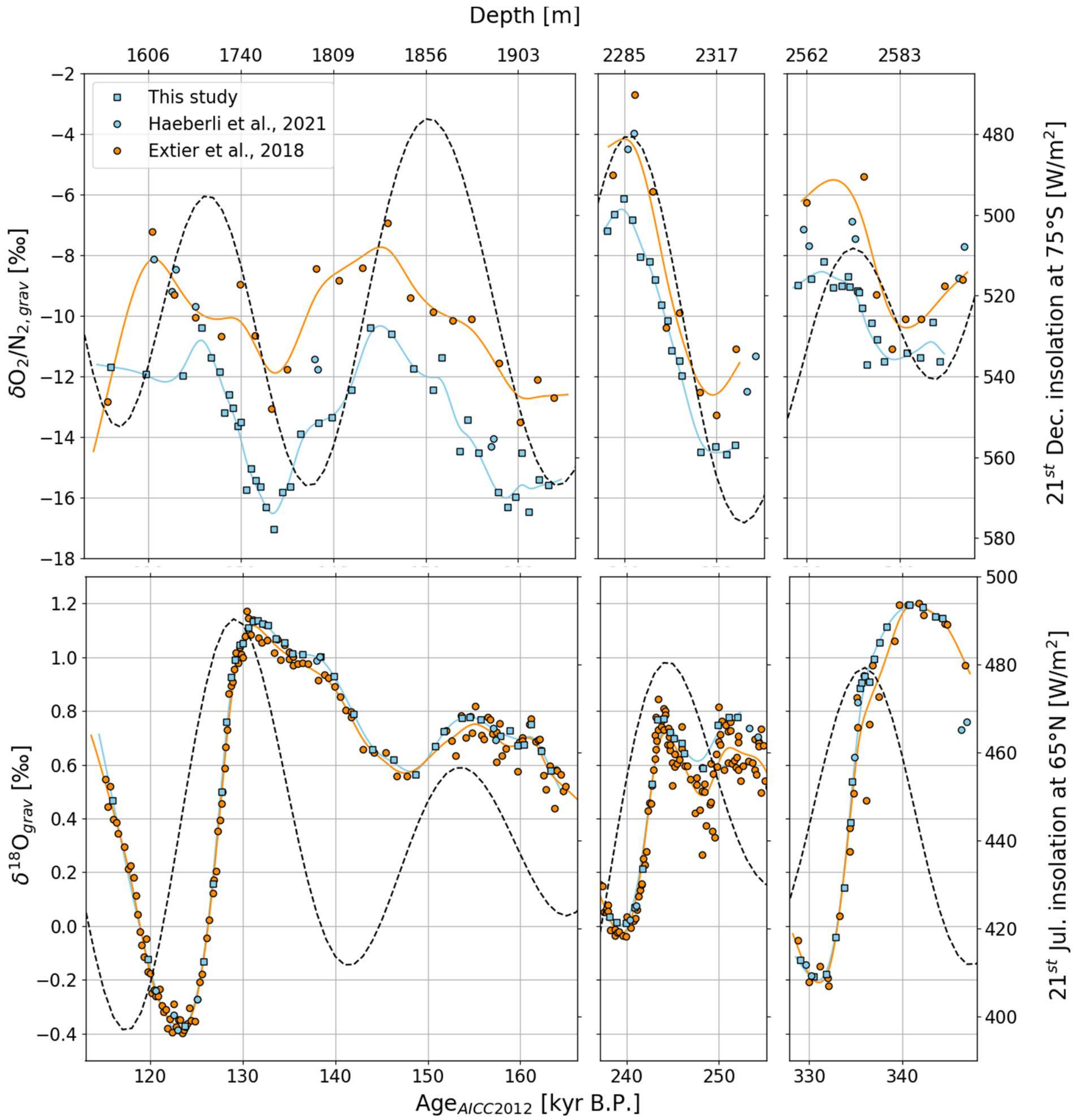

Figure 3.3.: Comparison between $\delta O_2/N_2$ (upper panel) and $\delta^{18}O_2$ (lower panel) measured in Bern and at the LSCE in Paris by Extier et al., 2018 as a proxy for post-coring gas loss. Data are corrected for gravitational fractionation. Additionally, $\delta^{18}O_2$ is corrected for gas loss at bubble close off according to Extier et al., 2018. For orientation, we also draw the 21st December insolation at 75°S and the 21st July insolation at 65°N for $\delta O_2/N_2$ and $\delta^{18}O_2$, respectively (Laskar et al., 2004). Solid lines show cubic smoothing splines with cutoff frequencies of 5 kyr and 10 kyr for the data measured in Bern during 2022 and from Extier et al., 2018, respectively.

3.2. From firn ratios to atmospheric ratios: firn fractionation corrections

3.2.1. Gravitational enrichment

Gravitational enrichment is the most sizeable fractionation in the firn column by orders of magnitude. It is also the fractionation that has been studied for the longest time and is understood the best (Craig et al., 1988; Schwander, 1989; Sowers et al., 1989). Thus, despite its large size, gravitational enrichment can be corrected for very accurately. In an environment dominated by molecular diffusion, the concentration of each gas component is given by the barometric equation (3.2.) (Schwander, 1996). Heavier gas species are thus enriched relative to lighter ones towards the bottom of the firn column. For the ratio of two gases r at depth z, it follows from the barometric equation that:

$$r(z) = r_{atm} \cdot \exp\left(\frac{\Delta m \cdot g \cdot z}{R \cdot T}\right) \qquad (3.3.)$$

Mass difference Δm (in kg/mol), local gravitational acceleration g, universal gas constant R, and site temperature T (in K) are known or can be reconstructed from other ice core proxy data, such that we only need an estimate for the DCH z (in m below the surface) to determine the gravitational enrichment relative to the atmospheric ratio r_{atm}.

Herron and Langway, 1980 showed that the DCH largely depends on the local accumulation rate and the site temperature. Higher site temperature and lower accumulation rate generally lead to more rapid density changes with depth and thus a shallower firn layer. Firnification models predict a shallower firn column during interglacial periods than during glacial periods since the warmer interglacial temperatures are expected to outweigh the opposing effect of elevated accumulation. Model predictions are typically in good agreement for ice cores from Greenland and Western Antarctica (Landais et al., 2006). However, the opposite is found for EDC, where the interglacial DCH is bigger by about 20 m (Figure 3.4.). This is in good agreement with many other East Antarctic sites (e.g., Bender et al., 2006; Oyabu et al., 2021) but in disagreement with model prediction. Proposed processes to explain this discrepancy include variations in the thickness of the convective zone (Kawamura et al., 2013; Severinghaus et al., 2010), a (significant) influence of impurities on the densification process (Hörhold et al., 2012), and overestimation of past accumulation rates (Landais et al., 2006). Indeed, the use of borehole-thermometry-informed reconstructions of LGM Antarctic temperatures (Buizert et al., 2021) and updated reconstructions of past accumulation rate

(Kahle et al., 2021), in combination with the right choice of densification model, appear to resolve most of the model-data mismatch (Buizert, 2021).

To determine the DCH, we start out with the ratio of two gases at depth z as given in (3.3.), now written in δ-notation:

$$\delta(z) = \frac{r(z)}{r_0} - 1 = \frac{r_{atm} \cdot \exp\left(\frac{\Delta m \cdot g \cdot z}{R \cdot T}\right)}{r_0} - 1 = (\delta_{atm} + 1) \cdot \exp\left(\frac{\Delta m \cdot g \cdot z}{R \cdot T}\right) - 1 \qquad (3.4.)$$

r_0 is the ratio of the same two gas components in our working standard. We can identify the effect of gravitational settling δ_{grav} as the difference between the atmospheric δ-value, and the δ-value at depth z:

$$\delta_{grav} = \delta(z) - \delta_{atm} = (\delta_{atm} + 1) \cdot \exp\left(\frac{\Delta m \cdot g \cdot z}{R \cdot T}\right) - 1 - \delta_{atm} \qquad (3.5.)$$

For noble gas isotopic ratios, we may assume that the atmospheric ratios are unaffected by changes in the ocean solubility (unlike for elemental ratios of these gases). This is supported by the two-box model calculations of Haeberli et al., 2021, who found glacial-interglacial changes in the atmospheric noble gas isotope composition of less than 0.001‰ using the seawater solubility fractionation factors of different noble-gas isotopes given in Seltzer et al., 2019. Thus, we consider atmospheric concentration changes of noble gas isotopic ratios to be negligible on glacial–interglacial timescale, i.e., $\delta_{atm} = 0$. We can then solve for the DCH z:

$$z = \ln\,(\delta^*_{grav} + 1) \cdot \frac{R \cdot T}{\Delta m^* \cdot g} \qquad (3.6.)$$

In (3.6.) and in equations to follow, an asterisk signifies that the respective value has been normalized to unit mass difference (i.e., $\Delta m^* = 0.001$ kg/mol). Following Birner et al., 2018, normalizing to unit mass difference is done in q-notation, with $q = \delta + 1$. Thus, to normalize any δ-value, we write:

$$\delta^* = (\delta + 1)^{\frac{1}{1000 \cdot \Delta m}} - 1 \qquad (3.7.)$$

Using (3.2.), we can derive δ^*_{grav} from any isotope pair that is not affected by gas loss ($\delta^*_{gas\ loss} = 0$):

$$\delta^*_{grav} = \delta^*_{meas} - \delta^*_{therm} - \delta^*_{kin} \qquad (3.8.)$$

Typically, the DCH is determined using either $\delta^{40/36}$Ar or $\delta^{15}N_2$ measurements. For both ratios, our analytical precision per mass unit is good (Tables 2.7.–2.9.) and both are thus valid choices to reconstruct the DCH. Indeed, they give similar result for the DCH of individual sample ages, as can be seen in Figure 3.4. However, since our analytical precision for $\delta^{40/36}$Ar is somewhat better, we use this isotopic ratio to determine z. As can be seen in (3.8.), this requires us to first derive corrections for thermal diffusion and kinetic fractionation.

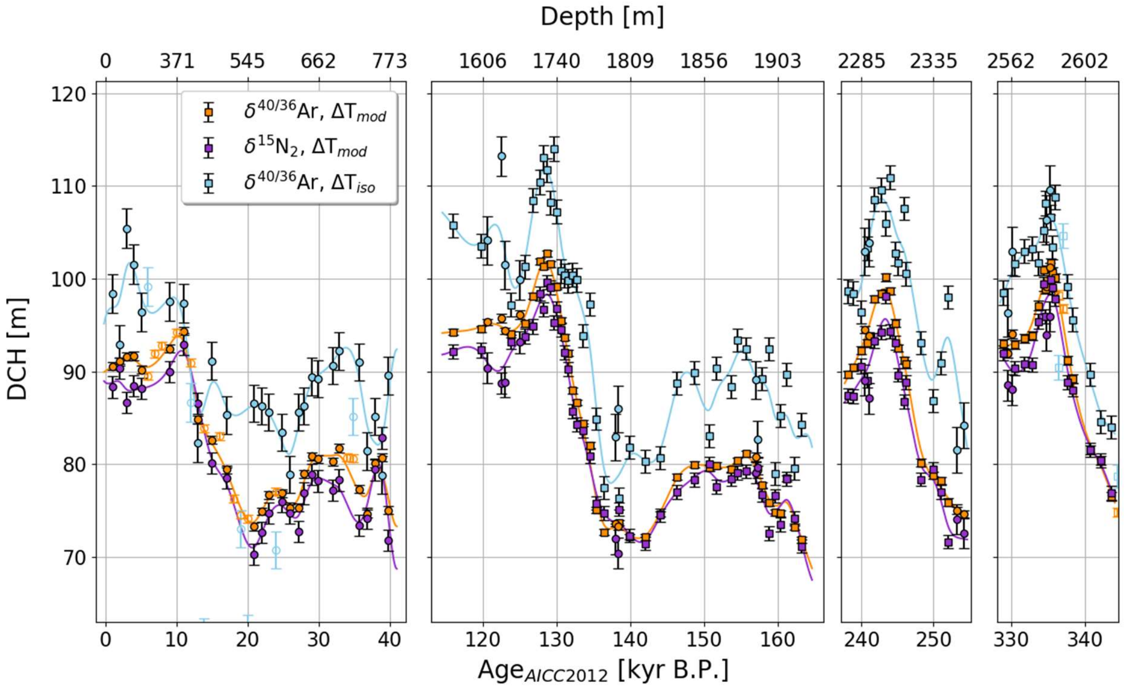

Figure 3.4.: Termination I–IV DCH at Dome C as inferred from $\delta^{40/36}$Ar and $\delta^{15}N_2$, using two different estimates for the top−bottom firn temperature difference ΔT: modelled ΔT from an ice flow-heat flow model of Michel, 2016; and ΔT derived from noble gas isotopic ratios. For isotope-derived ΔT, DCH based on $\delta^{15}N_2$ is nearly identical to the one based on $\delta^{40/36}$Ar and is thus not plotted here. Shapes and fillings of markers and lines are the same as in Figure 3.1.

3.2.2. Thermal diffusion

The molecular diffusion regime in the firn leads to a second, less-sizable form of diffusive fractionation, thermal diffusion. In the presence of a temperature gradient between the top and bottom of the firn column, heavier gas species are slightly enriched at the colder side of the column. In the summer, when surface temperatures are substantially warmer than those at the bottom of the firn column, a strong thermal diffusion signal can be found in the upper 10–20 m of the firn. In the case of $\delta^{15}N_2$, for example, a typical Dome C seasonal temperature difference of 30 °C translates to thermal fractionation of about 0.2‰. Over the course of a year, however, the effects of seasonal variations on gas ratios should – at first order – balance out, although seasonal rectification of isotopic ratios has recently been detected in the South Pole and Dome Fuji ice cores (Morgan et al., 2022). Below roughly 20 m, seasonality in firn temperature is not detectable anymore (Figure 3.2.). Bar potential seasonal rectification and a second-order effect due to the dependency of diffusion constants on temperature, seasonal temperature variations should thus not affect the air composition at bubble close-off.

On longer timescales, abrupt changes in $\delta^{15}N_2$ caused by rapid changes in the top−bottom firn temperature difference can be used to detect rapid surface temperature changes in Greenland associated to Dansgaard-Oeschger (D-O) events (e.g., Huber et al., 2006b; Kobashi et al., 2007; Severinghaus and Brook, 1999). Such dynamic firn processes lead to considerable uncertainty in the size of firn fractionations and are, thus, prohibitive for precise MOT reconstruction for time intervals affected by such rapid climate changes. In the southern hemisphere, the response to D/O events is a more gradual build-up and release of energy. At Dome C, temperature variations have therefore been considerably smaller and slower than in Greenland. This allows us to better constrain firn fractionation corrections and, thus, determine past MOT with lower uncertainty. Consequently, MOT reconstructions are almost solely done on ice from Antarctica, although periods without D-O events may also be studied on Greenland ice.

Under these more stable temperature conditions with a quasi-stable firn temperature profile, a steady state between thermal diffusion and opposing diffusion along the thereby created concentration gradient establishes itself. This steady state for gases x and y can be described as:

$$\delta_{therm}^{x/y} = \Omega^{x/y} \cdot \Delta T \tag{3.9.}$$

ΔT is the temperature difference between top and bottom of the DCH. $\Omega^{x/y}$ represents the thermal diffusion factor for the gas pair x and y. Thermal diffusion factors for noble gas thermometry have been experimentally determined (Grachev and Severinghaus, 2003a, 2003b; Headly, 2008; Kawamura et al., 2013).

All we lack to determine the strength of thermal diffusion is an estimate of ΔT. ΔT is controlled by the advective flux of cold ice from the surface and the conductive geothermal heat flux, which warms the ice sheet from below. At a low accumulation site like Dome C (today about 3 cm we/yr), we, thus, expect to find a negative ΔT, meaning that the surface temperature should be lower than the temperature at greater depths in the ice sheet. Indeed, borehole temperature measurements in 2008 found a 0.008 °C/m vertical temperature gradient in the present EDC firn column between 20 m and 100 m (Buizert, 2021; Parrenin et al., 2012). As surface temperature and firn column depth undergo substantial variations on glacial–interglacial timescales, ΔT needs to be reconstructed for each of our gas sample ages. In the following, two means of doing so are presented: a 1D ice flow model connected to a dynamic heat advection and diffusion model (Michel, 2016), and a purely data-based approach using noble gas isotopic ratios.

3.2.2.a. Ice flow-heat flow model

The first option for reconstructing ΔT is to use a model that solves the equations for ice advection and firn compaction and combines them with those for heat advection and diffusion. This is exactly what the one-dimensional ice flow-heat flow model of Michel, 2016 does for Dome C. With a depth resolution of 1 m, this model yields a vertical temperature profile every 100 years over the past million years. A detailed description of how the model achieves this can be found in the Master's thesis of Adrien Michel, a former student at the Climate and Environmental Physics Division here at the University of Bern. Here, only a brief overview will be given.

At the centre of any ice flow-heat flow model stands a heat transfer equation, which typically considers at least the three effects of heat diffusion, advection, and internal heat production (Cuffey and Paterson, 2010). To solve this mathematical expression of physical processes transiently over the last million years, the individual parts of the equation need to be parametrized. For heat diffusion and heat conductivity, Michel's model uses the parametrization of Cuffey and Paterson, 2010. For the firn densification process, a somewhat altered Herron-Langway approach (Herron and Langway, 1980) is used, in which the pure ice density is dependent on temperature and pressure. The parametrizations for the internal heat production, which include ice deformation and firn compaction, are from Dahl-Jensen, 1989 and again from Cuffey and Paterson, 2010. The model also takes the topography at Dome C and the associated heat flux at the bottom into account.

Additionally, several boundary conditions need to be prescribed, i.e., the temporal changes in ice thickness, surface temperature, and accumulation rate. Surface temperature and snow accumulation over the last 800 kyr are derived from EDC δD (Jouzel et al., 2007). Both time series are extended to 1 Myr using a scaled version of the marine δ^{18}O stack of Lisiecki and Raymo, 2005 (LR04). In a similar fashion, ice thickness is taken from Parrenin et al., 2007 and then extended to 1 Myr using the LR04 stack.

The geothermal heat flux and the ice's thinning function are chosen as free parameters. These free parameters are tuned to bring the modelled temperature profile into agreement with measurements, i.e., the 2008 borehole temperature profile (Parrenin et al., 2012).

Furthermore, the parameters were chosen such that the modelled age-depth profile is in good agreement with the age-depth relation of the AICC2012. To further improve the fit with the 2008 borehole temperature measurements, Michel adjusted the heat diffusivity of the porous top 10 m of the firn according to the correction suggested by Weller and Schwerdtfeger, 1970. Additionally, glacial temperatures over the entire ice thickness had to be raised by 2 °C, which, however, only had a very minor effect on firn ΔT. After all these adjustments, the recently measured ΔT was matched by the model within ±0.2 °C. These ±0.2 °C are, thus, our best estimate for the analytical uncertainty of Michel's firn temperature model.

To obtain ΔT for all sample ages, the modelled firn temperature is read out at both ends of the estimated DCH. DCH is obtained from $\delta^{40/36}$Ar using (3.6.). As this equation includes a correction for thermal diffusion, it is solved using an iterative approach in which thermal diffusion is neglected for the first run to obtain an estimate for ΔT. This initial estimate of ΔT is then used for the thermal diffusion correction of the next run, and so on. The iteration is stopped once the DCH changes by less than 0.4 m between runs, a condition that is given by our measurement precision for $\delta^{40/36}$Ar in the 2022 measurement period (Table 2.9.) and the assumed uncertainty of the model. The condition is fulfilled after just two iterations. The resulting Termination I–IV DCH for EDC can be found in Figure 3.4.

While the physical equations involved in this ice flow-heat flow model are well-understood, it should be noted that the model does have its weak points. A model can only be as good as its inputs, and there exist considerable uncertainties in both reconstructed site temperature and accumulation rate, in particular for the older datasets used by Michel, 2016 (see e.g., Buizert et al., 2021). Additionally, the model neglects seasonal temperature variations, whose thermal fractionation effect on measured ratios might not cancel out over the year, as recently found to be the case at South Pole and Dome Fuji (Morgan et al., 2022). Such a seasonal bias can occur when the isotope signal of one season in the gas parameters is mixed down further into the firn than the opposite signal of the following season, e.g., by buoyancy-driven Rayleigh-Bénard convection (Morgan et al., 2022). Thus, the ΔT affecting gases in the firn might be different from the annual mean ΔT obtained by the model. Indeed, a comparison of ΔT obtained from the model to those derived from isotope data (Figure 3.5.) supports the notion that seasonal rectification might have occurred at Dome C as well. A further potential issue of using modelled ΔT is that the model does not consider the existence of a convective zone, which furthermore might change in depth over time. However, this should only lead to minor uncertainties in derived ΔT.

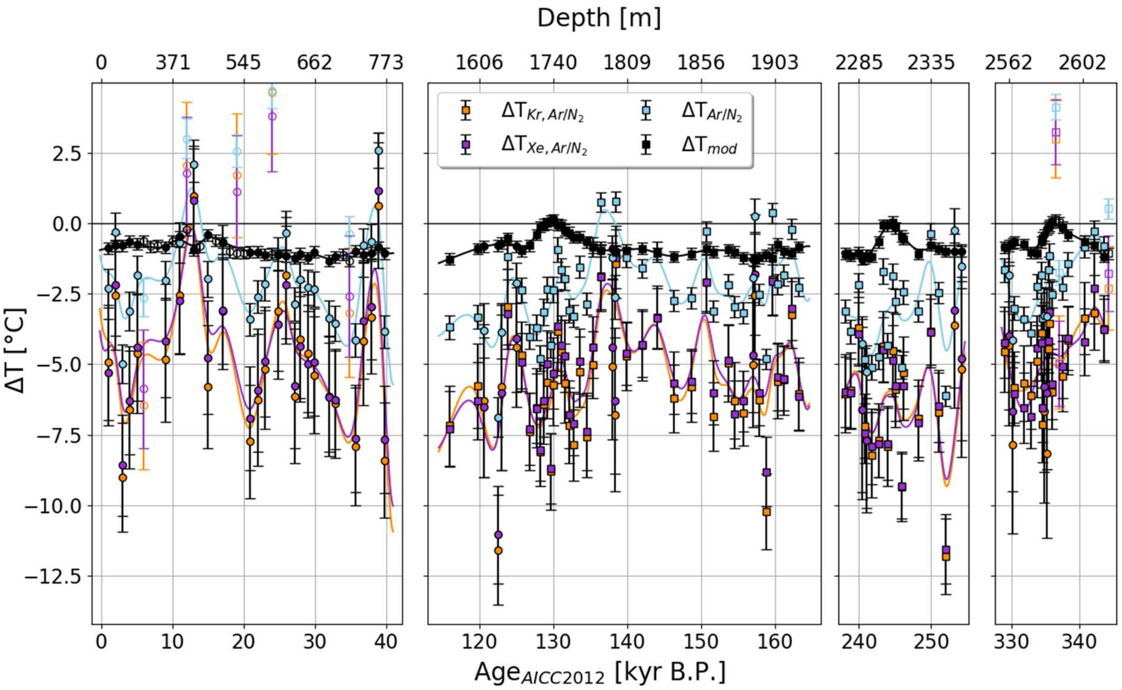

Figure 3.5.: Comparison of the EDC top−bottom firn temperature difference ΔT during Terminations I–IV. Reconstructions of ΔT were obtained from a heat flow-ice flow model (Michel, 2016), derived from the difference between $\delta^{40/36}$Ar and $\delta^{15}N_2$, and derived from that same difference which was furthermore corrected for kinetic fractionation using either the difference between Kr and Ar isotopes or the difference between Xe and Ar isotopes. Shapes and fillings of markers and lines are the same as in Figure 3.1.

3.2.2.b. Set of isotopes

The second option to reconstruct the firn temperature difference is to use a set of noble gas isotopic ratios measured in the same ice sample. Neglecting kinetic fractionation for now, (3.2.) solved for δ_{ther} looks as follows:

$$\delta_{therm} = \delta_{meas} - \delta_{atm} - \delta_{grav} = \delta_{meas} - \delta_{grav} \tag{3.10.}$$

Since we are working with isotopic ratios, $\delta_{atm} = 0$ can be assumed (Haeberli et al., 2021). Using the combination of $\delta^{40/36}$Ar and $\delta^{15}N_2$, we can disentangle gravitational and thermal fractionation (Severinghaus et al., 1998). Since the (unit mass normalized) gravitational fractionation is the same for both ratios, (3.10.) can be written as:

$$\Delta T \cdot \left(\Omega^{{}^{40/36}Ar^{*}} - \Omega^{{}^{15}N_2{}^{*}}\right) = \delta_{therm}^{{}^{40/36}Ar^{*}} - \delta_{therm}^{{}^{15}N_2{}^{*}} = \delta_{meas}^{{}^{40/36}Ar^{*}} - \delta_{meas}^{{}^{15}N_2{}^{*}} \tag{3.11.}$$

Solving for ΔT yields:

$$\Delta T = \frac{\delta_{meas}^{{}^{40/36}Ar^{*}} - \delta_{meas}^{{}^{15}N_2{}^{*}}}{\Omega^{{}^{40/36}Ar^{*}} - \Omega^{{}^{15}N_2{}^{*}}} \tag{3.12.}$$

As stated, for now we neglect kinetic fractionation. Although the effect of kinetic fractionation is only minor for Ar and N_2 isotopes, correction for kinetic fractionation would consistently slightly reduce $\delta^{40/36}$Ar, whereas $\delta^{15}N_2$ would be unaffected, thereby leading to slightly more negative ΔT throughout. Therefore, $\Delta T_{Ar/N_2}$ serves as an upper limit for ΔT. Using this isotope-based approach yields substantially different results to modelled ΔT (Figure 3.5.). On average, $\Delta T_{Ar/N_2}$ is about 1.5 °C colder than ΔT_{mod}, disregarding samples affected by drilling fluid contamination. As drilling fluid contamination leads to anomalous $\delta^{15}N_2$, isotope-based ΔT of affected samples was approximated by a cubic smoothing spline with cutoff frequency of 5 kyr through the isotope-based ΔT of unaffected samples. Interestingly, there appears to be a tendency towards more negative isotope-based ΔT during interglacials, contrary to what might be expected from surface temperature reconstructions and, thus, contrary to model prediction. This might be an indication of a seasonal rectifier effect with enhanced wintertime intrusion of cold air, which is especially pronounced during interglacial periods. However, parts of the effect may be due to the temperature dependence of diffusion constants.

While this approach of using isotope ratios to determine ΔT does circumvent the caveats of the ice flow-heat flow model mentioned above, it is considerably less precise as it introduces the analytical uncertainty of a second isotopic ratio. Compared to the assumed model uncertainty of 0.2 °C, the analytical uncertainty of $\Delta T_{Ar/N_2}$ is on the order of 0.9 °C for samples measured in 2022 and up to 2.1 °C for samples of earlier measurement periods. The above approach also neglects the fact that isotopic ratios are affected by kinetic fractionation. To account for kinetic fractionation, a third isotopic ratio is required, which introduces yet another source of uncertainty and, thus, further lowers the analytical precision of isotope-based ΔT. At the same time, this is the most accurate approach, and it is thus worthwhile to see whether it on average agrees with the somewhat less accurate but more precise $\Delta T_{Ar/N_2}$. Before deriving the expression for isotope-based ΔT corrected for kinetic fractionation, we first take a closer look at the kinetic fractionation correction itself.

3.2.3. Kinetic fractionation

Corrections for gravitational enrichment (e.g., Craig et al., 1988) and thermal diffusion (Severinghaus et al., 1998) have been around for several decades. Both fractionations are associated to the first order mode of transport in the firn column, molecular diffusion. Already in these early publications on firn transport processes, however, the authors were well-aware of how intrusions of turbulent air may bring the diffusive equilibrium in the firn column out of balance. Various such intrusions were identified already back then. These include buoyancy-driven convection (Powers et al., 1985) and wind-induced mixing due to wind-topography interactions (Colbeck, 1989), which are the dominating mode of transport in the near-surface layer, the convective zone. Another small disturbance of the diffusive equilibrium is caused by gradual downward advection of air with the ice matrix, which is partially compensated by a small return air flow due to firn compression (Craig et al., 1988; Craig and Wiens, 1996). More recently, dispersive flow driven by deep firn pumping caused by synoptic pressure variations has been suggested as the primary mode of transport in the lock-in zone (Birner et al., 2018; Buizert et al., 2023; Buizert and Severinghaus, 2016). However, although these mixing processes had been identified for quite some time, it proved to be difficult to quantify the effect they have on the firn air composition at bubble close-off. Through recent advances in observations and firn modelling, a correction for these second-order effects of firn air transport has been suggested (Birner et al., 2018; Buizert and Severinghaus, 2016; Kawamura et al., 2013; Severinghaus et al., 2010).

If molecular diffusion were the only mode of air transport in the firn column, we would expect no difference between the individual isotopic ratios after normalizing them to unit mass difference and correcting for thermal diffusion. Thus, any difference between these isotopic ratios is indicative of an additional source of fractionation. Indeed, isotopic ratios at Dome C shown in Figure 3.6. feature clear and systematic differences with heavier isotopes being less fractionated towards atmospheric air than lighter ones. Compared to what is expected if the firn air transport were purely characterized by molecular diffusion, the heavier isotopes appear depleted at the bottom of the firn column. Thus, if gravitational enrichment, thermal diffusion, and fractionation due to convective mixing fully describe the fractionation processes that occur in the firn, this difference is indicative of the presence of kinetic fractionation at Dome C.

Birner et al., 2018 discovered that this kinetic fractionation occurs in fixed ratios. Importantly, these ratios are independent of the convective mixing process such that a single correction for kinetic fractionation is sufficient for all convective mixing processes. This is explained by the intrusion of turbulent air bringing the firn air out of diffusive equilibrium. Lighter gas species with higher diffusivities return more readily to their diffusive equilibrium state and show therefore lower kinetic fractionation than heavier, more slowly diffusing gases.

The degree of fractionation is, thus, only a factor of gas diffusivities. Birner et al., 2018 found that these fixed ratios hold for a wide range of firn regimes and are independent of depth. They may thus also be applied to the EDC ice core. Using these fixed ratios, the kinetic fractionation strength inferred from the difference of any two isotopic ratios can be scaled to correct the kinetic fractionation of all other isotopic and elemental ratios.

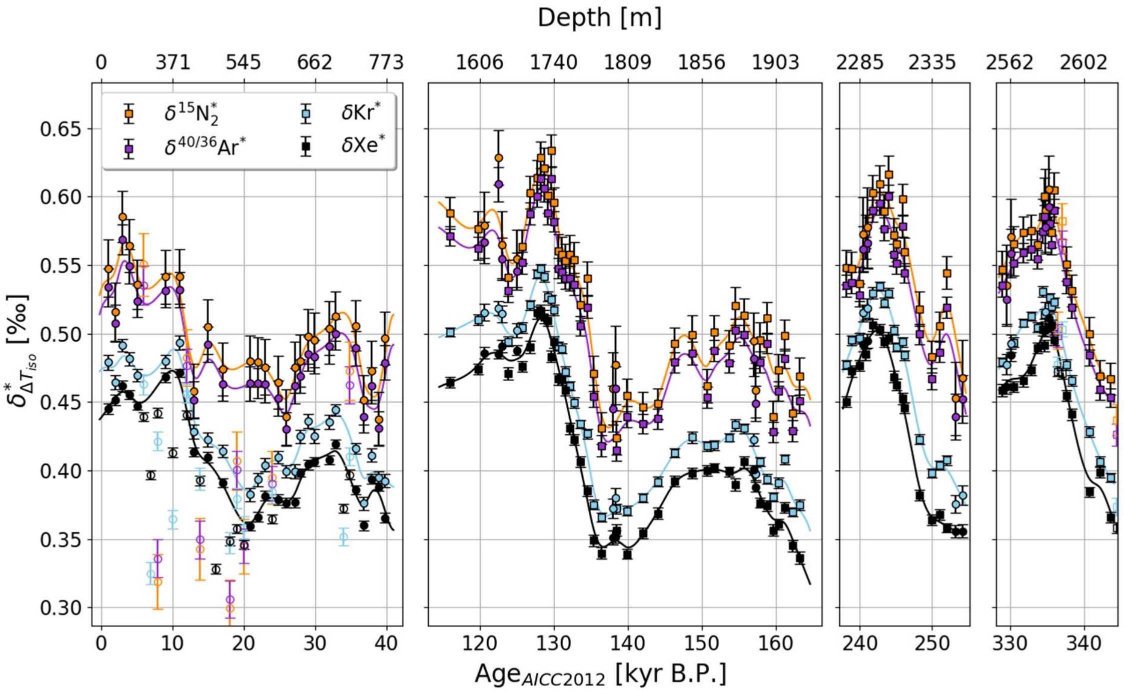

Figure 3.6.: Unit mass isotopic ratios corrected for thermal diffusion using isotope-based ΔT for Terminations I–IV. Shapes and fillings of markers and lines are the same as in Figure 3.1. Here and in the following, we combine all isotopic ratios of Kr and Xe to derive uncertainty weighted mean isotopic ratios δKr^* and δXe^*, respectively (see text for more detail). The larger uncertainty in $\delta^{15}N_2^*$ and $\delta^{40/36}Ar^*$ compared to δKr^* and δXe^* is due to their higher temperature sensitivity.

As described above, kinetic fractionation is defined as the deviation from diffusive equilibrium, which for a mass-normalized isotopic ratio may be written as:

$$\delta^*_{kin} = \delta^*_{meas} - \delta^*_{grav} - \delta^*_{therm} \tag{3.13.}$$

Again, we use the fact that the mass normalized gravitational fractionation is the same for all gas species when subtracting the kinetic fractionation of isotopic ratio k, ${\delta^{k}_{kin}}^{*}$, from that of isotopic ratio j, ${\delta^{j}_{kin}}^{*}$:

$${\delta^{j}_{kin}}^{*} - {\delta^{k}_{kin}}^{*} = {\delta^{j}_{meas}}^{*} - {\delta^{k}_{meas}}^{*} - \Delta T \cdot \left(\Omega^{j^*} - \Omega^{k^*}\right) \tag{3.14.}$$

Following Birner et al., 2018, we can express the kinetic fractionation of gas ratio j by scaling that of ratio i with a fixed scaling factor $\varepsilon_{i,j}$:

$$\delta_{kin}^{j\;*} = \delta_{kin}^{i\;*} \cdot \varepsilon_{i,j} \tag{3.15.}$$

We can, thus, solve for the kinetic fractionation of isotopic ratio i, $\delta_{kin}^{i\;*}$, from which then the kinetic fractionation of all other isotopic and elemental ratios can be derived.

$$\delta_{kin}^{i\;*} \cdot (\varepsilon_{i,j} - \varepsilon_{i,k}) = \delta_{meas}^{j\;*} - \delta_{meas}^{k\;*} - \Delta T \cdot \left(\Omega^{j^*} - \Omega^{k^*}\right)$$

$$\delta_{kin}^{i\;*} = \frac{\delta_{meas}^{j\;*} - \delta_{meas}^{k\;*} - \Delta T \cdot \left(\Omega^{j^*} - \Omega^{k^*}\right)}{(\varepsilon_{i,j} - \varepsilon_{i,k})} \tag{3.16.}$$

Since Birner et al., 2018 found fixed ratios for isotopic and elemental ratios of N_2, Ar, Kr, and Xe, $\delta_{kin}^{i\;*}$ may be determined from any two isotopic ratios of these four gases. Figure 3.7. shows the temporal evolution of $\delta_{kin}^{i\;*}$ across Termination I–IV at Dome C based on different isotope pairs. The agreement between $\delta_{kin}^{i\;*}$ based on the three possible combinations of isotope pairs is substantially better if we use ΔT derived from isotope data instead of model-based ΔT.

We may now revisit the isotope-based reconstruction of ΔT, this time considering kinetic fractionation. For modelled ΔT, inclusion of a kinetic fractionation correction has negligible influence, as it shifts the DCH by less than 1 m. If ΔT should be reconstructed from a set of isotopes instead, we start from (3.11.), now also considering kinetic fractionation.

$$\delta_{meas}^{{}^{40/36}Ar^*} - \delta_{meas}^{{}^{15}N_2{}^*} = \Delta T \cdot \left(\Omega^{{}^{40/36}Ar^*} - \Omega^{{}^{15}N_2{}^*}\right) + \delta_{kin}^{{}^{40/36}Ar^*} - \delta_{kin}^{{}^{15}N_2{}^*}$$

$$= \Delta T \cdot \left(\Omega^{{}^{40/36}Ar^*} - \Omega^{{}^{15}N_2{}^*}\right) + \varepsilon_{Ar-N_2}^* \tag{3.17.}$$

Here, we define $\varepsilon_{Ar-N_2}^* = \delta_{kin}^{{}^{40/36}Ar^*} - \delta_{kin}^{{}^{15}N_2{}^*}$. Similar as for $\delta^{40/36}Ar$ and $\delta^{15}N_2$, we can write the difference between measured ratios of $\delta^{15}N_2$ and δXe as:

$$\delta_{meas}^{Xe\;*} - \delta_{meas}^{{}^{15}N_2{}^*} = \Delta T \cdot \left(\Omega^{Xe^*} - \Omega^{{}^{15}N_2{}^*}\right) + \delta_{kin}^{Xe\;*} - \delta_{kin}^{{}^{15}N_2{}^*}$$

$$= \Delta T \cdot \left(\Omega^{Xe^*} - \Omega^{{}^{15}N_2{}^*}\right) + \varepsilon_{Xe-N_2}^* = \Delta T \cdot \left(\Omega^{Xe^*} - \Omega^{{}^{15}N_2{}^*}\right) + \varepsilon_{Ar-N_2}^* \cdot \varepsilon_{Xe} \tag{3.18.}$$

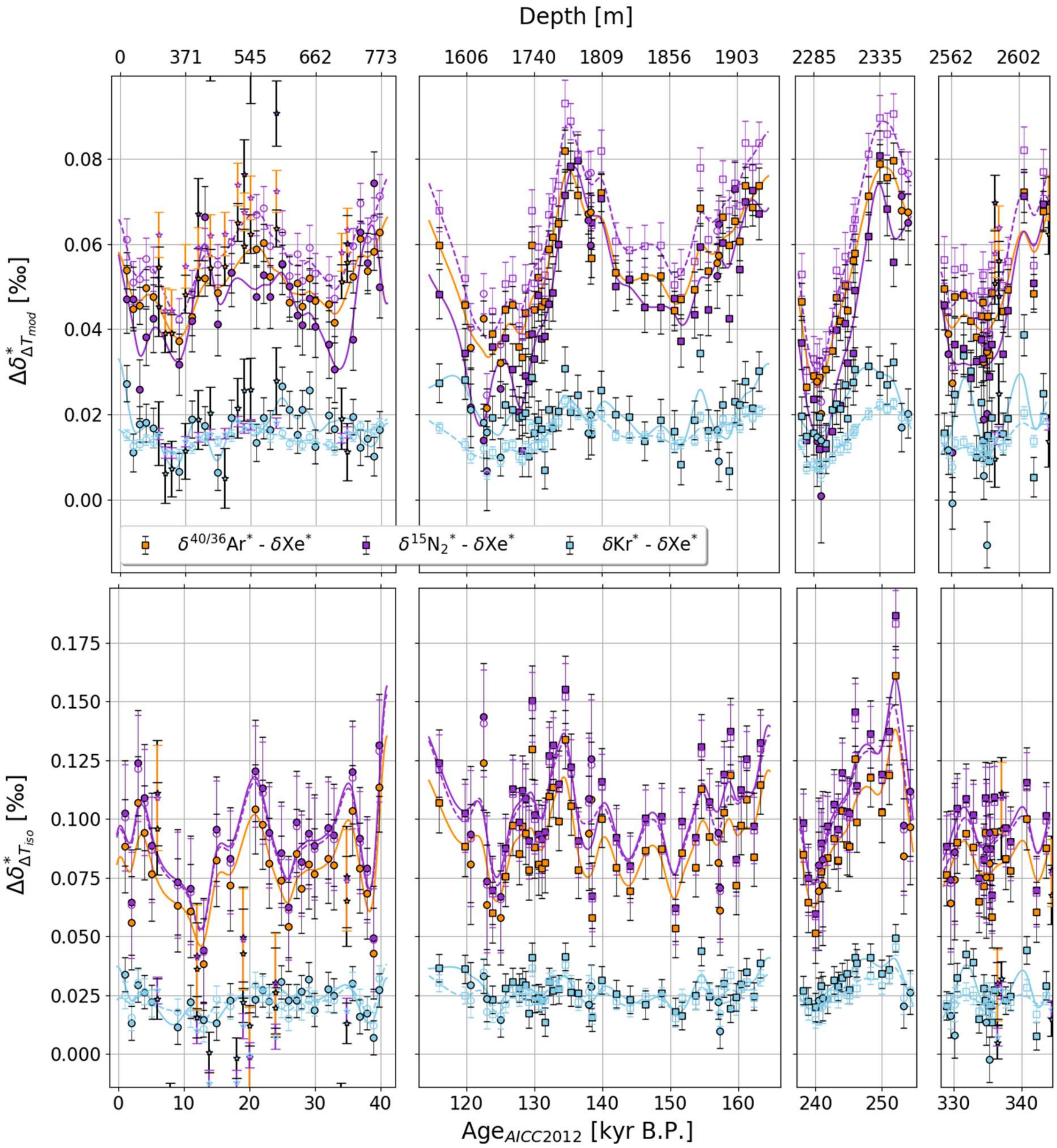

Figure 3.7.: Differences between unit mass isotopic ratios corrected for thermal diffusion using model-derived ΔT, in the upper panel, and isotope-derived ΔT, in the lower panel. Full symbols indicate measured data points. Empty symbols in purple and blue show $\delta^{15}N_2^*-\ \delta Xe^*$ and $\delta Kr^*-\ \delta Xe^*$, respectively, calculated from measured $\delta^{40/36}Ar^*-\ \delta Xe^*$ (in orange) and the scaling factors from Birner et al., 2018. They serve as a measure for how good our data agrees with the fixed ratios suggested by the firn model of Birner. Starshaped datapoints indicate samples affected by drilling fluid and, thus, anomalous $\delta^{15}N_2$. Solid and dotted lines are cubic smoothing splines with 5 kyr cutoff periods through filled and empty markers, respectively.

In the above equation, δXe^* is the unit-mass uncertainty weighted mean of all measured Xe isotopic ratios. These uncertainty-weighted means x_{wm} of values x_i with uncertainties σ_i are calculated as follows:

$$x_{wm} = \frac{\sum x_i w_i}{\sum w_i} \text{ with } w_i = \frac{1}{\sigma_i^2} \tag{3.19.}$$

Kr isotopic ratios are combined in a similar fashion, although only $\delta^{86/84}$Kr can be used for samples affected by drilling fluid contamination. These uncertainty-weighted means δKr* and δXe* will be used throughout this thesis. For Ar, we stick to $\delta^{40/36}$Ar as we do not fully trust $\delta^{40/38}$Ar as the ^{40}Ar-tail correction (see Section 2.3.3.d.) has only been determined after the measurement period.

To make use of the fixed ratios found by Birner et al., 2018, we express kinetic fractionation of Xe isotopes as a scaled version of $\varepsilon^*_{Ar-N_2}$ with $\varepsilon'_{Xe} = 7.3$. We then solve (3.17.) and (3.18.) for $\varepsilon^*_{Ar-N_2}$, i.e., the ${\delta^i_{kin}}^*$ in (3.16.).

$$\varepsilon^*_{Ar-N_2} = \delta_{meas}^{{}^{40/36}Ar^*} - \delta_{meas}^{{}^{15}N_2{}^*} - \Delta T \cdot \left(\Omega^{{}^{40/36}Ar^*} - \Omega^{{}^{15}N_2{}^*}\right)$$

$$= \frac{{\delta^{Xe}_{meas}}^* - \delta_{meas}^{{}^{15}N_2{}^*} - \Delta T \cdot \left(\Omega^{Xe^*} - \Omega^{{}^{15}N_2{}^*}\right)}{\varepsilon_{Xe}} \tag{3.20.}$$

Next, we isolate ΔT in (3.17.) and insert the obtained expression for ΔT in (3.20.):

$$\Delta T = \frac{\delta_{meas}^{{}^{40/36}Ar^*} - \delta_{meas}^{{}^{15}N_2{}^*} - \varepsilon^*_{Ar-N_2}}{\Omega^{{}^{40/36}Ar^*} - \Omega^{{}^{15}N_2{}^*}} \tag{3.21.}$$

$$\varepsilon^*_{Ar-N_2} = \frac{{\delta^{Xe}_{meas}}^* - \delta_{meas}^{{}^{15}N_2{}^*} - \alpha \cdot \left(\delta_{meas}^{{}^{40/36}Ar^*} - \delta_{meas}^{{}^{15}N_2{}^*}\right)}{\varepsilon_{Xe} - \alpha} \tag{3.22.}$$

For the sake of readability, we define $\alpha = \frac{\Omega^{Xe^*} - \Omega^{{}^{15}N_2{}^*}}{\Omega^{{}^{40/36}Ar^*} - \Omega^{{}^{15}N_2{}^*}}$. Finally, (3.22.) is inserted back into (3.17.), which yields the following expression for ΔT:

$$\Delta T_{Xe,Ar/N_2} = \frac{\delta_{meas}^{{}^{40/36}Ar^*} - \delta_{meas}^{{}^{15}N_2{}^*} - \frac{{\delta^{Xe}_{meas}}^* - \delta_{meas}^{{}^{15}N_2{}^*} - \alpha \cdot \left(\delta_{meas}^{{}^{40/36}Ar^*} - \delta_{meas}^{{}^{15}N_2{}^*}\right)}{\varepsilon_{Xe} - \alpha}}{\left(\Omega^{{}^{40/36}Ar^*} - \Omega^{{}^{15}N_2{}^*}\right)} \tag{3.23.}$$

Other combinations of isotopic ratios are also possible to determine isotope-based ΔT corrected for kinetic fractionation as in (3.23.). We measure isotopes of four noble gases, N_2, Ar, Kr, and Xe, yielding four different isotope-based reconstructions of ΔT. These four reconstructions do not show perfect agreement (Figure 3.8.) as $\Delta T_{Xe,Kr/N_2}$ and $\Delta T_{Xe,Kr/Ar}$ are considerably more variable than $\Delta T_{Kr,Ar/N_2}$ and $\Delta T_{Xe,Ar/N_2}$ and frequently yield unrealistically warm ΔT. Both $\Delta T_{Xe,Kr/N_2}$ and $\Delta T_{Xe,Kr/Ar}$ strongly covary with the ratio of kinetic fractionation factors for Xe and Kr, $\varepsilon_{Xe}/\varepsilon_{Kr}$, calculated from measurement data (Figure 3.8.). Whenever $\varepsilon_{Xe}/\varepsilon_{Kr}$ substantially deviates from the theoretical value of ~1.4 (Birner et al., 2018), $\Delta T_{Xe,Kr/N_2}$ and $\Delta T_{Xe,Kr/Ar}$ are considerably different from $\Delta T_{Kr,Ar/N_2}$ and $\Delta T_{Xe,Ar/N_2}$. This suggests that the discrepancy between the four isotope-based reconstructions of ΔT can largely be explained by the lower analytical precision of Xe and Kr isotopes, which lead to lower precision in $\Delta T_{Xe,Kr/N_2}$ and $\Delta T_{Xe,Kr/Ar}$. Indeed, when averaged over all four terminations, the four ΔT reconstructions are in agreement within their uncertainties, with $\overline{\Delta T_{Kr,Ar/N_2}} = -5.5 \pm 2.1$ °C, $\overline{\Delta T_{Xe,Ar/N_2}} = -5.3 \pm 2.1$ °C, $\overline{\Delta T_{Xe,Kr/N_2}} = -3.9 \pm 3.6$ °C, and $\overline{\Delta T_{Xe,Kr/Ar}} = -2.6 \pm 6.3$ °C.

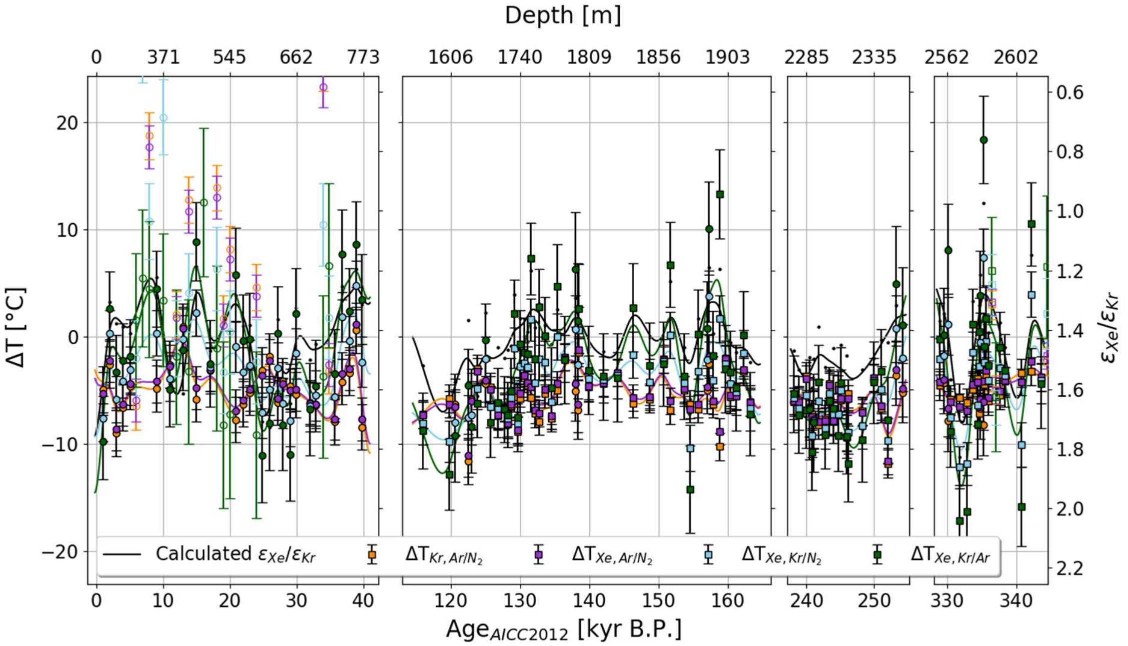

Figure 3.8.: Top–bottom firn temperature difference ΔT derived from different combinations of noble gas isotopic ratios. Helped by their better analytical precision, $\Delta T_{Kr,Ar/N_2}$ *and* $\Delta T_{Xe,Ar/N_2}$ *show the least variability through time. The strong covariation of the other two reconstructions of ΔT,* $\Delta T_{Xe,Kr/N_2}$ *and* $\Delta T_{Xe,Kr/Ar}$ *with calculated* $\varepsilon_{Xe}/\varepsilon_{Kr}$ *indicates that the variations in these other two reconstructions of* ΔT *are largely due to measurement uncertainties in Kr and Xe isotopic ratios. Shapes and fillings of markers and lines are the same as in Figure 3.1.*

In general, the full-isotope approach yields the most accurate but least precise values for ΔT, as it incorporates the analytical uncertainties of three isotopic ratios, compared to that of just two or one isotopic ratios for $\Delta T_{Ar/N_2}$ and ΔT_{mod}, respectively. Figure 3.5. shows the two isotope-based ΔT corrected for kinetic fractionation with the highest analytical precision,

$\Delta T_{Kr,Ar/N_2}$ and $\Delta T_{Xe,Ar/N_2}$, and compares them to $\Delta T_{Ar/N_2}$ and ΔT_{mod}. $\Delta T_{Kr,Ar/N_2}$ and $\Delta T_{Xe,Ar/N_2}$ are consistently lower than $\Delta T_{Ar/N_2}$, which is the expected as $\Delta T_{Ar/N_2}$ gives an upper limit for ΔT. In most periods, the three isotope-based ΔT records evolve in parallel as kinetic fractionation strength is roughly constant throughout most of the four Terminations (Figure 3.7.).

In summary, there exist multiple possibilities for reconstructing both the top–bottom firn temperature difference ΔT and the kinetic fractionation strength ε^*_{Ar/N_2}. Going forward in the reconstruction of past MOT, we will use an uncertainty-weighted mean of $\Delta T_{Kr,Ar/N_2}$ and $\Delta T_{Xe,Ar/N_2}$, which we write as ΔT_{iso}, to reconstruct ΔT for samples not affected by drilling fluid contamination. ΔT_{iso} of affected samples is approximated by the value of a cubic smoothing spline with cutoff frequency of 5 kyr through all ΔT_{iso} of unaffected samples. Similarly, considering the good agreement between the three reconstructions of kinetic fractionation strength (Figure 3.7.), we again use an uncertainty-weighted mean, which we call $\varepsilon^*_{\overline{Ar-N_2}}$. All these uncertainty-weighted means are calculated according to (3.19.).

3.2.4. ^{40}Ar degassing

Radioactive decay of ^{40}K into ^{40}Ar in Earth's crust and mantle, brought to the surface through tectonics and weathering, leads to a gradual degassing of ^{40}Ar to the atmosphere. Bender et al., 2008 found an increase in atmospheric ^{40}Ar relative to the stable ^{36}Ar of $6.6 \pm 0.7 \cdot 10^{-5}$ ‰/kyr. We find a similar value of $5.8 \pm 0.5 \cdot 10^{-5}$ ‰ per kyr for EDC samples (Figure 2.14.). Helped by the larger sample basis, our slope has a slightly reduced uncertainty range. However, considering that we applied our ^{40}Ar-tail correction only after the measurement period (see Section 2.3.3.d.), we decided to stick to the slope given by Bender et al., 2008. Thus, to correct for this atmospheric ^{40}Ar increase, $\delta^{40/36}$Ar is adjusted to today's atmospheric ^{40}Ar concentration for each sample of age t_{gas} (in kyr) as follows:

$$\Delta\delta^{40/36}Ar_{outgas} = 6.6 \cdot 10^{-5}‰/kyr \cdot t_{gas} \tag{3.24.}$$

It should be noted that the other ratios involving ^{40}Ar, i.e., δXe/Ar, δKr/Ar, and δAr/N_2, are combined to δXe/N_2 and δKr/N_2 in the final MOT product to avoid the issue of close-off fractionation. Consequently, the degassing correction cancels out for elemental ratios.

3.2.5. Putting it all together: from measured ratios to atmospheric ratios

To calculate the gravitational enrichment of an elemental ratio, we isolate δ_{atm} in (3.5.) to obtain:

$$\delta_{atm} = \left(\delta_{grav} + \delta_{atm} + 1\right) \cdot \exp\left(-\frac{\Delta m \cdot g \cdot z}{R \cdot T}\right) - 1 \tag{3.25.}$$

Solving for $\delta_{grav} + \delta_{atm}$ in (3.2., no gas loss) and inserting the result into (3.25.) yields:

$$\delta_{atm} = (\delta_{meas} - \delta_{therm} - \delta_{kin} + 1) \cdot \exp\left(-\frac{\Delta m \cdot g \cdot z}{R \cdot T}\right) - 1 \tag{3.26.}$$

Finally, by inserting our solution for z (3.6.) and the expressions for δ_{therm} and δ_{kin} (3.9. and 3.16.), we obtain $\delta_{atm}^{x/y}$ for the atmospheric ratio between gas species x and gas species y:

$$\delta_{atm}^{x/y} = \left(\delta_{meas}^{x/y} - \Omega^{x/y} \cdot \Delta T - \left(\varepsilon_{x/y}^{*} \cdot \varepsilon_{Ar/N_2}^{*} + \delta_{kin}^{^{15}N_2}\right) \cdot \frac{\Delta m_{x-y}}{\Delta m^{*}} + 1\right)$$

$$\cdot \left(\delta_{grav}^{*} + 1\right)^{\frac{\Delta m_{x-y}}{\Delta m^{*}}} - 1 \tag{3.27.}$$

The gravitational fractionation observed for any measured isotopic ratio corrected for thermal diffusion and kinetic fractionation can be scaled to correct the gravitational enrichment effect on elemental ratios. ΔT may be reconstructed using either the ice flow-heat flow model of Michel, 2016, or a combination of isotope ratios. The kinetic fractionation strength ε_{Ar/N_2}^{*} can be derived from the difference of any two unit-mass isotopic ratios corrected for thermal diffusion. In practise, we use $\delta^{40/36}Ar^{*}$, ΔT_{iso}, and $\varepsilon_{\overline{Ar-N_2}}^{*}$ to correct for gravitational enrichment, thermal diffusion, and kinetic fractionation, respectively. To account for the geological outgassing of ^{40}Ar, we use the slope determined by Bender et al., 2008. Furthermore, we assume no kinetic fractionation of $\delta^{15}N_2$, i.e., $\delta_{kin}^{^{15}N_2} = 0$. Firn air data and modelling studies suggest $\delta_{kin}^{^{15}N_2} < 5$ per meg at WAIS Divide (Battle et al., 2011; Birner et al., 2018; Buizert and Severinghaus, 2016). In lack of firn air data from Dome C, we choose to neglect this small fractionation, which would translate into an absolute offset in MOT on the order of 0.01 °C. Thermal diffusivity $\Omega^{x/y}$ of elemental ratios is known from laboratory measurements (Headly, 2008), and the kinetic fractionation factors $\varepsilon_{x/y}^{*}$ are given by the 2D firn model of Birner et al., 2018. The resulting atmospheric noble-gas ratios can be found in Figure 3.9.

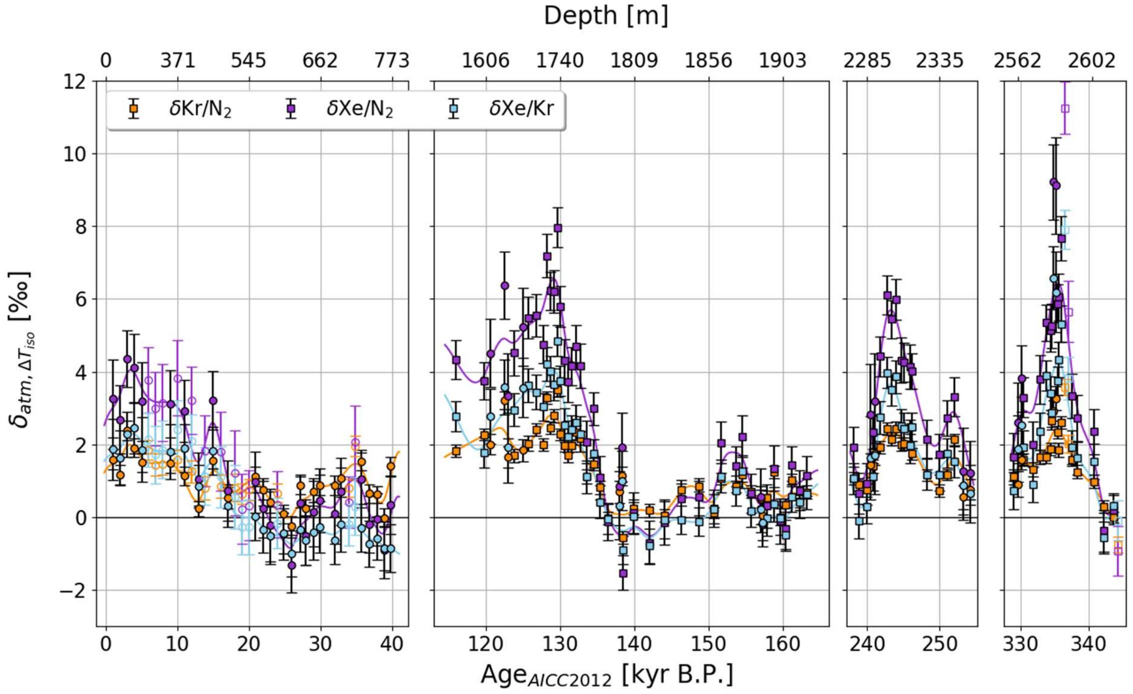

Figure 3.9.: Atmospheric noble-gas ratios from the EDC ice core for Terminations I–IV. The ratios were corrected for gravitational enrichment, thermal diffusion, and kinetic fractionation using $\delta^{40/36}Ar$*,* $\Delta T_{\overline{iso}}$*, and* $\varepsilon^{*}_{\overline{Ar-N_2}}$*, respectively. Shapes and fillings of markers and lines are the same as in Figure 3.1.*

After applying these corrections, we find systematic offsets between δ^{132}Xe/Kr and δ^{129}Xe/Kr, but no systematic offsets between δ^{132}Xe/N_2 and δ^{129}Xe/N_2 (Figure 3.10.). Considering that an offset is only found for one of the elemental ratios involving Xe, it is unlikely to be caused by a wrong firn fractionation correction. The only option we see is if the kinetic fractionation factor for δXe/Kr determined by Birner et al., 2018 were to be substantially too high, which would lead to a bigger increase in δ^{132}Xe/Kr than in δ^{129}Xe/Kr due to the larger mass difference. Alternatively, the offset might be caused by a missing or suboptimal mass spectrometry correction of δXe/Kr. However, considering that corrections for pressure imbalance, a potential chemical slope, and bellow gas amount should be very similar for both δ^{132}Xe/Kr and δ^{129}Xe/Kr, it is unclear how this may cause the offset. Indeed, we do not find any clear dependence of the offset on the date of measurement, as would be expected if the offset were due to a faulty mass spectrometry correction, although the offset does appear to have been strongest for samples measured in 2016. As the offset translates into a difference in MOT on the order of 0.1 °C, it does not substantially change our findings. We will use an uncertainty-weighted mean of δ^{132}Xe/Kr and δ^{129}Xe/Kr, and of δ^{132}Xe/N_2 and δ^{129}Xe/N_2, to retrieve atmospheric δXe/Kr and δXe/N_2.

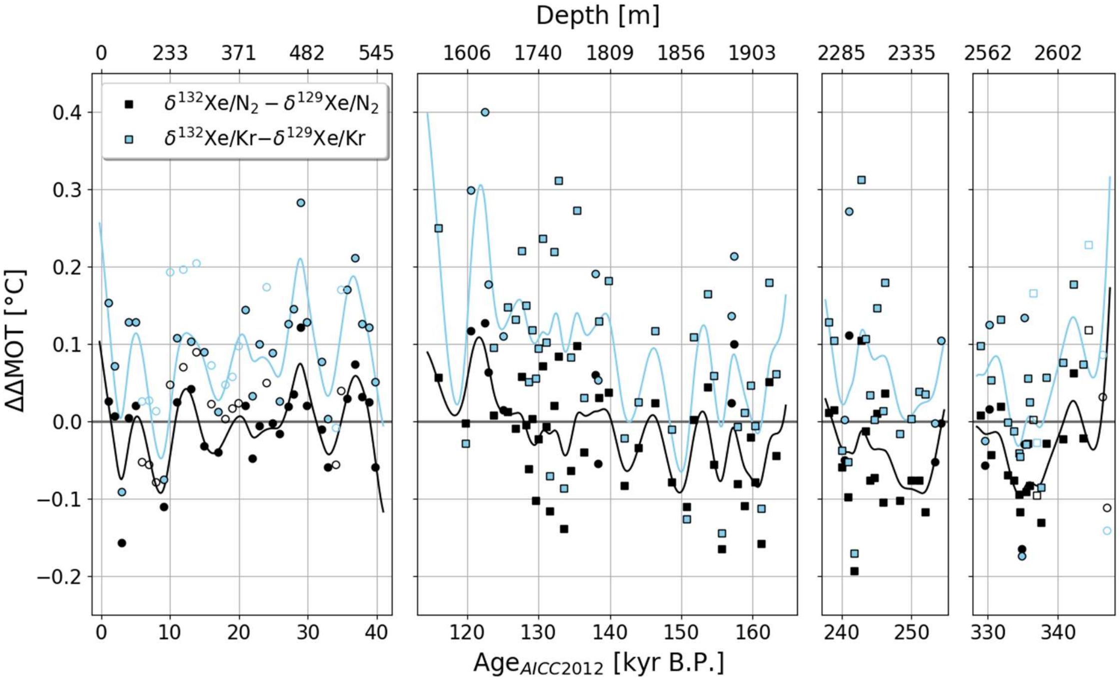

Figure 3.10.: Difference between MOT derived from reconstructed atmospheric δ^{132}Xe/Kr and δ^{129}Xe/Kr, and between MOT based on δ^{132}Xe/N$_2$ and δ^{129}Xe/N$_2$. Atmospheric δ^{132}Xe/N$_2$ and δ^{129}Xe/N$_2$ on average yield the same MOT, whereas there appears to be a systematic offset between MOT based on δ^{132}Xe/Kr and MOT derived from δ^{129}Xe/Kr, as δ^{129}Xe/Kr on average yields warmer MOT by almost 0.1 °C. However, no clear dependency of this offset on sample age or measurement date (not shown) can be found. Shapes and fillings of markers and lines are the same as in Figure 3.1. For readability, no uncertainty estimates are drawn.

3.3. From atmospheric ratios to MOT using an atmosphere-ocean box-model

The last step from ice samples to MOT is to convert atmospheric noble-gas ratios into MOT. For this, we utilise an atmosphere-ocean box-model developed by Bereiter et al., 2018a. Although simplistic, the validity of such a box-model approach has been confirmed by Ritz et al., 2011, who showed good agreement between MOT derived from a simple box-model and Bern 3D, an intermediate complexity Earth System Model in the absence of strong changes in sea ice induced air-sea gas-exchange (see discussion on undersaturation below). Further confirmation comes from comparison of MOT reconstructions to other ocean temperature reconstructions (Elderfield et al., 2012; Shakun et al., 2015). Consequently, the ocean-atmosphere box-model of Bereiter et al., 2018a has been utilised by all recent MOT publications (Baggenstos et al., 2019; Bereiter et al., 2018b; Haeberli et al., 2021; Shackleton et al., 2021, 2020, 2019).

The box model consists of one atmospheric box and three oceanic boxes, one representing Antarctic Bottom Water (AABW), one for North Atlantic Deep Water (NADW), and a box for the residual ocean. The model assumes that the noble gases N_2, Kr, and Xe are conserved in the atmosphere-ocean system. Each ocean box has a set volume and is characterised by its temperature and salinity. For each datapoint, temperature and salinity are iterated until they can explain the input atmospheric noble-gas ratios within 1 per meg, given the input sea level. To determine oceanic noble gas concentrations, we use the updated solubility equations by Hamme et al., 2019. The model is run such that it changes the temperatures of the different ocean boxes equally unless a box (typically AABW, in extreme cases NADW) reaches the freezing temperature of ocean water of −2 °C. In that case, further cooling is partitioned equally between the remaining boxes. Bereiter et al., 2018b tested a more realistic scenario of changing the volumes of the three boxes but found it had minimal influence on the resulting MOT. The model further accounts for minor effects such as changes in atmospheric water vapour content and a small sea-surface-pressure correction for high latitudes, where most of the deep-water formation occurs. A more detailed description of the model is given in Bereiter et al., 2018b, 2018a.

The box model requires input values for past sea level. Sea level influences the inferred MOT in multiple ways. First and foremost, sea level is needed to determine the total ocean volume and, thus, the amount of water in which noble gases are dissolved. Furthermore, sea level controls ocean salinity and atmospheric pressure at sea level, both of which affect solubility of gases in ocean water. Depending on the noble-gas ratio, a change in sea level by 120 m translates to a MOT difference of up to 0.8 °C (Figure 3.11.). Age scale uncertainties of ice core and sea sediment records can, thus, become critical in periods of rapid sea level change, i.e., during terminations. The full scope of the dating uncertainty of marine sediment records may be seen in Figure 3.12., which shows the most recent sea-level reconstructions over the past four terminations. Temporal offsets between sea-level curves for the onsets of glacial–interglacial sea-level rise can be as high as 10 kyr.

Considering that the sea-level record of Lambeck et al., 2014 is based on absolutely dated sediment and coral records, we use this as our benchmark and as our box-model input for the last 30.5 kyr. For the period prior to 30.5 kyr, we rely on the combined sea level and DOT record of Shakun et al., 2015, for which we adjust the age scale such that their DOT reconstruction aligns with our MOT curve. We note that this approach could also be applied to the combined sea level and DOT reconstruction of Rohling et al., 2021. However, considering that their reconstruction shows a considerably earlier onset of sea-level rise than any other sea-level curve across Termination I and most terminations before that, we decided to use the record of Shakun et al., 2015 instead, which is well-aligned with the absolutely dated record of Lambeck et al., 2014.

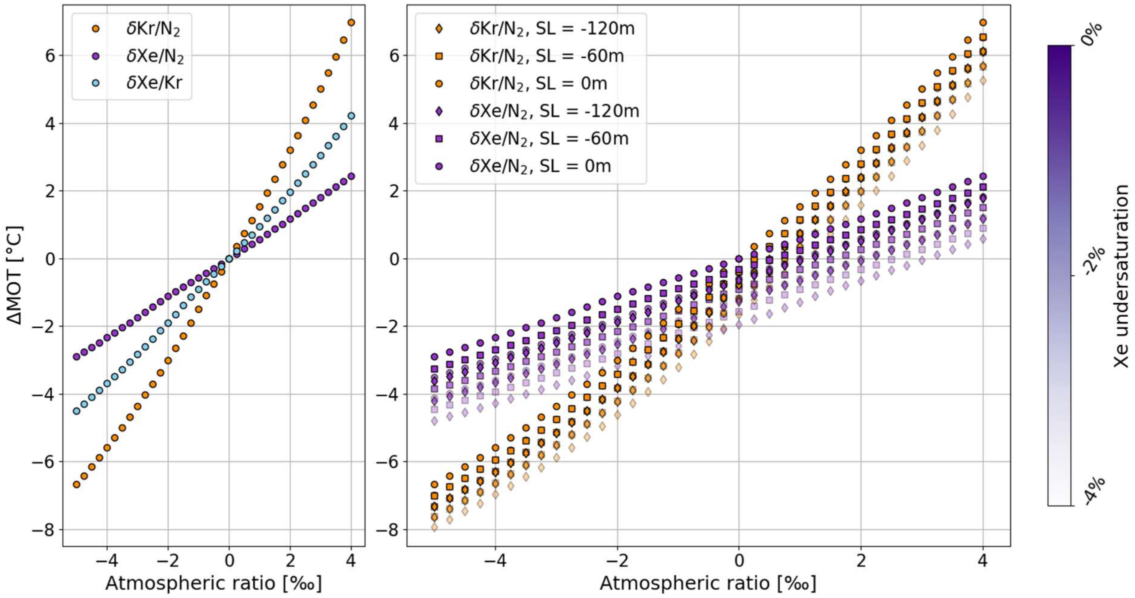

Figure 3.11.: The left-hand panel shows the relationship between atmospheric noble-gas ratio and inferred ΔMOT by the atmosphere-ocean box model of Bereiter et al., 2018a. The right-hand panel shows the model sensitivity to changes in sea level and the Kr and Xe saturation state for δKr/N$_2$ and δXe/N$_2$. Kr undersaturation is set to be half of the Xe undersaturation.

The box model generally assumes that noble gases are in solubility equilibrium between atmosphere and ocean, such that the gas content of a water parcel is representative of the parcel's temperature. However, in the modern ocean, the heavy noble gases Ar, Kr and Xe are considerably undersaturated (Hamme et al., 2019; Loose et al., 2016), challenging this fundamental assumption. The equilibrium gas concentration of a water parcel is mostly determined by the water parcel's temperature and salinity, but sea surface pressure also plays a role. Cooling of a water parcel leads to an air-sea partial pressure gradient, which is stronger for heavier noble gases (Figure 1.2.). If this cooling happens sufficiently quickly in a region of deep-water formation, gases might not reach solubility equilibrium before the water parcel is advected down. We expect higher undersaturation the faster cooling, the stronger the overturning circulation, and the slower the air-sea gas-exchange rate of the gas. Air-sea gas-exchange constantly occurs via diffusion and is controlled by the diffusivity of the gas in ocean water. Gases also find their way into the ocean through dissolution after wind-driven bubble-injection. The effectiveness of both processes, diffusion and bubble injection, increases with surface wind speed. Air-sea gas-exchange is also affected by sea ice, which strongly restricts gas exchange, whereas heat can still be transferred through the ice (Pöppelmeier et al., 2023). Thus, a water parcel that cools under sea ice before being advected to the deep ocean may be undersaturated. Furthermore, mixing of water masses with different temperatures leads to oversaturation due to the nonlinear temperature-solubility relationship (Figure 1.2.). Today, water with higher-than-equilibrium heavy noble-gas concentrations can mostly be found in the shallow equatorial ocean (Hamme et al., 2019).

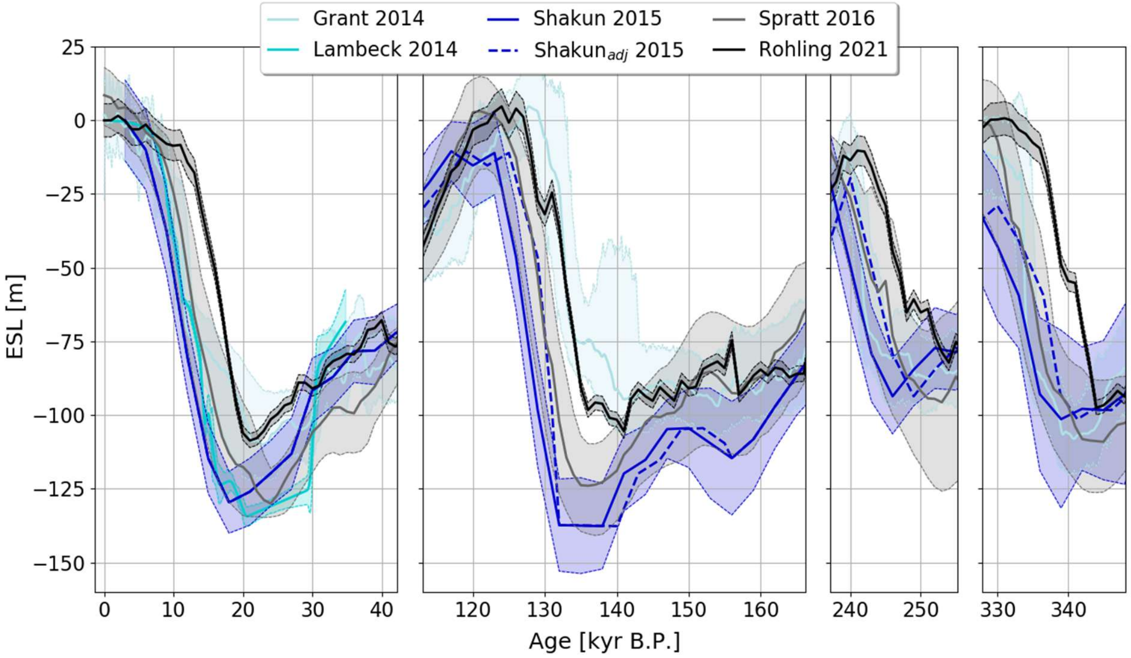

Figure 3.12.: Eustatic sea level (ESL) records for the last four glacial terminations. The high resolution Termination I record of Lambeck et al., 2014 uses inversion of sea-level observations far from former ice margins to reconstruct ESL for the last 35 kyr. The record of Grant et al., 2014 (based on earlier work by Grant et al., 2012; Rohling et al., 2009; and Siddall et al., 2003) covers the last 500 kyr and is based on planktonic $\delta^{18}O_C$ records from the Red Sea. Shakun et al., 2015 reconstructed sea level for the last 800 kyr using a stack of 49 planktonic $\delta^{18}O_C$ records. Spratt and Lisiecki, 2016 derive their 430 kyr sea-level record from a principal component analysis on 7 benthic $\delta^{18}O_C$ records. Finally, the ESL record of Rohling et al., 2021 spans the last 5.3 Myr. It is based on the Mediterranean planktonic $\delta^{18}O_C$ record from Rohling et al., 2014, which they refine through process-based modelling of different parameters affecting measured $\delta^{18}O_C$. Shown for each record are the best estimate and their 2σ uncertainty as drawn line and shaded area, respectively. The dashed line indicates the record of Shakun et al., 2015 on the adjusted age scale, which we use as box-model ESL input (see text).

Many of these processes controlling equilibrium gas concentration and air-sea gas-exchange are influenced by climate and were most likely of different strength or effectiveness in the past. Lower sea level during glacial periods meant that equilibrium gas concentrations during these periods were lower, too. Glacial periods are also typically characterised by larger sea-ice extent, more sluggish ocean circulation, and higher wind speeds, all of which have a, in parts compensating, influence on air-sea gas-exchange. Consequently, past ocean saturation state might have been significantly different from today. Using the intermediate complexity Earth System Model Bern 3D, recent modelling studies have found saturation concentrations to be especially dependent on sea-ice extent and overturning circulation (Liu, 2021; Pöppelmeier et al., 2023). Pöppelmeier et al., 2023 found that the LGM-Holocene MOT difference might be overestimated by about 0.5 °C if changes in the ocean saturation state are not considered. Furthermore, changes in the ocean saturation state may also explain minor offsets between MOT values obtained from the three noble-gas ratios.

Some aspects of the ocean's changing saturation state in response to changes in climate are taken into consideration by the box model, namely changes in equilibrium gas-concentration due to sea level. However, processes controlling the air-sea gas-exchange by far exceed the complexity of our box-model approach and instead have to be accounted for by estimating their effect on saturation concentration. Unfortunately, no proxy data on past oceanic saturation concentrations exists and we would rely on model output for estimates of the ocean's past saturation state. For now, we refrain from applying a correction of our MOT for changes in the ocean saturation state and instead assume no undersaturation. The MOT sensitivity to changes in the ocean saturation state can be gauged from Figure 3.11.

There are further processes that challenge the fundamental assumption of noble-gas thermometry of the noble-gas content of a water parcel always being representative of the parcel's temperature. Most notably, geothermal heating leads to a warming of bottom-water temperatures, which is not represented in its noble-gas content. Geothermal heat flux and ocean circulation, and, thus, the exposure duration of bottom water to geothermal heating, varied in the past, and the bias in MOT caused by geothermal heating may not be constant over time. However, the energy provided by the geothermal heat flux of typically less than 0.1 Wm^{-2} is small compared to the input at the ocean surface (Baggenstos et al., 2019). Ritz et al., 2011 found that the geothermal heat flux adds an uncertainty of less than ± 0.15 °C to MOT values, which is below our 1σ measurement precision.

A second process that can lead to a decoupling of noble-gas content and temperature of a water parcel is sub-shelf melting of glacial ice. When glacial ice melts at depth, the gases contained in the ice, altered from their atmospheric concentrations by firn fractionation processes, are forced into solution. Thereby, melt of glacial ice adds considerable quantities of low-solubility gases and smaller quantities of high-solubility gases to a water parcel in solubility equilibrium (Loose and Jenkins, 2014). The glacial meltwater also alters temperature and salinity and thereby the equilibrium saturation state of the water parcel, leading to an undersaturation of heavy noble gases (Loose and Jenkins, 2014). Loose et al., 2016 found a meltwater fraction of AABW of about 3.5‰. At these amounts, the direct temperature effect on MOT is negligible (Liu, 2021). However, the influence on the saturation state of noble gases in the modern ocean might be significant (Loose et al., 2016) and furthermore may have been different for different subglacial melting rates in the past, contributing to the uncertainty of changes in past oceanic saturation state discussed above.

Keeping all these minor caveats of the box-model approach in mind, we can get an idea of its validity by comparing MOT values obtained from the three noble-gas ratios. The resulting MOT for Terminations I–IV can be found in Figure 3.13., using $\delta^{40/36}\mathrm{Ar}^*$, $\Delta T_{\overline{iso}}$, and $\varepsilon^*_{\overline{Ar-N_2}}$ to correct for gravitational enrichment, thermal diffusion, and kinetic fractionation, respectively. Indeed, there appear to be some issues with our reconstruction in a few periods, e.g., in the brittle ice zone older than 25 kyr, where MOT derived from the three noble-gas ratios do not agree with one another within uncertainties. Furthermore, all three MOT values are considerably too warm relative to the Holocene. Additionally, comparison with published MOT data for the last two terminations from the WAIS Divide ice core (Bereiter et al., 2018b) and Taylor Glacier (Shackleton et al., 2020) reveals discrepancies between MOT reconstructions from different ice cores. At the same time, the comparison also shows that other MOT records face similar issues. These issues will be discussed in more detail in the last section of this chapter.

The current way forward is to assume that the process responsible for the offsets is site specific but approximately constant in time. If the offset is indeed constant in time, we may correct for it by subtracting the Holocene value, i.e., the 0–10 kyr mean, of each reconstructed atmospheric noble-gas ratio. Doing so not only removes the Holocene offset (as expected) but also leads to considerably better agreement between the three ratios (Figure 3.13.). Thus, although reconstructed absolute MOT values are clearly too high, relative changes in MOT appear to be largely unaffected. In the following, we therefore only interpret MOT relative to the Holocene, $\Delta\mathrm{MOT}_{\mathrm{Hol}}$.

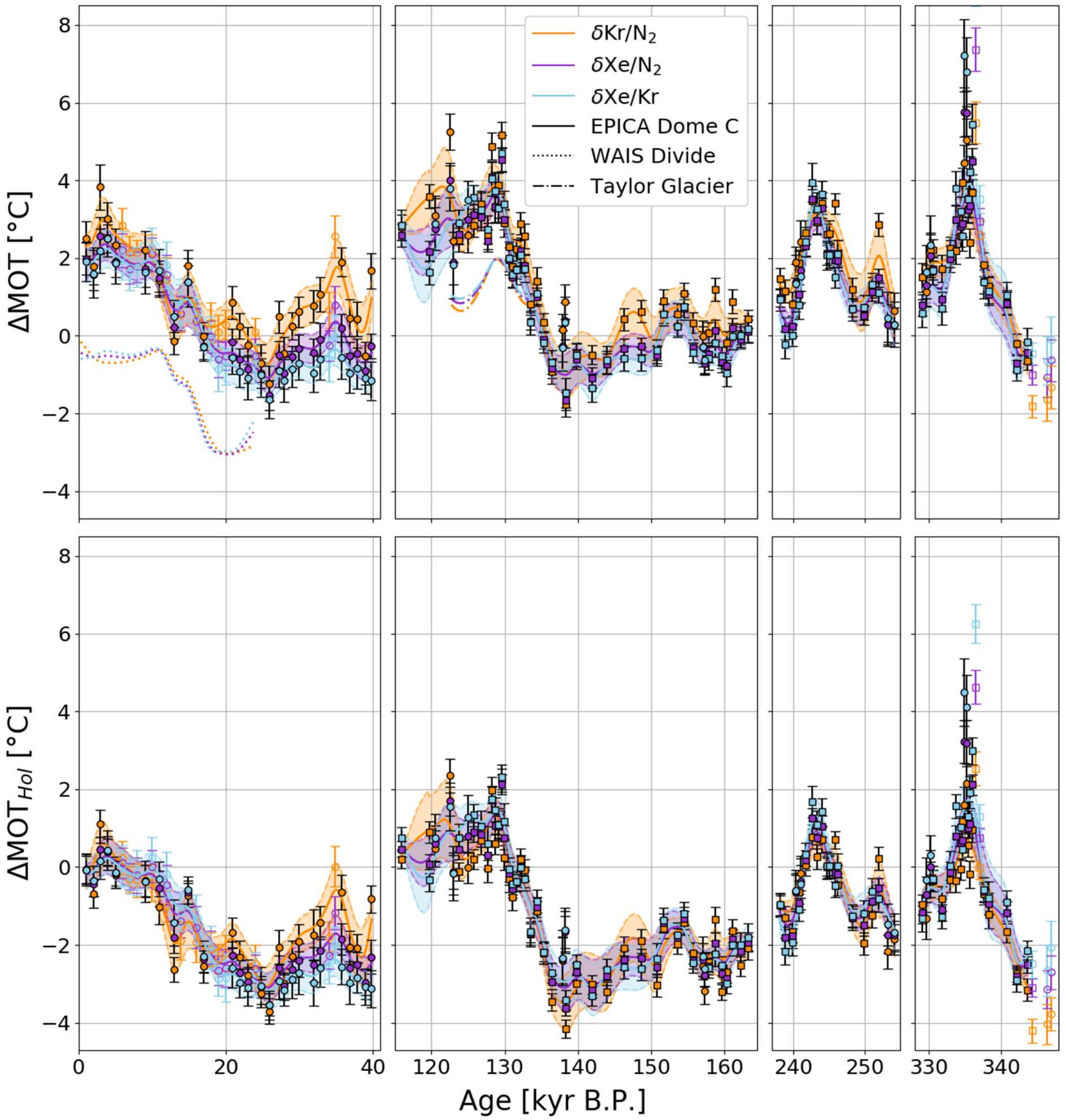

Figure 3.13.: Termination I–IV ΔMOT based on noble-gas ratios from the EDC ice core. Ratios were corrected for gravitational enrichment, thermal diffusion, and kinetic fractionation using $\delta^{40/36}Ar$, $\Delta T_{\overline{iso}}$, and $\varepsilon^{*}_{\overline{Ar-N_2}}$, respectively. Shapes and fillings of markers are the same as in Figure 3.1. Solid lines show cubic smoothing splines with cutoff frequency of 5 kyr through the individual datapoints of each ratio. The 1σ uncertainty bands of these splines are indicated by the shaded areas. The ΔMOT in the upper panel clearly shows a Holocene offset. Holocene offsets, albeit of different size, are also found for the three noble-gas ratios of a Termination I MOT reconstruction from the WAIS Divide ice core (dotted line, Bereiter et al., 2018b) and a LIG record from Taylor Glacier (dashed line, Shackleton et al., 2021). In the lower panel, each ratio of our record is expressed relative to its Holocene (0–10 kyr) mean, yielding ΔMOT_{Hol}.

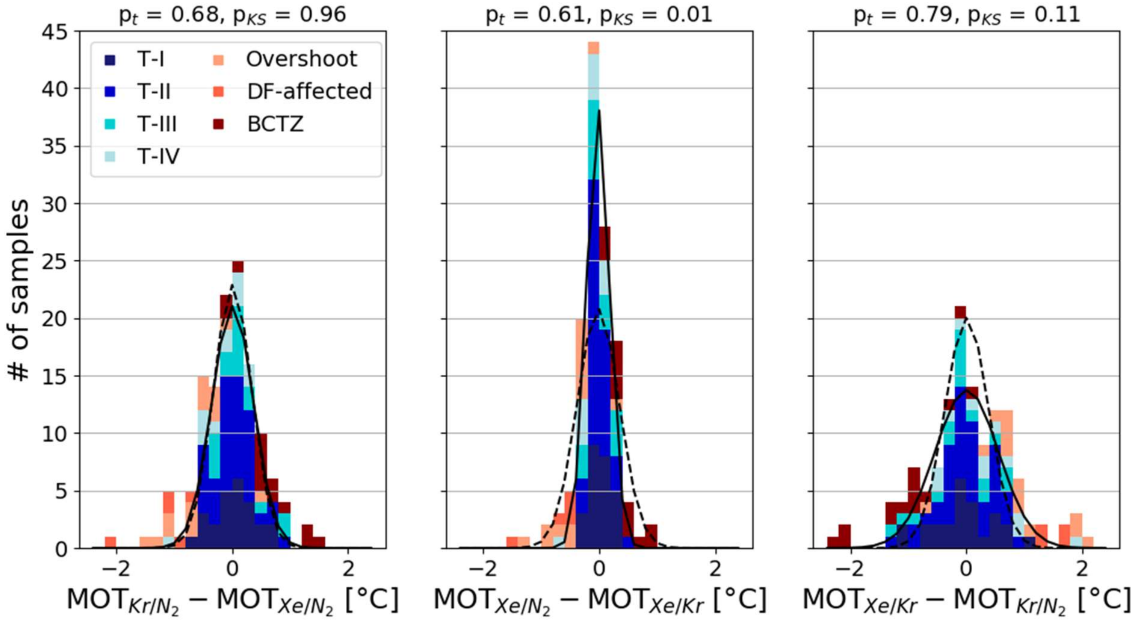

Figure 3.14.: Histogram of pair differences for MOT derived from the three noble-gas ratios. A two-sided t-test revealed that the mean of all three pair-differences is not significantly different from the expected value of 0 ($p_t > 0.05$). We then used a Kolmogorow-Smirnow-test to assess whether the distribution of our data (solid black lines) was significantly different from the expected normal distribution with a mean of 0 and a standard deviation given by our analytical uncertainties (dashed black lines). We find no significant difference ($p_{KS} > 0.05$) except for the pair differences of MOT derived from δXe/N$_2$ and δXe/Kr. However, in that case the variability in pair differences is smaller than what we would expect from our analytical uncertainties, i.e., we seem to overestimate the uncertainty of these two ratios. These statistical analyses are only based on the samples plotted in blue. Samples from the BCTZ, the MOT overshoots at the end of Terminations III and IV and in the 4 kyr after the Termination II overshoot, as well as the Termination IV samples affected by drilling fluid contamination drawn in red were excluded from the analysis. Thus, they are treated differently when assessing measurement uncertainties (see Section 3.4.).

Considering the good agreement between reconstructed MOT derived from the three noble-gas ratios, we may in a final step combine the three MOT values to form MOT$_{mix}$, the average of the three ratios. Doing so reduces the influence of analytical noise from any single ratio. However, this step requires that the three ratios indeed measure the same metric, i.e., that there are no systematic differences between them. However, closer inspection of Figure 3.13. reveals some potentially systematic disagreement between the three ratios for samples from 40–25 kyr and during the two MOT overshoots at the end of Terminations III and IV. This can be assessed statistically by analysing pair differences between the three ratios. In Figure 3.14., we test whether i) the averages of these three pair-differences are 0, and ii) their standard deviation is not significantly different from the expected standard deviation given by our analytical uncertainty. Indeed, we find that the above null-hypotheses only hold when excluding samples from 40–25 kyr, the Termination III and IV overshoots and the 4 kyr after the Termination II overshoot, as well as Termination IV samples affected by drilling fluid from the analysis.

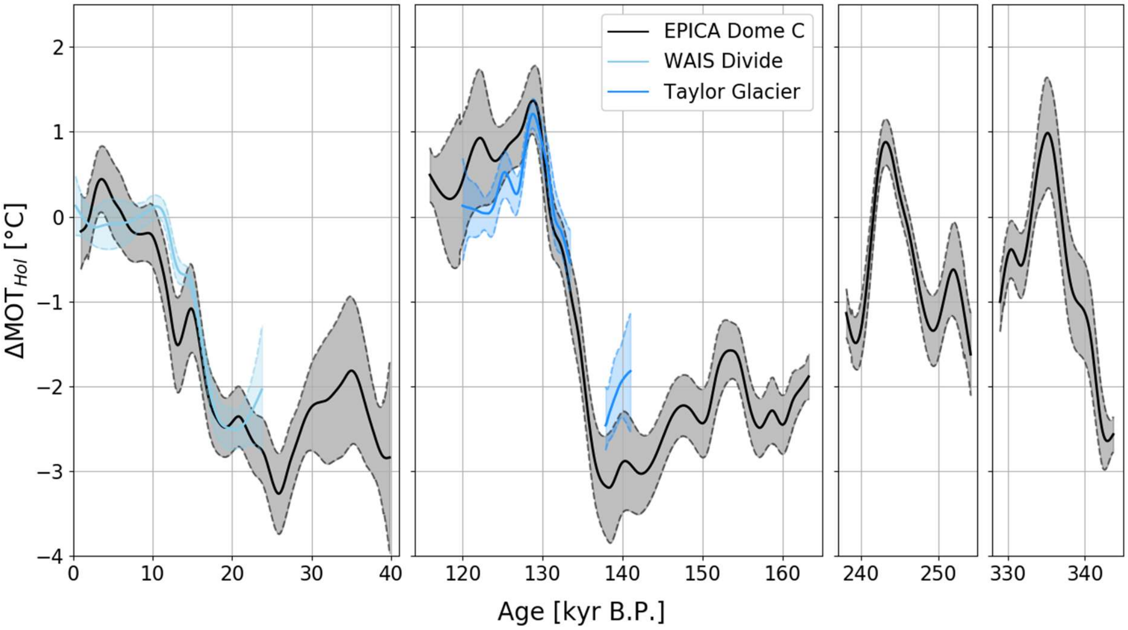

Figure 3.15.: The resulting EDC Termination I–IV ΔMOT_{Hol} *record, based on a cubic smoothing spline with cutoff frequency of 5 kyr through* MOT_{mix}*. Also shown are the Termination I record from the WAIS Divide ice core (Bereiter et al., 2018b) and the LIG record from Taylor Glacier (Shackleton et al., 2020). As no splined record is provided for the WAIS Divide data, we applied the same splining method as for EDC, whereas the published spline of the Taylor Glacier record has a cutoff frequency of 2.5 kyr. All three records are plotted on their own age scale and are expressed relative to their Holocene (0–10 kyr) mean. Lines and shaded areas indicate the best estimate and the 1σ uncertainty bands of each record, respectively.*

Finding systematic disagreement for samples from 40–25 kyr is not unexpected, as they stem from the BCTZ, which is characterised by more brittle ice and may, thus, be affected by fractionating post-coring gas loss (Haeberli et al., 2021). The reason for the disagreement during the two MOT overshoots is less clear and might be linked to some dynamic firn fractionation process which only occurs during these periods of rapid climate change, and for which we for now cannot correct. For both periods, Haeberli et al., 2021 suspect fractionating gas-loss that affects ratios involving Xe. They, thus, consider MOT derived from $\delta Kr/N_2$ as the most trustworthy during these periods. However, considering the lack of evidence for gas loss for any of our samples from $\delta O_2/N_2$ measurements (Figure 3.3.), we refrain from excluding $\delta Xe/N_2$ and $\delta Xe/Kr$ of these datapoints solely based on a lack of agreement between the three ratios. Instead, we use the average of the three ratios throughout our record and address the brief periods of poor agreement between the three noble-gas ratios in our uncertainty estimation. The resulting MOT record for Terminations I–IV is shown in Figure 3.15, together with the Termination I WAIS Divide record of Bereiter et al., 2018b, and the Taylor Glacier LIG record from Shackleton et al., 2020. Expressed relative to their respective Holocene mean, the three records show good agreement, giving further support that the offset in absolute MOT is indeed constant in time.

3.4. Uncertainty estimation and cubic smoothing spline

To determine the uncertainty of our MOT record, we start by propagating the analytical uncertainties of each isotopic and elemental ratio, sea-level stand, and sample age in a Monte Carlo fashion. We create 10,000 Monte Carlo realisations for each sample and each of the three MOT values derived from the noble-gas ratios. We then take the standard deviation of these Monte Carlo realisations as our uncertainty of individual MOT datapoints. For samples measured in 2022, the resulting 1σ uncertainties are between 0.2–0.35 °C for all three ratios. Small differences in uncertainty between ratios and individual datapoints are due to differences in analytical precision, differences in the relevance of firn fractionation corrections for individual ratios, and differences in sample age and, thus, different uncertainty of the ^{40}Ar degassing correction. Samples from earlier measurement periods were measured at slightly lower analytical precision, resulting in 1σ uncertainties of 0.3–0.6 °C for most datapoints.

To determine the uncertainty of MOT_{mix}, we distinguish between regular samples (i.e., the blue datapoints in Figure 3.14.) and samples from periods of systematic disagreement between the MOT derived from the three noble-gas ratios (Figure 3.13.). For regular samples, we assume the uncertainty of MOT_{mix}, $\sigma_{MOT_{mix}}$, to be given by the uncertainties of the three noble-gas ratios $\sigma_{MOT_{\delta_i}}$:

$$\sigma_{MOT_{mix}} = \sqrt{\frac{\sum \sigma^2_{MOT_{\delta_i}}}{3}} \tag{3.28.}$$

To account for the systematic differences of samples from 40–25 kyr and the MOT during or shortly after the Termination II–IV overshoots, we additionally take the level of disagreement amongst the three noble-gas ratios into consideration. Consequently, we calculate $\sigma_{MOT_{mix}}$ for these samples as follows:

$$\sigma_{MOT_{mix}} = \sqrt{\frac{\sum \sigma^2_{MOT_{\delta_i}}}{3} + \left(\frac{max\left(MOT_{\delta_i}\right) - min\left(MOT_{\delta_i}\right)}{2}\right)^2} \tag{3.29.}$$

Therefore, the size of $\sigma_{MOT_{mix}}$ strongly depends on the level of agreement between the MOT values obtained from the three noble-gas ratios. Consequently, $\sigma_{MOT_{mix}}$ may be as large as 1 °C during periods of low agreement. For regular samples, $\sigma_{MOT_{mix}}$ is 0.3–0.5 °C for samples measured in 2022 and 0.4–0.6 °C for samples from earlier measurement periods.

To assess MOT throughout the last four Terminations and their subsequent interglacials, we interpolate between our discrete MOT reconstructions using a cubic smoothing spline with a cutoff period of 5 kyr. Such a high cutoff period does cause the spline to not capture the full range of variability in periods of rapid MOT change. Consequently, our spline likely somewhat underestimates the peak in MOT at the ends of Terminations II–IV. However, splines with cutoff periods < 4 kyr lead to unrealistic artefacts in other parts of the record, whereas larger cutoff periods cause stronger dampening of millennial-scale variability and even reduce the amplitude of glacial–interglacial differences. To assess the uncertainty of the cubic smoothing splines, we again use a Monte Carlo approach. Additionally, each Monte Carlo realisation undergoes a bootstrapping procedure, in which the datapoints are resampled. This assures that the uncertainty in time intervals with low sampling resolution is accurately represented. The resulting best estimate and the corresponding 1σ uncertainty bands of our record are given in Figure 3.15. Compared to other MOT reconstructions from Termination I and the LIG, our record features somewhat larger uncertainty bands. This may be explained by the lower temporal resolution of our record.

3.5. Incomplete understanding of firn fractionation processes

Each of the three atmospheric noble-gas ratios reconstructed in Section 3.2. yields a MOT value, using the box model described in Section 3.3. These three ratios are proxies for the same metric, and the resulting MOT values should agree with one another within analytical uncertainty. However, with the chosen firn fractionation corrections, which do explain the differences between isotopic ratios (Figure 3.6.), the MOT values inferred from the three noble-gas ratios show considerable discrepancies in some time intervals. Furthermore, our MOT record is clearly offset from the expected Holocene value of 0 (Figure 3.13.). Both issues are not new to MOT reconstructions. In fact, no published MOT dataset manages to get all three MOT values to agree with one another, have a Holocene offset of 0, and simultaneously explain the differences between isotopic ratios. Most published records, thus, express their MOT data relative to a reference period, typically the Holocene. Doing so assumes that whatever process causes the offset is constant in time, resulting in flawed absolute MOT but largely unaffected relative MOT. Indeed, this is also the approach we use to interpret our MOT record. However, before doing so in Chapter 4, we want to explore some potential causes of the found offsets.

In the above sections, potential candidates causing biases in our MOT values have already been hinted at. Changes in the ocean saturation state, geothermal heating of bottom water, or sub-shelf glacial melting all challenge the fundamental assumption of noble-gas thermometry that the noble-gas content of a water parcel is always representative of its temperature. All these processes thereby question our way of translating reconstructed atmospheric ratios into MOT. They thereby might explain offsets between the three noble-gas ratios and potentially also cause absolute offsets in reconstructed MOT. However, reconstructed atmospheric ratios are unaffected by them, such that these processes should lead to consistent offsets in MOT reconstruction from different ice cores. By now, MOT datasets from three different ice cores exist. In addition to EDC, these are MOT datasets using ice from the WAIS Divide ice core (Bereiter et al., 2018b) and Taylor Glacier (Shackleton et al., 2021, 2020, 2019). Although other datasets face similar issues with offsets between MOT values based on the three noble-gas ratios, these offsets are distinctly different between ice cores, as evident in Figure 3.13. Therefore, the cause for these offsets must be site-specific. The most likely candidate for an unaccounted fractionation process is located in the firn column. In the following, we want to first gain a better understanding of the effects of the individual firn corrections on reconstructed MOT. In a second subsection, we then hypothesise about potential firn processes that might explain these offsets.

3.5.1. Effects of different firn fractionation corrections on MOT estimates

Gravitational fractionation correction is by far the largest correction we apply to our noble-gas ratios (Figure 3.1.). In theory, a correction for gravitational enrichment can be obtained from any isotopic ratio. In practise, we want to use either $\delta^{40/36}Ar$ or $\delta^{15}N_2$, as these two ratios can be measured most precisely. Out of the two, we chose $\delta^{40/36}Ar$ because its analytical precision is better than that of $\delta^{15}N_2$, because it is not affected by drilling fluid contamination, and because $\delta^{40/36}Ar$ is less temperature sensitive than $\delta^{15}N_2$. MOT corrected for gravitational enrichment using $\delta^{40/36}Ar$ thus differs from MOT corrected with $\delta^{15}N_2$ in multiple ways (Figure 3.16.). Most noticeably, the scatter for N_2-corrected MOT is somewhat higher due to the lower analytical precision of $\delta^{15}N_2$. As both Ar and N_2 are hardly affected by kinetic fractionation, any difference between the reconstructed MOT is mainly due to the higher thermal sensitivity of $\delta^{15}N_2$. For the most part, elemental ratios gravitationally corrected with $\delta^{15}N_2$ yield somewhat higher MOT than the same ratios corrected with $\delta^{40/36}Ar$. This is expected if $\delta^{15}N_2$ is lower than $\delta^{40/36}Ar$, which is the case in a firn with negative top−bottom temperature difference ΔT, in which, due to its higher thermal sensitivity, $\delta^{15}N_2$ increases more than $\delta^{40/36}Ar$ at the colder, upper end of the firn column.

It is also noteworthy that the difference between MOT corrected with $\delta^{15}N_2$ and those corrected with $\delta^{40/36}Ar$ is different for the three noble-gas ratios. The difference is largest for $\delta Kr/N_2$ due to its large conversion rate from atmospheric ratio to MOT of about 2:1 (Figure 3.11.). The second biggest change occurs for $\delta Xe/N_2$, the ratio with the largest mass difference, which is, thus, affected by changes in gravitational correction more strongly than the other two. The larger mass difference outweighs the slightly higher conversion rate of $\delta Xe/Kr$, for which the smallest change in MOT can be observed. Rather intriguingly, the three MOT values corrected for gravitational enrichment using $\delta^{40/36}Ar$ show a minimal Holocene offset and mostly agree with one another within uncertainties. Large discrepancies can only be found between 25–40 kyr, a period likely affected by fractionating post-coring gas loss (Haeberli et al., 2021), and during interglacial periods prior to the Holocene. Even smaller differences between the three MOT values and no Holocene offset at all is found when gravitational fractionation is corrected using $\delta^{15}N_2$.

The discrepancies between MOT corrected with $\delta^{15}N_2$ and those corrected with $\delta^{40/36}Ar$ are largely due to neglecting thermal diffusion. Thermal diffusion correction has multiple influences on the resulting MOT (Figure 3.17.). On the one hand, the noble-gas ratios are corrected directly for thermal diffusion. The size of this direct thermal-fractionation correction is determined by each ratio's thermal diffusivity. The correction is largest for $\delta Kr/N_2$, followed by $\delta Xe/N_2$. The thermal diffusivity correction for $\delta Xe/Kr$ is considerably smaller than that for the other two ratios and almost negligible. Thus, a negative ΔT results in a stronger shift upwards in MOT based on $\delta Kr/N_2$ than for $\delta Xe/Kr$. This is further helped by the conversion rates from atmospheric ratio to MOT (Figure 3.11.).

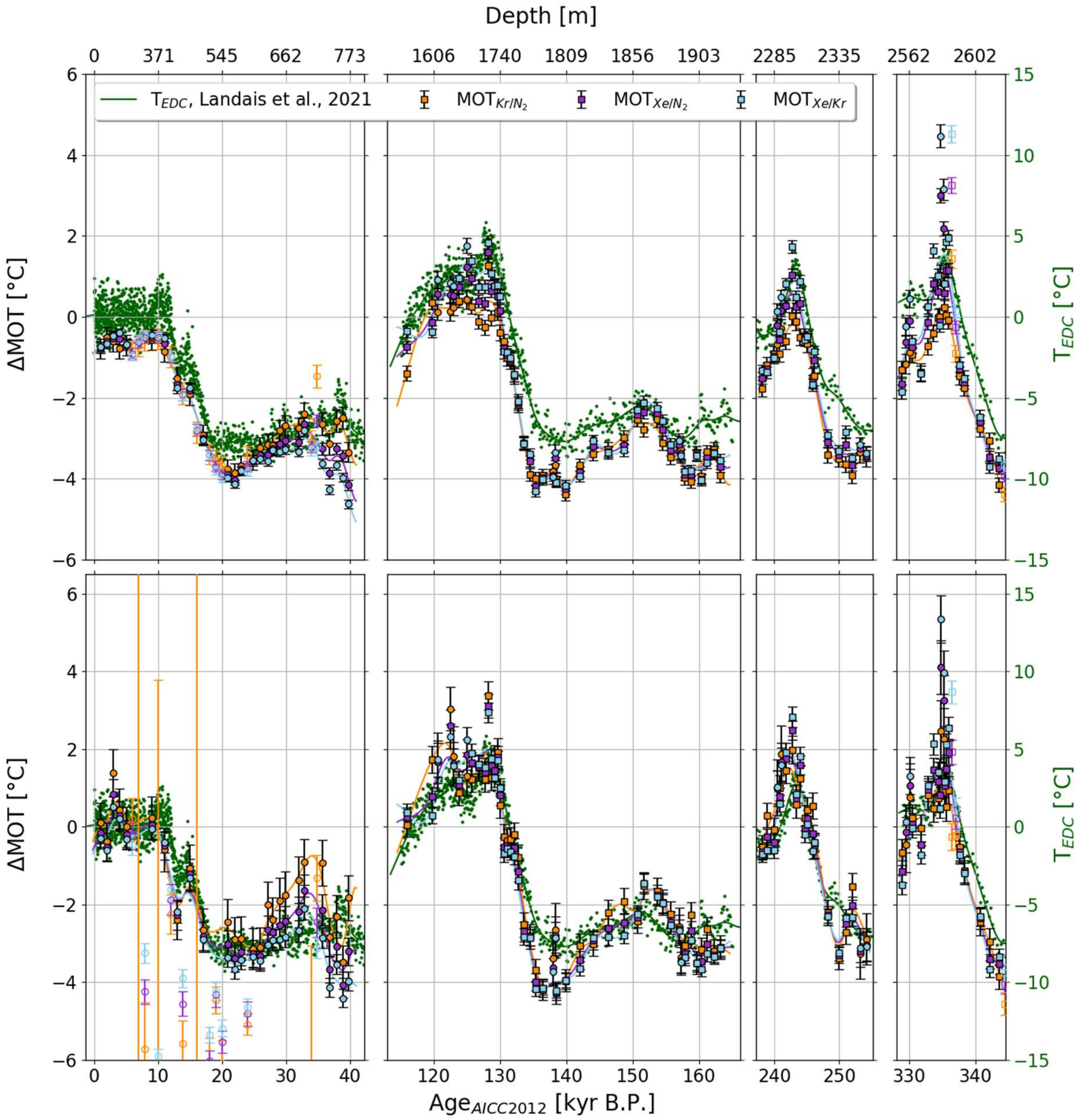

Figure 3.16.: ΔMOT based on noble-gas ratios corrected for gravitational enrichment only, i.e., without thermal and kinetic fractionation corrections, using either $\delta^{40/36}Ar$ (upper panel), or $\delta^{15}N_2$ (lower panel). For orientation, EDC site temperature from Landais et al., 2021 is plotted alongside the MOT data. Shapes and fillings of markers and lines are the same as in Figure 3.1.

On the other hand, gravitational fractionation correction also depends on the thermal diffusion correction and thus on ΔT. Negative ΔT increases the gravitational fractionation correction and reduces MOT. This partly counteracts the direct effect of thermal-diffusion correction on the noble-gas ratios. Again, the effect is largest for δKr/N$_2$-based MOT and smallest for δXe/Kr. Somewhat counterintuitively, MOT based on the thermally insensitive δXe/Kr is affected the most by thermal diffusion correction (Figure 3.17.). This can be explained if the direct and indirect effects of thermal diffusion correction are almost perfectly compensating for δKr/N_2, but less so for δXe/Kr. Consequently, MOT based on δXe/Kr is shifted by about 1.7 °C on average when correcting for thermal diffusion using $\Delta T_{\overline{iso}}$, whereas those based on δKr/N_2 are hardly shifted at all.

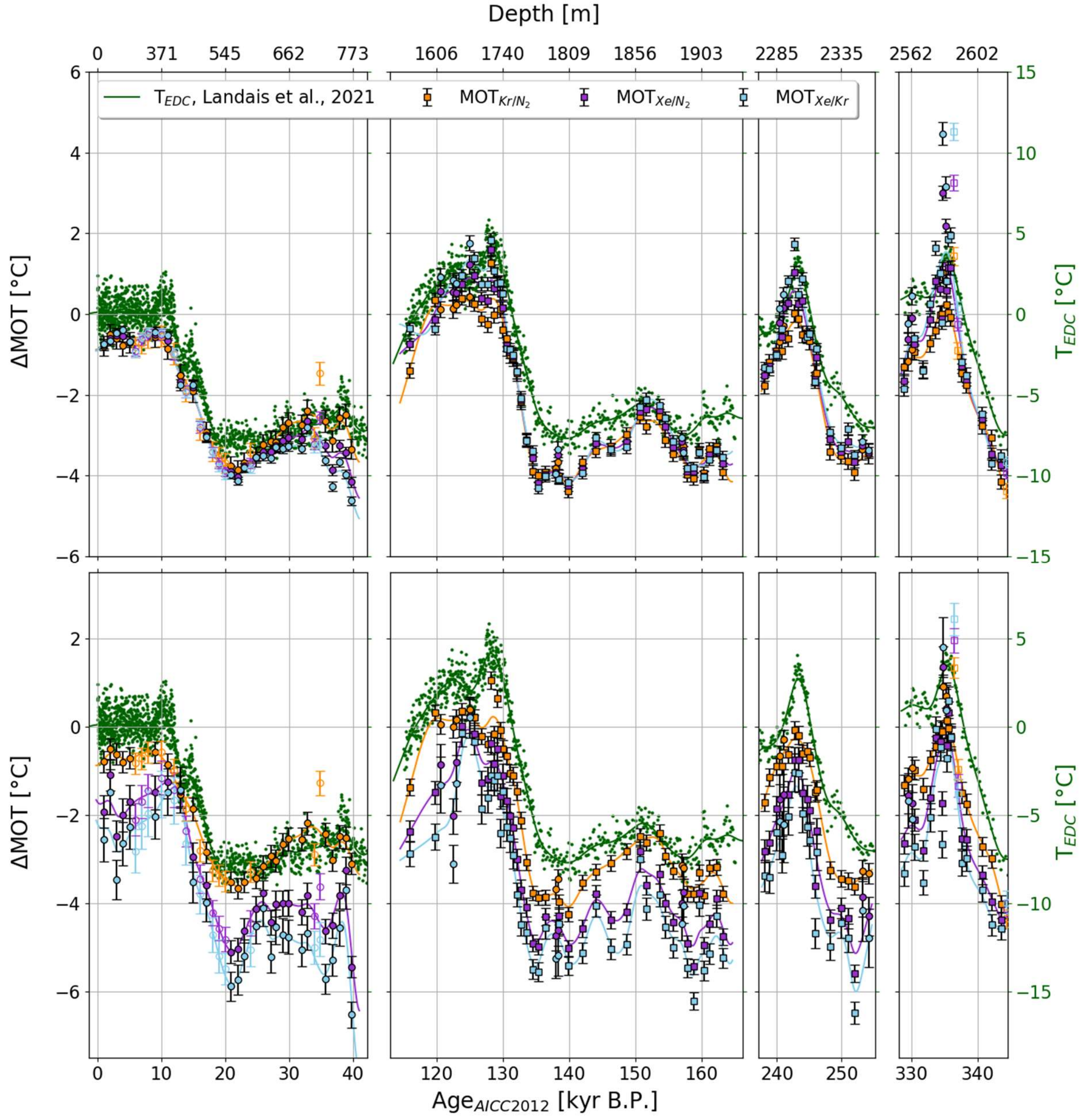

Figure 3.17.: ΔMOT based on noble-gas ratios that have been corrected for gravitational enrichment only, using $\delta^{40/36}$Ar. The datapoints in the lower panel have additionally been corrected for thermal diffusion, using ΔT_{iso}. No correction for kinetic fractionation was applied. For orientation, EDC site temperature from Landais et al., 2021 is plotted alongside the MOT data. Shapes and fillings of markers and lines are the same as in Figure 3.1.

Gravitational and thermal fractionation alone are unable to explain the differences we find between isotope ratios of different gas species (Figure 3.6.), pointing towards a second-order fractionation effect in the firn. As seen in Section 3.2., kinetic fractionation can explain the observed heavy isotope deficit at the bottom of the firn column (Figure 3.7.). Thus, a kinetic fractionation correction is required to account for the missing heavy noble gases at the bottom of the firn column. It thereby also leads to elevated δXe/N$_2$, δKr/N$_2$, and δXe/Kr.

How much the noble-gas ratios are increased by the kinetic fractionation correction is decided by three factors. Firstly, the strength of kinetic fractionation, which is determined from the difference in isotopic ratios of different gas species. It should be noted that kinetic fractionation strength is strongly influenced by ΔT. For negative ΔT, heavy isotopes are drawn to the colder, upper end of the firn column. Temperature sensitivity of lighter gases is typically higher, such that δ^{15}N$_2$ gets more enriched at the colder end of the firn column than δ$^{40/36}$Ar (and even more than δKr and δXe). Hence, a more negative ΔT leads to an increase in kinetic fractionation strength and, thus, a higher kinetic fractionation correction. Between modelled ΔT and isotope-based ΔT lies almost a factor of 2 in reconstructed kinetic fractionation strength (Figure 3.7.). The second factor affecting the size of the kinetic fractionation correction are the kinetic fractionation factors, which are obtained from a 2D firn model (Birner et al., 2018). The fractionation factor is highest for δXe/Kr and lowest for δKr/N$_2$. Finally, kinetic fractionation correction is influenced by the conversion rate from atmospheric ratio to MOT, which is largest for δKr/N$_2$ and smallest for δXe/N$_2$ (Figure 3.11.).

The kinetic fractionation correction also has a secondary effect on MOT. As kinetic fractionation correction increases isotopic ratios of heavy noble gases, it also increases the gravitational fractionation correction based on Ar, Kr, or Xe isotopes, thereby decreasing MOT. The contribution is largest if gravitational fractionation were to be corrected with δXe. For our choice of using δ$^{40/36}$Ar, the effect is relatively small. Nonetheless, this secondary aspect partly compensates for the increase in reconstructed MOT caused by the direct effect of the kinetic fractionation correction on elemental ratios. The combined effects of the kinetic fractionation correction on MOT can be found in Figure 3.18. For our choice of using $\varepsilon^{*}_{\overline{Ar-N_2}}$, MOT is increased by about 3.7 °C, 4.7 °C, and 5.5 °C for δKr/N$_2$, δXe/N$_2$, and δXe/Kr, respectively. Thus, kinetic fractionation correction leads to better agreement between reconstructed isotopic ratios but yields too warm MOT.

For completeness, the effects of the fourth correction we apply to our measured firn ratios should also be mentioned. The Ar-outgassing correction increases δ$^{40/36}$Ar to compensate for the geological outgassing of ^{40}Ar. It thereby affects all three fractionation corrections: it increases the gravitational fractionation correction, leads to more negative ΔT, and increases kinetic fractionation strength. The correction is negligible for samples from Termination I but gets more sizable the older the sample is. Using the outgassing rate determined by Bender et al., 2008, this correction reduces MOT by about 0.2 °C for samples from MIS 9e.

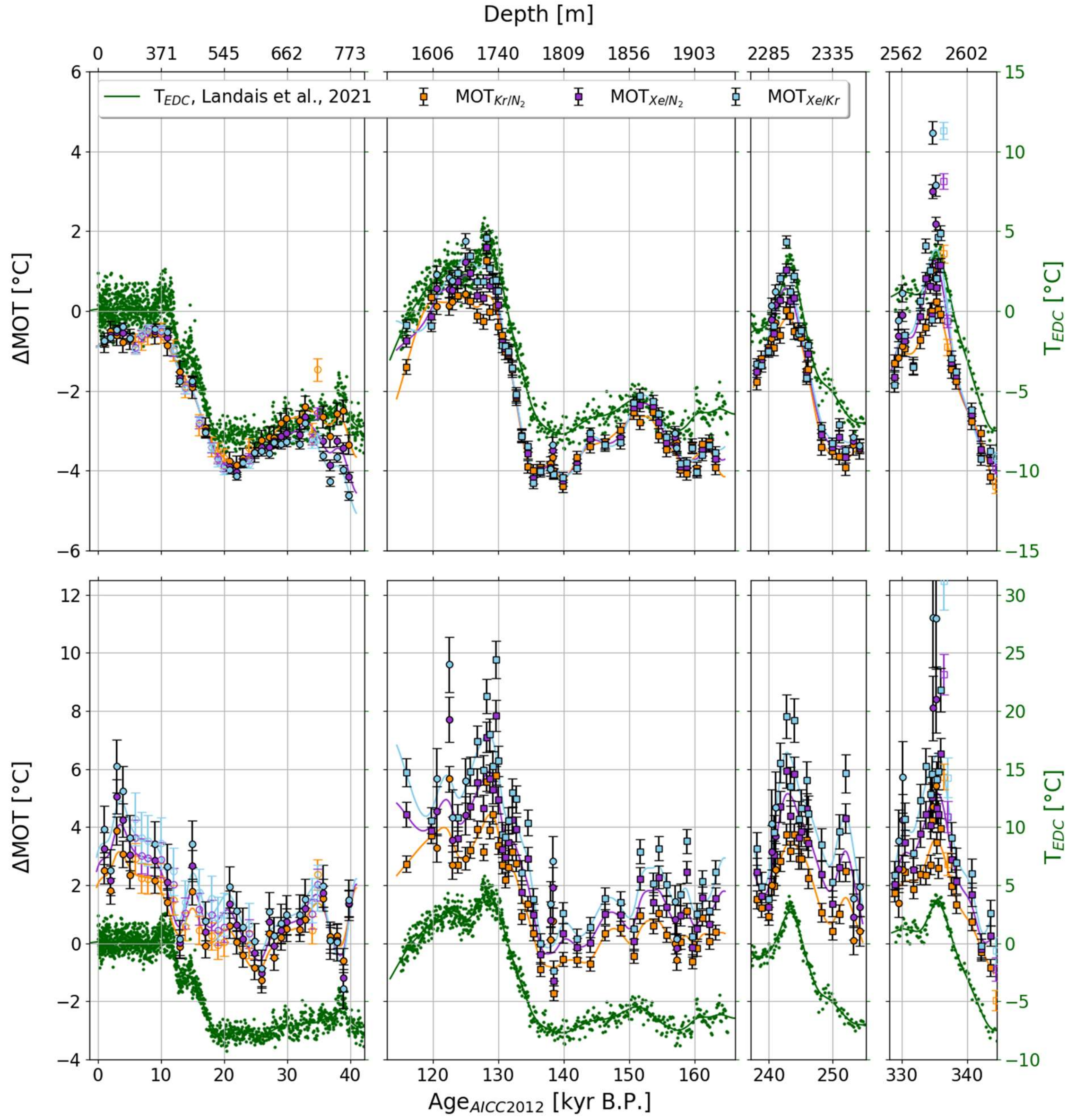

Figure 3.18.: ΔMOT based on noble-gas ratios that have been corrected for gravitational enrichment only, using $\delta^{40/36}Ar$*. The datapoints in the lower panel have additionally been corrected for kinetic fractionation, using* $\varepsilon^{*}_{\overline{Ar-N_2}}$*. No correction for thermal diffusion was applied. For orientation, EDC site temperature from Landais et al., 2021 is plotted alongside the MOT data. Shapes and fillings of markers and lines are the same as in Figure 3.1.*

3.5.2. Potential missed firn fractionation processes

3.5.2.a. Water vapour transport

Air sampled in sand dunes shows depleted values of N_2 and O_2 isotopic ratios (Severinghaus et al., 1996). The authors of the study suggest that this is due to a diffusive flux of water vapour out of the dune, which drags along other gases and thereby forces them to diffuse back into the dune. Due to their lower diffusivities, heavier isotopes diffuse back more slowly, resulting in a steady-state depletion. The same, but due to the low absolute water vapor content at ice sheet temperatures reduced, effect may occur in the porous firn column of polar ice sheets, where seasonal temperature variations in the top ~20 m of the firn column and to a lesser extent the top−bottom firn temperature difference lead to different water vapour pressures and, thus, possibly a fractionation induced by water vapour transport.

The water vapour transport effect can be calculated as follows (Severinghaus et al., 1996):

$$\delta_{i/j} = \left[\left(\frac{1-x_{H_2O}(T_1)}{1-x_{H_2O}(T_2)}\right)^{\left(D_{j,H_2O}/D_{i,H_2O}\right)-1} - 1\right] \cdot 10^3\ ‰ \qquad (3.30.)$$

In the above equation, $x_{H_2O}(T)$ is the water vapour pressure at temperature T and D_{i,H_2O} is the binary diffusion coefficient of gas i into water. Vapour pressure over ice is calculated using the Magnus formula:

$$x_{H_2O}(T) = 6.112\, mbar \cdot \exp\left(\frac{22.46\,°C \cdot T}{272.62\,°C + T}\right) \cdot 10^{-3};\ -65\,°C \leq T \leq 0\,°C \qquad (3.31.)$$

The factor of 10^{-3} transforms from units of mbar to mole fraction.

The diffusivity ratios $D_{j,H_2O}/D_{i,H_2O}$ required in (3.30.) can be found in Table 3.1. for selected isotopic and elemental ratios. They are a function of molecular mass only (Reid, et al., 1977):

$$D_{j,H_2O}/D_{i,H_2O} = \left[\frac{\frac{m_j+m_{H_2O}}{m_j \cdot m_{H_2O}}}{\frac{m_i+m_{H_2O}}{m_i \cdot m_{H_2O}}}\right]^{0.5} \qquad (3.32.)$$

At Dome C, surface summer temperatures may reach about −25 °C, i.e., about 30 °C more than the average temperature of the firn column. In that case, the vapour pressure ratio equals to ~0.99939, resulting in a vapour transport effect on $\delta^{15}N_2$ of about 4 per meg. For $\delta^{40/36}Ar$, an effect of roughly 2.5 per meg per unit mass occurs. The effect on $\delta Xe/N_2$ is about 123 per meg, that on $\delta Kr/N_2$ ~100 per meg, and that on $\delta Xe/Kr$ only about 20 per meg. The resulting difference between $\delta^{15}N_2$ and $\delta^{40/36}Ar$ of about 1.5 per meg translates into an overestimation of the average ΔT of roughly 0.3 °C. Thus, during the warmest two months of the year, water vapour transport may lead to a fractionation of isotopic and elemental ratios on the order of our analytical precision. This fractionation is not compensated during the rest of the year, as vapour transport is essentially non-existent in winter. However, as such a strong water vapour transport only occurs during the two warmest months of the year, it should only have a minor effect on measured ratios. In terms of the average top−bottom firn temperature difference, the water vapour transport effect is negligible. Assuming an extreme case of a top−bottom temperature gradient of −5 °C, i.e., −55 °C at the top, −50 °C at the bottom of the firn column, the water vapour transport effect for $\delta^{15}N_2$ is about 0.1 per meg. In summary, fractionation associated to water vapour transport cannot explain the observed Holocene offsets but might be able to explain some of the offset between the three MOT curves.

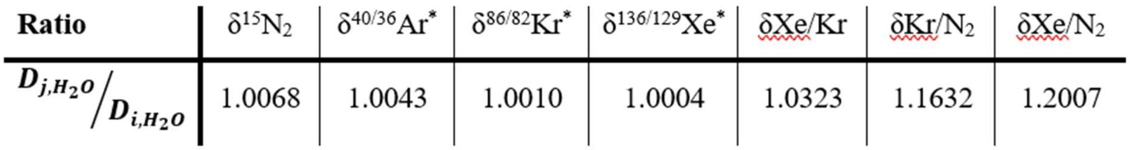

Ratio	$\delta^{15}N_2$	$\delta^{40/36}Ar^*$	$\delta^{86/82}Kr^*$	$\delta^{136/129}Xe^*$	$\delta Xe/Kr$	$\delta Kr/N_2$	$\delta Xe/N_2$
$D_{j,H_2O}/D_{i,H_2O}$	1.0068	1.0043	1.0010	1.0004	1.0323	1.1632	1.2007

Table 3.1: Diffusivity ratios for selected isotopic and elemental ratios.

3.5.2.b. Mischaracterisation of kinetic fractionation

Kinetic fractionation explains the heavy isotope deficit we observe for our samples (Figure 3.7.). However, when applied to elemental ratios, correction for kinetic fractionation yields too warm MOT (Figures 3.13., 3.18.). In her PhD-thesis, Shackleton, 2019 performed dedicated experiments to study this decoupling of the noble-gas content found in ice samples from that of the past atmosphere. To do so, she compared reconstructed MOT based on noble-gas ratios measured in firn air and in near-surface air samples for a variety of sites in Antarctica and Greenland, using different sets of firn fractionation corrections. She found that, while adding a correction for kinetic fractionation performs best for firn samples by yielding Holocene offsets close to 0 for all sites, it leads to artefacts in near-surface ice samples. These artefacts appear to be site-specific with samples from cold, low accumulation sites yielding the largest positive biases in MOT, in line with our findings for EDC. Interestingly, the ordering of the biases was largely independent of the chosen set of firn fractionation corrections. Shackleton, 2019 concluded that this may indicate that the process responsible for the biases only affects elemental ratios, whereas isotopic ratios are unaffected.

As discussed in Section 3.5.1., the positive bias in absolute MOT at EDC is caused by the kinetic fractionation correction of elemental ratios, which is partly compensated by the kinetic fractionation correction of isotopic ratios. If kinetic fractionation factors of elemental ratios were to be different from what is suggested by firn modelling (Birner et al., 2018), the Holocene offset and systematic offsets between MOT values derived from the three noble-gas ratios could be explained. However, in our current understanding, kinetic fractionation of elemental ratios is a precondition for kinetic fractionation of isotopic ratios. It is the lower diffusivity of heavier gases that causes them to be further away from diffusive equilibrium and, thus, reduces the size of their gravitational and thermal fractionation. This effectively reduced diffusive column height of heavier gas species causes unit mass isotopic ratios of these gases to be less enriched than those of faster diffusing gases. Considering the excellent agreement between kinetic fractionation factors calculated from isotopic ratios measured at EDC and those suggested by a 2D firn model (Birner et al., 2018), major flaws in the modelled kinetic fractionation factors of isotope ratios seem unlikely.

However, although firn models accurately explain the observed differences between isotope ratios, they underestimate the absolute value of kinetic fractionation (Birner et al., 2018). Such a mischaracterisation might be due to our incomplete understanding of firn fractionating processes, thus limiting model performance, but may also be the result of a firn air sampling artefact and, thus, wrong model input. Indeed, when choosing the kinetic fractionation factors of elemental ratios such as to minimize the Holocene offset of the three noble-gas ratios, the agreement between the three ratios is good during most periods (Figure 3.19.). However, there are considerable systematic differences between the three ratios for interglacial periods prior to the Holocene. Thus, we stick to the fractionation factors for elemental ratios suggested by Birner et al., 2018. Nonetheless, in the last paragraphs of this chapter, we summarise processes mentioned in the literature that have the potential to lead to a different perceived kinetic fractionation of elemental ratios.

Battle and Severinghaus, 2006 analysed firn air from two sampling campaigns that took place at Siple Dome and South Pole in 1996 and 2001, respectively. In the South Pole data, they found that $\delta Kr/N_2$ was in good agreement with their firn model prediction, indicating that gravitational fractionation could explain most of the observed fractionation. However, $\delta Xe/N_2$ was enriched by several permille relative to the model. This enrichment was larger towards the bottom of the firn column. The authors speculated that this enrichment might be due to the formation of a Xe-H_2O complex, which has greater mass and would thus be more strongly affected by gravitational settling than Xe (Severinghaus and Battle, 2006). This excess in δXe/N_2 and by consequence also in δXe/Kr relative to δKr/N_2 is observed in data from WAIS Divide (Bereiter et al., 2018b) and Taylor Glacier (Shackleton et al., 2020), although the effect is not large. At EDC, the effect is more pronounced (Figure 3.9.). However, in addition to δXe/N_2 and δXe/Kr, δKr/N_2 is also strongly enriched. Although no anomaly in δKr/N_2 was recorded at South Pole, a Kr-H_2O complex might be able to form under EDC temperature conditions. Also, due to its higher conversion rate from atmospheric ratio to MOT (Figure 3.11.), the anomaly in δKr/N_2 does not have to be as strong as the one in δXe/N_2 and δXe/Kr. Thus, formation of H_2O complexes may serve as a potential explanation for the Holocene offsets and between-ratio offsets of MOT, but so far lack an experimental proof of their existence.

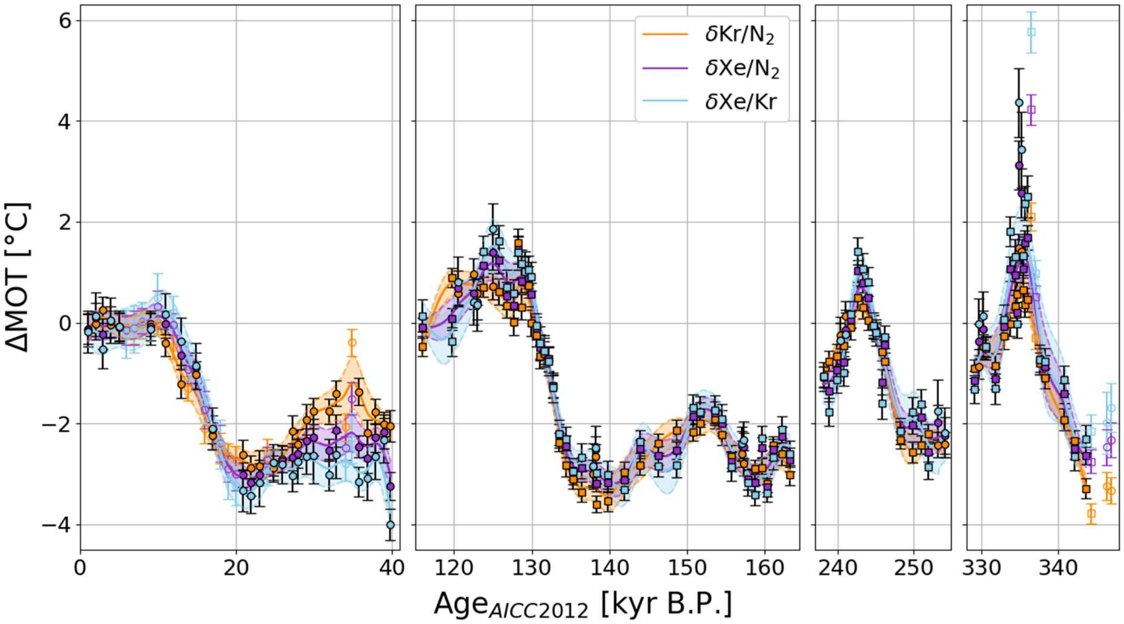

Figure 3.19.: Termination I–IV ΔMOT based on noble-gas ratios from the EDC ice core. Ratios were corrected for gravitational enrichment, thermal diffusion, and kinetic fractionation using $\delta^{40/36}Ar$, $\Delta T_{\overline{iso}}$, *and* $\varepsilon^*_{\overline{Ar-N_2}}$, *respectively. Kinetic fractionation factors for elemental ratios were adjusted such as to minimize the Holocene offset. Shapes and fillings of markers are the same as in Figure 3.1, lines and shading are the same as in Figure 3.13.*

Dispersion is the main mode of gas transport in the deep firn, where it leads to kinetic fractionation (Buizert and Severinghaus, 2016). However, dispersive flow may also cause artefacts when sampling firn air from these depths. One way this may occur is if there happens to be a bias towards sampling firn air from low-tortuosity pathways, in which dispersive mixing is reduced (Shackleton, 2019). If this were the case, the sampled firn air would not see the full degree of kinetic fractionation found in ice samples, which integrate over all pockets. This may explain the underestimation of kinetic fractionation strength by firn models trained on firn air data (Birner et al., 2018), which may, thus, yield kinetic fractionation factors that only apply to the sampled firn air composition. A similar effect would be expected if there happened to be adsorption of heavy noble gases onto the ice surface within the firn (Shackleton, 2019). The adsorbed noble gases would not be included in sampled firn air, thus, leading to too high kinetic fractionation factors of elemental ratios derived by firn models. Also, adsorption of heavy noble gases would preferentially occur at colder sites, which is consistent with the positively biased MOT we find at EDC.

All processes mentioned here must stay hypotheses for now as we are lacking appropriate firn air data for EDC, which would be required to test any of these hypotheses and to test whether there indeed exists a seasonal rectification of the thermal signal at Dome C as suggested by our isotope data (Figure 3.5.). However, there are ongoing efforts to get a better understanding of Dome C firn processes. In 2022, a year-round sampling campaign of the upper 20 m of the firn column took place at Dome C. Furthermore, the entire firn column was sampled at Little Dome C, the European site for oldest ice drilling located some 30 km to the South of Dome C, in the summer season 2022/23. The sampled flasks are currently being analysed at LSCE in Paris and will undergo further noble gas analysis here in Bern in 2024.

References

Baggenstos, D., Häberli, M., Schmitt, J., Shackleton, S.A., Birner, B., Severinghaus, J.P., Kellerhals, T., Fischer, H., 2019. Earth's radiative imbalance from the Last Glacial Maximum to the present. Proc Natl Acad Sci USA 116, 14881–14886. https://doi.org/10.1073/pnas.1905447116

Battle, M.O., Severinghaus, J.P., Sofen, E.D., Plotkin, D., Orsi, A.J., Aydin, M., Montzka, S.A., Sowers, T., Tans, P.P., 2011. Controls on the movement and composition of firn air at the West Antarctic Ice Sheet Divide. Atmos. Chem. Phys. 11, 11007–11021. https://doi.org/10.5194/acp-11-11007-2011

Bender, M.L., Barnett, B., Dreyfus, G., Jouzel, J., Porcelli, D., 2008. The contemporary degassing rate of 40Ar from the solid Earth. Proceedings of the National Academy of Sciences 105, 8232–8237. https://doi.org/10.1073/pnas.0711679105

Bender, M.L., Floch, G., Chappellaz, J., Suwa, M., Barnola, J.-M., Blunier, T., Dreyfus, G., Jouzel, J., Parrenin, F., 2006. Gas age–ice age differences and the chronology of the Vostok ice core, 0–100 ka. J. Geophys. Res. 111, D21115. https://doi.org/10.1029/2005JD006488

Bereiter, B., Kawamura, K., Severinghaus, J.P., 2018a. New methods for measuring atmospheric heavy noble gas isotope and elemental ratios in ice core samples. Rapid Commun Mass Spectrom 32, 801–814. https://doi.org/10.1002/rcm.8099

Bereiter, B., Shackleton, S., Baggenstos, D., Kawamura, K., Severinghaus, J., 2018b. Mean global ocean temperatures during the last glacial transition. Nature 553, 39–44. https://doi.org/10.1038/nature25152

Birner, B., Buizert, C., Wagner, T.J.W., Severinghaus, J.P., 2018. The influence of layering and barometric pumping on firn air transport in a 2-D model. The Cryosphere 12, 2021–2037. https://doi.org/10.5194/tc-12-2021-2018

Buizert, C., 2021. The Ice Core Gas Age-Ice Age Difference as a Proxy for Surface Temperature. Geophysical Research Letters 48, e2021GL094241. https://doi.org/10.1029/2021GL094241

Buizert, C., Fudge, T.J., Roberts, W.H.G., Steig, E.J., Sherriff-Tadano, S., Ritz, C., Lefebvre, E., Edwards, J., Kawamura, K., Oyabu, I., Motoyama, H., Kahle, E.C., Jones, T.R., Abe-Ouchi, A., Obase, T., Martin, C., Corr, H., Severinghaus, J.P., Beaudette, R., Epifanio, J.A., Brook, E.J., Martin, K., Chappellaz, J., Aoki, S., Nakazawa, T., Sowers, T.A., Alley, R.B., Ahn, J., Sigl, M., Severi, M., Dunbar, N.W., Svensson, A., Fegyveresi, J.M., He, C., Liu, Z., Zhu, J., Otto-Bliesner, B.L., Lipenkov, V.Y., Kageyama, M., Schwander, J., 2021. Antarctic surface temperature and elevation during the Last Glacial Maximum. Science 372, 1097–1101. https://doi.org/10.1126/science.abd2897

Buizert, C., Martinerie, P., Petrenko, V.V., Severinghaus, J.P., Trudinger, C.M., Witrant, E., Rosen, J.L., Orsi, A.J., Rubino, M., Etheridge, D.M., Steele, L.P., Hogan, C., Laube, J.C., Sturges, W.T., Levchenko, V.A., Smith, A.M., Levin, I., Conway, T.J., Dlugokencky, E.J., Lang, P.M., Kawamura, K., Jenk, T.M., White, J.W.C., Sowers, T., Schwander, J., Blunier, T., 2012. Gas transport in firn: multiple-tracer characterisation and model intercomparison for NEEM, Northern Greenland. Atmos. Chem. Phys. 12, 4259–4277. https://doi.org/10.5194/acp-12-4259-2012

Buizert, C., Severinghaus, J.P., 2016. Dispersion in deep polar firn driven by synoptic-scale surface pressure variability. The Cryosphere 10, 2099–2111. https://doi.org/10.5194/tc-10-2099-2016

Buizert, C., Shackleton, S., Severinghaus, J.P., Roberts, W.H.G., Seltzer, A., Bereiter, B., Kawamura, K., Baggenstos, D., Orsi, A.J., Oyabu, I., Birner, B., Morgan, J.D., Brook, E.J., Etheridge, D.M., Thornton, D., Bertler, N., Pyne, R.L., Mulvaney, R., Mosley-Thompson, E., Neff, P.D., Petrenko, V.V., 2023. The new Kr-86 excess ice core proxy for synoptic activity: West Antarctic storminess possibly linked to Intertropical Convergence Zone (ITCZ) movement through the last deglaciation. Clim. Past 19, 579–606. https://doi.org/10.5194/cp-19-579-2023

Buizert, C., Sowers, T., Blunier, T., 2013. Assessment of diffusive isotopic fractionation in polar firn, and application to ice core trace gas records. Earth and Planetary Science Letters 361, 110–119. https://doi.org/10.1016/j.epsl.2012.11.039

Colbeck, S.C., 1989. Air Movement in Snow Due to Windpumping. J. Glaciol. 35, 209–213. https://doi.org/10.3189/S0022143000004524

Craig, H., Horibe, Y., Sowers, T., 1988. Gravitational Separation of Gases and Isotopes in Polar Ice Caps. Science 242, 1675–1678. https://doi.org/10.1126/science.242.4886.1675

Craig, H., Wiens, R.C., 1996. Gravitational Enrichment of 84Kr/36Ar Ratios in Polar Ice Caps: A Measure of Firn Thickness and Accumulation Temperature. Science 271, 1708–1709.

Cuffey, K.M., Paterson, W.S.B., 2010. The physics of glaciers, 4. ed. ed. Butterworth-Heineman, Amsterdam Heidelberg.

Dahl-Jensen, D., 1989. Steady thermomechanical flow along two-dimensional flow lines in large grounded ice sheets. Journal of Geophysical Research: Solid Earth 94, 10355–10362. https://doi.org/10.1029/JB094iB08p10355

Elderfield, H., Ferretti, P., Greaves, M., Crowhurst, S., McCave, I.N., Hodell, D., Piotrowski, A.M., 2012. Evolution of Ocean Temperature and Ice Volume Through the Mid-Pleistocene Climate Transition. Science 337, 704–709. https://doi.org/10.1126/science.1221294

Extier, T., Landais, A., Bréant, C., Prié, F., Bazin, L., Dreyfus, G., Roche, D.M., Leuenberger, M., 2018. On the use of δ18Oatm for ice core dating. Quaternary Science Reviews 185, 244–257. https://doi.org/10.1016/j.quascirev.2018.02.008

Grachev, A.M., Severinghaus, J.P., 2003a. Determining the Thermal Diffusion Factor for ^{40} Ar/ ^{36} Ar in Air To Aid Paleoreconstruction of Abrupt Climate Change. J. Phys. Chem. A 107, 4636–4642. https://doi.org/10.1021/jp027817u

Grachev, A.M., Severinghaus, J.P., 2003b. Laboratory determination of thermal diffusion constants for 29N2/28N2 in air at temperatures from −60 to 0°C for reconstruction of magnitudes of abrupt climate changes using the ice core fossil–air paleothermometer. Geochimica et Cosmochimica Acta 67, 345–360. https://doi.org/10.1016/S0016-7037(02)01115-8

Grant, K.M., Rohling, E.J., Bar-Matthews, M., Ayalon, A., Medina-Elizalde, M., Ramsey, C.B., Satow, C., Roberts, A.P., 2012. Rapid coupling between ice volume and polar temperature over the past 150,000 years. Nature 491, 744–747. https://doi.org/10.1038/nature11593

Grant, K.M., Rohling, E.J., Ramsey, C.B., Cheng, H., Edwards, R.L., Florindo, F., Heslop, D., Marra, F., Roberts, A.P., Tamisiea, M.E., Williams, F., 2014. Sea-level variability over five glacial cycles. Nat Commun 5, 5076. https://doi.org/10.1038/ncomms6076

Haeberli, M., Baggenstos, D., Schmitt, J., Grimmer, M., Michel, A., Kellerhals, T., Fischer, H., 2021. Snapshots of mean ocean temperature over the last 700 000 years using noble gases in the EPICA Dome C ice core. Clim. Past 17, 843–867. https://doi.org/10.5194/cp-17-843-2021

Hamme, R.C., Nicholson, D.P., Jenkins, W.J., Emerson, S.R., 2019. Using Noble Gases to Assess the Ocean's Carbon Pumps. Annu. Rev. Mar. Sci. 11, 75–103. https://doi.org/10.1146/annurev-marine-121916-063604

Headly, M.A., 2008. Krypton and xenon in air trapped in polar ice cores: Paleo-atmospheric measurements for estimating past mean ocean temperature and summer snowmelt frequency (diss.). University of California, San Diego.

Herron, M.M., Langway, C.C., 1980. Firn Densification: An Empirical Model. J. Glaciol. 25, 373–385. https://doi.org/10.3189/S0022143000015239

Hörhold, M.W., Laepple, T., Freitag, J., Bigler, M., Fischer, H., Kipfstuhl, S., 2012. On the impact of impurities on the densification of polar firn. Earth and Planetary Science Letters 325–326, 93–99. https://doi.org/10.1016/j.epsl.2011.12.022

Huber, C., Beyerle, U., Leuenberger, M., Schwander, J., Kipfer, R., Spahni, R., Severinghaus, J.P., Weiler, K., 2006a. Evidence for molecular size dependent gas fractionation in firn air derived from noble gases, oxygen, and nitrogen measurements. Earth and Planetary Science Letters 243, 61–73. https://doi.org/10.1016/j.epsl.2005.12.036

Huber, C., Leuenberger, M., Spahni, R., Flückiger, J., Schwander, J., Stocker, T.F., Johnsen, S., Landais, A., Jouzel, J., 2006b. Isotope calibrated Greenland temperature record over Marine Isotope Stage 3 and its relation to CH4. Earth and Planetary Science Letters 243, 504–519. https://doi.org/10.1016/j.epsl.2006.01.002

Jouzel, J., Masson-Delmotte, V., Cattani, O., Dreyfus, G., Falourd, S., Hoffmann, G., Minster, B., Nouet, J., Barnola, J.M., Chappellaz, J., Fischer, H., Gallet, J.C., Johnsen, S., Leuenberger, M., Loulergue, L., Luethi, D., Oerter, H., Parrenin, F., Raisbeck, G., Raynaud, D., Schilt, A., Schwander, J., Selmo, E., Souchez, R., Spahni, R., Stauffer, B., Steffensen, J.P., Stenni, B., Stocker, T.F., Tison, J.L., Werner, M., Wolff, E.W., 2007. Orbital and Millennial Antarctic Climate Variability over the Past 800,000 Years. Science 317, 793–796. https://doi.org/10.1126/science.1141038

Kahle, E.C., Steig, E.J., Jones, T.R., Fudge, T.J., Koutnik, M.R., Morris, V.A., Vaughn, B.H., Schauer, A.J., Stevens, C.M., Conway, H., Waddington, E.D., Buizert, C., Epifanio, J., White, J.W.C., 2021. Reconstruction of Temperature, Accumulation Rate, and Layer Thinning From an Ice Core at South Pole, Using a Statistical Inverse Method. Journal of Geophysical Research: Atmospheres 126, e2020JD033300. https://doi.org/10.1029/2020JD033300

Kaspers, K.A., van de Wal, R.S.W., van den Broeke, M.R., Schwander, J., van Lipzig, N.P.M., Brenninkmeijer, C. a. M., 2004. Model calculations of the age of firn air across the Antarctic continent. Atmospheric Chemistry and Physics 4, 1365–1380. https://doi.org/10.5194/acp-4-1365-2004

Kawamura, K., Severinghaus, J.P., Albert, M.R., Courville, Z.R., Fahnestock, M.A., Scambos, T., Shields, E., Shuman, C.A., 2013. Kinetic fractionation of gases by deep air convection in polar firn. Atmos. Chem. Phys. 13, 11141–11155. https://doi.org/10.5194/acp-13-11141-2013

Kawamura, K., Severinghaus, J.P., Ishidoya, S., Sugawara, S., Hashida, G., Motoyama, H., Fujii, Y., Aoki, S., Nakazawa, T., 2006. Convective mixing of air in firn at four polar sites. Earth and Planetary Science Letters 244, 672–682. https://doi.org/10.1016/j.epsl.2006.02.017

Kobashi, T., Severinghaus, J.P., Brook, E.J., Barnola, J.-M., Grachev, A.M., 2007. Precise timing and characterization of abrupt climate change 8200 years ago from air trapped in polar ice. Quaternary Science Reviews 26, 1212–1222. https://doi.org/10.1016/j.quascirev.2007.01.009

Kobashi, T., Severinghaus, J.P., Kawamura, K., 2008. Argon and nitrogen isotopes of trapped air in the GISP2 ice core during the Holocene epoch (0–11,500 B.P.): Methodology and implications for gas loss processes. Geochimica et Cosmochimica Acta 72, 4675–4686. https://doi.org/10.1016/j.gca.2008.07.006

Lambeck, K., Rouby, H., Purcell, A., Sun, Y., Sambridge, M., 2014. Sea level and global ice volumes from the Last Glacial Maximum to the Holocene. Proceedings of the National Academy of Sciences 111, 15296–15303. https://doi.org/10.1073/pnas.1411762111

Landais, A., Barnola, J.M., Kawamura, K., Caillon, N., Delmotte, M., Van Ommen, T., Dreyfus, G., Jouzel, J., Masson-Delmotte, V., Minster, B., Freitag, J., Leuenberger, M., Schwander, J., Huber, C., Etheridge, D., Morgan, V., 2006. Firn-air δ15N in modern polar sites and glacial–interglacial ice: a model-data mismatch during glacial periods in Antarctica? Quaternary Science Reviews 25, 49–62. https://doi.org/10.1016/j.quascirev.2005.06.007

Landais, A., Stenni, B., Masson-Delmotte, V., Jouzel, J., Cauquoin, A., Fourré, E., Minster, B., Selmo, E., Extier, T., Werner, M., Vimeux, F., Uemura, R., Crotti, I., Grisart, A., 2021. Interglacial Antarctic–Southern Ocean climate decoupling due to moisture source area shifts. Nat. Geosci. 14, 918–923. https://doi.org/10.1038/s41561-021-00856-4

Laskar, J., Robutel, P., Joutel, F., Gastineau, M., Correia, A.C.M., Levrard, B., 2004. A long-term numerical solution for the insolation quantities of the Earth. A&A 428, 261–285. https://doi.org/10.1051/0004-6361:20041335

Lisiecki, L.E., Raymo, M.E., 2005. A Pliocene-Pleistocene stack of 57 globally distributed benthic δ ^{18} O records: PLIOCENE-PLEISTOCENE BENTHIC STACK. Paleoceanography 20, n/a-n/a. https://doi.org/10.1029/2004PA001071

Liu, Z., 2021. Noble Gases as Mean Ocean Temperature Proxies in Preindustrial and Last Glacial Maximum Simulations. University of Bern, Bern.

Loose, B., Jenkins, W.J., 2014. The five stable noble gases are sensitive unambiguous tracers of glacial meltwater: LOOSE AND JENKINS; NOBLE GASES ARE TRACERS OF MELTWATER. Geophys. Res. Lett. 41, 2835–2841. https://doi.org/10.1002/2013GL058804

Loose, B., Jenkins, W.J., Moriarty, R., Brown, P., Jullion, L., Naveira Garabato, A.C., Torres Valdes, S., Hoppema, M., Ballentine, C., Meredith, M.P., 2016. Estimating the recharge properties of the deep ocean using noble gases and helium isotopes. J. Geophys. Res. Oceans 121, 5959–5979. https://doi.org/10.1002/2016JC011809

Michel, A., 2016. Transient Modeling of Borehole Temperature and Basal Melting in an Ice Sheet (Master's Thesis). University of Bern, Bern.

Morgan, J.D., Buizert, C., Fudge, T.J., Kawamura, K., Severinghaus, J.P., Trudinger, C.M., 2022. Gas isotope thermometry in the South Pole and Dome Fuji ice cores provides evidence for seasonal rectification of ice core gas records. The Cryosphere 16, 2947–2966. https://doi.org/10.5194/tc-16-2947-2022

Oyabu, I., Kawamura, K., Uchida, T., Fujita, S., Kitamura, K., Hirabayashi, M., Aoki, S., Morimoto, S., Nakazawa, T., Severinghaus, J.P., Morgan, J.D., 2021. Fractionation of O<sub>2</sub>∕N<sub>2</sub> and Ar∕N<sub>2</sub> in the Antarctic ice sheet during bubble formation and bubble–clathrate hydrate transition from precise gas measurements of the Dome Fuji ice core. The Cryosphere 15, 5529–5555. https://doi.org/10.5194/tc-15-5529-2021

Parrenin, F., Barker, S., Blunier, T., Chappellaz, J., Jouzel, J., Landais, A., Masson-Delmotte, V., Schwander, J., Veres, D., 2012. On the gas-ice depth difference (Δdepth) along the EPICA Dome C ice core (preprint). Proxy Use-Development-Validation/Ice Cores/Pleistocene. https://doi.org/10.5194/cpd-8-1089-2012

Parrenin, F., Jouzel, J., Kawamura, K., Lemieux-Dudon, B., Loulergue, L., Masson-Delmotte, V., Narcisi, B., Raisbeck, G., Raynaud, D., Ruth, U., Schwander, J., Severi, M., Spahni, R., Steffensen, J.P., Svensson, A., Udisti, R., Waelbroeck, C., Wolff, E., 2007. The EDC3 chronology for the EPICA Dome C ice core. Clim. Past 13.

Pöppelmeier, F., Baggenstos, D., Grimmer, M., Liu, Z., Schmitt, J., Fischer, H., Stocker, T.F., 2023. The Effect of Past Saturation Changes on Noble Gas Reconstructions of Mean Ocean Temperature. Geophysical Research Letters 50, e2022GL102055. https://doi.org/10.1029/2022GL102055

Powers, D., O'Neill, K., Colbeck, S.C., 1985. Theory of natural convection in snow. J. Geophys. Res. 90, 10641–10649. https://doi.org/10.1029/JD090iD06p10641

Reid, R.C., Prausnitz, J.M., Sheerwood, T.K., 1977. The Properties of Gases and Liquids, 3rd ed, Chem. Eng. Series. McGraw-Hill, New York.

Ritz, S.P., Stocker, T.F., Severinghaus, J.P., 2011. Noble gases as proxies of mean ocean temperature: sensitivity studies using a climate model of reduced complexity. Quaternary Science Reviews 30, 3728–3741. https://doi.org/10.1016/j.quascirev.2011.09.021

Rohling, E.J., Foster, G.L., Grant, K.M., Marino, G., Roberts, A.P., Tamisiea, M.E., Williams, F., 2014. Sea-level and deep-sea-temperature variability over the past 5.3 million years. Nature 508, 477–482. https://doi.org/10.1038/nature13230

Rohling, E.J., Grant, K., Bolshaw, M., Roberts, A.P., Siddall, M., Hemleben, C., Kucera, M., 2009. Antarctic temperature and global sea level closely coupled over the past five glacial cycles. Nature Geosci 2, 500–504. https://doi.org/10.1038/ngeo557

Rohling, E.J., Yu, J., Heslop, D., Foster, G.L., Opdyke, B., Roberts, A.P., 2021. Sea level and deep-sea temperature reconstructions suggest quasi-stable states and critical transitions over the past 40 million years. Sci. Adv. 7, eabf5326. https://doi.org/10.1126/sciadv.abf5326

Rommelaere, V., Arnaud, L., Barnola, J.-M., 1997. Reconstructing recent atmospheric trace gas concentrations from polar firn and bubbly ice data by inverse methods. J. Geophys. Res. 102, 30069–30083. https://doi.org/10.1029/97JD02653

Schwander, J., 1996. Gas diffusion in firn, in: Chemical Exchange between the Atmosphere and Polar Snow, NATO ASI Series. Series I: Global Environmental Change. Springer-Verlag, Berlin, Heidelberg and New York, pp. 527–540.

Schwander, J., 1989. The transformation of snow to ice and the occlusion of gases. The Environmental Record in Glaciers and Ice Sheets 53–67. https://doi.org/10.48350/161003

Schwander, J., Stauffer, B., Sigg, A., 1988. Air mixing in firn and the age of the air at pore close-off. Annals of Glaciology 10, 141–145.

Seltzer, A.M., Ng, J., Severinghaus, J.P., 2019. Precise determination of Ar, Kr and Xe isotopic fractionation due to diffusion and dissolution in fresh water. Earth and Planetary Science Letters 514, 156–165. https://doi.org/10.1016/j.epsl.2019.03.008

Severinghaus, J., Battle, M., 2006. Fractionation of gases in polar ice during bubble close-off: New constraints from firn air Ne, Kr and Xe observations. Earth and Planetary Science Letters 244, 474–500. https://doi.org/10.1016/j.epsl.2006.01.032

Severinghaus, J.P., Albert, M.R., Courville, Z.R., Fahnestock, M.A., Kawamura, K., Montzka, S.A., Mühle, J., Scambos, T.A., Shields, E., Shuman, C.A., Suwa, M., Tans, P., Weiss, R.F., 2010. Deep air convection in the firn at a zero-accumulation site, central Antarctica. Earth and Planetary Science Letters 293, 359–367. https://doi.org/10.1016/j.epsl.2010.03.003

Severinghaus, J.P., Beaudette, R., Headly, M.A., Taylor, K., Brook, E.J., 2009. Oxygen-18 of O2 Records the Impact of Abrupt Climate Change on the Terrestrial Biosphere. Science 324, 1431–1434. https://doi.org/10.1126/science.1169473

Severinghaus, J.P., Bender, M.L., Keeling, R.F., Broecker, W.S., 1996. Fractionation of soil gases by diffusion of water vapor, gravitational settling, and thermal diffusion. Geochimica et Cosmochimica Acta 60, 1005–1018.

Severinghaus, J.P., Brook, E.J., 1999. Abrupt Climate Change at the End of the Last Glacial Period Inferred from Trapped Air in Polar Ice. Science 286, 930–934. https://doi.org/10.1126/science.286.5441.930

Severinghaus, J.P., Sowers, T., Brook, E.J., Alley, R.B., Bender, M.L., 1998. fractionated gases in polar ice 391, 6.

Shackleton, S., 2019. Tracking Past Changes in Ocean Heat Content with Atmospheric Noble Gases in Ice Cores. University of California, San Diego.

Shackleton, S., Baggenstos, D., Menking, J.A., Dyonisius, M.N., Bereiter, B., Bauska, T.K., Rhodes, R.H., Brook, E.J., Petrenko, V.V., McConnell, J.R., Kellerhals, T., Häberli, M., Schmitt, J., Fischer, H., Severinghaus, J.P., 2020. Global ocean heat content in the Last Interglacial. Nat. Geosci. 13, 77–81. https://doi.org/10.1038/s41561-019-0498-0

Shackleton, S., Bereiter, B., Baggenstos, D., Bauska, T.K., Brook, E.J., Marcott, S.A., Severinghaus, J.P., 2019. Is the Noble Gas-Based Rate of Ocean Warming During the Younger Dryas Overestimated? Geophys. Res. Lett. 2019GL082971. https://doi.org/10.1029/2019GL082971

Shackleton, S., Menking, J.A., Brook, E., Buizert, C., Dyonisius, M.N., Petrenko, V.V., Baggenstos, D., Severinghaus, J.P., 2021. Evolution of mean ocean temperature in Marine Isotope Stage 4. Clim. Past 17, 2273–2289. https://doi.org/10.5194/cp-17-2273-2021

Shakun, J.D., Lea, D.W., Lisiecki, L.E., Raymo, M.E., 2015. An 800-kyr record of global surface ocean δ 18 O and implications for ice volume-temperature coupling. Earth and Planetary Science Letters 426, 58–68. https://doi.org/10.1016/j.epsl.2015.05.042

Siddall, M., Rohling, E.J., Almogi-Labin, A., Hemleben, C., Meischner, D., Schmelzer, I., Smeed, D.A., 2003. Sea-level fluctuations during the last glacial cycle. Nature 423, 853–858. https://doi.org/10.1038/nature01690

Sowers, T., Bender, M., Raynaud, D., 1989. Elemental and isotopic composition of occluded O2 and N2 in polar ice. Journal of Geophysical Research: Atmospheres 94, 5137–5150. https://doi.org/10.1029/JD094iD04p05137

Sowers, T., Bender, M., Raynaud, D., Korotkevich, Y.S., 1992. δ15N of N2 in air trapped in polar ice: A tracer of gas transport in the firn and a possible constraint on ice age-gas age differences. Journal of Geophysical Research: Atmospheres 97, 15683–15697. https://doi.org/10.1029/92JD01297

Spratt, R.M., Lisiecki, L.E., 2016. A Late Pleistocene sea level stack. Clim. Past 12, 1079–1092. https://doi.org/10.5194/cp-12-1079-2016

Sturges, W.T., McIntyre, H.P., Penkett, S.A., Chappellaz, J., Barnola, J.-M., Mulvaney, R., Atlas, E., Stroud, V., 2001. Methyl bromide, other brominated methanes, and methyl iodide in polar firn air. J. Geophys. Res. 106, 1595–1606. https://doi.org/10.1029/2000JD900511

Weller, G., Schwerdtfeger, P., 1970. Thermal properties and heat transfer processes of the snow of the central Antarctic plateau. International Association of Hydrological Sciences 86, 284–297.

4. Strong influence of millennial-scale variability on mean ocean temperature evolution across the last four glacial terminations

Throughout the Quaternary, Earth's climate system has repeatedly undergone major reorganisations as it transitioned from its cold, glacial state to its warmer, interglacial state. At least within the last 800 thousand years (800 kyr), these glacial terminations have been accompanied by millennial-scale variability, which is believed to be linked to oscillations in ocean circulation, in particular the Atlantic Meridional Overturning Circulation (AMOC; Barker et al., 2019; Barker and Knorr, 2021; Böhm et al., 2015; Cheng et al., 2016; Deaney et al., 2017; McManus et al., 2004). This millennial-scale variability most prominently manifests itself in intermittent slowdowns or reversals of deglacial trends and early interglacial peaks in a variety of climate records (e.g., Bereiter et al., 2015; Cheng et al., 2016; Hodell et al., 2023; Landais et al., 2021; Loulergue et al., 2008). Recent climate modelling results suggest that millennial-scale variations of the AMOC also affect ocean heat content (OHC), one of Earth's two major energy reservoirs on glacial–interglacial timescale (Baggenstos et al., 2019). Under a weak AMOC, poleward heat transport to the North Atlantic is reduced, and instead heat gradually accumulates in the ocean interior (Galbraith et al., 2016; Pedro et al., 2018). Reconstructions of past mean ocean temperature (MOT), which through the water's heat capacity is directly linked to OHC, provide some first support for this mechanism across Termination I and the Last Interglacial (LIG; Bereiter et al., 2018b; Shackleton et al., 2020).

MOT can be reconstructed using noble-gas ratios in polar ice cores (Bereiter et al., 2018a; Headly and Severinghaus, 2007; Ritz et al., 2011). Due to the temperature-dependent solubilities of noble gases in water, atmospheric noble-gas ratios $\delta Kr/N_2$, $\delta Xe/N_2$, and $\delta Xe/Kr$ act as tracer of past changes in MOT and thus OHC. As these atmospheric noble-gas ratios are reconstructed from inclusions of ancient air in ice cores, the resulting record has good age control (Bazin et al., 2013; Veres et al., 2013). Furthermore, as an ice core record, MOT is on the same age scale as other key climate records such as atmospheric CO_2, CH_4, and Antarctic temperature, circumventing the issue of age scale uncertainty, bar some minor uncertainty in ice core gas-ice age difference. Here, we present the first Termination I–IV MOT record from the EPICA Dome C (EDC) ice core, which allows us to study the temporal evolution of the last four glacial–interglacial transitions from an OHC perspective. The record suggests strong influence of AMOC-induced millennial-scale variability on MOT evolution across all four terminations and their subsequent interglacials.

4.1. MOT during Terminations I–IV and their subsequent interglacials

From a MOT perspective, the past four glacial terminations show considerable similarities (Figure 4.1.). During all terminations, MOT increases at similar rates of about 0.5–0.6 °C/kyr. The deglacial increase in MOT is interrupted by brief periods of reduced MOT increase or even short reversals of typically 1–2 kyr. These interruptions are particularly pronounced during the Bølling-Allerød interstadial of Termination I and early in Termination III but can also be found during Terminations II and IV. Furthermore, the ends of Terminations II–IV are marked by a brief peak in MOT, similar to what is found in reconstructions of Antarctic temperature and – even more pronounced – in CO_2 or CH_4 (Figures 4.1., 4.2.) These short-lived peaks at the onset of interglacials are often referred to as overshoots, a terminology which we adopt here. The three overshoots represent the warmest MOT conditions of their respective interglacial and of our record in general.

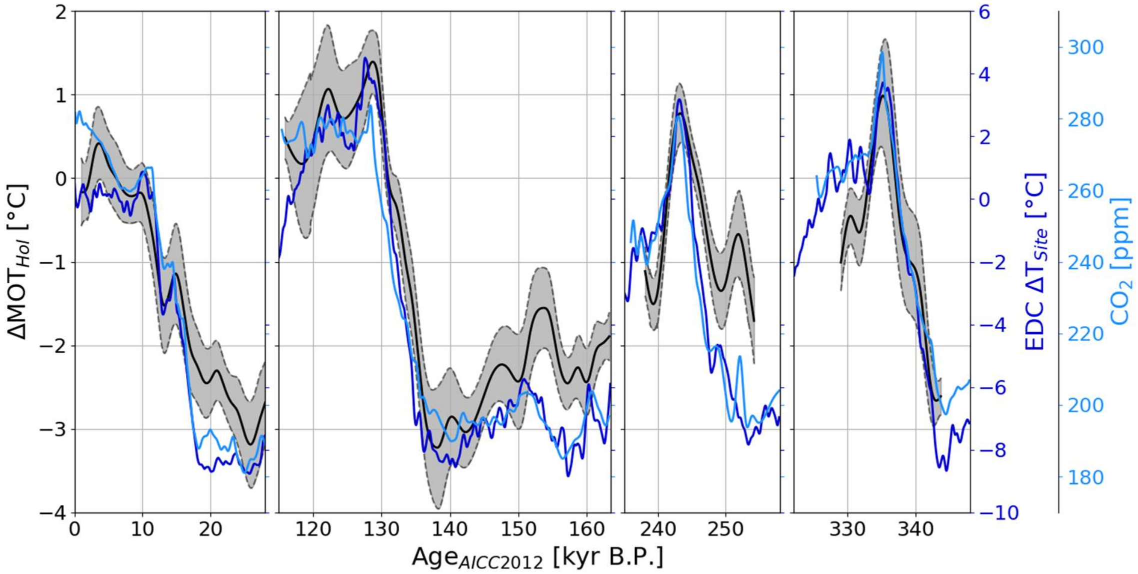

Figure 4.1.: Comparison between our EDC Termination I–IV MOT record, EDC site temperature (Landais et al., 2021), and CO_2 (Bereiter et al., 2015; Nehrbass-Ahles et al., 2020; Shin et al., 2020). The black line and shading indicate the cubic smoothing spline with cutoff frequency of 5 kyr and its 1σ-uncertainty through our reconstructed MOT_{mix} datapoints. For EDC site temperature and CO_2, we show a spline with cutoff frequency of 1 kyr through the original data.

Relative to the Holocene (0–10 kyr, 10 samples), our record suggests MOT of −2.7 ± 0.2 °C during the Last Glacial Maximum (LGM; 18.5–26 kyr, 8 samples), which is consistent with earlier reconstructions (Bereiter et al., 2018b). Our record is also in rough agreement with a previous study on MOT during the LIG, using ice from Taylor Glacier (Shackleton et al., 2020). Our record suggests slightly higher MOT, both during the early overshoot (128–

130 kyr, 5 samples) and during the later stages of the LIG (120–128 kyr, 8 samples) of 1.5 ± 0.2 °C and 0.8 ± 0.2 °C, respectively. The small discrepancy may in part be explained by the use of different sea-level reconstructions (Grant et al., 2014; Shakun et al., 2015), with Shakun et al., 2015 suggesting a later sea-level rise, yielding higher MOT. Consequently, we find a larger glacial–interglacial MOT difference from the penultimate glacial maximum (136–144 kyr, 7 samples) to early LIG conditions of 4.2 ± 0.2 °C, compared to 3.4 ± 0.5 by Shackleton et al., 2020. For Terminations III and IV, no other MOT data exists for comparison. Both terminations produce an overshoot, which feature MOT 1.0 ± 0.3 °C (Marine Isotope Stage (MIS) 7e, 242–244 kyr, 3 samples) and 1.6 ± 0.4 °C (MIS 9e, 334.5–336 kyr, 6 samples) warmer than the Holocene. The later stages of MIS 7e and MIS 9e are considerably colder with MOT of −0.8 ± 0.2 °C (238–242 kyr, 7 samples) and −0.3 ± 0.2 °C (328–334.5 kyr, 8 samples) relative to the Holocene. Furthermore, our record suggests glacial conditions of −1.8 ± 0.4 °C and −2.6 ± 0.2 °C relative to the Holocene for MIS 8 (253–255 kyr, 2 samples) and MIS 10 (341–344 kyr, 2 samples), respectively. However, it is unclear whether these two values represent full glacial maximum conditions; MIS 8 most likely experienced colder MOT at around 270 kyr (Haeberli et al., 2021).

4.2. Close coupling between MOT, Antarctic temperature, and CO_2

Earlier MOT studies have pointed out the strong correlation between MOT, Antarctic temperature, and CO_2 (Bereiter et al., 2018b; Shackleton et al., 2021, 2020, 2019), which can be found during most periods covered by our record (Figure 4.1.). This correlation may be explained in multiple ways (Shackleton et al., 2021). Due to the large volume of the deep ocean, MOT is dominated by DOT, which is largely an integrated sea surface temperature (SST) signal from the deepwater forming high latitudes with contributions from the last ~1.5 kyr (DeVries and Holzer, 2019; Matsumoto, 2007). Thus, changes in MOT are either due to i) a change in high-latitude SST, or ii) a change in ocean water-mass distribution, which may happen in response to changes in the rate of deepwater formation or changes in the density of the two main bodies of deepwater, Antarctic Bottom Water (AABW) and North Atlantic Deep Water (NADW). Today, the deep ocean is dominated by AABW, which is formed around the continental margins of Antarctica and accounts for roughly 65% of the deep ocean volume (Johnson, 2008). Ocean circulation and water mass distribution under glacial conditions is still debated, but was likely characterised by a weakened, more shallow North Atlantic overturning cell (Curry and Oppo, 2005; Skinner et al., 2017) and accordingly a more extensive AABW cell (Yi et al., 2023), or similar to the modern state (Böhm et al., 2015;

Pöppelmeier et al., 2020). Considering this dominant role of AABW, southern Hemisphere high-latitude temperatures may play a key role for setting MOT through their control on Southern Ocean SST and overturning rate (Bereiter et al., 2018b). However, the causality may also run the other way round, as MOT warming is suggested to lead to an enhanced temperature gradient across the Antarctic Circumpolar Current (ACC), increasing the effectiveness of eddy induced stirring and mixing of the signal across the ACC and thereby enhancing poleward heat fluxes with associated Antarctic warming (Pedro et al., 2018).

Alternatively, the link between Antarctic temperature and MOT may also be established through a third variable that controls both parameters, which most likely would be the strength of the AMOC. For Antarctic temperature, the link to AMOC is explained through the well-established thermal bipolar ocean seesaw hypothesis, as proposed by Stocker and Johnsen, 2003. The hypothesis states that the causal link between sharp millennial-scale oscillations observed in Greenland ice cores (e.g., North Greenland Ice Core Project members, 2004) and their more gradual counterparts in Antarctic records (e.g., EPICA community members, 2004) may be found in changes in the rate of cross-equatorial ocean heat exchange in the Atlantic. The warm surface branch of the AMOC transports heat in the form of warm water from the South Atlantic to the North Atlantic, where the water cools and eventually sinks in the deepwater forming regions of the polar North Atlantic to then return south as the cold deep branch of the AMOC. When the AMOC is in a weak state, northward heat transport is subdued, bringing cold stadial climate conditions to Greenland. In the southern hemisphere, heat accumulates, and warmer water masses are brought into the sea ice zone, leading to a slow reduction in Southern Ocean sea ice and, thus, gradual warming in Antarctica (Pedro et al., 2018). Once the AMOC reinvigorates, Antarctica slowly cools again, whereas the North Atlantic region experiences a rapid, strong warming, called Dansgaard-Oeschger (D-O) event, and remains in warm interstadial conditions until AMOC weakens again. Thus, variations in AMOC lead to an anti-phasing of Antarctic and Greenland climate on millennial timescale.

The link between MOT and AMOC strength, which has been suggested by multiple climate models (Galbraith et al., 2016; Pedro et al., 2018), is closely connected to the thermal bipolar seesaw hypothesis. When AMOC is weak, northward oceanic heat transport is reduced and heat instead accumulates in the subsurface Atlantic, where it leads to gradual increase of heat in a southern heat reservoir. This southern heat reservoir was initially suggested to be the Southern Ocean (Stocker and Johnsen, 2003), but more recent findings instead point towards a warming of the global ocean interior north of the ACC (Pedro et al., 2018). This increased subsurface warming more than compensates the surface cooling in the North Atlantic and thereby leads to an increase in OHC. Upon AMOC reinvigoration, the accumulated heat is advected from the ocean interior back up to the surface and radiated to the atmosphere. Indeed, MOT warming has been observed to occur concurrently with periods of weak AMOC (Bereiter et al., 2018b; Shackleton et al., 2020, 2019).

As for CO_2, a high correlation to global temperature is expected, due to its role as one of the two main amplifying climatic feedbacks (the other being albedo), which cause relatively minor and slow, orbital changes in insolation to lead to fast-paced and large amplitude glacial terminations (Rothlisberger et al., 2008; Shakun et al., 2012; Wolff et al., 2009). This strong mechanistic link to global temperatures may explain the tight coupling between CO_2 and MOT, as higher temperatures, in combination with polar amplification, will lead to elevated high-latitude SST and thus an increase in MOT. It is worth noting that the coupling may also run in the opposite direction through the temperature-solubility relationship, i.e., more CO_2 dissolving in a colder ocean. However, glacial–interglacial changes in MOT can only account for a ~30–40 ppm CO_2 change (Shackleton et al., 2021; Williams and Follows, 2011), such that this link cannot explain the full extent of observed CO_2–MOT coupling.

The cause of the tight coupling between CO_2 and the regional temperature signal in Antarctica throughout the last 800 kyr (Bereiter et al., 2015; Lüthi et al., 2008; Petit et al., 1999; Siegenthaler et al., 2005), is likely to be found in high latitude Southern Hemisphere temperature in general and Southern Ocean temperature in particular, which have been shown to evolve in parallel with Antarctic temperature during the last glacial cycle (Shakun et al., 2012). Southern Ocean vertical mixing is believed to be the main mechanism that controls glacial-interglacial variations in CO_2, with a glacial Southern Ocean being more stratified, leading to increased CO_2 sequestration in the deep ocean (Fischer et al., 2010; Köhler and Fischer, 2006; Sigman et al., 2010). With AMOC being one of the likely controls on Southern Ocean upwelling (Anderson et al., 2009; Skinner et al., 2010), variations in the Atlantic overturning circulation may prove to be one of the key mechanisms that explains the high correlation between CO_2, Antarctic temperature, and MOT.

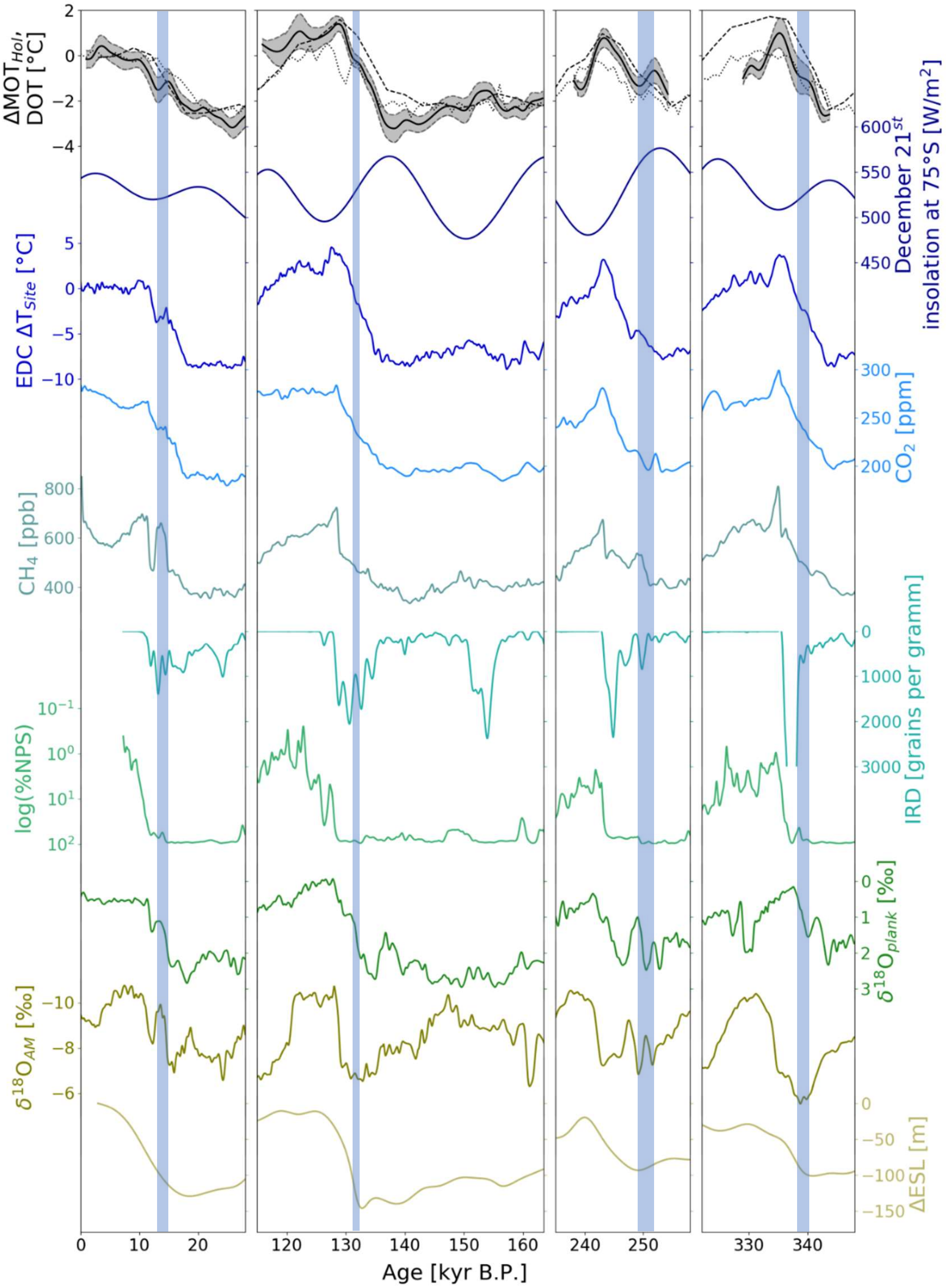

Figure 4.2.: Comparison of our EDC Termination I–IV MOT record to other climate records. From top to bottom, we show MOT with DOT stacks from Shakun et al., 2015 (dashed line) and Rohling et al., 2021 (dotted line); 21st December insolation at 75°S (Laskar et al., 2004); EDC site temperature (Landais et al., 2021); CO_2 (Bereiter et al., 2015; Nehrbass-Ahles et al., 2020; Shin et al., 2020); CH_4 (Loulergue et al., 2008; Nehrbass-Ahles et al., 2020; Schmidely et al., 2021; Shin et al., 2020); IRD and %NPS from ODP site 983, southwest of Iceland (Barker et al., 2015); planktic $\delta^{18}O$ from IODP site U1385 on the Iberian margin (Hodell et al., 2023); the composite record of Eastern Chinese speleothem $\delta^{18}O$ representing Asian summer monsoon strength (Cheng et al., 2016); and eustatic sea level (Shakun et al., 2015; on an adjusted age scale, see Section 3.3.). Periods of reduced deglacial MOT increase are highlighted in blue.

4.3. A tight link between MOT and AMOC

For all past four glacial terminations, periods of reduced MOT warming, and for some even brief episodes of MOT cooling can be found (Figure 4.1). These periods of reduced deglacial MOT warming typically occur concurrently with variations in other climate records that point towards short-term reinvigorations of the AMOC. This has already been pointed out for Termination I, where the Bølling-Allerød interstadial, or rather its Antarctic counterpart, the Antarctic Cold Reversal (ACR), leaves a clear imprint on MOT (Bereiter et al., 2018b; Shackleton et al., 2019). Despite lower temporal resolution, our MOT record clearly captures this major millennial-scale oscillation, which occurs in phase with Antarctic temperature and a concurrent plateau in CO_2. The intermittent strengthening of the AMOC, which is clearly evidenced by Atlantic circulation proxies such as εNd, $^{231}Th/^{230}Pa$, and benthic carbon isotopes (Böhm et al., 2015; Roberts et al., 2010), leaves also clear imprints in other climate records, as for example a major peak in CH_4, warm North Atlantic SST, or strengthened East Asian summer monsoon (Figure 4.2.). Elevated North Atlantic SST are for example indicated by a decrease in the abundance of the polar foraminifera *Neogloboquadrina pachyderma* (%NPS) at ODP site 983 south of Iceland and lighter planktic $\delta^{18}O$ at IODP site U1385 on the Iberian Margin (which in parts may be due to the concurrent sea-level rise). The increased poleward heat transport caused by the AMOC reinvigoration also accentuates the interhemispheric temperature contrast (Broccoli et al., 2006), which leads to a northwards shift of the Intertropical Convergence Zone (ITCZ) and its associated rain belt (Bock et al., 2017; Schmidely et al., 2021). It is this shift in low-latitude precipitation that likely causes an increase in low-latitude wetland emissions recorded in ice core CH_4 records. Finally, through teleconnection, an increase in North Atlantic heat and subsequent reduction in (winter) sea ice extent is thought to cause a shift towards increased East Asian summer monsoon intensity (Cheng et al., 2009). Hence, there is strong evidence for concurrent intermittent AMOC invigoration and MOT reduction during Termination I.

Although largely based on one datapoint, a similarly strong or even stronger MOT reversal as during Termination I is also found during early Termination III at around 252 kyr. However, contrary to Termination I, no concurrent reversal in Antarctic temperature is present. Instead, a reversal in Antarctic temperature only occurs at around 248 kyr, for which we find no counterpart in our MOT record. How can we explain this temporal offset in MOT and Antarctic temperature? The 252 kyr MOT reversal occurs roughly at the same time as a peak in CO_2 (Figure 4.1.), which may point towards increased ventilation of deep, carbon-rich water masses, possibly due to a strengthened AMOC. However, it should be noted that the

Termination III CO_2 record is based on the relatively low-resolution Vostok record (Petit et al., 1999), which potentially suffers from some minor contamination issues (Shin et al., 2020). Recent EDC CO_2 measurements suggest a later and less pronounced CO_2 peak, albeit still earlier than the one in Antarctic temperature (Etienne Legrain, pers. comm.). Nonetheless, likely counterparts to the early Termination III MOT peak can also be found in the Asian monsoon composite record and in Iberian margin planktic $\delta^{18}O$, both of which show a brief excursion towards lighter $\delta^{18}O$ that may match the 252 kyr peak in MOT (Figure 4.2.). Lighter $\delta^{18}O$ in Eastern Chinese speleothem records imply an increase in the East Asian summer monsoon intensity (Cheng et al., 2006), whereas the lighter planktic $\delta^{18}O$ likely suggest higher local SST, as sea-level reconstructions indicate relatively stable seawater $\delta^{18}O$ around that period (e.g., Shakun et al., 2015). Thus, both records may point towards a phase of strengthened AMOC. A strengthened overturning circulation typically leads to a decrease in Antarctic temperature through the bipolar seesaw mechanism (Pedro et al., 2018; Stocker and Johnsen, 2003). However, it is conceivable that the strong Southern Hemisphere high-latitude insolation forcing during that time partly compensated the expected decrease in Antarctic temperature. Furthermore, as we are using EDC site temperature as a proxy for (East) Antarctic temperature, local effects such as ice sheet elevation changes may also play a role. Nonetheless, the absence of an Antarctic temperature counterpart to the relatively strong MOT reversal suggested by our record is surprising. Considering the relatively large spread between MOT derived from the three noble-gas ratios for the datapoint responsible for the large amplitude of the 252 kyr MOT peak (Figure 3.13.), it is possible that the strength of the peak is somewhat overestimated.

The later Termination III reversal in Antarctic temperature at around 248 kyr occurs roughly concurrently with a major peak in atmospheric CH_4 (Figure 4.2.), suggesting an intermittent strengthening of the AMOC. An AMOC reinvigoration is also suggested by a strong peak in Asian summer monsoon intensity around that time. This event has been coined Bølling-Allerød-III due to its similarity to the Termination I Bølling-Allerød interstadial (Cheng et al., 2009). As was already the case for the 252 kyr MOT reversal, the Asian monsoon peak is mirrored in planktic $\delta^{18}O$ at the Iberian margin. Thus, we have multiproxy evidence for an intermittent reinvigoration of the AMOC at around 248 kyr. Considering the strong peak in MOT we observe in response to a suspected minor reinvigoration of the AMOC at around 252 kyr, not finding a MOT reversal at 248 kyr is unexpected. As our record has a 2 kyr sampling gap between 246 kyr and 248 kyr, we may have missed the MOT response to this major Termination III AMOC reinvigoration.

The less pronounced 1–2 kyr reductions in MOT increase during Terminations II and IV have counterparts in other records, too, albeit less clearly associated with AMOC changes. Although not aligned with a CH_4 peak, the Termination IV reduction appears to be linked to a first short-pulsed reduction in %NPS at ODP site 983 – the strongest excursion in %NPS for any of the four terminations – and an initial strengthening of the Asian monsoon. It may also be connected to a first peak in Iberian margin planktic $\delta^{18}O$, assuming that the age scale of that record is somewhat offset to the AICC2012 during Termination IV. Together, these records may indicate an interval of somewhat strengthened AMOC. During Termination II, there is little evidence for a reinvigoration of AMOC (Deaney et al., 2017). However, high-resolved sea-level reconstructions suggest a brief phase of reduced sea-level rise and, thus, reduced freshwater input into the North Atlantic, potentially leading to a somewhat strengthened AMOC (Grant et al., 2014; Rohling et al., 2021). Additionally, the first step of the two-step increase in Iberian margin planktic $\delta^{18}O$ and a brief episode towards more warm foraminiferal species with a simultaneous peak in planktic $\delta^{18}O$ at ODP site 1063 in the northwest Atlantic (Deaney et al., 2017) might point towards warmer SST at least in the southern part of the North Atlantic and, hence, potentially minor AMOC strengthening.

The influence of AMOC variability on MOT evolution seems to have persisted during interglacial periods, too. This is most evident at the end of Terminations II–IV, when CH_4 shows a strong, abrupt peak, which at least for MIS 9e occurs concurrently with a centennial-scale jump in CO_2 (Nehrbass-Ahles et al., 2020). These overshoots are mirrored by more gradual but nonetheless pronounced early interglacial peaks in Antarctic temperature and MOT. Considering the major CH_4 jumps, it seems highly likely that strong and abrupt AMOC reinvigoration is at the origin of these overshoots. From a MOT perspective, the first half of the overshoot, the (late) deglacial rise, appears similar for all three terminations, although Termination II and IV slopes may be somewhat steeper (Figure 4.3.). However, the second half of the overshoot, the early interglacial decrease, shows different patterns with strong MOT reduction in MIS 7e and MIS 9e compared to only a minor and more gradual cooldown in MIS 5e.

AMOC variability may explain this difference in (MOT) overshoot strength. A wide range of proxy records suggests that the early MIS 5e likely had a less vigorous AMOC resumption or at least multiple phases of weaker AMOC compared to MIS 7e and MIS 9e. Partially subdued formation of deepwater in the North Atlantic during early MIS 5e is for example suggested by not yet fully interglacial North Atlantic benthic $\delta^{13}C$ records (Barker et al., 2019; Hodell et al., 2009; Raymo et al., 2004; Venz et al., 1999) and emphasised by the continued presence of IRD and consequently relatively high %NPS south of Iceland (Barker et al., 2015). High concentrations of IRD are indicative of elevated freshwater input, which in the North Atlantic can contribute to a reduction in deepwater formation and thus reduced AMOC strength (Barker et al., 2015). Consequently, these phases of weaker AMOC were concluded to be due to a continued melting of proximal ice sheets throughout the first few millennia of MIS 5e (Deaney et al., 2017; Hodell et al., 2009; Tzedakis et al., 2018). Continued melting of ice sheets is also supported by models (Stone et al., 2016), and may explain the delayed and relatively weak peak in North Atlantic SST (Hoffman et al., 2017). We suggest that this somewhat subdued interglacial AMOC lead to only minor MOT cooling after the Termination II overshoot and contributed to higher-than-Holocene MOT throughout most of MIS 5e.

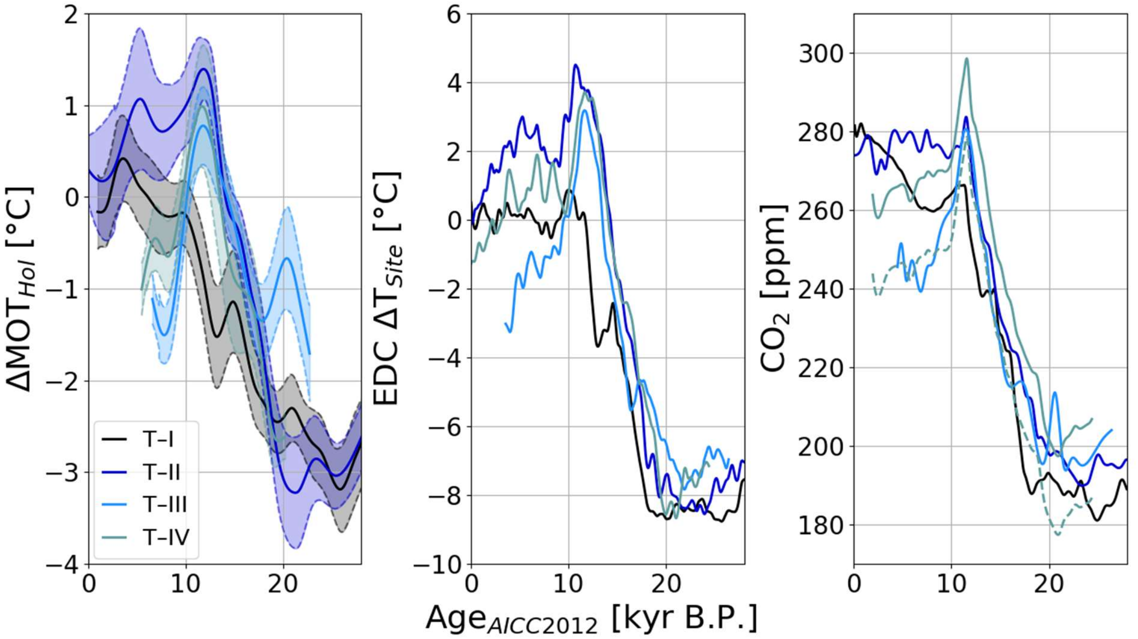

Figure 4.3.: Aligned Termination I–IV records of MOT (this study), EDC site temperature (Landais et al., 2021), and CO2 (Bereiter et al., 2015; Nehrbass-Ahles et al., 2020; Shin et al., 2020). The dashed line in the CO_2 panel shows Termination IV CO_2 reduced by 20 ppm to highlight the similarity of the Termination III and IV overshoots.

In contrast, AMOC resumption after Terminations III and IV appears to have been more abrupt and subsequent interglacial AMOC more stable than after Termination II. A recent study finds strongly reduced inflow of AABW to the eastern Pacific during MIS 7e and MIS 9e compared to the two most recent interglacial periods, from which a reduction in AABW extent is inferred (Yi et al., 2023). This reduction would most likely have led to a more vigorous AMOC, which is supported e.g., by the consistently low interglacial %NPS and absence of IRD at ODP site 983 south of Iceland, or by an alkenone-based SST record from the Iberian margin (Hodell et al., 2013). In response to this suggested strong interglacial AMOC, our record shows strong decreases in MOT of almost 2 °C for both MIS 7e and MIS 9e, considerably more than after the Termination II overshoot.

It is worth noting that, as for other climate records, MOT records do not show a Termination I overshoot (Bereiter et al., 2018b; Shackleton et al., 2019). The absence of a Termination I overshoot has been suggested to be the consequence of the strong millennial-scale oscillation relatively late in the termination in the form of the ACR (Barker and Knorr, 2021). The Younger Dryas stadial that followed before the onset of the Holocene may have been too short to lead to a major build-up of heat in the ocean interior, such that, despite a likely stable and strong Holocene AMOC (Lippold et al., 2019), no Termination I overshoot occurred. Furthermore, there are indications that the Holocene AMOC stability may have been only a perceived one and the result of compensating opposite trends in the different contributions to NADW formation (Lippold et al., 2019; Renssen et al., 2005; Thornalley et al., 2013). Such a more gradual strengthening of deepwater formation (at least regionally) in the early Holocene is also be suggested by sea-level reconstructions, as the melting of continental ice sheets and thus likely North Atlantic freshwater input likely continued until about 8 kyr (Lambeck et al., 2014). Hence, the (minor) build-up of heat in the ocean interior may have been released over a more extended period.

In addition to these deglacial and interglacial co-occurrences of variations in AMOC strength and MOT, there are also indications towards AMOC-induced MOT variability during glacial periods. Our record shows relatively warm glacial MOT between 156 kyr and 152 kyr, which most likely corresponds to a major Heinrich stadial, that is, a D-O-like stadial associated with a Heinrich-event, i.e., a strong peak in North Atlantic IRD. The major IRD event that started at around 157 kyr is linked to a meltwater phase of the Eurasian ice sheet that occurred between about 160 kyr and 145 kyr (Boswell et al., 2019; Wegwerth et al., 2020). In response to the freshwater input, several North Atlantic marine proxy records suggest low SST and a likely reduction in AMOC strength during that period (Barker et al., 2015; Hodell et al., 2013; Margari et al., 2014; Martrat et al., 2007; Zhang et al., 2023). MOT responds strongly to this meltwater pulse and increases by almost 1 °C within about 2 kyr, before then plateauing until its similarly steep decrease at around 152 kyr. Unlike MOT, greenhouse gases and Antarctic temperature show a delayed or, in the case of CH_4, hardly any response. The event also appears to not have influenced East Asian monsoon strength. Thus, the Heinrich stadial appears to have led to a reduced AMOC, as evidenced by the North Atlantic marine records and the gradual increase in Antarctic temperature and CO_2. However, the reduction in AMOC was not strong enough to cause a major shift in the position of the ITCZ, and accordingly no peak in CH_4 and speleothem $\delta^{18}O$. Upon AMOC resumption, which is evidenced by the end of the IRD peak and a simultaneous decrease %NPS, MOT, Antarctic temperature, and CO_2 again evolve in parallel.

4.4. Interglacial intensity from a MOT perspective

Based on a North Atlantic IRD record from ODP 983, Barker et al., 2019 suggested that, rather than parts of the subsequent interglacial, overshoots should be considered transient features of the preceding termination, i.e., early interglacial legacies of a deglacial climate. They argue that the CO_2 decrease following the overshoot is indicative that the climate system has not yet reached interglacial "equilibrium" conditions as ocean circulation is in continued adjustment (Barker and Knorr, 2021). Similar arguments have been made by other proxy-based (Deaney et al., 2017) and modelling studies (Ganopolski and Brovkin, 2017).

Considering the consistent influence of AMOC variability during deglaciations as well as during glacial millennial-scale oscillations, we may expect that these early interglacial adjustments of ocean circulation also cause a response in MOT. Indeed, as discussed above, strong overshoots in MOT, like those in CO_2 and Antarctic temperature, can be found in MOT for Terminations III and IV and to a lesser extent also for Termination II. Furthermore, it appears that the strength of the MOT response, i.e., the decrease in MOT after its initial overshoot, was definite, there was no recovery. Terminations with a stronger overshoot and, hence, a stronger decrease after the overshoot as evidenced in CO_2, Antarctic temperature, and MOT, show lower interglacial intensity. There thus appears to be an interglacial legacy of these "early interglacial legacies of deglacial climate instabilities", with MOT potential playing a crucial role.

Our record suggests a decrease of ~2 °C between the overshoot and later interglacial conditions for MIS 7e and MIS 9e. Such an MOT cooling has substantial consequences in terms of interglacial intensity. If we exclude the strong MOT overshoots at the onset of MIS 9e and MIS 7e (as well as the weaker MOT overshoot at the onset of MIS 5e) from our analysis, MIS 9e and particularly MIS 7e appear as relatively cold interglacials (see Section 4.1.). in line with the relatively low MIS 7e interglacial intensity suggested by marine proxy records (Past Interglacials Working Group of PAGES, 2016). Furthermore, it appears that the strength of the MOT response to the AMOC strengthening, i.e., the decrease in MOT after its initial overshoot, is definite, as there is no evidence of a later interglacial increase in MOT, at least for MIS 7e and MIS 9e. In contrast, after an only weak overshoot, MOT, Antarctic temperature, and CO_2 remain at elevated levels throughout the LIG, the strongest interglacial of the last 800 kyr (Past Interglacials Working Group of PAGES, 2016). There thus appears to be a late interglacial legacy of these “early interglacial legacies of deglacial climate instabilities”.

The MOT response to early-interglacial AMOC reinvigoration may play a crucial role in setting the intensity of the subsequent interglacial. As one of Earth’s two fast-exchanging heat reservoirs, lower OHC (MOT) quite simply means that there is less energy in the climate system (Baggenstos et al., 2019). Furthermore, through the solubility pump, lower MOT leads to a significant decrease in atmospheric CO_2 and hence lower greenhouse gas forcing. The ~2 °C decrease in MOT after the MIS 7e and MIS 9e overshoot translates to a ~20 ppm uptake of atmospheric CO_2 by the ocean (Shackleton et al., 2021; Williams and Follows, 2011). Several climate models of intermediate complexity suggest a weakening of the reverse cell of the Indo-Pacific overturning circulation (Brovkin et al., 2012; Schmittner, 2005) in combination with a temperature-induced shoaling of the remineralisation depth in the Atlantic (Ganopolski and Brovkin, 2017) in response to AMOC weakening to be the main causes of millennial-scale increases in CO_2. Upon AMOC reinvigoration, these processes reverse. The large amplitude in early-interglacial MOT decrease suggests that there may additionally be a MOT contribution to the MIS 7e and MIS 9e CO_2 decrease. On the other hand, the frequent AMOC interruptions during early MIS 5e would likely have contributed to sustaining elevated MOT throughout the LIG, and, hence, only a minor effect on CO_2. Thus, mean ocean cooling may not only play a dominant role for the initial CO_2 drawdown at the end of the LIG (Shackleton et al., 2021) and potentially other interglacials, but may contribute significantly to the strength of (i.e., the drawdown after) early-interglacial CO_2 overshoots and, hence, interglacial intensity.

4.5. Conclusions

Our Termination I-IV MOT record reveals millennial-scale variability during the past four glacial terminations, albeit not as pronounced as during the Bølling-Allerød interstadial. We argue that this millennial-scale variability is the result of intermittent reinvigorations of the AMOC. Similarly, MOT at least in the early phases of all four interglacials appears to be controlled by variations in AMOC (or absence thereof). Furthermore, our MOT record suggests MOT variability during MIS 6e full glacial conditions, likely in response to a major freshwater input into the North Atlantic and inferred AMOC disruption. Thus, AMOC variability appears to influence MOT evolution across the full spectrum of glacial–interglacial climate states. Considering the strong MOT response to early interglacial AMOC reinvigorations, MOT may play a significant role for setting interglacial intensity.

References

Baggenstos, D., Häberli, M., Schmitt, J., Shackleton, S.A., Birner, B., Severinghaus, J.P., Kellerhals, T., Fischer, H., 2019. Earth's radiative imbalance from the Last Glacial Maximum to the present. Proc Natl Acad Sci USA 116, 14881–14886. https://doi.org/10.1073/pnas.1905447116

Bajo, P., Drysdale, R.N., Woodhead, J.D., Hellstrom, J.C., Hodell, D., Ferretti, P., Voelker, A.H.L., Zanchetta, G., Rodrigues, T., Wolff, E., Tyler, J., Frisia, S., Spötl, C., Fallick, A.E., 2020. Persistent influence of obliquity on ice age terminations since the Middle Pleistocene transition. Science 367, 1235–1239. https://doi.org/10.1126/science.aaw1114

Barker, S., Chen, J., Gong, X., Jonkers, L., Knorr, G., Thornalley, D., 2015. Icebergs not the trigger for North Atlantic cold events. Nature 520, 333–336. https://doi.org/10.1038/nature14330

Barker, S., Knorr, G., 2021. Millennial scale feedbacks determine the shape and rapidity of glacial termination. Nat Commun 12, 2273. https://doi.org/10.1038/s41467-021-22388-6

Barker, S., Knorr, G., Conn, S., Lordsmith, S., Newman, D., Thornalley, D., 2019. Early Interglacial Legacy of Deglacial Climate Instability. Paleoceanography and Paleoclimatology 34, 1455–1475. https://doi.org/10.1029/2019PA003661

Batchelor, C.L., Margold, M., Krapp, M., Murton, D.K., Dalton, A.S., Gibbard, P.L., Stokes, C.R., Murton, J.B., Manica, A., 2019. The configuration of Northern Hemisphere ice sheets through the Quaternary. Nat Commun 10, 3713. https://doi.org/10.1038/s41467-019-11601-2

Bazin, L., Landais, A., Lemieux-Dudon, B., Toyé Mahamadou Kele, H., Veres, D., Parrenin, F., Martinerie, P., Ritz, C., Capron, E., Lipenkov, V., Loutre, M.-F., Raynaud, D., Vinther, B., Svensson, A., Rasmussen, S.O., Severi, M., Blunier, T., Leuenberger, M., Fischer, H., Masson-Delmotte, V., Chappellaz, J., Wolff, E., 2013. An optimized multi-proxy, multi-site Antarctic ice and gas orbital chronology (AICC2012): 120–800 ka. Clim. Past 9, 1715–1731. https://doi.org/10.5194/cp-9-1715-2013

Bereiter, B., Eggleston, S., Schmitt, J., Nehrbass-Ahles, C., Stocker, T.F., Fischer, H., Kipfstuhl, S., Chappellaz, J., 2015. Revision of the EPICA Dome C CO $_2$ record from 800 to 600 kyr before present: Analytical bias in the EDC CO2 record. Geophys. Res. Lett. 42, 542–549. https://doi.org/10.1002/2014GL061957

Bereiter, B., Kawamura, K., Severinghaus, J.P., 2018a. New methods for measuring atmospheric heavy noble gas isotope and elemental ratios in ice core samples. Rapid Commun Mass Spectrom 32, 801–814. https://doi.org/10.1002/rcm.8099

Bereiter, B., Shackleton, S., Baggenstos, D., Kawamura, K., Severinghaus, J., 2018b. Mean global ocean temperatures during the last glacial transition. Nature 553, 39–44. https://doi.org/10.1038/nature25152

Bock, M., Schmitt, J., Beck, J., Seth, B., Chappellaz, J., Fischer, H., 2017. Glacial/interglacial wetland, biomass burning, and geologic methane emissions constrained by dual stable isotopic CH $_4$ ice core records. Proc. Natl. Acad. Sci. U.S.A. 114. https://doi.org/10.1073/pnas.1613883114

Böhm, E., Lippold, J., Gutjahr, M., Frank, M., Blaser, P., Antz, B., Fohlmeister, J., Frank, N., Andersen, M.B., Deininger, M., 2015. Strong and deep Atlantic meridional overturning circulation during the last glacial cycle. Nature 517, 73–76. https://doi.org/10.1038/nature14059

Boswell, S.M., Toucanne, S., Pitel-Roudaut, M., Creyts, T.T., Eynaud, F., Bayon, G., 2019. Enhanced surface melting of the Fennoscandian Ice Sheet during periods of North Atlantic cooling. Geology 47, 664–668. https://doi.org/10.1130/G46370.1

Broccoli, A.J., Dahl, K.A., Stouffer, R.J., 2006. Response of the ITCZ to Northern Hemisphere cooling. Geophysical Research Letters 33. https://doi.org/10.1029/2005GL024546

Brovkin, V., Ganopolski, A., Archer, D., Munhoven, G., 2012. Glacial CO_2 cycle as a succession of key physical and biogeochemical processes. Climate of the Past 8, 251–264. https://doi.org/10.5194/cp-8-251-2012

Cheng, H., Edwards, R.L., Broecker, W.S., Denton, G.H., Kong, X., Wang, Y., Zhang, R., Wang, X., 2009. Ice Age Terminations. Science 326, 248–252. https://doi.org/10.1126/science.1177840

Cheng, H., Edwards, R.L., Sinha, A., Spötl, C., Yi, L., Chen, S., Kelly, M., Kathayat, G., Wang, X., Li, X., Kong, X., Wang, Y., Ning, Y., Zhang, H., 2016. The Asian monsoon over the past 640,000 years and ice age terminations. Nature 534, 640–646. https://doi.org/10.1038/nature18591

Cheng, H., Edwards, R.L., Wang, Y., Kong, X., Ming, Y., Kelly, M.J., Wang, X., Gallup, C.D., Liu, W., 2006. A penultimate glacial monsoon record from Hulu Cave and two-phase glacial terminations. Geol 34, 217. https://doi.org/10.1130/G22289.1

Curry, W.B., Oppo, D.W., 2005. Glacial water mass geometry and the distribution of δ13C of ΣCO2 in the western Atlantic Ocean. Paleoceanography 20. https://doi.org/10.1029/2004PA001021

Deaney, E.L., Barker, S., van de Flierdt, T., 2017. Timing and nature of AMOC recovery across Termination 2 and magnitude of deglacial CO2 change. Nat Commun 8, 14595. https://doi.org/10.1038/ncomms14595

DeVries, T., Holzer, M., 2019. Radiocarbon and Helium Isotope Constraints on Deep Ocean Ventilation and Mantle-3He Sources. Journal of Geophysical Research: Oceans 124, 3036–3057. https://doi.org/10.1029/2018JC014716

EPICA community members, 2004. Eight glacial cycles from an Antarctic ice core. Nature 429, 623–628. https://doi.org/10.1038/nature02599

Fischer, H., Schmitt, J., Lüthi, D., Stocker, T.F., Tschumi, T., Parekh, P., Joos, F., Köhler, P., Völker, C., Gersonde, R., Barbante, C., Le Floch, M., Raynaud, D., Wolff, E., 2010. The role of Southern Ocean processes in orbital and millennial CO2 variations – A synthesis. Quaternary Science Reviews, Climate of the Last Million Years: New Insights from EPICA and Other Records 29, 193–205. https://doi.org/10.1016/j.quascirev.2009.06.007

Galbraith, E.D., Merlis, T.M., Palter, J.B., 2016. Destabilization of glacial climate by the radiative impact of Atlantic Meridional Overturning Circulation disruptions: RADIATIVE IMPACT OF AMOC DISRUPTIONS. Geophys. Res. Lett. 43, 8214–8221. https://doi.org/10.1002/2016GL069846

Ganopolski, A., Brovkin, V., 2017. Simulation of climate, ice sheets and CO_2 evolution during the last four glacial cycles with an Earth system model of intermediate complexity. Climate of the Past 13, 1695–1716. https://doi.org/10.5194/cp-13-1695-2017

Grant, K.M., Rohling, E.J., Ramsey, C.B., Cheng, H., Edwards, R.L., Florindo, F., Heslop, D., Marra, F., Roberts, A.P., Tamisiea, M.E., Williams, F., 2014. Sea-level variability over five glacial cycles. Nat Commun 5, 5076. https://doi.org/10.1038/ncomms6076

Haeberli, M., Baggenstos, D., Schmitt, J., Grimmer, M., Michel, A., Kellerhals, T., Fischer, H., 2021. Snapshots of mean ocean temperature over the last 700 000 years using noble gases in the EPICA Dome C ice core. Clim. Past 17, 843–867. https://doi.org/10.5194/cp-17-843-2021

Headly, M.A., Severinghaus, J.P., 2007. A method to measure Kr/N $_2$ ratios in air bubbles trapped in ice cores and its application in reconstructing past mean ocean temperature. J. Geophys. Res. 112, D19105. https://doi.org/10.1029/2006JD008317

Hodell, D.A., Crowhurst, S.J., Lourens, L., Margari, V., Nicolson, J., Rolfe, J.E., Skinner, L.C., Thomas, N.C., Tzedakis, P.C., Mleneck-Vautravers, M.J., Wolff, E.W., 2023. A 1.5-million-year record of orbital and millennial climate variability in the North Atlantic. Climate of the Past 19, 607–636. https://doi.org/10.5194/cp-19-607-2023

Hodell, D.A., Lourens, L., Stow, D. a. V., Hernández-Molina, J., Alvarez Zarikian, C.A., the Shackleton Site Project Members, 2013. The “Shackleton Site” (IODP Site U1385) on the Iberian Margin. Scientific Drilling 16, 13–19. https://doi.org/10.5194/sd-16-13-2013

Hodell, D.A., Minth, E.K., Curtis, J.H., McCave, I.N., Hall, I.R., Channell, J.E.T., Xuan, C., 2009. Surface and deep-water hydrography on Gardar Drift (Iceland Basin) during the last interglacial period. Earth and Planetary Science Letters 288, 10–19. https://doi.org/10.1016/j.epsl.2009.08.040

Hoffman, J.S., Clark, P.U., Parnell, A.C., He, F., 2017. Regional and global sea-surface temperatures during the last interglaciation. Science 355, 276–279. https://doi.org/10.1126/science.aai8464

Johnson, G.C., 2008. Quantifying Antarctic Bottom Water and North Atlantic Deep Water volumes. Journal of Geophysical Research: Oceans 113. https://doi.org/10.1029/2007JC004477

Köhler, P., Fischer, H., 2006. Simulating low frequency changes in atmospheric CO_2 during the last 740 000 years. Climate of the Past 2, 57–78. https://doi.org/10.5194/cp-2-57-2006

Lambeck, K., Rouby, H., Purcell, A., Sun, Y., Sambridge, M., 2014. Sea level and global ice volumes from the Last Glacial Maximum to the Holocene. Proceedings of the National Academy of Sciences 111, 15296–15303. https://doi.org/10.1073/pnas.1411762111

Landais, A., Stenni, B., Masson-Delmotte, V., Jouzel, J., Cauquoin, A., Fourré, E., Minster, B., Selmo, E., Extier, T., Werner, M., Vimeux, F., Uemura, R., Crotti, I., Grisart, A., 2021. Interglacial Antarctic–Southern Ocean climate decoupling due to moisture source area shifts. Nat. Geosci. 14, 918–923. https://doi.org/10.1038/s41561-021-00856-4

Lang, N., Wolff, E.W., 2011. Interglacial and glacial variability from the last 800 ka in marine, ice and terrestrial archives. Climate of the Past 7, 361–380. https://doi.org/10.5194/cp-7-361-2011

Laskar, J., Robutel, P., Joutel, F., Gastineau, M., Correia, A.C.M., Levrard, B., 2004. A long-term numerical solution for the insolation quantities of the Earth. A&A 428, 261–285. https://doi.org/10.1051/0004-6361:20041335

Lippold, J., Pöppelmeier, F., Süfke, F., Gutjahr, M., Goepfert, T.J., Blaser, P., Friedrich, O., Link, J.M., Wacker, L., Rheinberger, S., Jaccard, S.L., 2019. Constraining the Variability of the Atlantic Meridional

Overturning Circulation During the Holocene. Geophysical Research Letters 46, 11338–11346. https://doi.org/10.1029/2019GL084988

Loulergue, L., Schilt, A., Spahni, R., Masson-Delmotte, V., Blunier, T., Lemieux, B., Barnola, J.-M., Raynaud, D., Stocker, T.F., Chappellaz, J., 2008. Orbital and millennial-scale features of atmospheric CH4 over the past 800,000 years. Nature 453, 383–386. https://doi.org/10.1038/nature06950

Lüthi, D., Le Floch, M., Bereiter, B., Blunier, T., Barnola, J.-M., Siegenthaler, U., Raynaud, D., Jouzel, J., Fischer, H., Kawamura, K., Stocker, T.F., 2008. High-resolution carbon dioxide concentration record 650,000–800,000 years before present. Nature 453, 379–382. https://doi.org/10.1038/nature06949

Margari, V., Skinner, L.C., Hodell, D.A., Martrat, B., Toucanne, S., Grimalt, J.O., Gibbard, P.L., Lunkka, J.P., Tzedakis, P.C., 2014. Land-ocean changes on orbital and millennial time scales and the penultimate glaciation. Geology 42, 183–186. https://doi.org/10.1130/G35070.1

Martrat, B., Grimalt, J.O., Shackleton, N.J., de Abreu, L., Hutterli, M.A., Stocker, T.F., 2007. Four Climate Cycles of Recurring Deep and Surface Water Destabilizations on the Iberian Margin. Science 317, 502–507. https://doi.org/10.1126/science.1139994

Matsumoto, K., 2007. Radiocarbon-based circulation age of the world oceans. J. Geophys. Res. 112, C09004. https://doi.org/10.1029/2007JC004095

McManus, J.F., Francois, R., Gherardi, J.-M., Keigwin, L.D., Brown-Leger, S., 2004. Collapse and rapid resumption of Atlantic meridional circulation linked to deglacial climate changes. Nature 428, 834–837. https://doi.org/10.1038/nature02494

Mitsui, T., Tzedakis, P.C., Wolff, E.W., 2022. Insolation evolution and ice volume legacies determine interglacial and glacial intensity. Climate of the Past 18, 1983–1996. https://doi.org/10.5194/cp-18-1983-2022

Nehrbass-Ahles, C., Shin, J., Schmitt, J., Bereiter, B., Joos, F., Schilt, A., Schmidely, L., Silva, L., Teste, G., Grilli, R., Chappellaz, J., Hodell, D., Fischer, H., Stocker, T.F., 2020. Abrupt CO2 release to the atmosphere under glacial and early interglacial climate conditions 7.

North Greenland Ice Core Project members, 2004. High-resolution record of Northern Hemisphere climate extending into the last interglacial period. Nature 431, 147–151. https://doi.org/10.1038/nature02805

Past Interglacials Working Group of PAGES, 2016. Interglacials of the last 800,000 years. Rev. Geophys. 54, 162–219. https://doi.org/10.1002/2015RG000482

Pedro, J.B., Jochum, M., Buizert, C., He, F., Barker, S., Rasmussen, S.O., 2018. Beyond the bipolar seesaw: Toward a process understanding of interhemispheric coupling. Quaternary Science Reviews 192, 27–46. https://doi.org/10.1016/j.quascirev.2018.05.005

Petit, J.R., Jouzel, J., Raynaud, D., Barkov, N.I., Delaygue, G., Delmotte, M., Kotlyakov, V.M., Legrand, M., Lipenkov, V.Y., Lorius, C., Saltzman, E., 1999. Climate and atmospheric history of the past 420,000 years from the Vostok ice core, Antarctica 399.

Pöppelmeier, F., Blaser, P., Gutjahr, M., Jaccard, S.L., Frank, M., Max, L., Lippold, J., 2020. Northern-sourced water dominated the Atlantic Ocean during the Last Glacial Maximum. Geology 48, 826–829. https://doi.org/10.1130/G47628.1

Raymo, M.E., Oppo, D.W., Flower, B.P., Hodell, D.A., McManus, J.F., Venz, K.A., Kleiven, K.F., McIntyre, K., 2004. Stability of North Atlantic water masses in face of pronounced climate variability during the Pleistocene. Paleoceanography 19. https://doi.org/10.1029/2003PA000921

Renssen, H., Goosse, H., Fichefet, T., 2005. Contrasting trends in North Atlantic deep-water formation in the Labrador Sea and Nordic Seas during the Holocene. Geophysical Research Letters 32. https://doi.org/10.1029/2005GL022462

Ritz, S.P., Stocker, T.F., Severinghaus, J.P., 2011. Noble gases as proxies of mean ocean temperature: sensitivity studies using a climate model of reduced complexity. Quaternary Science Reviews 30, 3728–3741. https://doi.org/10.1016/j.quascirev.2011.09.021

Roberts, N.L., Piotrowski, A.M., McManus, J.F., Keigwin, L.D., 2010. Synchronous Deglacial Overturning and Water Mass Source Changes. Science 327, 75–78. https://doi.org/10.1126/science.1178068

Rohling, E.J., Yu, J., Heslop, D., Foster, G.L., Opdyke, B., Roberts, A.P., 2021. Sea level and deep-sea temperature reconstructions suggest quasi-stable states and critical transitions over the past 40 million years. Sci. Adv. 7, eabf5326. https://doi.org/10.1126/sciadv.abf5326

Rothlisberger, R., Mudelsee, M., Bigler, M., de Angelis, M., Fischer, H., Hansson, M., Lambert, F., Masson-Delmotte, V., Sime, L., Udisti, R., Wolff, E.W., 2008. The Southern Hemisphere at glacial terminations: insights from the Dome C ice core. Clim. Past.

Schmidely, L., Nehrbass-Ahles, C., Schmitt, J., Han, J., Silva, L., Shin, J., Joos, F., Chappellaz, J., Fischer, H., Stocker, T.F., 2021. CH<sub>4</sub> and N<sub>2</sub>O fluctuations during the penultimate deglaciation. Clim. Past 17, 1627–1643. https://doi.org/10.5194/cp-17-1627-2021

Schmittner, A., 2005. Decline of the marine ecosystem caused by a reduction in the Atlantic overturning circulation. Nature 434, 628–633. https://doi.org/10.1038/nature03476

Shackleton, S., Baggenstos, D., Menking, J.A., Dyonisius, M.N., Bereiter, B., Bauska, T.K., Rhodes, R.H., Brook, E.J., Petrenko, V.V., McConnell, J.R., Kellerhals, T., Häberli, M., Schmitt, J., Fischer, H., Severinghaus, J.P., 2020. Global ocean heat content in the Last Interglacial. Nat. Geosci. 13, 77–81. https://doi.org/10.1038/s41561-019-0498-0

Shackleton, S., Bereiter, B., Baggenstos, D., Bauska, T.K., Brook, E.J., Marcott, S.A., Severinghaus, J.P., 2019. Is the Noble Gas-Based Rate of Ocean Warming During the Younger Dryas Overestimated? Geophys. Res. Lett. 2019GL082971. https://doi.org/10.1029/2019GL082971

Shackleton, S., Menking, J.A., Brook, E., Buizert, C., Dyonisius, M.N., Petrenko, V.V., Baggenstos, D., Severinghaus, J.P., 2021. Evolution of mean ocean temperature in Marine Isotope Stage 4. Clim. Past 17, 2273–2289. https://doi.org/10.5194/cp-17-2273-2021

Shakun, J.D., Clark, P.U., He, F., Marcott, S.A., Mix, A.C., Liu, Z., Otto-Bliesner, B., Schmittner, A., Bard, E., 2012. Global warming preceded by increasing carbon dioxide concentrations during the last deglaciation. Nature 484, 49–54. https://doi.org/10.1038/nature10915

Shakun, J.D., Lea, D.W., Lisiecki, L.E., Raymo, M.E., 2015. An 800-kyr record of global surface ocean δ 18 O and implications for ice volume-temperature coupling. Earth and Planetary Science Letters 426, 58–68. https://doi.org/10.1016/j.epsl.2015.05.042

Shin, J., Nehrbass-Ahles, C., Grilli, R., Chowdhry Beeman, J., Parrenin, F., Teste, G., Landais, A., Schmidely, L., Silva, L., Schmitt, J., Bereiter, B., Stocker, T.F., Fischer, H., Chappellaz, J., 2020. Millennial-scale atmospheric CO<sub>2</sub> variations during the Marine Isotope Stage 6 period (190–135 ka). Clim. Past 16, 2203–2219. https://doi.org/10.5194/cp-16-2203-2020

Siegenthaler, U., Stocker, T.F., Monnin, E., Lüthi, D., Schwander, J., Stauffer, B., Raynaud, D., Barnola, J.-M., Fischer, H., Masson-Delmotte, V., Jouzel, J., 2005. Stable Carbon Cycle Climate Relationship During the Late Pleistocene. Science 310, 1313–1317. https://doi.org/10.1126/science.1120130

Sigman, D.M., Hain, M.P., Haug, G.H., 2010. The polar ocean and glacial cycles in atmospheric CO2 concentration. Nature 466, 47–55. https://doi.org/10.1038/nature09149

Skinner, L.C., Primeau, F., Freeman, E., de la Fuente, M., Goodwin, P.A., Gottschalk, J., Huang, E., McCave, I.N., Noble, T.L., Scrivner, A.E., 2017. Radiocarbon constraints on the glacial ocean circulation and its impact on atmospheric CO2. Nat Commun 8, 16010. https://doi.org/10.1038/ncomms16010

Spratt, R.M., Lisiecki, L.E., 2016. A Late Pleistocene sea level stack. Clim. Past 12, 1079–1092. https://doi.org/10.5194/cp-12-1079-2016

Stocker, T.F., Johnsen, S.J., 2003. A minimum thermodynamic model for the bipolar seesaw: THERMAL BIPOLAR SEESAW. Paleoceanography 18, n/a-n/a. https://doi.org/10.1029/2003PA000920

Stone, E.J., Capron, E., Lunt, D.J., Payne, A.J., Singarayer, J.S., Valdes, P.J., Wolff, E.W., 2016. Impact of meltwater on high-latitude early Last Interglacial climate. Climate of the Past 12, 1919–1932. https://doi.org/10.5194/cp-12-1919-2016

Thornalley, D.J.R., Blaschek, M., Davies, F.J., Praetorius, S., Oppo, D.W., McManus, J.F., Hall, I.R., Kleiven, H., Renssen, H., McCave, I.N., 2013. Long-term variations in Iceland–Scotland overflow strength during the Holocene. Climate of the Past 9, 2073–2084. https://doi.org/10.5194/cp-9-2073-2013

Tzedakis, P.C., Drysdale, R.N., Margari, V., Skinner, L.C., Menviel, L., Rhodes, R.H., Taschetto, A.S., Hodell, D.A., Crowhurst, S.J., Hellstrom, J.C., Fallick, A.E., Grimalt, J.O., McManus, J.F., Martrat, B., Mokeddem, Z., Parrenin, F., Regattieri, E., Roe, K., Zanchetta, G., 2018. Enhanced climate instability in the North Atlantic and southern Europe during the Last Interglacial. Nat Commun 9, 4235. https://doi.org/10.1038/s41467-018-06683-3

Venz, K.A., Hodell, D.A., Stanton, C., Warnke, D.A., 1999. A 1.0 Myr Record of Glacial North Atlantic Intermediate Water Variability from ODP Site 982 in the Northeast Atlantic. Paleoceanography 14, 42–52. https://doi.org/10.1029/1998PA900013

Veres, D., Bazin, L., Landais, A., Toyé Mahamadou Kele, H., Lemieux-Dudon, B., Parrenin, F., Martinerie, P., Blayo, E., Blunier, T., Capron, E., Chappellaz, J., Rasmussen, S.O., Severi, M., Svensson, A., Vinther, B., Wolff, E.W., 2013. The Antarctic ice core chronology (AICC2012): an optimized multi-parameter and multi-site dating approach for the last 120 thousand years. Clim. Past 9, 1733–1748. https://doi.org/10.5194/cp-9-1733-2013

Wegwerth, A., Kaiser, J., Dellwig, O., Arz, H.W., 2020. Impact of Eurasian Ice Sheet and North Atlantic Climate Dynamics on Black Sea Temperature Variability During the Penultimate Glacial (MIS 6, 130–184 ka BP). Paleoceanography and Paleoclimatology 35, e2020PA003882. https://doi.org/10.1029/2020PA003882

Williams, R.G., Follows, M.J., 2011. Ocean Dynamics and the Carbon Cycle: Principles and Mechanisms. Cambridge University Press, Cambridge. https://doi.org/10.1017/CBO9780511977817

Wolff, E.W., Fischer, H., Röthlisberger, R., 2009. Glacial terminations as southern warmings without northern control. Nature Geosci 2, 206–209. https://doi.org/10.1038/ngeo442

Yi, L., Medina-Elizalde, M., Tan, L., Kemp, D.B., Li, Y., Kletetschka, G., Xie, Q., Yao, H., He, H., Deng, C., Ogg, J.G., 2023. Plio-Pleistocene deep-sea ventilation in the eastern Pacific and potential linkages with Northern Hemisphere glaciation. Sci. Adv. 9, eadd1467. https://doi.org/10.1126/sciadv.add1467

Zhang, H., Huang, Y., Wijker, R., Cacho, I., Torner, J., Santos, M., Kost, O., Wei, B., Stoll, H., 2023. Iberian Margin surface ocean cooling led freshening during Marine Isotope Stage 6 abrupt cooling events. Nat Commun 14, 5390. https://doi.org/10.1038/s41467-023-41142-8

5. Co-authored publications

Snapshots of mean ocean temperature over the last 700 000 years using noble gases in the EPICA Dome C ice core

Abstract

Together with the latent heat stored in glacial ice sheets, the ocean heat uptake carries the lion's share of glacial–interglacial changes in the planetary heat content, but little direct information on the global mean ocean temperature (MOT) is available to constrain the ocean temperature response to glacial–interglacial climate perturbations. Using ratios of noble gases and molecular nitrogen trapped in the Antarctic EPICA Dome C ice core, we are able to reconstruct MOT for peak glacial and interglacial conditions during the last 700 thousand years (kyr) and explore the differences between these extrema. To this end, we have to correct the noble-gas ratios for gas transport effects in the firn column and gas loss fractionation processes of the samples after ice core retrieval using the full elemental matrix of N2, Ar, Kr, and Xe in the ice and their individual isotopic ratios. The reconstructed MOT in peak glacials is consistently about 3.3 ± 0.4 °C cooler compared to the Holocene. Lukewarm interglacials before the Mid-Brunhes Event 450 kyr ago are characterized by 1.6 ± 0.4 °C lower MOT than the Holocene; thus, glacial–interglacial amplitudes were only about 50% of those after the Mid-Brunhes Event, in line with the reduced radiative forcing by lower greenhouse gas concentrations and their Earth system feedbacks. Moreover, we find significantly increased MOTs at the onset of Marine Isotope Stage 5e and 9e, which are coeval with CO_2 and CH_4 overshoots at that time. We link these CO_2 and CH_4 overshoots to a resumption of the Atlantic Meridional Overturning Circulation, which is also the starting point of the release of heat previously accumulated in the ocean during times of reduced overturning.

Contribution

My contribution to Haeberli et al., 2021 was as follows: Together with Marcel Haeberli, I performed the data analysis; I did the figure crafting; I contributed to discussing the data and in the manuscript-writing process.

Clim. Past, 17, 843–867, 2021
https://doi.org/10.5194/cp-17-843-2021

Climate of the Past

Snapshots of mean ocean temperature over the last 700 000 years using noble gases in the EPICA Dome C ice core

Marcel Haeberli[1], Daniel Baggenstos[1], Jochen Schmitt[1], Markus Grimmer[1], Adrien Michel[1,2], Thomas Kellerhals[1], and Hubertus Fischer[1]

[1]Climate and Environmental Physics & Oeschger Centre for Climate Change Research, University of Bern,
Sidlerstrasse 5, 3012 Bern, Switzerland
[2]Laboratoire des Sciences Cryosphérique, EPFL, ENAC IIE CRYOS GR A0 455 (Bâtiment GR),
Station 2, 1015 Lausanne, Switzerland

Correspondence: Hubertus Fischer (hubertus.fischer@climate.unibe.ch)

Received: 25 September 2020 – Discussion started: 8 October 2020
Revised: 15 February 2021 – Accepted: 21 February 2021 – Published: 14 April 2021

Abstract. Together with the latent heat stored in glacial ice sheets, the ocean heat uptake carries the lion's share of glacial–interglacial changes in the planetary heat content, but little direct information on the global mean ocean temperature (MOT) is available to constrain the ocean temperature response to glacial–interglacial climate perturbations. Using ratios of noble gases and molecular nitrogen trapped in the Antarctic EPICA Dome C ice core, we are able to reconstruct MOT for peak glacial and interglacial conditions during the last 700 000 years and explore the differences between these extrema. To this end, we have to correct the noble gas ratios for gas transport effects in the firn column and gas loss fractionation processes of the samples after ice core retrieval using the full elemental matrix of N_2, Ar, Kr, and Xe in the ice and their individual isotopic ratios. The reconstructed MOT in peak glacials is consistently about 3.3 ± 0.4 °C cooler compared to the Holocene. Lukewarm interglacials before the Mid-Brunhes Event 450 kyr ago are characterized by 1.6 ± 0.4 °C lower MOT than the Holocene; thus, glacial–interglacial amplitudes were only about 50 % of those after the Mid-Brunhes Event, in line with the reduced radiative forcing by lower greenhouse gas concentrations and their Earth system feedbacks. Moreover, we find significantly increased MOTs at the onset of Marine Isotope Stage 5.5 and 9.3, which are coeval with CO_2 and CH_4 overshoots at that time. We link these CO_2 and CH_4 overshoots to a resumption of the Atlantic Meridional Overturning Circulation, which is also the starting point of the release of heat previously accumulated in the ocean during times of reduced overturning.

1 Introduction

Over the last million years, Earth's climate has experienced pronounced changes in global ice volume (Bintanja et al., 2005) and hence sea level, accompanied by significant temperature changes between cold glacials and warmer interglacials. These temperature changes are observed with different amplitudes both on land (EPICA community members, 2004; Tzedakis et al., 2006; Melles et al., 2012) and in the ocean (Elderfield et al., 2012; Shakun et al., 2012, 2015). In particular, due to the large size and heat capacity of the ocean reservoir, global mean ocean temperature (MOT) changes (together with the latent heat stored in waxing ice sheets) represent an integrated signal of Earth's energy imbalance in the past (Baggenstos et al., 2019). For example, today, the global ocean is taking up about 90 % of the excess heat from anthropogenic global warming, dominating the current changes in the planetary energy budget (Gleckler et al., 2016; von Schuckmann et al., 2020).

In contrast to today's warming, where radiative forcing is caused through anthropogenic emissions of CO_2, past climate cycles are generally believed to have been driven by orbital changes in the latitudinal and seasonal distribution of incoming solar radiation (Milankovic, 1941), with changing greenhouse gas concentrations representing an important amplifying feedback. Only recently did Tzedakis et al. (2017) propose a simple rule for the occurrence of full deglaciations based on the amount of effective incoming energy flux (defined as the caloric summer half-year insolation at 65° N corrected by a term that takes into account the time elapsed since the previous deglaciation). While this rule is in agreement with the occurrence of all full deglaciations over the last million years, it does not intend to predict differences between individual interglacials in ice volume and climate. For example, Marine Isotope Stage (MIS) 11 is characterized by a very long interval of interglacial conditions and a sea level at least equally high as in MIS 5.5 and likely more than 6 m higher than in the Holocene (Dutton et al., 2015) . However, its effective energy is just reaching the threshold suggested by Tzedakis et al. (2017), while MIS 5.5 exhibits the largest effective energy over the last 800 kyr and the second largest over the last 2.6 Myr (Tzedakis et al., 2017). Moreover, lukewarm interglacials (i.e., interglacials significantly colder than the Holocene with increased ice volume) were observed in local temperature reconstructions and global sea level (EPICA community members, 2004; PAGES Past Interglacials Working Group, 2016; Shakun et al., 2015; Elderfield et al., 2012) in the time interval 800–450 kyr BP (before present; present is defined as 1950). Again, the effective energy during these lukewarm interglacials is not systematically lower than for the subsequent interglacials, requiring additional energetic or radiative changes in the climate system to explain the difference between the individual interglacials. MOT may play an important role in explaining these features, as a higher ocean heat content could represent a compensating mechanism for the excess energy not used for the melting of the larger remnant ice sheets during lukewarm interglacials. The opposite is also true: if lower MOT parallels larger ice volume during lukewarm interglacials, changes in the radiative balance of the Earth are required to explain the differences between the interglacials before and after 450 kyr BP.

Quantitative estimates of the integrated heat content of the entire ocean are required to answer these questions. However, obtaining a representative estimate of the whole-ocean heat content represents a formidable challenge (Hoffman et al., 2017; Shakun et al., 2015). Marine sediments are available for many but not all ocean areas and record only local sea surface conditions or deep-ocean temperatures at the coring site. Moreover, the proxy temperature information gained from marine sediments may be affected by biological processes, sea level changes, or limited precision, especially for cold deep-ocean temperatures. Finally, obtaining globally representative MOT from individual marine archives requires the compilation of a globally representative set of marine sediment cores, including rigorous cross-dating of all the records, which is difficult for the pre-^{14}C period.

The measurement of atmospheric noble gases trapped in Antarctic ice provides a unique opportunity to reconstruct changes in MOT independently from marine records (Craig and Wiens, 1996; Bereiter et al., 2018b; Headly and Severinghaus, 2007; Ritz et al., 2011) and may overcome these limitations. Changes in the atmospheric concentrations of xenon, krypton, and nitrogen (we liberally add N_2 to the noble gases, as its atmospheric residence time amounts to tens of millions of years) mirror the anomalies in total ocean heat content, as they are driven by changes in their temperature-dependent physical solubilities in ocean water. This allows us to reconstruct MOT in the past from the noble gas composition of a single ice core sample. A minor exception is the small amount of geothermal heating of ocean water, which is not connected to a noble gas change. Note that the MOT at a given time in the past represents a snapshot of the heat (and noble gas) content of all water parcels of the ocean and thus integrates over water bodies with different ventilation ages. Importantly, MOT is therefore not directly linked to mean global sea surface temperature at the same time, a point that has caused some confusion in the past.

Here we extend previous efforts in reconstructing MOT using noble gases in ice cores (Bereiter et al., 2018b; Baggenstos et al., 2019; Shackleton et al., 2020), which were limited to the last and penultimate glacial terminations, by reconstructing the glacial–interglacial MOT range for snapshots of all glacial and interglacial intervals over the last 700 000 years using the EPICA Dome C (EDC) ice core. To obtain quantitative MOT values, large corrections of the raw data for physical transport processes in the firn have to be applied, which affect the precision and accuracy of the MOT data. Moreover, gas fractionation processes in the ice between bubbles and clathrates in connection with potential post-coring gas loss have been observed (Bender et al., 1995), which have to be unambiguously identified to allow us to derive an unbiased MOT estimate, as described in detail in this study. Despite these corrections, we are able to derive quantitative MOT values from high-precision measurements of noble gas mixing ratios in the EDC ice core.

The paper is organized as follows: in Sect. 2 we describe the overall analytical procedure to obtain noble gas isotopic and elemental ratios with the associated uncertainty as well as the corrections that have to be applied to correct for systematic transport effects in the firn column. As EDC is a very low-accumulation site, which exhibits a permanent firn temperature gradient larger than 1 °C, thermal diffusion has to be precisely quantified. Moreover, we describe in detail for the first time the correction of kinetic fractionation by non-diffusive transport, adding an additional layer of complexity and uncertainty. Another process acting on the noble gas composition in the EDC ice core is post-coring gas loss that affects samples from the bubble–clathrate transition zone and, more severely, fully clathrated ice from the deepest ice at Dome C, which is close to the pressure melting point. These effects are described in detail for the first time in Sect. 3, and a hypothesis on how these lead to systematic noble gas fractionation is presented. For the reader only interested in the final results of our MOT reconstruction over the last 700 kyr and their discussion, we refer directly to Sect. 4 and the Conclusions section.

2 Measurement and corrections

2.1 Determination of noble gas elemental and isotopic ratios in ice cores

The data set presented here consists of 88 EDC ice samples (39 samples span the last 40 kyr, and 49 samples are from MIS 5 to MIS 17; Baggenstos et al., 2019) that were analyzed at the University of Bern. In order to test the representativeness of our EDC MOT data, 4 samples from the EPICA Dronning Maud Land (EDML) ice core, 4 samples from the Greenland Ice Core Project (GRIP) ice core, 4 samples from the Greenland NEEM ice core, 4 samples from the Antarctic Talos Dome ice core, and 13 blue ice samples from Taylor Glacier were measured. The Taylor Glacier samples stem from a lab intercomparison with the Scripps Institution of Oceanography in San Diego and showed excellent agreement within the analytical uncertainties between the two labs. Two samples from EDC (age > 700 kyr BP) were discarded due to bad ice quality together with drill fluid contamination, and one sample was rejected due to a procedural problem.

The gas extraction and processing broadly follow the method described in detail by Bereiter et al. (2018a). In short, after shaving off the outer surface ~ 600 g of ice is melt-extracted (equivalent to ~ 55 mL at the standard temperature and pressure (STP) of extracted air) and the released air is quantitatively frozen into stainless-steel dip tubes in a helium exchange cryostat. To equilibrate the sample and to avoid fractionation by thermal gradients in the dip tube, the dip tubes are kept for at least 10 h in a ventilated isothermal box. The samples are then split into two aliquots. The larger (~ 53 mL STP) aliquot is exposed to a Zr/Al getter alloy at 900 °C to remove all reactive gases and is analyzed in a peak-jumping routine on a Thermo Finnigan MAT 253 dual-inlet isotope ratio mass spectrometer (IRMS) for the isotopic ratios of xenon, krypton, and argon as well as their elemental ratios. The smaller aliquot (~ 2 mL STP) is passed through a CO_2 trap and measured on a Thermo Finnigan MAT Delta V dual-inlet IRMS in parallel for argon, oxygen, and nitrogen isotopes and their elemental ratios. The measurements were corrected for pressure imbalance and chemical slope according to the procedure described in Severinghaus et al. (2003). All data are reported in the delta notation with respect to a modern atmosphere standard collected outside the lab in Bern, Switzerland. Note that this atmospheric value reflects the current dissolution equilibrium of the studied gases between the atmosphere and the global ocean; this atmospheric standard is not subject to fractionation processes in the firn that affect air samples from ice cores. Accordingly, in the absence of any long-term changes in the total abundance of noble gas isotopes in the combined atmosphere and ocean reservoirs, each determined ice core value provides a measure of the difference in the ocean heat content at the age of the sample relative to today.

Table 1. Long-term reproducibility of the analyses (1 standard deviation) derived from 51 measurements of outside air on the MAT 253 and 46 measurements of outside air on the Delta V Plus.

Ratio	Uncert. (1σ)	IRMS
$\delta^{136/129}$Xe	0.037 ‰	MAT 253
$\delta^{132/129}$Xe	0.033 ‰	MAT 253
$\delta^{86/84}$Kr	0.014 ‰	MAT 253
$\delta^{86/82}$Kr	0.021 ‰	MAT 253
$\delta^{40/36}$Ar	0.006 ‰	MAT 253
δ^{15}N	0.007 ‰	Delta V Plus
δ^{132}Xe/^{84}Kr	0.148 ‰	MAT 253
δ^{129}Xe/^{84}Kr	0.156 ‰	MAT 253
δ^{132}Xe/^{40}Ar	0.197 ‰	MAT 253
δ^{129}Xe/^{40}Ar	0.173 ‰	MAT 253
δ^{84}Kr/^{40}Ar	0.125 ‰	MAT 253
δ^{40}Ar/^{28}N$_2$	0.052 ‰	Delta V Plus
δ^{32}O$_2$/^{28}N$_2$	1.117 ‰	Delta V Plus

The long-term reproducibility of our system, which was determined using outside air samples, may be found in Table 1. When normalized to one unit of mass difference, all isotopic ratios can be quantified to better than 10 per meg with uncertainties as low as 5 per meg per difference mass unit for $\delta^{136/129}$Xe, 7 per meg per difference mass unit for $\delta^{86/84}$Kr, and as low as 1.5 per meg per unit mass difference for $\delta^{40/36}$Ar. Only δ^{15}N values measured in this study did not yet reach the expected precision per unit mass difference. Accordingly, we refrain from using δ^{15}N to correct for gravitational or thermal diffusion fractionation in this study.

Despite this high analytical long-term reproducibility derived from outside air samples, some species showed a much higher scatter in ice core samples due to remnants of drill fluid in the gas sample after processing. Drill fluid interference in the mass spectrometer alters δ^{15}N and $\delta^{40/36}$Ar in the analysis of the smaller, non-gettered aliquot. The affected samples can be identified using an outlier routine and removed from the data set. Nitrogen isotopes were precisely measured by Dreyfus et al. (2010), Landais et al. (2013), and Bréant et al. (2019) in previous studies. Despite the lower precision of our δ^{15}N analyses, our results for samples not affected by drill fluid contamination are on average in good agreement with these values (see also Fig. 3). Nevertheless, we refrain from using the δ^{15}N and $\delta^{40/36}$Ar values measured using the smaller aliquot.

Unexpectedly, we also see outliers in $\delta^{86/82}$Kr and $\delta^{84/82}$Kr values in the gettered larger aliquot in the same samples in which we find the δ^{15}N and $\delta^{40/36}$Ar outliers, which points to an interference at mass 82. We have no conclusive evidence yet to indicate what is causing this interference. Potentially, the large variety of higher organic compounds in the drill fluid allows some component not to be completely gettered if the drill fluid contamination is too large and causes the mass 82 interference. Further lab experiments are required to elucidate this issue. In summary, we only use $\delta^{86/84}$Kr values in our further data evaluation.

To derive MOT, we need to know the changes in the noble gas mixing ratios (δKr/N$_2$, δXe/N$_2$, and δXe/Kr). To obtain them, we mathematically combine δXe/Ar, δKr/Ar, and δAr/N$_2$. Ar itself is not used as a reference element because argon is preferentially excluded relative to N$_2$, xenon, and krypton during bubble formation at the firn–ice transition (Severinghaus and Battle, 2006). The uncertainties calculated by error propagation of the analytical errors in the elemental ratios used in this calculation are 0.136 ‰ and 0.181 ‰ for δKr/N$_2$ and δXe/N$_2$, respectively.

2.2 Inferring atmospheric noble gas ratios from raw data

While the troposphere is well-mixed through turbulent processes, the low permeability of the firn restricts bulk flow; thus, the gas transport is controlled by molecular diffusion. All measured isotope and elemental ratios we extract from the ice core samples (reported as "raw ratios") are therefore highly fractionated with respect to the atmospheric values (as illustrated by the strongly positive δ values in Fig. 1), mainly due to gravitational enrichment in the diffusive zone of the firn but also thermal diffusion if a temperature gradient is present in the firn column (Schwander et al., 1988) or non-diffusive transport processes that disturb the diffusive equilibrium (so-called kinetic fractionation). These systematic fractionations in the isotopic and elemental ratios have to be corrected for, as illustrated in Fig. 2.

Moreover, post-coring gas losses accompanied by gas fractionation processes have been observed in our samples in the bubble–clathrate transition zone (BCTZ) and in poorly preserved and cracked ice, mainly in the deepest section of the ice core. While the gas fractionation processes mentioned above can be corrected for using the full matrix of noble gases and their isotopes, the gas loss fractionation cannot yet be quantitatively corrected for, and affected samples have to be unambiguously identified using clear detection criteria and removed from the data set. In the following sections, the systematic correction of the isotopic and elemental ratios is described, while the post-coring gas loss and its detection are described in Sect. 3.

2.2.1 Systematic processes altering the isotopic and elemental ratios

Geological outgassing of ^{40}Ar

In contrast to the nitrogen, krypton, and xenon isotopes as well as ^{36}Ar and ^{38}Ar, the atmospheric abundance of ^{40}Ar has gradually increased over time. This atmospheric ^{40}Ar increase is caused by integrated ^{40}Ar outgassing throughout Earth's history due to the radioactive decay of ^{40}K in the crust and mantle (Bender et al., 2008). Assuming the ^{40}Ar increase is constant in time, the effect can be corrected if the age of the sample is known. In this study, we use $\delta^{40/36}$Ar values corrected for outgassing according to Bender et al. (2008).

$$\Delta\delta^{40/36}\mathrm{Ar}_{\mathrm{outgas}} = 6.6 \times 10^{-5}\,‰/\mathrm{kyr} \times t_{\mathrm{gas}} \tag{1}$$

Here, the gas age t_{gas} has units of thousands of years before present (kyr BP). The outgassing effect on MOT is small for samples from the last transition (< 0.1 °C), but it becomes more important for samples in the deeper and older ice (on the order of 1 °C for the oldest samples).

Gravitational enrichment

Gas transport in the pore space of the firn column is controlled by molecular diffusion below a convective zone in the top meters of the firn. In this diffusive column molecules of different masses are separated, leading to gravitational enrichment of the heavier gases and isotopes at the bottom of the firn column where bubble close-off occurs. Thus, all elemental and isotopic ratios are strongly enriched in the heavier gases compared to the atmosphere according to

$$\Delta\delta_{\mathrm{grav}}(z) = \delta_{\mathrm{grav}}(z) - \delta_{\mathrm{atm}} = ((\delta_{\mathrm{atm}} + 1) \times e^{\frac{\Delta m g z}{R T}} - 1) - \delta_{\mathrm{atm}}, \tag{2}$$

where g is the local gravitational acceleration, R the gas constant, and T the mean firn temperature (Craig et al., 1988; Schwander, 1996). To correct for the gravitational enrichment of the elemental ratios at the lock-in depth, we have to know the diffusive column height (DCH) z of the firn (where z is defined positive downward), which can be directly derived from the isotopic enrichment of the individual gas species after corrections for thermal diffusion and kinetic effects (see below).

Thermal diffusion

The second diffusive process leading to fractionation of the air in the firn column is thermal diffusion. It refers to the fractionation of a gas mixture in the presence of a temperature gradient. This leads to an enrichment of the heavier components at the cold end of the firn column according to the laboratory-determined thermal diffusion sensitivity $\Omega^{X/Y}$ for

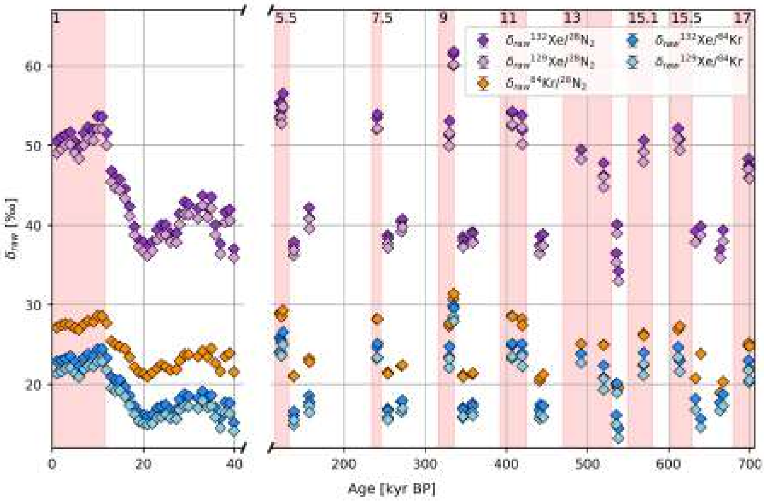

Figure 1. Measured delta values of the EDC elemental ratios from 700 kyr BP to the present. The analytical uncertainties of the elemental ratios are too small (on the order of 0.1 ‰; see text) to be displayed here. The red shaded intervals indicate interglacials as identified by Masson-Delmotte et al. (2010).

two gas or isotope species X and Y, where $\Omega^{X/Y}$ is specific for the gas mixture (Severinghaus et al., 2003).

$$\Delta\delta_{\mathrm{therm}} = \Omega^{X/Y} \times \Delta T \tag{3}$$

Here, ΔT is defined as the temperature difference between the top and the bottom of the DCH. As EPICA Dome C is a low-accumulation site, the mean annual firn temperature increases with depth (in the absence of temporal climate changes at the surface; Ritz et al., 1982) due to the geothermal heat flux at the bottom, and the gas enclosed in bubbles is expected to be slightly depleted by thermal diffusion relative to its gravitational value. Note that this thermal fractionation is gas-species-dependent and much larger for the lighter gases. Here we use the thermal diffusion sensitivities given by Kawamura et al. (2013) and Headly (2008).

Kinetic fractionation: the heavy isotope deficit

If only diffusive processes occurred in the firn column, the differences between any of the measured isotope ratios could be used to unambiguously reconstruct the thermal and gravitational fractionation components using the well-known thermal diffusion sensitivity parameters (Kawamura et al., 2013; Headly, 2008). In particular, as the gravitational enrichment of two gases only differs according to the mass difference between two gases, the gravitational enrichment normalized to unit mass difference should be the same for all gases. However, even after the thermal diffusion correction the isotopic ratios of different gases per unit mass difference still reveal systematic offsets (see Fig. 3a), indicating that there is another mechanism at play that we have yet to correct for.

The reason for the systematic differences in the isotopic ratios per unit mass difference between the different gases at Dome C in Fig. 3 is the occurrence of advective processes in the firn such as turbulent mixing at the surface (Kawamura et al., 2013), barometric pumping, and the net vertical movement of air by ice flow and compression (Buizert and Severinghaus, 2016; Birner et al., 2018) that all disturb the diffusive equilibrium in the firn column. The term coined for this difference in measured isotopic ratios per unit mass difference after thermal correction is heavy isotope deficit (HID) (Buizert and Severinghaus, 2016) or differential kinetic fractionation (Birner et al., 2018) between the isotopic or elemental ratio X and another isotopic or elemental ratio Y. Further on, we will use the difference between the kinetic fractionation of an isotopic or elemental ratio X per unit mass difference relative to the kinetic fractionation in N_2 isotopes (Kawamura et al., 2013; Birner et al., 2018; Buizert and Severinghaus, 2016). For example, for Ar isotopes this fractionation is defined as

$$\epsilon^*_{\mathrm{Ar-N_2}} = \Delta\delta^{40/36}\mathrm{Ar}^*_{\mathrm{kin}} - \Delta\delta^{15}\mathrm{N}^*_{\mathrm{kin}}. \tag{4}$$

Here, * indicates that the values are normalized to unit mass difference, for example $\delta^{40/36}\mathrm{Ar}^*_{\mathrm{kin}} = \delta^{40/36}\mathrm{Ar}_{\mathrm{kin}}/4$. Note that the heavier (and slowly diffusing) gases like xenon and krypton will be further from diffusive equilibrium than lighter (and faster-diffusing) gases like argon and nitrogen. Another way to put this is that the effective DCH of different gases is not the same, with z being a little shorter for heavier, less diffusive gases.

In our measurements the total deficit of xenon and krypton isotopes relative to argon isotopes per unit mass differ-

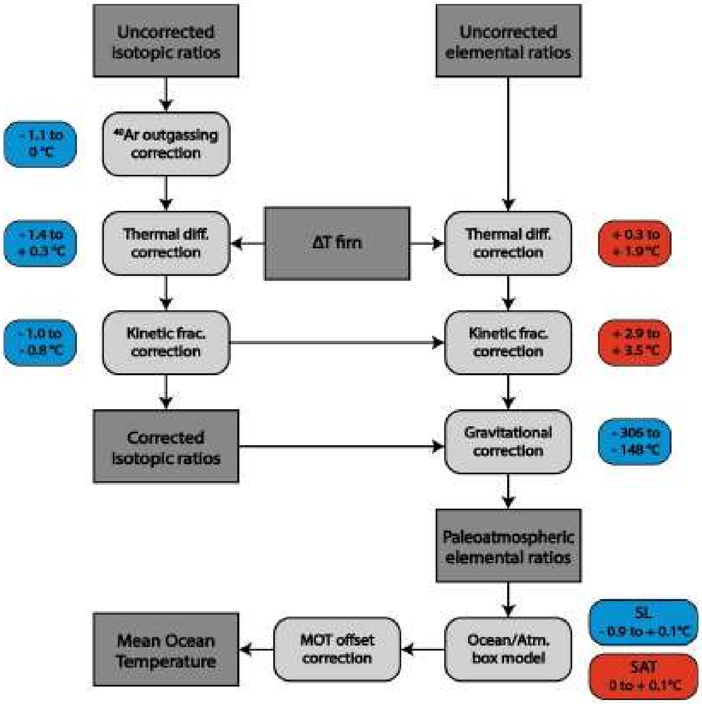

Figure 2. Flow scheme to infer paleo-atmospheric elemental ratios and finally MOT using the measured elemental ($\delta\mathrm{Kr/N_2}$, $\delta\mathrm{Xe/N_2}$, and $\delta\mathrm{Xe/Kr}$) and isotopic ratios ($\delta^{40/36}\mathrm{Ar}$, $\delta^{86/84}\mathrm{Kr}$, $\delta^{136/129}\mathrm{Xe}$). Values are indicated by dark grey square boxes, while applied corrections are illustrated by rounded boxes in lighter grey. In a first step, the $\delta^{40/36}\mathrm{Ar}$ isotope ratios have to be corrected for changes in $^{40}\mathrm{Ar}$ due to geological outgassing. The isotopic and elemental ratios are then corrected for thermal diffusion and kinetic fractionation. The temperature difference between the top and the bottom of the diffusive column height required for the correction of thermal diffusion is derived using either a firn column model (Michel, 2016) or the full matrix of noble gas isotopes. For the kinetic fractionation, we assume fixed ratios between isotopic and elemental ratios (Birner et al., 2018). Finally, the corrected isotopic ratios are used to correct the elemental ratios for the gravitational enrichment. The corrected elemental ratios are then translated into MOT using an ocean atmosphere box model. Here, we correct for the influences of sea level (SL) change and the saturation state (SAT) of the global ocean. In a last step, the resulting MOTs are corrected for their Holocene offset (see text for details). The approximate range of the respective correction performed on all our samples for MOT values can be found in the colored boxes. Positive values (red boxes) imply that the correction leads to an increase in absolute MOT values. It is important to stress that the size of the correction is not a measure of the uncertainty associated with it. The gravitational enrichment correction, for example, dominates all other corrections by orders of magnitude. Nonetheless, the analytical uncertainty of that correction is only minor, as it is largely given by the uncertainty in diffusive column height, the exact determination of which is one of our analytical foci. Also note that it is the size of the range of a correction, rather than the absolute value of the correction, that has an influence on glacial–interglacial MOT differences. For example, although the correction of elemental ratios for kinetic fractionation appears to be the second most influential correction, when considering its absolute value, its range is only narrow. Thus, it alters the glacial–interglacial MOT difference only slightly.

ence over the last 40 kyr is on average -0.046 ± 0.007 ‰ and -0.029 ± 0.007 ‰, respectively (here and throughout the paper all uncertainties refer to 1σ). This total deficit comes about through the combined effect of different thermal diffusion sensitivities of the different gases and gas-specific kinetic fractionation. Separation of these two effects on the total deficit requires corrections for the thermal gradient, as described in Sect. 2.2.2.

Birner et al. (2018) discovered that while the absolute magnitude of kinetic fractionation $\Delta\delta^{*}_{\mathrm{kin}}$ may vary substantially between different ice core sites, the kinetic fractionations between two gases occur in fixed ratios between isotopic and elemental ratios for a variety of firn regimes. Thus, although we do not know the absolute kinetic fractionation at Dome C for an individual gas for past firn conditions a priori, we can use the results by Birner et al. (2018) together with our multiple gas species and transient firn temperature modeling to correct for the HID and other gas transport effects. It is worth noting that the ratios of the mean kinetic fractionations over the last 40 kyr as displayed in Fig. 3 agree well within uncertainties with the ratios predicted by Birner et al. (2018). Note that the kinetic fractionations for the last 40 kyr displayed in Fig. 3 also suggest, apart from substantial analytical scatter, some systematic variations. As these systematic variations are generally in line with the fractionation ratios predicted by Birner et al. (2018), the changes are likely caused by changing kinetic fractionation conditions with time (stronger barometric pumping, higher wind speeds at the surface, etc.). However, some samples older than 40 kyr show much higher deviations from the mean that cannot be explained by analytical uncertainty or changing kinetic fractionation. Accordingly, we do not use the individual HID values of each sample as displayed in Fig. 3b for samples older than 40 kyr to quantify $\epsilon^*_{\mathrm{Ar-N_2}}$. Instead, we use the mean isotopic fractionation derived for the last 40 kyr and assume that this mean value is also representative for the correction of our samples older than 40 kyr. As the choice of $\epsilon^*_{\mathrm{Ar-N_2}}$ has a systematic effect on the final reconstructed MOT, we also take the variation of $\epsilon^*_{\mathrm{Ar-N_2}}$ over the last 40 kyr into account to quantify the systematic uncertainty introduced by this choice. Thus, we use the mean kinetic fractionation over the last 40 kyr plus (minus) its standard deviation as upper (lower) bounds of the kinetic fraction to calculate MOT. We regard this as a systematic uncertainty in our MOT reconstruction and separate this uncertainty from the stochastic uncertainty introduced by the analytical error.

Gas loss effects on isotopic ratios

As mentioned in the previous paragraph, ice core samples with heavy post-coring gas loss exhibit enriched $\delta^{40/36}$Ar, while δ^{15}N is unaffected (J. Severinghaus, personal communication, 2021). Due to their large size, the krypton and xenon isotopes are also not affected. Correction coefficients for argon isotope enrichment in bubble ice have been suggested by Kobashi et al. (2008b), but it is not certain whether these correction factors describe the gas loss quantitatively and in particular whether they can be used for ice from any depth and for all ice cores. We refrain from trying to correct this effect because we do not see evidence for an isotope fractionating effect by artifactual gas loss (see Sect. 3.1) and because no correction coefficients have been established for clathrate ice.

2.2.2 Correcting isotopic ratios for transport processes in the firn column

As outlined above, the measured isotopic ratio δ^*_{meas} is influenced by a series of processes that alter the paleo-atmospheric value δ^*_{atm}. We can write the following for the measured isotopic ratio.

$$\delta^*_{\mathrm{meas}} = \delta^*_{\mathrm{atm}} + \Delta\delta^*_{\mathrm{grav}} + \Delta\delta^*_{\mathrm{therm}} + \Delta\delta^*_{\mathrm{kin}} \quad (5)$$

Note that we assume ocean solubility effects on the isotopic ratios to be negligible (in contrast to the elemental ratios, for which we use these effects to quantify MOT). This can be justified using a two-box model calculation with the recently determined solubility fractionation factors in seawater (Seltzer et al., 2019) and imposed ocean temperature differences, which yields glacial–interglacial changes in atmospheric noble gas isotope composition of less than 0.001 ‰ per unit mass difference. We can thus safely assume that for isotopic ratios $\delta^*_{\mathrm{atm}} = 0$ (where for Ar isotopes the atmospheric value has to be corrected for Ar outgassing as described in Sect. 2.2).

Using the measured isotopic ratios we are able to quantify the fractionation effects and correct the isotopic and elemental ratios. Here we explore two different correction pathways that differ in the derivation of ΔT, which is required to quantify the thermal diffusion effect. Both possibilities use the matrix of isotopic ratios to constrain the gravitational enrichment and the HID. However, one possibility uses a 1D ice flow model connected to a dynamic heat advection and diffusion model (Michel, 2016) to quantify the thermal diffusion effect, while the other uses the full matrix of noble gas isotopes measured in this study to quantify ΔT empirically.

(a) Correction using a firn temperature model

To correct for the strong gravitational enrichment (large mass difference) we can use the precisely measured isotopic ratios after correcting for thermal diffusion and kinetic fractionation. Due to the firn temperature slightly increasing with depth at EDC and due to the negative kinetic fractionation for heavier gases, the corrected isotopic ratios are slightly increased compared to the measured ratio. The results for the thermally corrected isotopic ratios reflecting the remnant kinetic fractionation are shown in Fig. 3a, where ΔT used for the thermal correction of each individual sample was calculated using an ice flow–heat flow model as described below. The isotopic ratio least affected by kinetic fractionation is δ^{15}N; however, our δ^{15}N measurements are not as precise as $\delta^{40/36}$Ar per unit mass difference, and some of the δ^{15}N values had to be discarded due to drill fluid contamination affecting the mass spectrometric analysis. Accordingly, we use $\delta^{40/36}$Ar as our reference isotope. In many applications to reconstruct temperature using isotopic ratios of permanent gases (e.g., Kobashi et al., 2008a), the small kinetic fraction of Ar relative to N_2 is neglected and the gravitational enrichment per unit mass difference $\Delta\delta^*_{\mathrm{grav}}$ in units of per mill is calculated according to

$$\Delta\delta^*_{\mathrm{grav}} = \delta^{40/36}\mathrm{Ar}^* - \Omega^{40/36*} \times \Delta T, \quad (6)$$

where the * in $\Omega^{40/36*}$ indicates that the thermal sensitivity has been normalized to unit mass difference.

However, firn gas pumping and modeling experiments (Kawamura et al., 2013) show that all gases are subject to

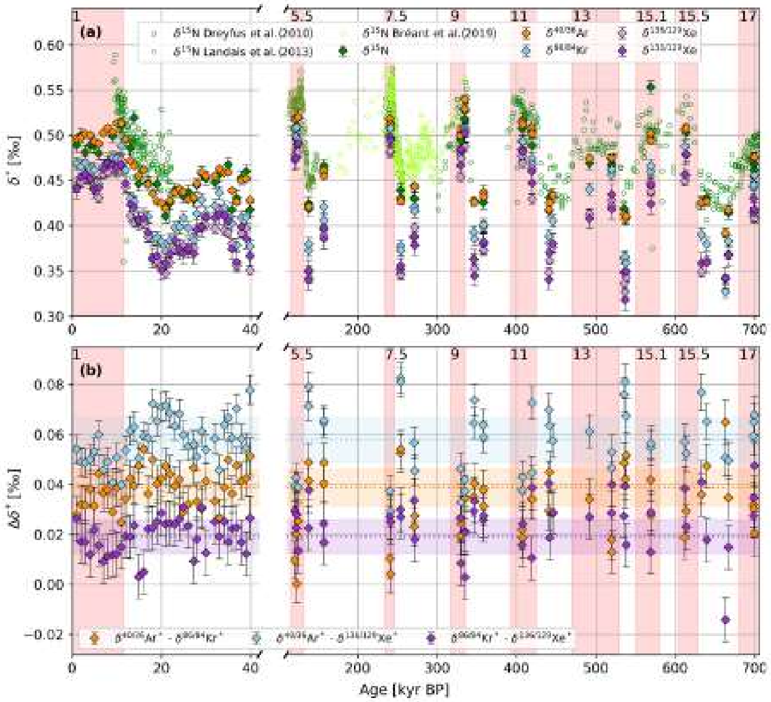

Figure 3. (a) Isotopic enrichment of the EDC samples from 700 kyr BP to the present. All isotopic data are shown per unit mass difference and reported relative to modern air sampled in Bern, Switzerland. The data are corrected for thermal fractionation as described in the text. In the case of δ^{15}N, data points contaminated with drilling fluid have been excluded. The circles in darker green, olive, and lighter green represent measurements from the EDC ice core from Dreyfus et al. (2010), Landais et al. (2013), and Bréant et al. (2019), which have been corrected for thermal fractionation using our model-derived firn temperatures. (b) Difference between the isotopic ratios of the EDC samples after correction for thermal fractionation. The dashed line is the mean difference from the samples over the last 40 kyr, with the shaded areas representing their standard deviation. The red shaded intervals and the MIS numbers on top indicate interglacials as identified by Masson-Delmotte et al. (2010).

kinetic fractionation, and therefore even Ar isotopes show a small heavy isotope deficit $\epsilon^*_{\mathrm{Ar-N_2}}$ after correction of thermal diffusion effects (Buizert and Severinghaus, 2016) compared to nitrogen isotopes. Thus, $\Delta\delta^*_{\mathrm{grav}}$ should be calculated according to

$$\begin{aligned}\Delta\delta^*_{\mathrm{grav}} &= \delta^{40/36}\mathrm{Ar}^* - \Omega^{40/36*}\cdot\Delta T - \Delta\delta^{40/36}\mathrm{Ar}^*_{\mathrm{kin}}\\ &= \delta^{40/36}\mathrm{Ar}^* - \Omega^{40/36*}\cdot\Delta T - \epsilon^*_{\mathrm{Ar-N_2}} - \Delta\delta^{29/28}\mathrm{N}^*_{2,\mathrm{kin}}.\end{aligned} \tag{7}$$

The absolute kinetic fractionation $\Delta\delta^{40/36}\mathrm{Ar}^*_{\mathrm{kin}}$ in Eq. (7) is not known a priori and is dependent on firn and meteorological conditions at the site that may have changed in the past. Using the equivalent equation for Xe isotopes and the linear relationship of the kinetic fractionations given by Birner et al. (2018), $\epsilon^*_{\mathrm{Ar-N_2}}$ can be calculated from our measurements according to

$$\begin{aligned}\epsilon^*_{\mathrm{Ar-N_2}} &= (\delta^{136/129}\mathrm{Xe}^*_{\mathrm{meas}} - \delta^{40/36}\mathrm{Ar}^*_{\mathrm{meas}}\\ &- (\Omega^{136/129*} - \Omega^{40/36*})\cdot\Delta T)/6.3.\end{aligned} \tag{8}$$

Note that while including the kinetic fractionation may improve the accuracy of the reconstruction, it slightly decreases the precision, as the analytical error for Xe isotopes also comes into play.

ΔT in Eqs. (7) and (8) is unknown but can be estimated for each individual sample using an ice flow–heat flow model that solves the ice advection–firn compaction and the heat advection and diffusion equation transiently over the last million years. Here we used the model by Michel (2016) and a parameterization of heat diffusion and heat conductivity according to Cuffey and Paterson (2010). The density of the firn was estimated by the Herron–Langway model (Michel, 2016). Heat diffusivity of the very porous top 10 m of the firn was corrected according to Weller and Schwerdtfeger (1970). The recent firn temperature difference ΔT in this run agreed within ±0.2 °C between the model and measured firn temperature profiles at Dome C (Buizert et al., 2020). We assume that ±0.2 °C represents the analytical uncertainty of the model. Surface temperature and snow accumulation used in the model are prescribed using the EDC temperature record over the last 800 000 years (Jouzel et al., 2007; Bazin et al., 2013), and a scaled version of the stacked marine δ^{18}O record (Lisiecki and Raymo, 2005) is used for earlier times. For an optimal fit with the measured temperature profile over the entire ice thickness at Dome C, a +2 °C correction of glacial temperatures was applied by Michel (2016); however, this has only a very small effect on the firn temperature difference. Ice thickness changes over the last 800 kyr are taken from Parrenin et al. (2007), and a scaled version of the stacked marine δ^{18}O record is used for earlier times. The constant geothermal heat flux and the thinning function were chosen to optimize the agreement of the modeled temperature profile with borehole temperature measurements (Buizert et al., 2020) and the age profile at Dome C (Bazin et al., 2013).

The DCH affects both the gravitational enrichment and the absolute value of the temperature gradient. Accordingly, we use an iterative approach for Eq. (7) to determine the firn temperature gradient from the model results. In the first step we neglect the temperature gradient, and thus thermodiffusion effects, to estimate the DCH:

$$z = \ln\left(\frac{\Delta\delta^*_{\mathrm{grav}}}{1000} + 1\right) \cdot \frac{\mathrm{R}T}{\Delta m^* \mathrm{g}}, \tag{9}$$

where Δm^* is the unit mass difference in kilograms per mole (kg mol^{-1}). After this first step we read out the modeled firn temperature difference for this depth and use it for the thermal diffusion correction in the next step. Using this iterative approach the firn column depth converges after two iterations. This model-based analysis shows that the firn column depth is about 70–80 m for glacial periods and 90–100 m for interglacials.

The kinetic fractionation $\epsilon^*_{\mathrm{Ar-N_2}}$ calculated using modeled ΔT is on average -0.009 ± 0.001 ‰ (1σ) over the last 40 kyr (note that the HID values given in Fig. 3b represent a measure of $\epsilon^*_{\mathrm{Ar-N_2}}$ scaled by a factor of 6.3, 4.25, and 2.05 for $\epsilon^*_{\mathrm{Xe-Ar}}$, $\epsilon^*_{\mathrm{Kr-Ar}}$, and $\epsilon^*_{\mathrm{Xe-Kr}}$, respectively, as derived from Birner et al., 2018). As described above, we use the mean plus or minus the standard deviation of the kinetic fractionation over the last 40 kyr to also correct the samples older than 40 kyr and to assess the uncertainty introduced by this correction.

The last unknown in Eqs. (7) and (4) is the amount of kinetic fractionation for nitrogen isotopes $\Delta\delta^{15}\mathrm{N}^*_{\mathrm{kin}}$. Modeling and firn air studies by Buizert and Severinghaus (2016) and Birner et al. (2018) show that at WAIS Divide, i.e., a site on the West Antarctic Plateau, this fractionation is less than 0.005 ‰, while at Law Dome, a site subject to strong barometric pumping, it may be larger (J. Severinghaus, personal communication, 2021). Assuming a kinetic fractionation at Dome C that is similar to WAIS, this small fractionation in $\Delta\delta^{15}\mathrm{N}^*_{\mathrm{kin}}$ translates into an offset in the final MOT values on the order of 0.01 °C and can therefore be safely neglected in our MOT reconstruction.

In the following, we assume $\Delta\delta^{15}\mathrm{N}^*_{\mathrm{kin}} = 0$ for Dome C, where synoptic pressure variations and wind speeds are rather low. Neglecting potential errors in the thermal diffusion sensitivities, the uncertainty in $\Delta\delta^*_{\mathrm{grav}}$ introduced by this model-based method to correct the data is 0.003 ‰ (1σ).

(b) Correction using measured isotopic ratios only

Using the firn temperature model as in (a) assumes that the firn temperature difference in the model over the DCH realistically resembles the temperature difference seen by the gas at the age of each individual sample. The model neglects, for example, seasonal variations in the temperature gradient, which may not cancel out in the long-term annual average, and also assumes that the current parameterizations used for firn density, heat conduction, and heat diffusivity profiles in the firn are also representative for past conditions. An alternative way is therefore to use only experimental evidence from our full matrix of isotope ratios. Assuming that gravitational enrichment, thermal diffusion, and kinetic fractionation completely describe the fractionation processes occurring in the firn column, this approach provides a purely measurement-based estimate of $\epsilon^*_{\mathrm{Ar-N_2}}$ and ΔT.

The equivalent to Eq. (8) for Kr isotopes is

$$\begin{aligned}\epsilon^*_{\mathrm{Ar-N_2}} &= (\delta^{86/84}\mathrm{Kr}^*_{\mathrm{meas}} - \delta^{40/36}\mathrm{Ar}^*_{\mathrm{meas}} \\ &- (\Omega^{86/84*} - \Omega^{40/36*}) \cdot \Delta T)/4.25,\end{aligned} \tag{10}$$

with the constant ratio of kinetic fractionations for different isotopes given by Birner et al. (2018).

Solving Eq. (8) for ΔT and inserting it into Eq. (10), it follows that

$$\begin{aligned}&\epsilon^*_{\mathrm{Ar-N_2}} \\ &= \frac{(\delta^{86/84}\mathrm{Kr}^* - \delta^{40/36}\mathrm{Ar}^*) - \alpha(\delta^{136/129}\mathrm{Xe}^* - \delta^{40/36}\mathrm{Ar}^*)}{4.25 - 6.3\alpha},\end{aligned} \tag{11}$$

where $\alpha = (\Omega^{86/84^*} - \Omega^{40/36*})/(\Omega^{136/129*} - \Omega^{40/36*})$. Note that the mean kinetic fractionation $\epsilon^*_{\mathrm{Ar-N_2}}$ derived using this data-based approach is on average -0.009 ‰ over the last 40 kyr and thus in perfect agreement with the results from the firn temperature model approach.

Using Eq. (11) in Eq. (8) finally leads to

$$\begin{aligned}&\Delta T \\ &= \frac{(\delta^{136/129}\mathrm{Xe}^* - \delta^{40/36}\mathrm{Ar}^*) - \frac{6.3}{4.25 - 6.3\alpha}((\delta^{86/84}\mathrm{Kr}^* - \delta^{40/36}\mathrm{Ar}^*) - \alpha(\delta^{136/129}\mathrm{Xe}^* - \delta^{40/36}\mathrm{Ar}^*))}{\Omega^{136/129*} - \Omega^{40/36*}}.\end{aligned} \tag{12}$$

While this method in principle avoids any potential systematic uncertainties in the firn temperature gradient, it substantially increases the uncertainty of the reconstruction, as now the analytical uncertainties of all three noble gas isotopic ratios have to be taken into account for each individual sample. Using Monte Carlo error propagation, the uncertainty in $\epsilon^*_{\mathrm{Ar-N_2}}$ derived in this approach is increased to 0.01 ‰

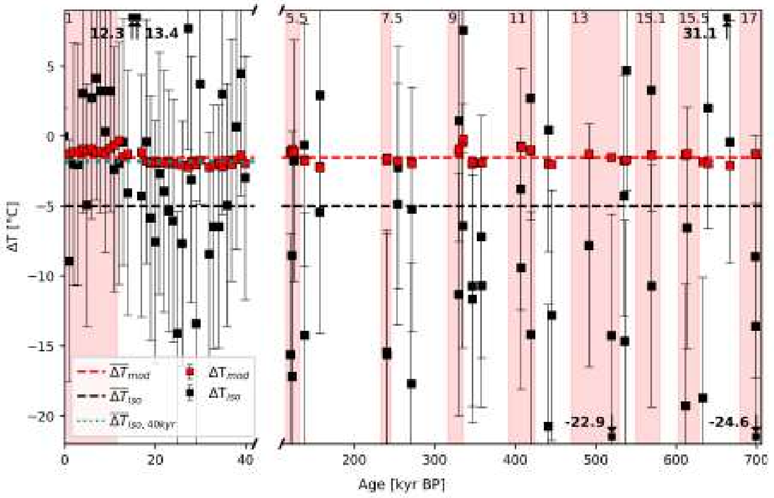

Figure 4. Comparison of the firn temperature difference ΔT_{mod}, as derived from the ice flow–heat flow model of Michel (2016) (red squares), and ΔT_{iso} obtained using measured isotopic ratios only (black squares). Dashed lines in red and black indicate the overall mean values for ΔT_{mod} and ΔT_{iso}, while the dotted line in cyan represents the mean ΔT_{iso} when considering samples from the first 40 kyr only. The red shaded intervals and the MIS numbers on top indicate interglacials as identified by Masson-Delmotte et al. (2010).

(i.e., roughly 10 times larger than in the model-based approach), and the uncertainty in ΔT becomes about 8 °C. This translates into an error for $\Delta\delta^*_{\mathrm{grav}}$ of roughly 0.08 ‰ (i.e., almost 30 times higher than in the model-based approach) and finally into an error in the corrected elemental ratios (see Sect. 2.2.3) of several per mill, which is prohibitive for a reliable reconstruction of MOT for individual samples.

The very high scatter in data-derived ΔT is displayed in Fig. 4. The standard deviation of ΔT over the last 40 kyr is 6 °C, which is of the same order as the expected analytical uncertainty in ΔT of 8 °C derived from error propagation. Hence, this large scatter can be explained by analytical noise and shows that any systematic variation in ΔT over the last 40 kyr cannot be reliably quantified using the data-based approach.

Looking at Fig. 4 it should be stressed that despite the large scatter the mean ΔT over the last 40 kyr derived in this data-based approach is in excellent agreement with ΔT derived in the model-based approach. This points to the fact that using our noble gas isotope measurements we are able to accurately (but not sufficiently precisely) reconstruct $\epsilon^*_{\mathrm{Ar-N_2}}$ and ΔT over the last 40 kyr and that thermal diffusion and kinetic fractionation fully explain the systematic offsets of the isotopic ratios.

However, for the samples older than 40 kyr the average ΔT is -7.7 ± 9.7 °C, which is physically not in line with the observed or modeled firn temperature differences and also not in line with the results younger than 40 kyr. As we do not expect that any unknown firn fractionation processes were active prior to 40 kyr BP that did not occur over the last 40 kyr, this apparent offset in ΔT either reflects the large scatter of the data or is related to an isotope fractionating Ar loss process during transport, when the samples got relatively warm for a short period of time.

As mentioned above, using the data-based approach to correct the elemental ratios for each individual sample is not a viable solution, as the scatter in reconstructed ΔT, $\epsilon^*_{\mathrm{Ar-N_2}}$, and thus MOT is too large. Therefore, we regard the mean $\epsilon^*_{\mathrm{Ar-N_2}}$ and ΔT values over the last 40 kyr to be representative for the entire record and use those to calculate $\Delta\delta^*_{\mathrm{grav}}$. To quantify the systematic uncertainty introduced by this choice of $\epsilon^*_{\mathrm{Ar-N_2}}$ and ΔT, we calculate an upper (lower) estimate of ΔT and $\epsilon^*_{\mathrm{Ar-N_2}}$ as defined by their mean values over the last 40 kyr plus (minus) their standard deviation. This provides us with a range of values for $\Delta\delta^*_{\mathrm{grav}}$ for the systematic corrections of the elemental ratios (see Sect. 2.2.3). We refer to this correction as the mean data-based approach further on.

We stress that while such a constant correction with a systematic range of possible values has a significant impact on the absolute reconstructed MOT value, the impact of the correction on the glacial–interglacial difference in MOT is small. Moreover, the glacial–interglacial difference in MOT is very similar whether one uses the model-based approach in (a) or the mean data-based approach in (b). Accordingly, only MOT differences relative to the Holocene are considered, as was also the case in the study by Shackleton et al. (2020).

In summary, the data-based approach shows that we can quantitatively correct the gas-transport-related fractionations that occur in the firn column; however, the precision of the data-based approach is not sufficient for single samples. Accordingly, in the discussion of our final MOT data in Sect. 4 we do not use the data-based approach and rely on the much more precise model-based correction.

2.2.3 Correction of the elemental ratios

Equivalent to isotopic ratios of one gas species, the ratios of two different gas species (here referred to as elemental ratios) have to be corrected for gravitational enrichment. Due to the large mass difference between two gas species, this gravitational correction of elemental ratios is substantial. In addition, thermal diffusion and kinetic fractionation have to be corrected in the elemental ratios. For the $\mathrm{Kr/N_2}$ ratio this can be summarized according to

$$\begin{aligned}&\delta \mathrm{Kr/N_{2,atm}} = (\delta \mathrm{Kr/N_{2,meas}} - \Omega^{\mathrm{Kr/N_2}} \Delta T \\ &- (\epsilon^{*}_{\mathrm{Kr/N_2-N_2}} + \Delta\delta^{15}\mathrm{N}^{*}_{\mathrm{kin}}) \cdot \Delta m/\Delta m^{*} + 1) \\ &\cdot (\Delta\delta^{*}_{\mathrm{grav}} + 1)^{-\Delta m/\Delta m^{*}} - 1, \qquad (13)\end{aligned}$$

where again we set $\Delta\delta^{15}\mathrm{N}^{*}_{\mathrm{kin}} = 0$, as the effect of $\Delta\delta^{15}\mathrm{N}^{*}_{\mathrm{kin}}$ is negligible compared to other uncertainties. The first factor in brackets on the right-hand side represents the measured value of the elemental ratio corrected for thermal diffusion and kinetic fractionation, while the second factor corrects this isotopic ratio for its gravitational enrichment. ΔT, $\epsilon^{*}_{\mathrm{Kr/N_2-N_2}}$, and $\Delta\delta^{*}_{\mathrm{grav}}$ can be calculated from the firn temperature model and from the isotopic data as described above using the fixed ratios of kinetic fractionation given by Birner et al. (2018). Note that the exponent $\Delta m/\Delta m^{*}$ is very large (e.g., 56 for $^{84}\mathrm{Kr}$ and $^{28}\mathrm{N_2}$); thus, the gravitational correction is substantial and sensitive to any analytical error in the isotopic ratios as well as in uncertainties in the thermal correction and the kinetic fractionation.

Here we use both the model-based and the mean data-based reconstruction of ΔT and $\epsilon_{\mathrm{Kr/N_2-N_2}}$ described above and apply these to Eq. (13) and equivalent equations for $\mathrm{Xe/N_2}$ and $\mathrm{Xe/Kr}$ ratios. The results of these corrections are shown in panel (a) (model-based reconstruction) and (b) (mean data-based reconstruction) of Fig. 5. Note that the whiskers in Fig. 5 represent the stochastic error (1σ) due to error propagation of the analytical uncertainties, while the size of the boxes represents the systematic uncertainties (1σ) introduced by our choice of mean ΔT and $\epsilon_{\mathrm{Kr/N_2-N_2}}$.

The first observation is that the three different atmospheric elemental ratios have different glacial–interglacial amplitudes, primarily reflecting the different temperature sensitivities of gas solubility in the ocean as expected. Secondly, the corrected elemental ratios show that although our data are referenced to recent outside air at Bern, reflecting late Holocene ocean temperatures, the Holocene elemental ratios after all corrections are not equal to zero but systematically shifted to positive values.

Holocene elemental ratios larger than zero have also been recently observed by Shackleton et al. (2020) using Taylor Glacier ice, reflecting our insufficient quantitative understanding of fractionation processes in the firn; this requires more dedicated firn gas sampling and firn gas transport modeling studies that realistically resolve seasonal variations in the gas transport, pressure variability, and kinetic fractionation. However, glacial–interglacial differences in our corrected elemental ratios are not sensitive to this overall offset. If we use changes in atmospheric elemental ratios relative to the Holocene mean, both the model-based and the mean data-based approach provide very similar results. For example, using the model-based approach, the corrected last glacial $\delta \mathrm{Xe/Kr}$ values are on average about 3.0 ‰ lower than the Holocene values, which is in agreement within uncertainties with the results by Bereiter et al. (2018b) using ice from the WAIS Divide ice core.

The final observation pertains to the scatter of the data. Elemental ratios corrected using ΔT and $\epsilon_{\mathrm{Kr/N_2-N_2}}$ derived using the data-based approach for each individual sample provide no meaningful results, as the analytical scatter introduced from all three isotopic ratios is too large.

Using the model-based approach, we introduce uncertainty through the elemental ratio analysis, the uncertainty in our model-based ΔT, and systematic uncertainty through our use of the mean $\epsilon_{\mathrm{Kr/N_2-N_2}}$ over the last 40 kyr to correct the kinetic fractionation. This leads to a substantially smaller scatter than in the individual data-based approach. The stochastic errors (1σ) in $\delta \mathrm{Kr/N_{2,atm}}$, $\delta \mathrm{Xe/N_{2,atm}}$, and $\delta \mathrm{Xe/Kr_{atm}}$ introduced by the measurement errors are 0.20 ‰, 0.45 ‰, and 0.32 ‰, respectively, in our model-based approach. The systematic uncertainty in this case is 0.23 ‰, 0.70 ‰, and 0.48 ‰, respectively.

Alternatively, we can use the mean data-based correction approach. Using the mean ΔT and $\epsilon_{\mathrm{Kr/N_2-N_2}}$ over the last 40 kyr leads to the smallest scatter in our atmospheric elemental ratios, as we average over 39 data points for our correction. However, this also implies a large systematic uncertainty that derives from the choice of mean ΔT and $\epsilon_{\mathrm{Kr/N_2-N_2}}$. Moreover, both parameters may have been subject to systematic changes over time that we cannot decipher using this mean correction. The stochastic errors (1σ) in $\delta \mathrm{Kr/N_{2,atm}}$, $\delta \mathrm{Xe/N_{2,atm}}$, and $\delta \mathrm{Xe/Kr_{atm}}$ introduced by the measurement errors are 1.68 ‰, 2.12 ‰, and 0.66 ‰, respectively, in our mean data-based approach. The systematic uncertainty in this case is on average 1.22 ‰, 1.49 ‰, and 0.40 ‰, respectively.

In summary, our different correction pathways lead to similar results in the differences of atmospheric elemental ratios relative to their Holocene value. In the following, we will use only the atmospheric elemental ratios after correction using the model-based approach, which is based on well-understood physical laws of heat conduction–advection and provides elemental ratios with sufficient precision and accuracy to reconstruct glacial–interglacial changes in MOT after correction for gravitational, thermal, and kinetic fractionation.

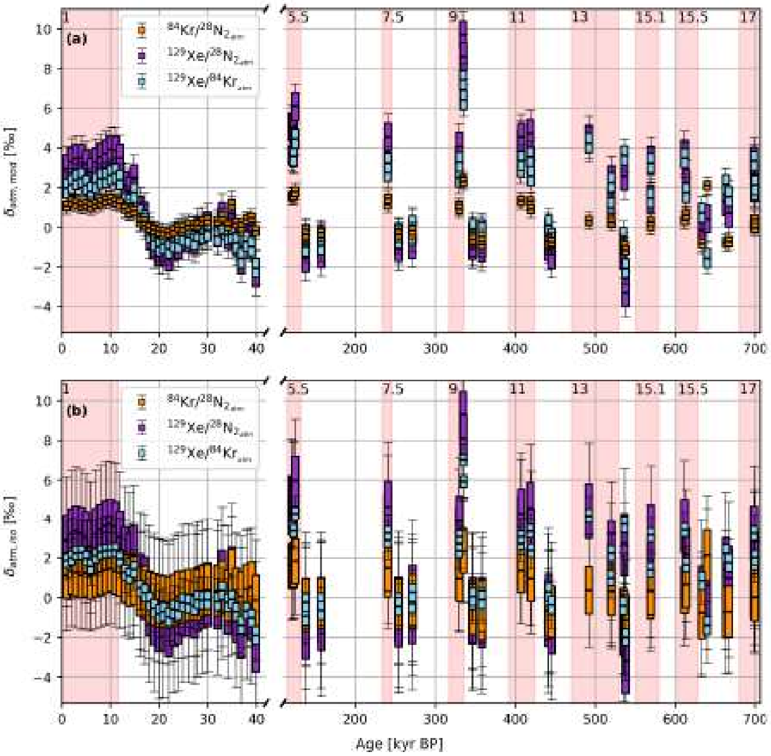

Figure 5. Comparison of the reconstructed atmospheric ratios of Kr/N_2 (orange), Xe/N_2 (purple), and Xe/Kr (blue) (**a**) as derived from the calibrated firn model of Michel (2016) (**b**) using measured isotopic ratios only. The reconstructed value is drawn as a black line in the middle of each box. The magnitude of the systematic uncertainty is indicated by the size of the colored boxes, and the statistical uncertainties are depicted as whiskers (1σ each). The red shaded intervals and the MIS numbers on top indicate interglacials as identified by Masson-Delmotte et al. (2010).

2.3 Box model to infer the MOT from atmospheric values

To reconstruct MOT values from the corrected elemental ratios, we use the ocean–atmosphere box model described by Bereiter et al. (2018b), except for one slight update, as we use the solubility equations given by Jenkins et al. (2019). The basic assumption in the model is that N_2, Kr, and Xe are conserved in the ocean–atmosphere system and that their distribution between the two reservoirs is controlled by the temperature-dependent dissolution in the ocean water. The model accounts for the effects of changes in ocean salinity, volume, and atmospheric pressure on the oceanic inventories of each of the three gases, which have individual temperature-dependent solubilities. The records of Lambeck et al. (2014) and Spratt and Lisiecki (2016) are used to reconstruct the sea level for the last 27 kyr and the time interval 28–800 kyr BP, respectively. We assume a constant undersaturation of the heavy noble gases in the ocean by 3 % for Xe and 1.5 % for Kr (Hamme and Severinghaus, 2007; Loose et al., 2016; Hamme et al., 2019). In contrast to Bereiter et al. (2018b) we do not impose a temporal change in this undersaturation, as we have no observational evidence about such a change in saturation state and we cannot provide a convincing argument on whether the saturation may have increased or decreased during glacial times. The overall slower ocean overturn in the glacial may suggest an increase in saturation, while the expansion of sea ice (especially in the Southern Ocean) would speak for a stronger undersaturation of the heavy noble gases. Accordingly, we refrain from changing the saturation state in our model. Sensitivity analyses show that a reduction of the glacial undersaturation to half its current value will lead to a warming of our glacial MOT reconstruction by a few tens of a degree.

Using this box model we can translate the reconstructed and corrected atmospheric elemental ratios (Kr/N_2, Xe/N_2, and Xe/Kr) into changes in MOT relative to the Holocene. Using our model-based correction approach described above leads to an MOT change over the last glacial–interglacial transition of on average 3.0 ± 0.4 °C, 3.3 ± 0.4 °C, and 3.6 ± 0.4 °C for δKr / $N_{2,\mathrm{atm}}$, δXe / $N_{2,\mathrm{atm}}$, and δXe/$\mathrm{Kr}_{\mathrm{atm}}$, respectively (see Fig. 6 and Table 2). This is in general agreement within uncertainties with independently derived results over the last glacial termination for the WAIS Divide ice core from Bereiter et al. (2018a).

As described above, the uncertainties in the model-based correction approach for elemental ratios are introduced by uncertainties in the modeled ΔT, the measurement errors of the elemental ratios, and the choice of $\epsilon_{\mathrm{Kr/N_2-N_2}}$. For the Ar isotopes we also corrected for the steady increase in ^{40}Ar through the decay of ^{40}K in the crust and mantle, which leads to a small long-term increase in $\delta^{40/36}$Ar. This increase was experimentally determined by Bender et al. (2008) and has a slope of 0.066 ± 0.007 ‰ per million years, which we include in our error propagation. Moreover, the box model approach may add some minor systematic uncertainty, which we cannot quantify. Using the analytical uncertainties in the elemental ratios in the model-based approach leads to a stochastic uncertainty (1σ) in the MOT values between 0.35 and 0.41 °C for all three elemental ratios and a systematic uncertainty of 0.38–0.51 °C.

3 Post-coring gas loss effects on MOT reconstructions

Additional changes in the elemental ratios may occur if post-coring gas loss leads to fractionation between different gases. While visible cracks are avoided in the sample preparation, previous ice core studies showed that invisible microcracks can occur, leading to gas loss fractionation processes that affect, for example, $\delta O_2/N_2$ and δAr/N_2, but little is known about gas loss effects on heavy noble gas ratios. Ice subject to such internal microcracks is most susceptible to post-coring gas loss, and accordingly we find systematic deviations in the MOT values derived from the three different elemental ratios in (i) ice from the bubble–clathrate transition zone (BCTZ), which is characterized by brittle ice, and (ii) in the oldest, bottommost meteoric ice of the EDC core, which is characterized by particularly large ice crystals and high in situ temperatures and which is prone to increased microfracturing. The following sections address potential gas loss fractionations in these ice zones.

3.1 Post-coring gas loss effects in the BCTZ

Post-coring fractionation of elemental gas ratios is caused by the selective loss of specific gases in poorly preserved samples or in samples from the bubble–clathrate transition zone (BCTZ), i.e., the depth section between the formation of the first clathrate and the disappearance of the last bubble (Lipenkov, 2000).

Bender (2002) called such gas loss through cracks or microcracks "core-cracking fractionation" and observed this effect to strongly affect O_2/N_2 in the BCTZ of the Vostok ice core. The effect is explained by gas fractionation occurring between coexisting bubbles and clathrates in combination with post-coring gas loss. In our record we observe small but linearly increasing differences with age (and depth) in the MOT derived from the different noble gas combinations in ice at the top of the BCTZ, i.e., in the zone where clathrates form (600–775 m; 24–40 kyr BP). In particular, MOTs derived from Kr/N_2 show higher temperatures compared to Xe/N_2 and Xe/Kr in this ice, while the three values agree within their uncertainties in pure bubble ice. Similar systematic offsets are observed around the BCTZ in cores from various sites (GRIP, NEEM, and Talos) but to a variable extent, as shown in Fig. 7b. Bereiter et al. (2018a) also observed pronounced alteration in the trapped gas towards the lower end of the BCTZ or even below for the WAIS ice core.

In the following discussion, we will try to motivate the processes that we think are responsible for this fractionation. Studies of air bubbles and clathrate inclusions on the Dome Fuji ice core provide information on clathrate formation and clathrate growth in cold Antarctic ice (Uchida et al., 2011). Clathrate formation starts when the bubble pressure, which increases linearly with depth due to the increasing hydrostatic pressure, reaches the dissociation pressure of air hydrate. The dissociation pressure of the air hydrate is given by the dissociation pressure of hydrates formed by the pure gas species multiplied by the mole fraction of the gas species in air (Miller 1969). Accordingly, the air hydrate dissociation pressure in the ice is mainly determined by the dissociation pressure of N_2 and O_2, with minor contributions from Ar or CO_2. We assume that any SII-clathrate-forming gas species (Sloan and Koh, 2007) will be quantitatively incorporated into the SII air hydrate structure during its nucleation from an air bubble; however, we speculate that SI-forming gases (such as Xe) may not (or not quantitatively) be incorporated into the SII air hydrate structure in the ice.

As described in Uchida et al. (2011), the number and also the radius of air hydrate crystals increase in the BCTZ at Dome Fuji, which has very similar climatic conditions compared to EDC. This can be interpreted in the BCTZ as more and more hydrates slowly nucleating from bubbles and bubbles and clathrates coexisting for a long time. Due to the higher partial pressures of gas species in bubbles compared to clathrates a constant permeation flux of gas from the bubbles to the clathrates exists, which is the main cause of clathrate growth in the BCTZ at Dome Fuji (or EDC). Note that due to the different permeation constants of different gas species in ice, this transport implies a fractionation of different gas species, which enriches fast-permeating gases (such as O_2; Ikeda et al., 2000) in the hydrate and depletes them in the remaining bubble. For Xe we speculate that there is either no permeation flux (if Xe is not included in the SII hydrate structure) or the permeation flux is very small due to the very low permeation coefficient of the large Xe atom. Thus, Xe is depleted in the air hydrate forming in the BCTZ and enriched

Table 2. Absolute MOT anomaly based on Kr/N_2 in degrees Celsius (°C) relative to the Holocene mean using both of our correction approaches. The Holocene value is the average of 10 EDC samples from 0–10.0 kyr BP, the LGM value is the average of nine samples between 17.8 and 26 kyr BP, LIG is the average of four samples between 120 and 129.9 kyr BP, and MIS 6 includes four samples from 135–160 kyr BP. MIS 9 and MIS 10 each comprise four samples.

Correction method	HOL	LGM	LIG	MIS 6	MIS 9	MIS 10	Stat. uncert.
Model-based	0.0	−3.0	0.8	−3.2	0.7	−3.6	0.4 (1σ)
Data-based	0.0	−3.0	0.8	−3.2	0.7	−3.6	2.9 (1σ)

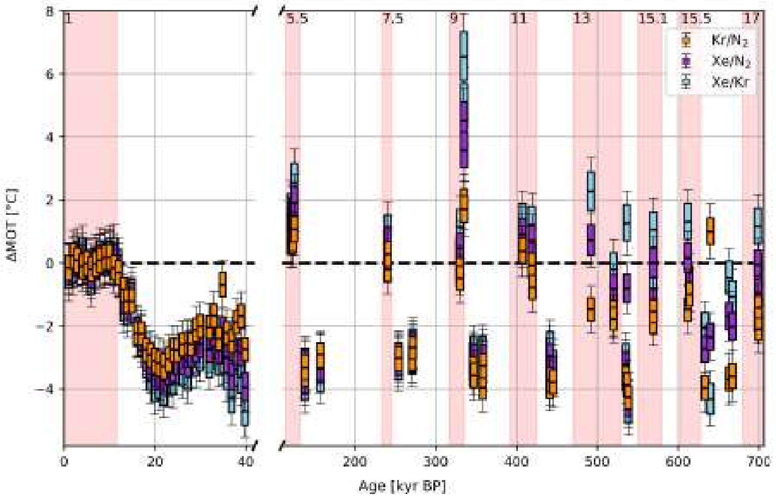

Figure 6. Reconstructed MOT for the EDC samples over the last 700 kyr relative to the Holocene value (using the model-based correction). MOTs are derived from $\delta Kr/N_2$ (orange), $\delta Xe/N_2$ (purple), and $\delta Xe/Kr$ (blue). The horizontal line in the middle of the filled box provides the corrected value. The boundaries of the filled boxes refer to the systematic uncertainty, while whiskers reflect the stochastic uncertainty introduced by the measurement errors (each 1σ). The red shaded intervals and the MIS numbers on top indicate interglacials as identified by Masson-Delmotte et al. (2010).

in the remaining bubbles. After complete collapse of the bubble, we expect the Xe to be "dissolved" in the ice matrix.

Below the BCTZ Uchida et al. (2011) observe an increase in hydrate radius and at the same time a decline in hydrate number. This can be explained by an Ostwald ripening process, leading to the growth of large hydrates at the cost of small ones through the Gibbs–Thomson effect (Uchida et al., 2011). Again, the accompanying gas transport from a small to a large hydrate crystal is supplied by (fractionating) permeation of gas species through the ice. If this process goes on for a sufficiently long time, however, a diffusive re-equilibration of the mole fractions of gas species in the hydrates (such as CO_2) is been observed (Lüthi et al., 2010). We assume that this permeation acts on all SII-forming gas species but that SI-forming Xe either does not permeate at all or that the permeation flux is strongly reduced compared to other gas species. Thus, Xe would be depleted in the large clathrates formed by this Ostwald ripening process and would remain dissolved in the ice matrix after complete disappearance of a small clathrate.

We attribute the gradually increasing offsets in reconstructed MOT at the top of the BCTZ to core-cracking gas loss in combination with the fractionation of gases by permeation. Gas enclosed in bubbles is more likely to be lost through cracks after core retrieval than gas in hydrates; thus, if post-coring gas loss from bubbles occurs, the remaining gas of the ice sample will be enriched in O_2 relative to N_2 and depleted in Xe. The small but significant $\delta Xe/Kr$ and $\delta Xe/N_2$ decrease in the BCTZ can therefore be explained by the observation that during the gas loss process, Xe is preferentially lost via cracks from the Xe-enriched bubbles.

To quantify a potential Xe loss we use a least squares approach that artificially changes the Xe abundance in the ice to minimize the difference between the three MOT proxies. The respective calculated post-coring Xe loss is shown in Fig. 7c, where the per mill value is the change in the elemental ratio used to minimize the MOT differences compared to Kr/N_2.

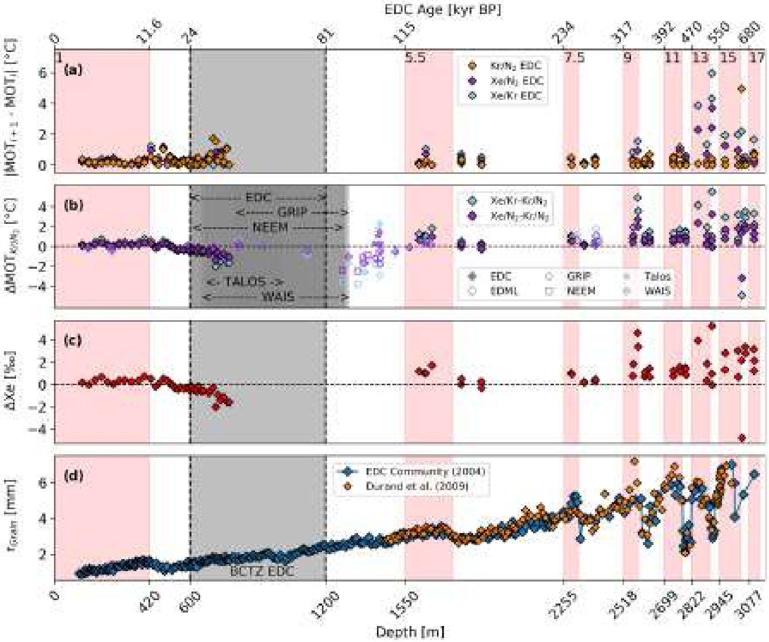

Figure 7. (a) Absolute MOT pair difference between two adjacent samples for the three different atmospheric noble gas ratios. (b) Difference in the MOT from δKr/Xe and δXe/N$_2$ compared to δKr/N$_2$. EDC, GRIP, NEEM, and Talos samples were measured at the University of Bern. WAIS samples were measured by Bereiter et al. (2018b). The grey shaded bars and arrows indicate the BCTZ for the different cores as identified by Neff (2014). All data are corrected for gravitational and thermal fractionation using argon isotopes. EDC samples are also corrected for HID fractionation. (c) Potential xenon change required for the EDC samples to match the MOTs using a least square approach. Given in red is the potential xenon change that minimizes the difference between the MOTs derived from Xe/Kr, Kr/N$_2$, and Xe/N$_2$. Negative values indicate a xenon loss, i.e., a depletion of the raw elemental ratios Xe/N$_2$ and Xe/Kr caused by post-coring gas loss. Positive values represent apparent net xenon "gains" due to higher losses of krypton and nitrogen compared to xenon. (d) Evolution of the grain radius in the EDC core (EPICA community members, 2004; Durand et al., 2009). Note that the ages provided on the upper x axis only apply for samples from the EDC ice core. MIS interglacials (red shaded intervals) as identified by Masson-Delmotte et al. (2010) are labeled at the top for orientation.

It shows that Xe loss is almost negligible in the top 500 m, i.e., in bubble ice, and increases to about 2 ‰, meaning that the Xe/N$_2$ elemental ratio is depleted in Xe by up to 2 ‰ caused by post-coring Xe loss from ice in the BCTZ.

Previous studies have shown that the gas loss effect on O$_2$/N$_2$ is most pronounced when the ice is brittle with an enhanced number of cracks but that the quality of the data is also affected in non-brittle ice if the samples are stored for an extended amount of time at relatively warm temperatures of around −25 °C (Ikeda-Fukazawa et al., 2005; Landais et al., 2012). The storage temperature may also affect our noble gas ratio results because our samples from the last transition were stored for about 15 years at about −22 °C. The samples from older climatic intervals presented in this study were stored at Dome C and later in Bern in a freezer at a temperature below −50 °C. Thus, no gas loss is expected for these samples during storage. However, these samples experienced a short-term warming during transport, when cooling failed during transit. Temperatures were as warm as −16 °C at the bottom of the well-insulated transport box and −6 °C on top of the box for several hours; however, the ice never reached the melting point.

To assess the potential loss of gas due to high storage or transport temperature, we compare the O$_2$/N$_2$ that we measure alongside the noble gases with previous O$_2$/N$_2$ measurements on EDC ice stored at −50 °C by Extier et al. (2018); the latter did not experience significant warming during transport. Similar to previous observations in BCTZ ice, our O$_2$/N$_2$ values suggest a variable enrichment of up to 4 ‰ in O$_2$ relative to N$_2$ at the top of the BCTZ and also slightly elevated Ar/N$_2$ relative to the values in pure bubble ice (as shown in Fig. 8). This suggests that our samples from the BCTZ are indeed subject to slight core-cracking fractionation. Note that for Kr/N$_2$ we do not see such an enrichment at the top of the BCTZ, which implies that the difference in permeation constants for Kr and N$_2$ is too small to create a siz-

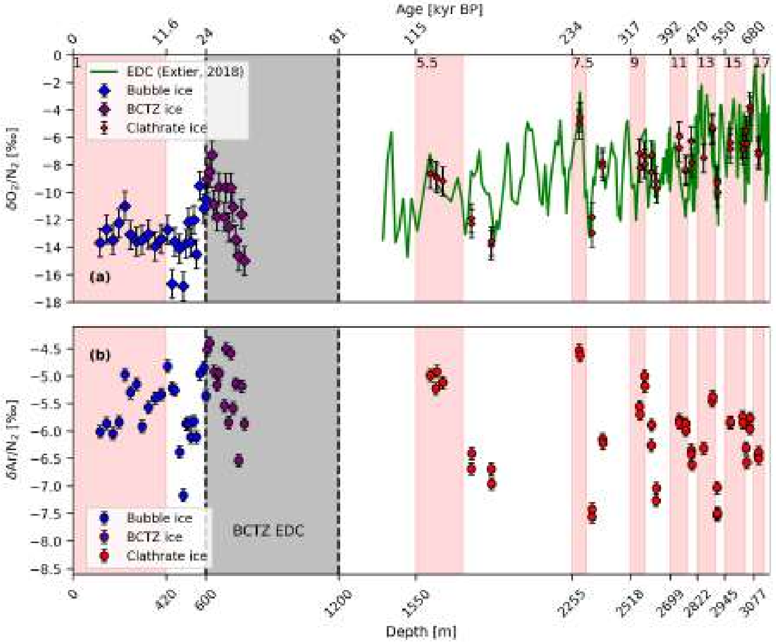

Figure 8. Measurements of $\delta O_2/N_2$ and $\delta Ar/N_2$ from the Dome C ice core on the EDC depth scale. The $\delta O_2/N_2$ record from Extier et al. (2018) is corrected for gravitational enrichment using $\delta^{15}N_2$. Our $\delta O_2/N_2$ data are corrected for gravitational enrichment using $\delta^{40/36}Ar$, while the $\delta Ar/N_2$ data are corrected for gravitational enrichment, thermal diffusion, kinetic fractionation, and geological Ar outgassing. The data show a large variability in the BCTZ and reproducible values for clathrated ice. **(a)** The green line represents measurements from Extier et al. (2018), and diamonds represent the EDC measurements of $\delta O_2/N_2$ in this study. **(b)** EDC measurements of $\delta Ar/N_2$ from this study. Interglacial MISs (red shaded areas) as identified by Masson-Delmotte et al. (2010) are labeled for orientation.

able anomaly. For the deeper ice no significant offset relative to the O_2/N_2 data from Extier et al. (2018) can be found, suggesting that the short cooling interruption during transport did not affect our elemental ratios. For the Ar/N_2 ratios of samples older than 40 kyr BP we see a number of glacial values that are more depleted than the average value during the Last Glacial Maximum (LGM); however, the large spread of the data does not allow us to draw a firm conclusion on an Ar loss for these older samples. Furthermore, both O_2/N_2 and Ar/N_2 of neighboring samples agree well with each other, indicating a common cause for the large overall variability. The main factor influencing O_2/N_2 on these timescales is a change in local summer insolation (Kawamura et al., 2007; Extier et al., 2018), and Ar/N_2 should be affected in a similar fashion. This suggests that gas loss during transport and storage is of minor importance, as such artifactual gas loss is typically a chaotic process that randomly affects some samples more than others. Based on this, we refrain from making a gas loss correction for $\delta^{40/36}Ar$ as described in Sect. 2.2.

In summary, although the Xe depletion is relatively small in the ice at the top of the BCTZ, we believe that the MOTs derived from our Xe/Kr and Xe/N_2 values are slightly biased towards overly cold temperatures. Accordingly, we use the MOT values derived from Kr/N_2 to quantitatively reconstruct changes in MOT for ice from the BCTZ, as Kr/N_2 appears not to be affected by gas loss and as Kr/N_2 replicates agree well within their analytical uncertainty thus making an effect of (unreproducible) gas loss unlikely. The latter also suggests that any fractionation of Kr relative to N_2 that may be caused by a permeation fractionation between bubbles and clathrates is too small to have a sizable effect on our measured values.

3.2 Post-coring gas loss in ice deeper than 2500 m

In clathrate ice below the BCTZ, MOT values derived from the three different elemental ratios showed good agreement down to an age of about 450 kyr BP but revealed systematic offsets mainly for the lowest 400 m, where the MOTs derived from $\delta Xe/Kr$ and $\delta Xe/N_2$ suggest much higher temperatures than those derived from $\delta Kr/N_2$. A similar observation can be made for two interglacial samples from MIS 9. Moreover, the values derived from $\delta Xe/Kr$ and $\delta Xe/N_2$ of neighboring quasi-replicate samples in the lowest 400 m of the core do not agree within their analytical uncertainties, while those for δKr/N$_2$ do, as shown by differences in the MOT of each sample pair in Fig. 7a. Each of the δKr/N$_2$ pairs (with the exception of one sample at a depth of about 3100 m from 630 kyr BP) agrees within less than 0.5 °C, in line with our stochastic error estimate (see Fig. 7). The cause of the outlier in δKr/N$_2$ at 630 kyr BP has not yet been identified. Interestingly, δKr/N$_2$ pair differences in the bottommost ice are also not elevated compared to shallower fully clathrated ice samples in the time interval 100–450 kyr BP. Taking the good reproducibility of δKr/N$_2$ and the elevated MOTs derived from δXe/Kr and δXe/N$_2$ in the deepest ice together, we conclude that a Kr and N$_2$ core-cracking loss must have occurred, which leaves the ice enriched in Xe.

In the EDC core, Durand et al. (2009) observed large variations in the fabric of the ice in different samples and extraordinarily large grains in interglacial ice below 2500 m, as shown in Fig. 7. A recent microscopic inspection of two deep EDC ice samples stored at the Alfred Wegener Institute in Bremerhaven at −30 °C showed significant visual glittering in this ice, indicative of so-called plate-like inclusions (PLIs) due to clathrate relaxation (Bereiter et al., 2015). These suggest the coexistence of reformed gaseous inclusions and clathrates in this increasingly relaxed ice. Weikusat et al. (2012) and Nedelcu et al. (2009) studied the ice structure and relaxation of the EDML core. Although the ice is comparatively young in this core and the accumulation rates are larger than at the EDC site, it is likely that the observations of EDML also apply to some degree to the EDC core. Particularly interesting are relaxation-induced air inclusions such as microscopic bubbles (“microbubbles”) and PLIs that are found with increasing depth at grain boundaries and clathrate hydrate surfaces (Nedelcu et al., 2009). The PLIs are flat inclusions of air (a few micrometer in thickness) and are more common in deep, fully clathrated ice, while the microbubbles are spherical objects and more common in shallower, bubbly ice (Weikusat et al., 2012). Direct measurements of such microscopic air inclusions are only possible for the main air constituents N$_2$ and O$_2$ using Raman spectroscopy. The results from Nedelcu et al. (2009) show substantially higher O$_2$/N$_2$ values in such inclusions compared to air, indicating an enrichment of O$_2$ in these gas-filled features similar in magnitude to the O$_2$ enrichment reported for air hydrates in the BCTZ of polar ice cores.

Diffusive gas loss from the outer surface of our samples can be safely ruled out due to the large sample size and the careful removal of several millimeters of ice from each surface (Bereiter et al., 2009). In combination with the complete gas extraction achieved in our melt extraction technique, any occurring net gas fractionation in our samples requires a gas loss process through microcracks and some gas fractionating exchange between gas enclosures in the ice. Similar to the core-cracking gas loss in the BCTZ discussed above, any gas loss through microcracks in the ice is more likely for gas-filled features such as bubbles and PLIs than for clathrates. Hence, we would assume that gas loss from O$_2$-enriched PLIs would lead to a depletion in the O$_2$/N$_2$ values measured in our ice samples. As shown in Fig. 8, however, an O$_2$ enrichment is observed that is increasing for older ice and that has been attributed to a long-term change in the O$_2$ content of the atmosphere over the last 800 kyr (Stolper et al., 2016). Thus, either an O$_2$ loss did not occur or it is very small and dwarfed by the atmospheric O$_2$ change.

Nevertheless, we suggest that the apparent enrichment of Xe relative to N$_2$ and Kr in our data is related to a fractionation and gas loss process that is opposite to that what is observed in the BCTZ and that is related to the clathrate relaxation process. The fractionation is apparently particularly pronounced in ice below 2500 m with large crystals (see Fig. 7d) and in situ temperatures warmer than −10 °C, at which this ice may experience enhanced microcracking during core retrieval and storage. Once the ice core is brought to the surface, it starts to relax and gas-filled features such as PLIs slowly form (the higher the storage temperature of the core, the faster the relaxation). Note that due to the very cold storage temperature of our samples older than 40 kyr (< −50 °C) at Concordia Station and later in a −50 °C freezer chest in our lab, relaxation of the core is strongly suppressed, and we expect far fewer PLIs to have formed in our samples compared to the EDML samples in Nedelcu et al. (2009). Thus, it is likely that any O$_2$ loss is too small to be discerned.

How can we explain a Xe enrichment in our samples without significant O$_2$/N$_2$ fractionation? As discussed in Sect. 3.1, the SII clathrates are likely to be depleted in Xe and part of the Xe is expected to remain dissolved in the ice matrix. Thus, while any gas inclusions reforming from clathrates will be depleted in Xe and can be subject to gas loss, the Xe molecules dissolved in the ice are not accessible to gas loss. Accordingly, we speculate that any gas loss leads to an enrichment of Xe in our deep EDC ice samples, while all other gas species do not show significant fractionation as long as very cold storage ensures the clathrate relaxation to be small. This is also the reason why Kr/N$_2$ ratios apparently do not show any signs of gas loss fractionation as illustrated by the small pair differences between adjacent samples in the deep ice. Experiments using old EDC ice that has been stored for an extended time at a higher storage temperature may help researchers to test this hypothesis in the future.

In summary, apart from analytical issues related to achieving the required high precision and accuracy in atmospheric values of elemental ratios, fractionation and gas loss effects also have to be taken into account when interpreting MOT values in deep ice cores. As observed earlier for δO$_2$/N$_2$, the gas composition in brittle ice from the BCTZ suffers from post-coring gas loss effects, while pure bubble ice provides good storage conditions for permanent gases. MOT values from pure clathrate ice below the BCTZ but well above the bedrock (> 400 m) show little signs of post-coring gas loss and provide reliable MOTs for all three elemental ratios. In the warm deep ice closer to the bedrock, we observed an apparent Xe enrichment, and the Xe/Kr and Xe/N$_2$ ratios did not allow us to derive reliable MOT values. The consistency of δKr/N_2 values over the entire record, particularly their reproducibility within the analytical uncertainty, gives us confidence that reliable MOT values can be derived from this parameter throughout the EDC ice core.

4 MOT snapshots of peak glacial and interglacial periods during the last 700 kyr

Following the discussion about gas loss above, MOTs derived from δXe/N_2 and δXe/Kr show significant anomalies in samples from the BCTZ, especially from very deep ice as shown in Fig. 6.

Based on the good reproducibility of δKr/N_2 values within the analytical uncertainty throughout the record, we conclude that the MOT derived from δKr/N_2 is not significantly affected by the gas loss described in Sect. 3 and shows consistent results throughout the record. One sample at 638 kyr BP is, however, considered an outlier for two reasons: the sample has a pair difference in δKr/N_2, which is larger than 3σ of the reproducibility, and the order of the three proxies indicates a substantial xenon loss in contrast to all other samples from pure clathrate ice. We neglect the value at 638 kyr BP and restrict our discussion of past MOT changes to the values derived from δKr/N_2 as presented in Fig. 9.

Despite the pointwise character of our data, the δKr/N_2-derived MOT record generally supports the main findings from the deep-ocean temperature reconstruction of Elderfield et al. (2012) and Shakun et al. (2015), but in contrast to these studies our record is based on a purely physical proxy and by definition is globally representative for MOT. The main findings are the following.

i. Some episodes during the interglacial periods MIS 5.5 and MIS 9.3 are significantly warmer than the Holocene.

ii. Glacial MOTs are similar throughout the last 800 kyr, although glacials prior to 450 kyr BP appear slightly colder.

iii. The MOTs during interglacial periods prior to 450 kyr BP are significantly colder than after the Mid-Brunhes Event.

Note that each of our samples only represents an MOT snapshot representative of a time interval of a few centuries (Fourteau et al., 2019) given by the width of the gas age distribution for the EDC ice core. Thus individual samples are not representative of the mean interglacial (or glacial) value but may be subject to the millennial-scale variability of MOT. We stress that MOT is strongly influenced by changes in the Atlantic Meridional Overturning Circulation (AMOC) (Baggenstos et al., 2019; Shackleton et al., 2020) and can therefore vary on multi-centennial to millennial timescales, as also seen in coupled climate model experiments (Pedro et al., 2018; Galbraith et al., 2016). A sudden slowdown of the AMOC leads to a long-lasting accumulation of heat in the ocean interior (Pedro et al., 2018; Galbraith et al., 2016; Ritz et al., 2011), while a recovery of the AMOC slowly lowers the MOT. Accordingly, samples very close to the onset of interglacials, which may still be affected by a previously reduced AMOC, may still show elevated MOTs. The heat stored in the global ocean is only removed in the course of 2000–3000 years into the subsequent interglacial after strengthening of the AMOC. This is clearly observed in higher-resolution data for MIS5.5 (Shackleton et al., 2020), which allowed us to temporally resolve this transient feature. Such a deepwater mass reorganization that marks the onset of the subsequent interglacial period is also inferred from changing ocean water tracer distributions (Deaney et al., 2017).

In line with this, our MOT data based on δKr/N_2 from the onset of MIS 5.5 are on average 1.0 ± 0.4 °C warmer than the Holocene and decline to interglacial values only 0.7 °C warmer than the Holocene later in MIS5.5. This is in agreement with the findings from Shackleton et al. (2020) that show significantly warmer MOTs reaching a maximum value of 1.1 ± 0.3 °C at about 129 kyr BP. Shackleton et al. (2020) attribute the early last interglacial maximum in MOT to the weakening of the AMOC that occurred over termination II during the major iceberg discharge event from Hudson Strait in the North Atlantic commonly known as Heinrich event 11 (Capron et al., 2014). The subsequent release of heat from the ocean after the AMOC resumed led to a MOT decrease of ~ 1 °C with stable MOT only reached after 127 kyr BP.

A similar but even more pronounced ocean warming feature is found in our new data during interglacial MIS 9.3. The samples later in the interglacial (329 and 330 kyr BP) show within uncertainty the same temperatures as the Holocene; however, the very early interglacial samples (334 and 335 kyr BP) show 1.8 ± 0.4 °C warmer MOTs than the Holocene. Similarly, global deep-ocean temperatures for early MIS 9.3 compiled from marine sediment records in the study by Shakun et al. (2015) are intermittently nearly 2 °C warmer than the Holocene. Our two early MIS 9.3 samples occur also in parallel with a rapid CO_2 and CH_4 increase at the very end of termination IV. At the onset of interglacial MIS 9.3, Nehrbass-Ahles et al. (2020) measured the highest CO_2 values during the last 800 kyr, coeval with the highest CH_4 levels (Loulergue et al., 2008) and warm Antarctic temperatures, providing an excellent chronological constraint for the timing of AMOC resumption. An intriguing hypothesis for the high values at the onset of interglacial MIS 9.3 is therefore that the MOT overshoot observed in the final phases of termination IV is also a result of a long preceding period of freshwater-induced AMOC suppression and deepwater mass reorganization (Ganopolski and Brovkin, 2017) that only ended with the AMOC resumption at that time. This suggests, similar to the case in MIS 5.5, that MOT was still

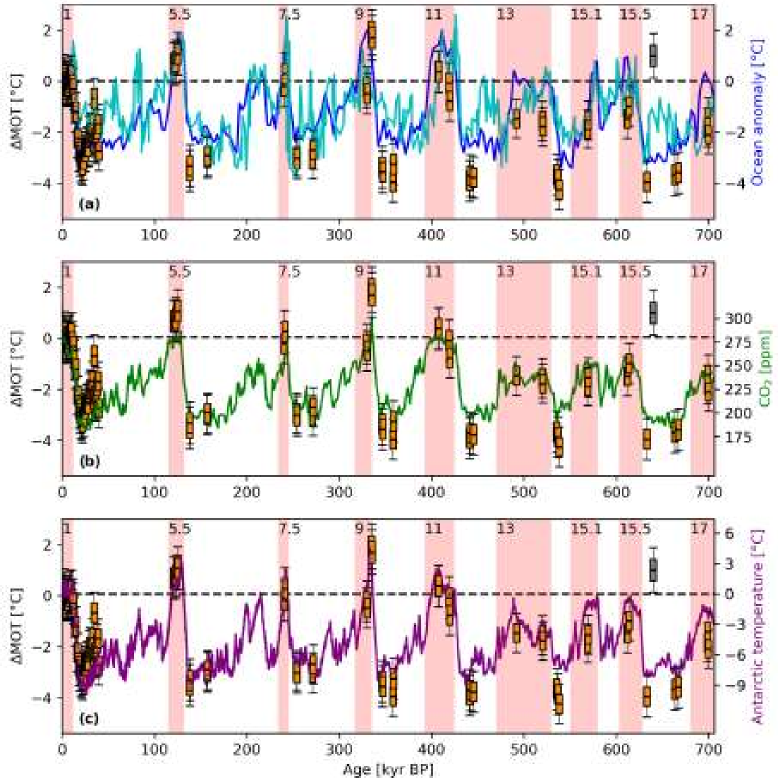

Figure 9. MOT record relative to the Holocene from the Kr/N_2 ratios in comparison with other climate records. The EDC record is based on 85 samples, which are displayed as orange boxes (except one outlier at 638 kyr BP indicated in grey). The uncertainty is shown as described in Sect. 2.3. **(a)** Deep-ocean reconstructions from a global compilation of 49 paired planktic $\delta^{18}O$ records are shown in dark blue (Shakun et al., 2015). Given in cyan is the benthic Mg/Ca-derived temperature from Elderfield et al. (2012). **(b)** The CO_2 record is based on measurements from the EDC and Vostok ice core (Nehrbass-Ahles et al., 2020; Bereiter et al., 2015; Lüthi et al., 2008; Petit et al., 1999). **(c)** Antarctic temperatures are taken from Parrenin et al. (2013). Red shaded bars and MIS numbers on top indicate interglacials according to Masson-Delmotte et al. (2010).

elevated by the reduced AMOC in the millennia before and was able to regain interglacial levels several millennia after the rapid CO_2 and CH_4 increases. This emphasizes the transient character of this feature and the role of an increasing AMOC in Antarctic and ocean temperature as well as in marine and terrestrial biogeochemical cycles.

Our data show glacial mean ocean temperatures very similar throughout the last 800 kyr. On average our measured glacial MOTs are 3.3 ± 0.4 °C colder than the Holocene. This is in agreement with the deep-ocean anomaly derived from Elderfield et al. (2012) based on a sediment record from Chatham rise east of New Zealand. There appears to be a slight increasing trend in glacial MOT over the last 700 kyr that is also suggested by the global ocean data compilation of Shakun et al. (2015); however, the trend in our data is of the same order as the uncertainty of our reconstruction. Accordingly, we refrain from interpreting this trend at this point in time; more higher-resolution MOT data are required to show whether this feature persists.

Our data also support the finding of lukewarm interglacials in MOT prior to the Mid-Brunhes Event 450 kyr ago (Shakun et al., 2015; Elderfield et al., 2012), as also seen in Antarctic temperatures (EPICA community members, 2004), but also lower interglacial concentrations of the greenhouse gases CO_2 (Bereiter et al., 2015; Lüthi et al., 2008) and CH_4 (Loulergue et al., 2008), at least for MIS 13–17. Thus, a potential compensation for the excess effective energy not used for ice sheet melting during lukewarm interglacials, as discussed in the Introduction, can be ruled out based on our ice core and the marine sediment data. Accordingly, the lukewarm interglacials must be connected to a net change in the radiative balance of the globe compared to later warmer interglacials. The MOT anomaly relative to the Holocene during the interglacials MIS 13, 15.1, 15.5, and 17 is -1.6 ± 0.4, -1.7 ± 0.4, -1.3 ± 0.4, and -1.8 ± 0.4 °C, respectively. Interglacial bottom-water temperatures also increased by about 1 °C after ~ 450 kyr BP (Elderfield et al., 2012; Shakun et al., 2015); however, Holocene bottom-water temperatures seem to be colder again than during the three preceding interglacials MIS 5.5, MIS 9.3, and MIS 11. Using the global benthic $\delta^{18}O$ stack by Lisiecki and Raymo (2005), Bintanja et al. (2005) reconstructed global ice volume changes and the contributions of individual ice sheets back in time. Again, the lukewarm interglacials are significantly different compared to the later interglacials in this model reconstruction and are characterized by up to 20 m lower sea level compared to the Holocene, with the largest contribution to this sea level reduction caused by larger ice sheets in Eurasia. Note, however, that sea levels lower than in the Holocene during lukewarm interglacials can be observed in some but not all sea level reconstructions from marine sediments (Rohling et al., 2014; Spratt and Lisiecki, 2016). In any case, an increase in ice volume during lukewarm interglacials cannot be easily attributed to changes in orbital forcing, as the effective energy at high northern latitudes (Tzedakis et al., 2017) during these intervals did not significantly differ from the insolation conditions during later interglacials. Thus, the lukewarm interglacials require additional changes in the Earth system that prevented Northern Hemisphere ice sheets from retreating and temperatures from increasing to the same extent as in later interglacials.

Irrespective of the ultimate cause of the incomplete deglaciation during the lukewarm interglacials, our significantly lower MOT values during these lukewarm interglacials provide robust evidence for a significantly altered energy budget of our planet compared to the Holocene. Note that an MOT lowering of about 1 °C translates into a decrease in the ocean heat content of $5\text{–}6 \times 10^{24}$ J, or about 30 % of our typical glacial–interglacial change in heat content. We can estimate whether the deviation in climate boundary conditions (greenhouse gas concentrations and albedo) is sufficient to explain the heat deficit. Lukewarm interglacial CO_2 concentrations are typically 245 ppm (instead of 280 ppm in later interglacials) and CH_4 concentrations 620 ppb (instead of 700 ppb thereafter). This translates into a radiative forcing of about $-0.8\,\mathrm{W\,m^{-2}}$ (Myhre et al., 1998), and using a recent paleo-based value of the equilibrium climate sensitivity of 3.8 °C for a doubling of CO_2 (Tierney et al., 2020) (which includes fast feedbacks such as sea ice coverage) it translates into a reduction of the global mean surface temperature (GMST) of about 0.8 °C. In addition, we also need to take into account the long-term Earth system feedbacks such as planetary albedo increase due to extended land ice coverage. For the LGM, the fraction of greenhouse gas forcing to total forcing has been estimated as approximately 0.4 (Baggenstos et al., 2019). Using the greenhouse gas forcing for the lukewarm interglacials as given above, the estimated total forcing is thus close to $2\,\mathrm{W\,m^{-2}}$, which yields an expected GMST decrease of 2.0 °C for the lukewarm interglacials. However, comparing global surface temperature to MOT is not straightforward (Bereiter et al., 2018b) because (i) MOT is biased towards sea surface temperatures in deep-water formation regions, for example in the North Atlantic, and is thus subject to polar amplification, and (ii) land temperature change is poorly known and cannot easily be linked to MOT change. However, a recent study has tightly constrained LGM GMST change to 6 °C (Tierney et al., 2020), which goes along with an approximately 3 °C MOT change for the LGM. Assuming this relationship also holds for earlier interglacials, we scale our average MOT decrease of 1.6 °C into a GMST reduction of 3.2 °C. This is somewhat larger than the expected GMST lowering of 2.0 °C due to radiative forcing and suggests that either the ratio of greenhouse gas forcing to total forcing or the scaling from MOT to GMST was different during the lukewarm interglacials. Note, however, that both of these factors are poorly constrained, and, for example, using 0.3 instead of 0.4 for the forcing ratio along with a slightly smaller MOT and GMST scaling would bring the two estimates into agreement. Thus, our MOT lowering during lukewarm interglacials is within the range expected from the radiative forcing caused by the lower CO_2 and CH_4 in those intervals and the connected longer-term Earth system feedbacks.

The close relationship of MOT and global radiative forcing with changing greenhouse gas concentrations is not only valid for lukewarm vs. full interglacials but to first order also holds for the entire noble-gas-based MOT record available so far. Bereiter et al. (2018b) showed that MOT is closely correlated with Antarctic temperature and the MOT evolution is essentially synchronous with CO_2 during the last transition. Our record from the last 40 kyr supports this correlation. The scatter plot presented in Fig. 10 shows the correlation between MOT and logarithmic CO_2, as expected from the radiative forcing of surface temperatures by CO_2 concentration (IPCC, 2013). The squared correlation coefficient for all the reconstructed MOTs from EDC and logarithmic CO_2 suggests that 75 % of the variance in the MOT record can be explained by changing CO_2 and the accompanying Earth system feedbacks. Taking a closer look at Fig. 10 we see again that the peak glacials and the lukewarm interglacials prior to 450 kyr BP show approximately 1 °C colder temperatures than expected from the CO_2 relationship derived for the last 40 kyr. In view of the considerable systematic uncertainties introduced by the correction of the data, we refrain from speculating on a possible cause of these lower temperatures at this point.

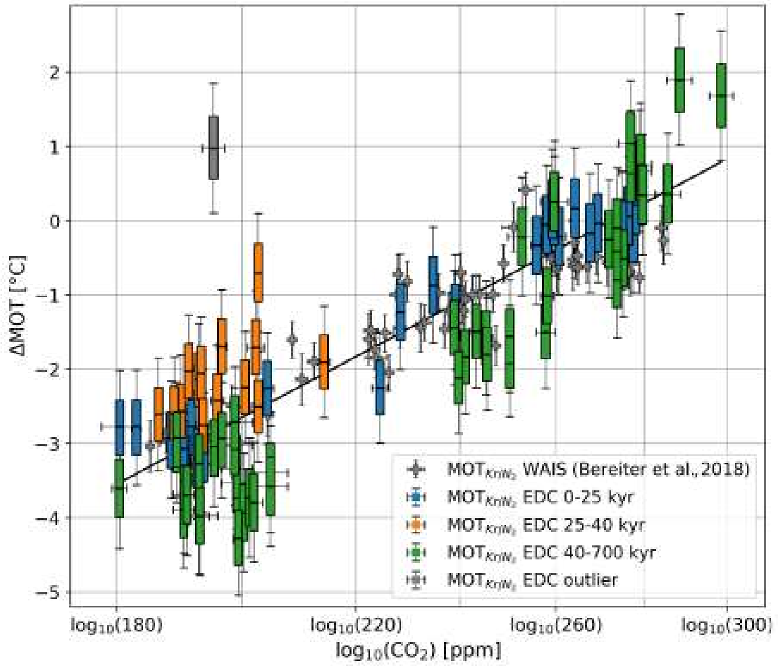

Figure 10. Scatter plot showing a linear relationship between logarithmic CO_2 (values taken from Bereiter et al., 2015) and the MOT relative to the Holocene. MOT reconstructions are based on Kr/N_2 and corrected for thermal, gravitational, and HID fractionation. MOTs from the last 25 kyr are shown in blue, samples from 25–40 kyr BP are shown in orange, and samples from 120 to 700 kyr BP are in green. The linear regression (black line) is based on EDC data only and has an r^2 of 0.75. Given in grey is the MOT reconstruction over the last 22 kyr from Bereiter et al. (2018b) relative to the Holocene.

5 Conclusions

Our study presents MOT snapshots of peak glacial and interglacial periods during the last 700 kyr. The comparison of MOT values derived from different elemental ratios revealed systematically lower MOTs based on $\delta Xe/N_2$ and $\delta Xe/Kr$ values from the BCTZ and higher MOTs from $\delta Xe/N_2$ and $\delta Xe/Kr$ in the ice deeper than 2500 m. We attribute this to a Xe depletion during clathrate formation through its low permeation coefficient and/or reduced incorporation of Xe in SII clathrates in the ice. This leads to an enrichment of Xe in bubbles in the BCTZ and a depletion of Xe in reforming PLIs in the deep ice. Together with gas loss through post-coring microcracks, this leads to a depletion of Xe relative to N_2 and Kr in the BCTZ and an enrichment in the deep ice. Continuing work on understanding firn gas, especially the HID, is crucial to reduce the uncertainties of the MOT reconstructions based on noble gases.

Despite these limitations we find that glacial MOTs based on $\delta Kr/N_2$, which appear to be free of gas loss and fractionation processes, are on average 3.3 ± 0.4 °C colder than the Holocene throughout this noble gas record and that the MOTs during interglacial periods prior to 450 kyr BP are on average 1.6 ± 0.4 °C lower compared to the Holocene. Episodes during the onsets of interglacials MIS 5.5 and 9.3 are significantly warmer than the Holocene and can be attributed to the ocean heat uptake during preceding times of lowered AMOC. The most pronounced feature of the record is the significantly increased MOT at the onset of MIS 9.3, which is coeval with the CO_2 and CH_4 overshoot at that time and reflects maximum ocean heat uptake before the AMOC resumption.

Our data provide only snapshots of MOT in glacial and interglacial conditions; however, these define the natural range in which the global heat budget has changed over the last 700 kyr. Our data show that the range in MOT can be quantitatively explained by changes in global radiative forcing (due to changes in greenhouse gas concentrations), taking into account long-term Earth system feedbacks, and that MOT is biased towards sea surface temperature changes in high latitudes. More high-resolution and high-precision MOT data from noble gases in ice cores (avoiding gas loss issues) and a better understanding of the firn fractionation processes affecting the gas composition in ice cores are needed to make use of the full potential of noble-gas-derived MOT in future studies.

Code and data availability. Noble gas data derived in this study will be made available on the NOAA paleoclimate database at https://www.ncdc.noaa.gov/paleo/study/33072 (Haeberli et al., 2021, last access: 31 March 2021). The Python code used for the correction of the data will be made available on request.

Author contributions. The concept of this study was created by HF, JS, and TK, and the research was supported by third-party funding by HF. The analytical method was established by TK, DB, and MH with input by JS and HF. The sample analyses were performed by MH and DB. Data evaluation was performed by MG and MH with inputs from DB and HF. The paper was written by HF and MH, with support by all coauthors, who also contributed heavily to the discussion of the data.

Competing interests. The authors declare that they have no conflict of interest.

Acknowledgements. We thank Eric Wolff, Gregory Teste, and Catherine Ritz for their help with sample selection and cutting. Catherine Ritz kindly provided borehole temperature profiles at Dome C. Most helpful discussions on noble gases as well as gas and heat transport in the firn with Jeff Severinghaus, Benjamin Birner, Sarah Shackleton, Bernhard Bereiter, and Jakob Schwander are gratefully acknowledged. The research leading to these results has received funding from the European Research Council (ERC) under the European Union's Seventh Framework Programme FP7/2007-2013 through ERC grant 226172 (ERC Advanced Grant Modern Approaches to Temperature Reconstructions in Polar Ice Cores (MATRICs)) and the Swiss National Science Foundation (grant numbers 200021-155906, 200020-172506). This work is a contribution to EPICA, a joint European Science Foundation/European Commission scientific program funded by the European Union and national contributions from Belgium, Denmark, France, Germany, Italy, The Netherlands, Norway, Sweden, Switzerland, and the United Kingdom. The main logistic support was provided by the Institut Polaire Français Paul-Emile Victor (IPEV), PNRA (at Dome C), and AWI (at EDML). This work is EPICA publication no. 317.

Financial support. This research has been supported by the European Research Council (grant no. 226172) and the Swiss National Science Foundation (SNF) (grant nos. 200021-155906, 200020-172506).

Review statement. This paper was edited by Amaelle Landais and reviewed by Jeff Severinghaus and one anonymous referee.

References

Baggenstos, D., Häberli, M., Schmitt, J., Shackleton, S. A., Birner, B., Fischer, H., Severinghaus, J., and Kellerhals, T.: The Earth's radiative imbalance from the Last Glacial Maximum to the present, P. Natl. Acad. Sci. USA, 110, 14881–14886, https://doi.org/10.1073/pnas.1905447116, 2019.

Bazin, L., Landais, A., Lemieux-Dudon, B., Toyé Mahamadou Kele, H., Veres, D., Parrenin, F., Martinerie, P., Ritz, C., Capron, E., Lipenkov, V., Loutre, M.-F., Raynaud, D., Vinther, B., Svensson, A., Rasmussen, S. O., Severi, M., Blunier, T., Leuenberger, M., Fischer, H., Masson-Delmotte, V., Chappellaz, J., and Wolff, E.: An optimized multi-proxy, multi-site Antarctic ice and gas orbital chronology (AICC2012): 120–800 ka, Clim. Past, 9, 1715–1731, https://doi.org/10.5194/cp-9-1715-2013, 2013.

Bender, M., Sowers, T., and Lipenkov, V.: On the concentrations of O_2, N_2, and Ar in trapped gases from ice cores, J. Geophys. Res., 100, 18651, https://doi.org/10.1029/94JD02212, 1995.

Bender, M. L.: Orbital tuning chronology for the Vostok climate record supported by trapped gas composition, Earth Planet. Sc. Lett., 204, 275–289, https://doi.org/10.1016/S0012-821X(02)00980-9, 2002.

Bender, M. L., Barnett, B., Dreyfus, G., Jouzel, J., and Porcelli, D.: The contemporary degassing rate of ^{40}Ar from the solid Earth, P. Natl. Acad. Sci. USA, 105, 8232–8237, https://doi.org/10.1073/pnas.0711679105, 2008.

Bereiter, B., Schwander, J., Lüthi, D., and Stocker, T. F.: Change in CO_2 concentration and O_2/N_2 ratio in ice cores due to molecular diffusion, Geophys. Res. Lett., 36, L05703, https://doi.org/10.1029/2008GL036737, 2009.

Bereiter, B., Eggleston, S., Schmitt, J., Nehrbass-Ahles, C., Stocker, T. F., Fischer, H., Kipfstuhl, S., and Chappellaz, J.: Revision of the EPICA Dome C CO_2 record from 800 to 600 kyr before present, Geophys. Res. Lett., 42, 542–549, https://doi.org/10.1002/2014GL061957, 2015.

Bereiter, B., Kawamura, K., and Severinghaus, J. P.: New methods for measuring atmospheric heavy noble gas isotope and elemental ratios in ice core samples, Rapid Commun. Mass Sp., 32, 801–814, https://doi.org/10.1002/rcm.8099, 2018a.

Bereiter, B., Shackleton, S., Baggenstos, D., Kawamura, K., and Severinghaus, J.: Mean global ocean temperatures during the last glacial transition, Nature, 553, 39, https://doi.org/10.1038/nature25152, 2018b.

Bintanja, R., Van De Wal, R. S., and Oerlemans, J.: Modelled atmospheric temperatures and global sea levels over the past million years, Nature, 437, 125–128, https://doi.org/10.1038/nature03975, 2005.

Birner, B., Buizert, C., Wagner, T. J. W., and Severinghaus, J. P.: The influence of layering and barometric pumping on firn air transport in a 2-D model, The Cryosphere, 12, 2021–2037, https://doi.org/10.5194/tc-12-2021-2018, 2018.

Bréant, C., Landais, A., Orsi, A., Martinerie, P., Extier, T., Prié, F., Stenni, B., Jouzel, J., Masson-Delmotte, V., and Leuenberger, M.: Unveiling the Anatomy of Termination 3 Using Water and Air Isotopes in the Dome C Ice Core, East Antarctica, Quat. Sci. Rev., 211, 156–165, https://doi.org/10.1016/j.quascirev.2019.03.025, 2019.

Buizert, C. and Severinghaus, J. P.: Dispersion in deep polar firn driven by synoptic-scale surface pressure variability, The Cryosphere, 10, 2099–2111, https://doi.org/10.5194/tc-10-2099-2016, 2016.

Buizert, C., Fudge, T., Roberts, W., Steig, E., Sherriff-Tadano, S., Ritz, C., Lefebvre, E., Kawamura, K., Oyabu, I., Motoyama, H., Kahle, E., Jones, T., Abe-Ouchi, A., Obase, T., Martin, C., Corr, H., Severinghaus, J., Beaudette, R., Epifanio, J., Brook, E., Martin, K., Chappellaz, J., Aoki, S., Nakazawa, T., Sowers, T., Ahn, J., Sigl, M., Severi, M., Dunbar, N., Svensson, A., Schwander, J., and Johnsen, S.: A revision of last glacial maximum temperatures in East Antarctica, submitted to Science, 2020.

Capron, E., Govin, A., Stone, E. J., Masson-Delmotte, V., Mulitza, S., Otto-Bliesner, B., Rasmussen, T. L., Sime, L. C., Waelbroeck, C., and Wolff, E. W.: Temporal and spatial structure of multi-millennial temperature changes at high latitudes during the Last Interglacial, Quat. Sci. Rev., 103, 116–133, https://doi.org/10.1016/j.quascirev.2014.08.018, 2014.

Craig, H. and Wiens, R.: Gravitational enrichment of ^{84}Kr/^{36}Ar ratios in polar ice caps: A measure of firn thickness and accumulation temperature, Science, 271, 1708–1710, 1996.

Craig, H., Horibe, Y., and Sowers, T.: Gravitational Separation of Gases and Isotopes in Polar Ice Caps, Science, 242, 1675–1678, https://doi.org/10.1126/science.242.4886.1675, 1988.

Cuffey, K. M. and Paterson, W. S. B.: The temperatures in ice masses, Butterworth-Heinemann, Burlington, MA, 704 pp., 2010.

Deaney, E. L., Barker, S., and van de Flierdt, T.: Timing and nature of AMOC recovery across Termination 2 and magnitude of deglacial CO_2 change, Nat. Commun., 8, 14595, https://doi.org/10.1038/ncomms14595, 2017.

Dreyfus, G. B., Jouzel, J., Bender, M. L., Landais, A., Masson-Delmotte, V., and Leuenberger, M.: Firn Processes and δ15N: Potential for a Gas-Phase Climate Proxy, Quat. Sci. Rev., 29, 28–42, https://doi.org/10.1016/j.quascirev.2009.10.012, 2010.

Durand, G., Svensson, A., Persson, A., Gagliardini, O., Gillet-Chaulet, F., Sjolte, J., Montagnat, M., and Dahl-Jensen, D.: Evolution of the texture along the EPICA Dome C ice core, Low Temp. Sci., 68, 91–105, https://eprints.lib.hokudai.ac.jp/dspace/handle/2115/45436 (last access: 28 March 2021), 2009.

Dutton, A., Carlson, A. E., Long, A. J., Milne, G. A., Clark, P. U., DeConto, R., Horton, B. P., Rahmstorf, S., and Raymo, M. E.: Sea-level rise due to polar ice-sheet mass loss during past warm periods, Science, 349, aaa4019, https://doi.org/10.1126/science.aaa4019, 2015.

Elderfield, H., Ferretti, P., Greaves, M., Crowhurst, S., McCave, I. N., Hodell, D., and Piotrowski, A. M.: Evolution of Ocean Temperature and Ice Volume Through the Mid-Pleistocene Climate Transition, Science, 337, 704–709, https://doi.org/10.1126/science.1221294, 2012.

EPICA community members: Eight glacial cycles from an Antarctic ice core., Nature, 429, 623–628, https://doi.org/10.1038/nature02599, 2004.

Extier, T., Landais, A., Bréant, C., Prié, F., Bazin, L., Dreyfus, G., Roche, D. M., and Leuenberger, M.: On the use of δ18Oatmfor ice core dating, Quat. Sci. Rev., 185, 244–257, https://doi.org/10.1016/j.quascirev.2018.02.008, 2018.

Fourteau, K., Martinerie, P., Faïn, X., Schaller, C. F., Tuckwell, R. J., Löwe, H., Arnaud, L., Magand, O., Thomas, E. R., Freitag, J., Mulvaney, R., Schneebeli, M., and Lipenkov, V. Ya.: Multi-tracer study of gas trapping in an East Antarctic ice core, The Cryosphere, 13, 3383–3403, https://doi.org/10.5194/tc-13-3383-2019, 2019.

Galbraith, E. D., Merlis, T. M., and Palter, J. B.: Destabilization of glacial climate by the radiative impact of Atlantic Meridional Overturning Circulation disruptions, Geophys. Res. Lett., 43, 8214–8221, https://doi.org/10.1002/2016GL069846, 2016.

Ganopolski, A. and Brovkin, V.: Simulation of climate, ice sheets and CO_2 evolution during the last four glacial cycles with an Earth system model of intermediate complexity, Clim. Past, 13, 1695–1716, https://doi.org/10.5194/cp-13-1695-2017, 2017.

Gleckler, P. J., Durack, P. J., Stouffer, R. J., Johnson, G. C., and Forest, C. E.: Industrial-era global ocean heat uptake doubles in recent decades, Nat. Clim. Change, 6, 394–398, https://doi.org/10.1038/nclimate2915, 2016.

Hamme, R. C. and Severinghaus, J. P.: Trace gas disequilibria during deep-water formation, Deep Sea-Res. Pt. I, 54, 939–950, https://doi.org/10.1016/j.dsr.2007.03.008, 2007.

Hamme, R. C., Nicholson, D. P., Jenkins, W. J., and Emerson, S. R.: Using Noble Gases to Assess the Ocean's Carbon Pumps, Annu. Rev. Mar. Sci., 11, 75–103, https://doi.org/10.1146/annurev-marine-121916-063604, 2019.

Headly, M. A.: Krypton and xenon in air trapped in polar ice cores: Paleo-atmospheric measurements for estimating past mean ocean temperature and summer snowmelt frequency, PhD thesis, University of California, San Diego, 229 pp., 2008.

Headly, M. A. and Severinghaus, J. P.: A method to measure Kr/N_2 ratios in air bubbles trapped in ice cores and its application in reconstructing past mean ocean temperature, J. Geophys. Res.-Atmos., 112, D19105, https://doi.org/10.1029/2006jd008317, 2007.

Hoffman, J. S., Clark, P. U., Parnell, A. C., and He, F.: Regional and global sea-surface temperatures during the last interglaciation, Science, 355, 276–279, https://doi.org/10.1126/science.aai8464, 2017.

Ikeda, T., Salamatin, A. N., Lipenkov, V. Y., Mae, S., and Hondoh, T.: Spatial distribution of air molecules within individual clathrate hydrates in polar ice sheets, in: Annals of Glaciology, Vol. 31, 2000, edited by: Steffen, K., Vol. 31 of Annals of Glaciology, 252–256, Int Glaciol Soc; ETH; Univ Zurich; Schweizer Akad Nat Wissensch; Schweizer Stift Alphine Forsch, Int glaciological soc, Lensfield rd, Cambridge, England, CB2 1er, https://doi.org/10.3189/172756400781820390, 2000.

Ikeda-Fukazawa, T., Fukumizu, K., Kawamura, K., Aoki, S., Nakazawa, T., and Hondoh, T.: Effects of molecular diffusion on trapped gas composition in polar ice cores, Earth Planet. Sc. Lett., 229, 183–192, https://doi.org/10.1016/j.epsl.2004.11.011, 2005.

IPCC: IPCC Climate Change 2013: The Physical Science Basis, edited by: Stocker, T. F., Dahe, Q., Plattner, G.-K., Tignor, M. M. B., Allen, S. K., Boschung, J., Nauels, A., Yu, X., Bex, V., and Midgley, P. M., Cambridge Univ. Press, Cambridge, 1535 pp., 2013.

Jenkins, W., Lott, D., and Cahill, K.: A Determination of Atmospheric Helium, Neon, Argon, Krypton, and Xenon Solubility Concentrations in Water and Seawater, Mar. Chem., 211, 94–107, https://doi.org/10.1016/j.marchem.2019.03.007, 2019.

Kawamura, K., Parrenin, F., Lisiecki, L., Uemura, R., Vimeux, F., Severinghaus, J. P., Hutterli, M. A., Nakazawa, T., Aoki, S., Jouzel, J., Raymo, M. E., Matsumoto, K., Nakata, H., Motoyama, H., Fujita, S., Goto-Azuma, K., Fujii, Y., and Watanabe, O.: Northern Hemisphere forcing of climatic cycles in Antarctica over the past 360,000 years, Nature, 448, 912–916, https://doi.org/10.1038/nature06015, 2007.

Kawamura, K., Severinghaus, J. P., Albert, M. R., Courville, Z. R., Fahnestock, M. A., Scambos, T., Shields, E., and Shuman, C. A.: Kinetic fractionation of gases by deep air convection in polar firn, Atmos. Chem. Phys., 13, 11141–11155, https://doi.org/10.5194/acp-13-11141-2013, 2013.

Kobashi, T., Severinghaus, J. P., and Barnola, J.-M.: 4 ± 1.5 °C abrupt warming 11,270 yr ago identified from trapped air in Greenland ice, Earth Planet. Sc. Lett., 268, 397–407, https://doi.org/10.1016/j.epsl.2008.01.032, 2008a.

Kobashi, T., Severinghaus, J. P., and Kawamura, K.: Argon and nitrogen isotopes of trapped air in the GISP2 ice core during the Holocene epoch (0-11,500 B.P.): Methodology and implications for gas loss processes, Geochim. Cosmochim. Ac., 72, 4675–4686, https://doi.org/10.1016/j.gca.2008.07.006, 2008b.

Lambeck, K., Rouby, H., Purcell, A., Sun, Y., and Sambridge, M.: Sea level and global ice volumes from the Last Glacial Maximum to the Holocene, P. Natl. Acad. Sci. USA, 111, 15296–15303, https://doi.org/10.1073/pnas.1411762111, 2014.

Landais, A., Dreyfus, G., Capron, E., Pol, K., Loutre, M. F., Raynaud, D., Lipenkov, V. Y., Arnaud, L., Masson-Delmotte, V., Paillard, D., Jouzel, J., and Leuenberger, M.: Towards orbital dating of the EPICA Dome C ice core using $\delta O_2/N_2$, Clim. Past, 8, 191–203, https://doi.org/10.5194/cp-8-191-2012, 2012.

Landais, A., Dreyfus, G., Capron, E., Jouzel, J., Masson-Delmotte, V., Roche, D. M., Prié, F., Caillon, N., Chappellaz, J., Leuenberger, M., Lourantou, A., Parrenin, F., Raynaud, D., and Teste, G.: Two-Phase Change in CO2, Antarctic Temperature and Global Climate during Termination II, Nat. Geosci., 6, 1062–1065, https://doi.org/10.1038/ngeo1985, 2013.

Lipenkov, V.: Air bubbles and air-hydrate crystals in the Vostok ice core, Physics of Ice Core Records, 327–358, 2000.

Lisiecki, L. E. and Raymo, M. E.: A Pliocene-Pleistocene stack of 57 globally distributed benthic δ^{18}O records, Paleoceanography, 20, PA1003, https://doi.org/10.1029/2005PA001164, 2005.

Loose, B., Jenkins, W. J., Moriarty, R., Brown, P., Jullion, L., Naveira Garabato, A. C., Torres Valdes, S., Hoppema, M., Ballentine, C., and Meredith, M. P.: Estimating the recharge properties of the deep ocean using noble gases and helium isotopes, J. Geophys. Res.-Oceans, 121, 5959–5979, https://doi.org/10.1002/2016JC011809, 2016.

Loulergue, L., Schilt, A., Spahni, R., Masson-Delmotte, V., Blunier, T., Lemieux, B., Barnola, J.-M., Raynaud, D., Stocker, T. F., and Chappellaz, J.: Orbital and millennial-scale features of atmospheric, Nature, 453, 383–386, https://doi.org/10.1038/nature06950, 2008.

Lüthi, D., Le Floch, M., Bereiter, B., Blunier, T., Barnola, J.-M., Siegenthaler, U., Raynaud, D., Jouzel, J., Fischer, H., Kawamura, K., and Stocker, T. F.: High-resolution carbon dioxide concentration record 650,000–800,000 years before present, Nature, 453, 379, https://doi.org/10.1038/nature06949, 2008.

Masson-Delmotte, V., Stenni, B., Pol, K., Braconnot, P., Cattani, O., Falourd, S., Kageyama, M., Jouzel, J., Landais, A., Minster, B., Barnola, J. M., Chappellaz, J., Krinner, G., Johnsen, S., Röthlisberger, R., Hansen, J., Mikolajewicz, U., and Otto-Bliesner, B.: EPICA Dome C record of glacial and interglacial intensities, Quat. Sci. Rev., 29, 113–128, https://doi.org/10.1016/j.quascirev.2009.09.030, 2010.

Melles, M., Brigham-Grette, J., Minyuk, P. S., Nowaczyk, N. R., Wennrich, V., DeConto, R. M., Anderson, P. M., Andreev, A. A., Coletti, A., Cook, T. L., Haltia-Hovi, E., Kukkonen, M., Lozhkin, A. V., Rosén, P., Tarasov, P., Vogel, H., and Wagner, B.: 2.8 Million Years of Arctic Climate Change from Lake El'gygytgyn, NE Russia, Science, 337, 315–320, https://doi.org/10.1126/science.1222135, 2012.

Michel, A.: Transient modeling of borehole temperature and basal melting in an ice sheet, Master thesis, University of Bern, 125 pp., 2016.

Milankovic, M.: Kanon der Erdbestrahlung und seine Anwendung auf das Eiszeitenproblem. Belgrade, Royal Serbian Acad. Sciences, Spec. Publ. 132, Sect. Math, Nat. Sci, 33, 633 pp., 1941.

Myhre, G., Highwood, E. J., Shine, K. P., and Stordal, F.: New estimates of radiative forcing due to well mixed greenhouse gases, Geophys. Res. Lett., 25, 2715–2718, https://doi.org/10.1029/98GL01908, 1998.

Nedelcu, A. F., Faria, S. H., and Kuhs, W. F.: Raman spectra of plate-like inclusions in the EPICA-DML (Antarctica) ice core, J. Glaciol., 55, 183–184, https://doi.org/10.3189/002214309788609010, 2009.

Neff, P. D.: A review of the brittle ice zone in polar ice cores, Ann. Glaciol., 55, 72–82, https://doi.org/10.3189/2014AoG68A023, 2014.

Nehrbass-Ahles, C., Shin, J., Schmitt, J., Bereiter, B., Joos, F., Schilt, A., Schmidely, L., Silva, L., Teste, G., Grilli, R., Chappellaz, J., Hodell, D., Fischer, H., and Stocker, T. F.: Abrupt CO2 release to the atmosphere under glacial and early interglacial climate conditions, Science, 369, 1000–1005, https://doi.org/10.1126/science.aay8178, 2020.

PAGES Past Interglacials Working Group, o. p.: Interglacials of the last 800,000 years, Rev. Geophys., 54, 162–219, https://doi.org/10.1002/2015RG000482, 2016.

Parrenin, F., Barnola, J.-M., Beer, J., Blunier, T., Castellano, E., Chappellaz, J., Dreyfus, G., Fischer, H., Fujita, S., Jouzel, J., Kawamura, K., Lemieux-Dudon, B., Loulergue, L., Masson-Delmotte, V., Narcisi, B., Petit, J.-R., Raisbeck, G., Raynaud, D., Ruth, U., Schwander, J., Severi, M., Spahni, R., Steffensen, J. P., Svensson, A., Udisti, R., Waelbroeck, C., and Wolff, E.: The EDC3 chronology for the EPICA Dome C ice core, Clim. Past, 3, 485–497, https://doi.org/10.5194/cp-3-485-2007, 2007.

Parrenin, F., Masson-Delmotte, V., Koehler, P., Raynaud, D., Paillard, D., Schwander, J., Barbante, C., Landais, A., Wegner, A., and Jouzel, J.: Synchronous change of atmospheric CO_2 and antarctic temperature during the last deglacial warming, Science, 339, 1060–1063, https://doi.org/10.1126/science.1226368, 2013.

Pedro, J. B., Jochum, M., Buizert, C., He, F., Barker, S., and Rasmussen, S. O.: Beyond the bipolar seesaw: Toward a process understanding of interhemispheric coupling, Quat. Sci. Rev., 192, 27–46, https://doi.org/10.1016/j.quascirev.2018.05.005, 2018.

Petit, J. R., Jouzel, J., Raynaud, D., Barkov, N. I., Barnola, J.-M., Basile, I., Bender, M., Chappellaz, J., Davis, M., Delaygue, G., Delmotte, M., Kotlyakov, V. M., Legrand, M., Lipenkov, V. Y., Lorius, C., Pepin, L., Ritz, C., Saltzman, E., and Stievenard, M.: Climate and atmospheric history of the past 420,000 years from the Vostok ice core, Antarctica, Nature, 399, 429–436, 1999.

Ritz, C., Lliboutry, L., and Rado, C.: Analysis of a 870 m Deep Temperature Profile at Dome C, Ann. Glaciol., 3, 284–289, https://doi.org/10.3189/S0260305500002937, 1982.

Ritz, S. P., Stocker, T. F., and Severinghaus, J. P.: Noble gases as proxies of mean ocean temperature: Sensitivity studies using a climate model of reduced complexity, Quat. Sci. Rev., 30, 3728–3741, https://doi.org/10.1016/j.quascirev.2011.09.021, 2011.

Rohling, E. J., Foster, G. L., Grant, K. M., Marino, G., Roberts, A. P., Tamisiea, M. E., and Williams, F.: Sea-level and deep-sea-temperature variability over the past 5.3 million years, Nature, 508, 477–482, https://doi.org/10.1038/nature13230, 2014.

Schwander, J.: Gas Diffusion in Firn, in: Chemical Exchange Between the Atmosphere and Polar Snow, Springer Berlin Heidelberg, Berlin, Heidelberg, 527–540, https://doi.org/10.1007/978-3-642-61171-1_22, 1996.

Schwander, J., Stauffer, B., and Sigg, A.: Air mixing in firn and the age of the air at pore close-off, Ann. Glaciol., 10, 141–145, https://doi.org/10.1017/S0260305500004328, 1988.

Seltzer, A. M., Pavia, F. J., Ng, J., and Severinghaus, J. P.: Heavy Noble Gas Isotopes as New Constraints on the Ventilation of the Deep Ocean, Geophys. Res. Lett., 46, 8926–8932, https://doi.org/10.1029/2019GL084089, 2019.

Severinghaus, J. P. and Battle, M. O.: Fractionation of gases in polar lee during bubble close-off: New constraints from firn air Ne, Kr and Xe observations, Earth Planet. Sc. Lett., 244, 474–500, https://doi.org/10.1016/j.epsl.2006.01.032, 2006.

Severinghaus, J. P., Grachev, A., Luz, B., and Caillon, N.: A method for precise measurement of argon 40/36 and krypton/argon ratios in trapped air in polar ice with applications to past firn thickness and abrupt climate change in Greenland and at Siple Dome, Antarctica, Geochim. Cosmochim. Ac., 67, 325–343, https://doi.org/10.1016/s0016-7037(02)00965-1, 2003.

Shackleton, S., Baggenstos, D., Menking, J. A., Dyonisius, M. N., Bereiter, B., Bauska, T. K., Rhodes, R. H., Brook, E. J., Petrenko, V. V., McConnell, J. R., Kellerhals, T., Häberli, M., Schmitt, J., Fischer, H., and Severinghaus, J. P.: Global ocean heat content in the Last Interglacial, Nat. Geosci., 13, 77–81, https://doi.org/10.1038/s41561-019-0498-0, 2020.

Shakun, J. D., Clark, P. U., He, F., Marcott, S. A., Mix, A. C., Liu, Z., Otto-Bliesner, B., Schmittner, A., and Bard, E.: Global warming preceded by increasing carbon dioxide concentrations during the last deglaciation, Nature, 484, 49–54, https://doi.org/10.1038/nature10915, 2012.

Shakun, J. D., Lea, D. W., Lisiecki, L. E., and Raymo, M. E.: An 800-kyr record of global surface ocean $\delta^{18}O$ and implications for ice volume-temperature coupling, Earth Planet. Sc. Lett., 426, 58–68, https://doi.org/10.1016/j.epsl.2015.05.042, 2015.

Sloan, E. D. and Koh, C. A.: Clathrate Hydrates of Natural Gases, Third Edition, CRC Press, 3 Edn., https://doi.org/10.1201/9781420008494, 2007.

Spratt, R. M. and Lisiecki, L. E.: A Late Pleistocene sea level stack, Clim. Past, 12, 1079–1092, https://doi.org/10.5194/cp-12-1079-2016, 2016.

Stolper, D. A., Bender, M. L., Dreyfus, G. B., Yan, Y., and Higgins, J. A.: A Pleistocene ice core record of atmospheric O_2 concentrations, Science, 353, 1427–1430, https://doi.org/10.1126/science.aaf5445, 2016.

Tiemey, J. E., Zhu, J., King, J., Malevich, S. B., Hakim, G. J., and Poulsen, C. J.: Glacial cooling and climate sensitivity revisited, Nature, 584, 569–573, https://doi.org/10.1038/s41586-020-2617-x, 2020.

Tzedakis, P. C., Hooghiemstra, H., and Pälike, H.: The last 1.35 million years at Tenaghi Philippon: revised chronostratigraphy and long-term vegetation trends, Quat. Sci. Rev., 25, 3416–3430, https://doi.org/10.1016/j.quascirev.2006.09.002, 2006.

Tzedakis, P. C., Crucifix, M., Mitsui, T., and Wolff, E. W.: A simple rule to determine which insolation cycles lead to interglacials, Nature, 542, 427–432, https://doi.org/10.1038/nature21364, 2017.

Uchida, T., Miyamoto, A., Shin'yama, A., and Hondoh, T.: Crystal growth of air hydrates over 720 ka in Dome Fuji (Antarctica) ice cores: microscopic observations of morphological changes below 2000 m depth, J. Glaciol., 57, 1017–1026, https://doi.org/10.3189/002214311798843296, 2011.

von Schuckmann, K., Cheng, L., Palmer, M. D., Hansen, J., Tassone, C., Aich, V., Adusumilli, S., Beltrami, H., Boyer, T., Cuesta-Valero, F. J., Desbruyères, D., Domingues, C., García-García, A., Gentine, P., Gilson, J., Gorfer, M., Haimberger, L., Ishii, M., Johnson, G. C., Killick, R., King, B. A., Kirchengast, G., Kolodziejczyk, N., Lyman, J., Marzeion, B., Mayer, M., Monier, M., Monselesan, D. P., Purkey, S., Roemmich, D., Schweiger, A., Seneviratne, S. I., Shepherd, A., Slater, D. A., Steiner, A. K., Straneo, F., Timmermans, M.-L., and Wijffels, S. E.: Heat stored in the Earth system: where does the energy go?, Earth Syst. Sci. Data, 12, 2013–2041, https://doi.org/10.5194/essd-12-2013-2020, 2020.

Weikusat, C., Freitag, J., and Kipfstuhl, S.: Raman spectroscopy of gaseous inclusions in EDML ice core: first results – microbubbles, J. Glaciol., 58, 761–766, https://doi.org/10.3189/2012JoG11J222, 2012.

Weller, G. and Schwerdtfeger, P.: Thermal properties and heat transfer processes of the snow of the central Antarctic Plateau, in: International Association of Scientific Hydrology, Publication No. 86, 284–298, 1970.

6. Conclusions and outlook

MOT is of high scientific interest, as it informs us on the amount of energy stored in one of Earth's two dominant fast-exchanging energy reservoirs on glacial–interglacial timescales (Baggenstos et al., 2019). Since its first successful application close to two decades ago (Headly and Severinghaus, 2007), the laboratory and analytical procedure for reconstructing MOT has constantly been upgraded, which has led to significant improvements in precision and accuracy (Bereiter et al., 2018a; Birner et al., 2018) and furthered our understanding of the metric as a whole (Pöppelmeier et al., 2023; Ritz et al., 2011). Reconstructing past MOT involves highly precise measurements of noble-gas elemental and isotopic ratios in ancient air trapped in polar ice. These elemental and isotopic ratios are affected by various firn fractionation processes, which require corrections that are based on our understanding of the complex gas transport in the firn. As the laboratory method is still novel, published MOT data is limited to a few select periods within the last 700 kyr (Baggenstos et al., 2019; Bereiter et al., 2018b; Haeberli et al., 2021; Shackleton et al., 2021, 2020, 2019). Thus, our new Termination I–IV record makes an important contribution to extending our knowledge of past MOT evolution and its connection to other climate parameters. In the following, we list some key points we learned on our journey that took us from a piece of Antarctic glacier ice to a MOT datapoint in one of the last four terminations. Starting from these key points, we then discuss future steps to further improve precision and accuracy of MOT reconstructions and point at periods within the past 800 kyr that we think are of particularly high interest for future MOT studies.

6.1. Laboratory procedure

In contrast to Scripps, the methodology we use in Bern puts a focus on the measurement of Xe isotopes. Due to their low atmospheric abundance, the measurement of Xe isotopes consumes a considerable amount of our sample gas. Furthermore, measuring Xe isotopes entails finding and tuning a filament which produces sufficiently high signal intensities requirements, which makes mass spectrometer analysis significantly more challenging. However, Xe isotopes do provide us with additional information on firn fractionating processes, which is of critical importance when analysing air that experienced significant thermal and kinetic fractionation. Having Xe isotopes available allowed us to state with higher confidence that gases in our EDC samples did experience significant seasonal rectification. Furthermore, they helped us to confirm that EDC noble gas isotopic ratios follow the kinetic fractionation factors suggested by firn modelling (Birner et al., 2018). Xe isotopes thereby support the sizable thermal and kinetic fractionation corrections we apply to our data. Finally, Xe isotopic information may eventually prove to be an invaluable source of information for furthering our understanding of firn fractionation processes. Thus, despite the considerable effort that is required to measure them with the required precision, doing so is worthwhile, especially when working with samples from an ice core with a dynamic firn column, such as EDC. As we will continue to analyse EDC samples here in Bern, measuring Xe isotopes should remain part of our routine. However, there are parts of the laboratory procedure that could be improved for future measurement campaigns, which may result in more accurate and precise MOT data.

One point in which our extraction system requires further improvement is its capacity to deal with samples affected by drilling fluid contamination, despite the significant improvements achieved during this PhD-project. These improvements were achieved by addition of glass capillaries to the LN_2 trap, which increased the available (glass) surface area of the trap. This resulted in only 3 samples measured during the 2022 measurement campaign being affected by drilling fluid contamination, compared to 13 samples in earlier campaigns. Nonetheless, further adjustments of the extraction system may bring even better results. For the Delta V aliquot, which when contaminated shows anomalous $\delta^{15}N_2$ and $\delta^{40/36}Ar$, this might be as simple as further increasing the available surface area of the LN_2 trap by addition of thinner glass capillaries. Although the initial addition of these capillaries did reduce the flow rate through the trap, our extraction method has sufficiently long capturing times to accommodate for even lower flow rates. As for the effect of drilling fluid contamination on ^{82}Kr, more theorising and experimenting is required.

Considering the improvements in the precision with which we can measure noble-gas elemental and isotopic ratios, gaining a more complete understanding of how mass spectrometer processes can affect these ratios becomes more relevant. One such process that requires further investigation is the bellow gas amount fractionation, which we noticed to have significantly changed over time, likely in response to changing filament and source configurations. This was unexpected, as we assumed that the fractionation was caused by the capillary that feeds into the change-over valve, which we do not adjust as we exchange the filament or source configurations. To account for the variable bellow gas amount fractionation, the necessary correction must be determined for each measurement period. To avoid this time-consuming procedure, a better understanding of the underlying physical process is required. The observed link to changes of the filament or source configurations seem to suggest that the source pressure and hence changed flow rate through the capillaries may affect the fractionation process. However, first experiments did not yield conclusive results but ask for more dedicated analysis of the phenomenon.

During the analysis of our Termination I–IV EDC samples we noticed systematic differences between reconstructed atmospheric δ^{132}Xe/Kr and δ^{129}Xe/Kr, whereas no effect was found for δ^{132}Xe/N$_2$ and δ^{129}Xe/N$_2$. These systematic differences lead to a bias in our MOT record on the order of 0.1 °C, considerably smaller than our analytical uncertainty. Nonetheless, as they are systematic, they may in parts explain the systematic differences we find between MOT derived from the three noble-gas ratios. Furthermore, the responsible process may cause other offsets and hence warrants investigation. As δXe/N$_2$ appears unaffected, the offset is unlikely due to a wrong firn fractionation correction; the only option we see would be a faulty kinetic fractionation factor for δXe/Kr. Alternatively, the offset might be caused by a suboptimal or missing mass spectrometry correction. Yet, we do not find any clear dependency of the offset on the date of measurement that may indicate so. More thorough investigation of the offset is thus required. Potential candidates to investigate might be the bellow gas amount correction or the desorption/sputtering effect. The bellow gas amount correction tends to be slightly different for δ^{132}Xe/Kr and δ^{129}Xe/Kr. Furthermore, it is rather poorly constrained due to the relatively low correlation between bellow gas amount difference and its effect for this ratio. The desorption/sputtering effect, on the other hand, has a slight bias towards heavier isotopes, and thus produces slightly elevated δ^{132}Xe/Kr compared to δ^{129}Xe/Kr for higher Ar content.

Potentially connected to the above offset between δ^{132}Xe/Kr and δ^{129}Xe/Kr is the perceived chemical slope of δXe/Kr and possibly other elemental ratios measured on the MAT 253. We observe that δXe/Kr shows a chemical-slope-like dependency on either δXe/Ar or δKr/Ar, or a combination of the two. This is unexpected because we are essentially measuring an Ar sample with trace gas amounts (~0.1‰) of Kr and Xe, such that addition of Ar should have no noticeable effect. The dependency can lead to biases in MOT of 0.2–0.3 °C, which furthermore may be systematically offsetting δXe/Kr-derived MOT. One candidate that may explain the dependency is the desorption/sputtering effect, which does cause elevated δXe/Kr for higher Ar content, roughly of similar size to the observed chemical slope of δXe/Kr. Alternatively, there might be an Ar background influencing Kr and Xe measurements, i.e., spurious Ar ions that happen to find their way into the cups even for Xe or Kr magnet current settings. Such an Ar background may lead to a chemical-slope-like effect, in that samples with higher Ar concentration and thus lower Xe and Kr concentration would experience a stronger Ar background. For both the desorption/sputtering effect and the Ar background, more testing is required.

Finally, we highly recommend measuring outside air samples at regular intervals throughout a measurement campaign. Thus far, a suit of outside air samples was measured at the start and at the end of an ice sample measurement campaign. The standard deviation of these outside air measurements then served as an estimate for the reproducibility of our MOT data. Having outside air datapoints at the start and at the end of a measurement campaign also allowed us to check for potential temporal drifts of the system. However, isotope data of the 2022 measurement campaign suggests that these drifts may not occur gradually over time but rather in steps, which makes correcting challenging and, in some instances, unfeasible. We thus suggest measuring at least one outside air sample per week throughout a measurement campaign, which should significantly improve our ability to correct for such drifts. Doing so does not increase the workload, as less outside air samples will have to be analysed before and after a measurement campaign to obtain a sufficient sample size from which to estimate reproducibility. In this context, it is also worth considering to upgrade our setup for outside air sampling to have an aspirated inlet tube (Headly and Severinghaus, 2007), which may lead to smaller drifts over time in outside air vs. working standard measurements.

6.2. Firn fractionation processes

Despite our best efforts of choosing adequate isotope-informed firn fractionation corrections, MOT values derived from the three reconstructed atmospheric noble-gas ratios are systematically different from one another. These differences appear to be particularly pronounced during periods of rapid climate change, such as the strong overshoot at the onset of MIS 9e. Furthermore, all three noble-gas ratios are considerably offset from the expected Holocene value of 0. These differences and offsets are also found in other MOT records, but they are different for records obtained from different ice cores (Bereiter et al., 2018b; Shackleton et al., 2020). This indicates that they are caused by a local effect, most likely by a firn fractionation process which our correction routine does not account for. Our MOT record thereby illustrates that there are still firn processes that we do not yet fully understand.

The Holocene offset and the systematic differences between the three noble-gas ratios appear to be roughly constant in time, which allows us to correct for them by referencing reconstructed atmospheric noble-gas ratios to their Holocene mean. Although this results in good agreement between MOT reconstructed from different ice cores, there is strong motivation to learn what causes these supposedly constant offsets. In Section 3.5.2., we hypothesised that they might be connected to a faulty kinetic fractionation correction, potentially linked to suboptimal firn air sampling and hence wrong input for the firn model that determined the kinetic fractionation factors (Birner et al., 2018). To progress in this, we require firn air data from EDC, which will soon be available as samples from the 2022/23 firn air sampling campaign are currently being analysed at LSCE and will later make their way to Bern. This campaign sampled the entire depth of the firn column at Little Dome C, about 30 km south of Dome C, and additionally retrieved closed-porosity samples. These may allow us to assess whether noble-gas elemental ratios from the closed porosity are indeed different to the ones in the open porosity, which may explain the constant offsets in our MOT record. However, differentiating between actual differences between open and closed-porosity samples and differences caused by potential sampling artefacts will be challenging. The separate year-round sampling campaign that took place at Dome C in 2022 will allow us to investigate seasonal differences in the top 20 m of the EDC firn column. From these measurements, we will be able to gauge whether gases in the EDC firn column indeed experience significant seasonal rectification of their thermal diffusion signal, as suggested by our MOT samples.

The larger spread between MOT derived from the three noble-gas ratios we observe during strong overshoots most likely has a different origin. As such large spread only seems to occur during periods of rapid climate change, we suspect a link to a dynamical firn process. Possible processes might be a rapidly shifting accumulation rate and, linked to that, abrupt changes in the density structure of the firn column and hence in firn column depth. Under such dynamical firn conditions, the assumed diffusive equilibrium may no longer be able to establish itself for gas species with lower diffusivities. Records of EDC site condition, such as for example NO_3 concentration as a proxy for accumulation rate, may help to develop a better understanding of what may cause the strong offsets during overshoots.

6.3. A wide range of scientific questions

Despite clearly not understanding the full cocktail of fractionation processes that occur in the firn column, the offsets caused by them appear to be roughly constant in time, and hence referencing noble-gas ratios to their Holocene mean resolves many of the issues. We account for the remaining offsets that are found during strong overshoots by factoring in their spread in our uncertainty estimate. Referencing reconstructed atmospheric ratios to their Holocene means results in good agreement between MOT records from different ice cores with very different firn properties, which bolsters the trust in our record. The record itself supports the strong link of past MOT evolution to variations in AMOC suggested by several modelling studies (Galbraith et al., 2016; Pedro et al., 2018). Furthermore, it emphasises that MOT can undergo rapid changes in both directions, exemplified by the two strong overshoots at the ends of Termination III and IV. Considering these rapid changes, MOT likely also significantly contributed to the strong CO_2 decrease observed after these two overshoots through the solubility pump. MOT may thereby also play an important role in determining the strength of an interglacial. Given that MOT is still a relatively novel metric, there are numerous scientific questions and time periods for which additional MOT data would be of great interest. An overview of the current EDC MOT record can be found in Figure 6.1., where we also highlight periods that will be sampled in upcoming measurement campaigns and indicate additional periods of interest, all of which we discuss in the following.

During our next measurement campaign, we plan to analyse EDC samples that span the entirety of MIS 8 in approximately 1kyr resolution. In combination with the data obtained during the 2022 campaign, this will yield the first MOT record of an entire interglacial–glacial–interglacial (MIS 9e–MIS 7e) cycle. DOT records suggest rather uneventful glacial periods as DOT tends to drop early during glacial inception and then remains roughly stable at about 2.5–3 °C below Holocene temperatures (Rohling et al., 2021; Shakun et al., 2015). However, our MIS 6 data shows that ocean temperature did experience fluctuations during glacial periods. These fluctuations appear to have been a combination of, on the one hand, adjustments to the long-term global cooling trend, and, on the other hand, more abrupt responses to intermittent AMOC reinvigorations. The MIS 9e–MIS 7e MOT record will not only allow us to study glacial MOT variability in further detail, which in MIS 8 with its exceptionally early glacial maximum conditions may be of particular interest, but will also for the first time provide us information on MOT evolution during a glacial inception. Furthermore, such a long record will allow us to study the temporal evolution of firn fractionation processes in greater detail and thereby potentially help us to better understand the mechanisms that drive them.

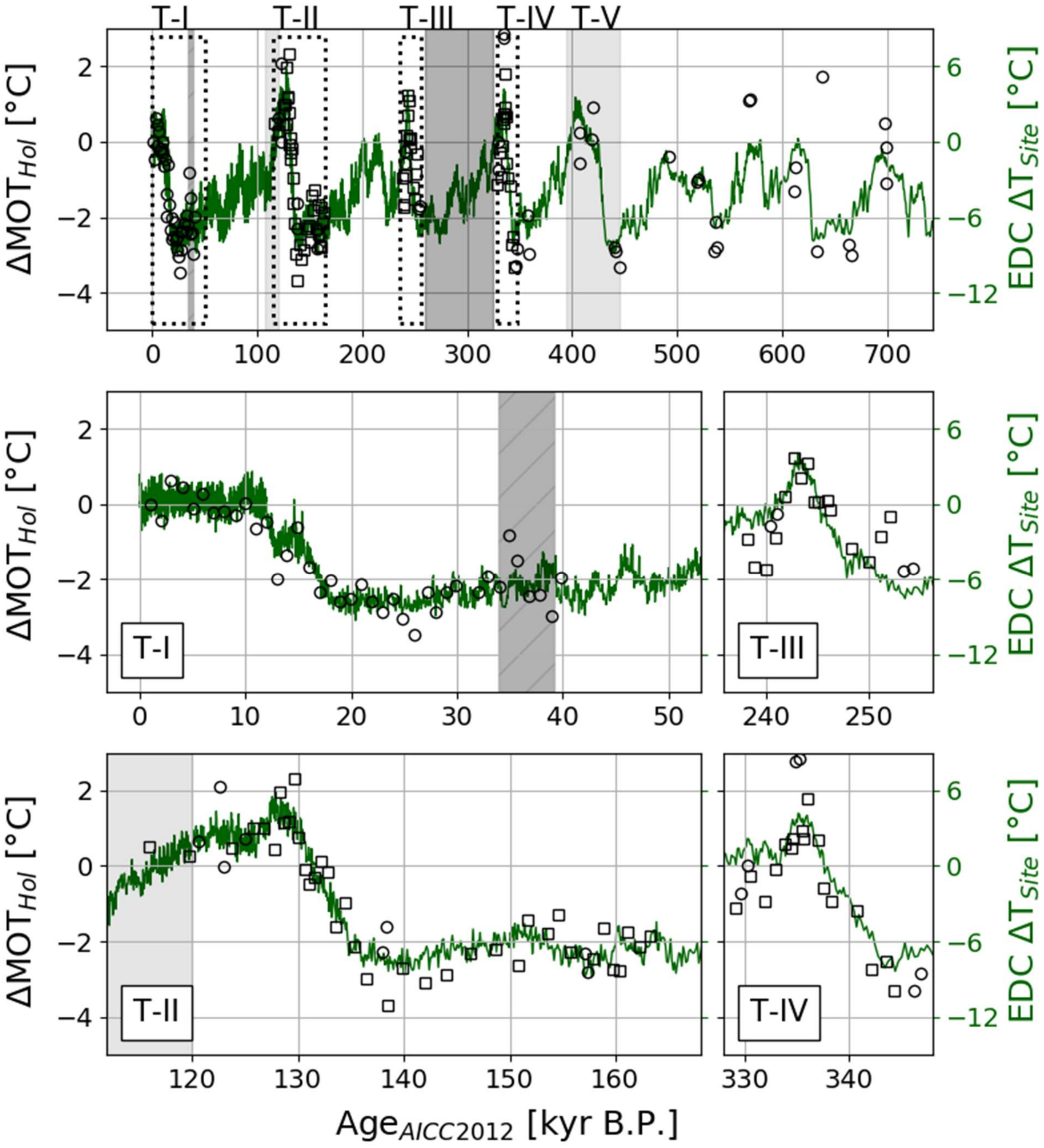

Figure 6.1.: Overview of all EDC MOT data. Datapoints measured during this PhD project are shown as squares, data from earlier measurement periods as circles (Baggenstos et al., 2019; Haeberli et al., 2021). Note that all data have been corrected using the correction routine laid out in Chapters 2 and 3. Datapoints before 350 kyr are solely based on δKr/N$_2$, whereas data from earlier periods are averages of the three noble-gas derived MOT values. Periods which we plan to analyse are highlighted in dark grey, further periods of interest (see text) in light grey. D-O events 7 and 8, which we plan to analyse on Skytrain ice, are indicated by hatching.

Highly resolved MOT records of glacial inceptions are of considerable interest. This interest is for example given by a recent study on MIS 5a and MIS 4 MOT, in which the authors argue for a similarly strong influence of MOT on CO$_2$ drawdown for the early phase of the last glacial inception as we suggest after early-interglacial overshoots (Shackleton et al., 2021). The authors infer this from the output of a carbon cycle model, which they constrain with two MOT datasets, one covering the LIG (Shackleton et al., 2020), the other one the end of MIS 5a and MIS 4 (Shackleton et al., 2021). However, no direct MOT information exists to date for this or any other glacial inception, such that it is unclear whether the reductions in MOT and CO_2 indeed occurred concurrently. The one datapoint of our record that does cover this interval seems to indicate that MOT, similar CO_2, stays at interglacial levels for longer than Antarctic temperature, giving some support to the suggested prominent role of MOT for CO_2 drawdown during that period. The last glacial inception is of particular interest in this respect due to the temporal mismatch between the inceptions in Antarctic temperature and CO_2, but other inceptions such as that of MIS 11c would allow for a similar analysis (Silva, 2022).

MIS 11c has attracted considerable scientific interest in recent years due to its exceptional length and strength under relatively weak insolation forcing (Tzedakis et al., 2022). Snapshot data may suggest gradually rising MOT (Haeberli et al., 2021), which would evolve in parallel with sea-level (Grant et al., 2014; Spratt and Lisiecki, 2016), possibly hinting at a period of extended energy uptake of the climate system. MIS 11c thereby would be a prime example for the heuristic rule that terminations with weaker insolation forcing and hence slower sea-level rise and, furthermore, terminations that are preceded by large glacial maximum ice sheet extent produce the strongest interglacials (Lang and Wolff, 2011; Mitsui et al., 2022). A continued MOT rise in response to extended freshwater-induced AMOC weakening as suggested by the bipolar seesaw mechanism (Pedro et al., 2018; Stocker and Johson, 2003), which is caused by, due to the low insolation only gradual, melting of Northern Hemisphere continental ice sheets (Bajo et al., 2020), may serve as a mechanistic explanation for this at first unintuitive observation. The required detailed analysis of ocean energy uptake during MIS 11c calls for high-resolution MOT data throughout Termination V and the subsequent interglacial.

The influence of AMOC variability on MOT evolution also deserves further attention. Our Termination I–IV record, together with other MOT datasets (Bereiter et al., 2018b; Shackleton et al., 2020), give multiple examples of periods during which AMOC strength and MOT show a negative correlation, supporting the causal link between the two suggested by climate models (Galbraith et al., 2016; Pedro et al., 2018). In parts thanks to our Termination I-IV dataset, this link is fairly established for terminations and early interglacial millennial-scale variability. However, although our MIS 6 data shows a MOT increase likely in response to the AMOC weakening during the Heinrich stadial that started at around 157 kyr, we lack highly resolved MOT data across regular D-O events, which would deliver experimental support that the causal link also exists under glacial background state. To resolve the response of MOT to D-O events, high-resolution data with a sample spacing of a few centuries is required, for which ice from a high-accumulation site is preferred. To this end, we plan to measure the large D-O events 7 and 8 in high resolution with ice from the new Skytrain ice core (Hoffmann et al., 2022; Mulvaney et al., 2023), which will happen in collaboration with the British Antarctic Survey.

Finally, the Mid-Pleistocene Transition (MPT) deserves an honourable mention. During the MPT, which occurred roughly between ~0.75–1.25 Myr, the periodicity of glacial cycles changed from 41 kyr before the MPT to an apparent 100 kyr cycle since without any corresponding change in the pacing of orbital forcing. The MPT therefore is one of the studied periods in paleoclimatology (see e.g., Herbert, 2023) and is the key motivation behind current international efforts of finding and drilling ice as old as 1.5 Myr. Having insights on how OHC responded to this change in periodicity would be of great interest. However, considering the high amounts of ice required for our analysis and the substantial thinning of layers for ancient ice, MOT data across the MPT will likely have to wait until several ice cores covering this period are available, or alternatively will have to compensate on the suit of ratios measured. Considering the many unanswered questions mentioned above, sufficient other periods exist that await to be analysed from a MOT perspective until then.

References

Baggenstos, D., Häberli, M., Schmitt, J., Shackleton, S.A., Birner, B., Severinghaus, J.P., Kellerhals, T., Fischer, H., 2019. Earth's radiative imbalance from the Last Glacial Maximum to the present. Proc Natl Acad Sci USA 116, 14881–14886. https://doi.org/10.1073/pnas.1905447116

Bajo, P., Drysdale, R.N., Woodhead, J.D., Hellstrom, J.C., Hodell, D., Ferretti, P., Voelker, A.H.L., Zanchetta, G., Rodrigues, T., Wolff, E., Tyler, J., Frisia, S., Spötl, C., Fallick, A.E., 2020. Persistent influence of obliquity on ice age terminations since the Middle Pleistocene transition. Science 367, 1235–1239. https://doi.org/10.1126/science.aaw1114

Bereiter, B., Kawamura, K., Severinghaus, J.P., 2018a. New methods for measuring atmospheric heavy noble gas isotope and elemental ratios in ice core samples. Rapid Commun Mass Spectrom 32, 801–814. https://doi.org/10.1002/rcm.8099

Bereiter, B., Shackleton, S., Baggenstos, D., Kawamura, K., Severinghaus, J., 2018b. Mean global ocean temperatures during the last glacial transition. Nature 553, 39–44. https://doi.org/10.1038/nature25152

Birner, B., Buizert, C., Wagner, T.J.W., Severinghaus, J.P., 2018. The influence of layering and barometric pumping on firn air transport in a 2-D model. The Cryosphere 12, 2021–2037. https://doi.org/10.5194/tc-12-2021-2018

Galbraith, E.D., Merlis, T.M., Palter, J.B., 2016. Destabilization of glacial climate by the radiative impact of Atlantic Meridional Overturning Circulation disruptions: RADIATIVE IMPACT OF AMOC DISRUPTIONS. Geophys. Res. Lett. 43, 8214–8221. https://doi.org/10.1002/2016GL069846

Grant, K.M., Rohling, E.J., Ramsey, C.B., Cheng, H., Edwards, R.L., Florindo, F., Heslop, D., Marra, F., Roberts, A.P., Tamisiea, M.E., Williams, F., 2014. Sea-level variability over five glacial cycles. Nat Commun 5, 5076. https://doi.org/10.1038/ncomms6076

Haeberli, M., Baggenstos, D., Schmitt, J., Grimmer, M., Michel, A., Kellerhals, T., Fischer, H., 2021. Snapshots of mean ocean temperature over the last 700 000 years using noble gases in the EPICA Dome C ice core. Clim. Past 17, 843–867. https://doi.org/10.5194/cp-17-843-2021

Headly, M.A., Severinghaus, J.P., 2007. A method to measure Kr/N $_2$ ratios in air bubbles trapped in ice cores and its application in reconstructing past mean ocean temperature. J. Geophys. Res. 112, D19105. https://doi.org/10.1029/2006JD008317

Herbert, T.D., 2023. The Mid-Pleistocene Climate Transition. Annual Review of Earth and Planetary Sciences 51, 389–418. https://doi.org/10.1146/annurev-earth-032320-104209

Hoffmann, H.M., Grieman, M.M., King, A.C.F., Epifanio, J.A., Martin, K., Vladimirova, D., Pryer, H.V., Doyle, E., Schmidt, A., Humby, J.D., Rowell, I.F., Nehrbass-Ahles, C., Thomas, E.R., Mulvaney, R., Wolff, E.W., 2022. The ST22 chronology for the Skytrain Ice Rise ice core – Part 1: A stratigraphic chronology of the last 2000 years. Climate of the Past 18, 1831–1847. https://doi.org/10.5194/cp-18-1831-2022

Lang, N., Wolff, E.W., 2011. Interglacial and glacial variability from the last 800 ka in marine, ice and terrestrial archives. Climate of the Past 7, 361–380. https://doi.org/10.5194/cp-7-361-2011

Mitsui, T., Tzedakis, P.C., Wolff, E.W., 2022. Insolation evolution and ice volume legacies determine interglacial and glacial intensity. Climate of the Past 18, 1983–1996. https://doi.org/10.5194/cp-18-1983-2022

Mulvaney, R., Wolff, E.W., Grieman, M.M., Hoffmann, H.H., Humby, J.D., Nehrbass-Ahles, C., Rhodes, R.H., Rowell, I.F., Parrenin, F., Schmidely, L., Fischer, H., Stocker, T.F., Christl, M., Muscheler, R., Landais, A., Prié, F., 2023. The ST22 chronology for the Skytrain Ice Rise ice core – Part 2: An age model to the last interglacial and disturbed deep stratigraphy. Climate of the Past 19, 851–864. https://doi.org/10.5194/cp-19-851-2023

Pedro, J.B., Jochum, M., Buizert, C., He, F., Barker, S., Rasmussen, S.O., 2018. Beyond the bipolar seesaw: Toward a process understanding of interhemispheric coupling. Quaternary Science Reviews 192, 27–46. https://doi.org/10.1016/j.quascirev.2018.05.005

Pöppelmeier, F., Baggenstos, D., Grimmer, M., Liu, Z., Schmitt, J., Fischer, H., Stocker, T.F., 2023. The Effect of Past Saturation Changes on Noble Gas Reconstructions of Mean Ocean Temperature. Geophysical Research Letters 50, e2022GL102055. https://doi.org/10.1029/2022GL102055

Ritz, S.P., Stocker, T.F., Severinghaus, J.P., 2011. Noble gases as proxies of mean ocean temperature: sensitivity studies using a climate model of reduced complexity. Quaternary Science Reviews 30, 3728–3741. https://doi.org/10.1016/j.quascirev.2011.09.021

Rohling, E.J., Yu, J., Heslop, D., Foster, G.L., Opdyke, B., Roberts, A.P., 2021. Sea level and deep-sea temperature reconstructions suggest quasi-stable states and critical transitions over the past 40 million years. Sci. Adv. 7, eabf5326. https://doi.org/10.1126/sciadv.abf5326

Shackleton, S., Baggenstos, D., Menking, J.A., Dyonisius, M.N., Bereiter, B., Bauska, T.K., Rhodes, R.H., Brook, E.J., Petrenko, V.V., McConnell, J.R., Kellerhals, T., Häberli, M., Schmitt, J., Fischer, H., Severinghaus, J.P., 2020. Global ocean heat content in the Last Interglacial. Nat. Geosci. 13, 77–81. https://doi.org/10.1038/s41561-019-0498-0

Shackleton, S., Bereiter, B., Baggenstos, D., Bauska, T.K., Brook, E.J., Marcott, S.A., Severinghaus, J.P., 2019. Is the Noble Gas-Based Rate of Ocean Warming During the Younger Dryas Overestimated? Geophysical Research Letters 46, 5928–5936. https://doi.org/10.1029/2019GL082971

Shackleton, S., Menking, J.A., Brook, E., Buizert, C., Dyonisius, M.N., Petrenko, V.V., Baggenstos, D., Severinghaus, J.P., 2021. Evolution of mean ocean temperature in Marine Isotope Stage 4. Clim. Past 17, 2273–2289. https://doi.org/10.5194/cp-17-2273-2021

Shakun, J.D., Lea, D.W., Lisiecki, L.E., Raymo, M.E., 2015. An 800-kyr record of global surface ocean δ 18 O and implications for ice volume-temperature coupling. Earth and Planetary Science Letters 426, 58–68. https://doi.org/10.1016/j.epsl.2015.05.042

Silva, L., 2022. High-resolution reconstruction of atmospheric CO2 concentrations during the last interglacial based on the EDC ice core. University of Bern, Bern.

Spratt, R.M., Lisiecki, L.E., 2016. A Late Pleistocene sea level stack. Clim. Past 12, 1079–1092. https://doi.org/10.5194/cp-12-1079-2016

Tzedakis, P.C., Hodell, D.A., Nehrbass-Ahles, C., Mitsui, T., Wolff, E.W., 2022. Marine Isotope Stage 11c: An unusual interglacial. Quaternary Science Reviews 284, 107493. https://doi.org/10.1016/j.quascirev.2022.107493

A. Annex

A.1. Ice sample protocols

The entire ice sample analysis consists of three major parts: sample preparation involving bringing the sample up to the temperature of the cutting room and subsequent cutting of the sample, sample extraction and splitting of the extracted gas into a noble gas aliquot and a split air aliquot, and measurement of the two sample aliquots on their respective IRMS. The protocols for these procedures can be found in the following.

A.1.1. Ice sample preparation

- The day before an ice sample extraction, place the ice sample in a Styrofoam box filled with −20 °C eutectics and then bring the sample from its −50 °C storage freezer to the −20 °C freezer. This is done to avoid abrupt temperature shifts, which might lead to (micro-)cracks.
- In the morning of the first day, bring the sample preparation material to the −18 °C cutting room. This involves the extraction vessel with its lid and screws, a copper gasket to seal that extraction vessel, the two wrenches necessary to do so, the large stainless-steel dewar (18 cm diameter), and a magnetic stirring bar. The cutting devices (band saw and scalpel) are constantly kept in the cutting room.
- Before cutting the sample, make sure that the cryostat is running, and that a sample finger is connected to C_1 (Figure 2.1.) and being evacuated. Use one of the short fingers for this, such that it fits under the equilibration box. Fill up the 12 L LN_2 container.
- Cut the ice sample in the early afternoon of the first day. For this, bring the sample from the −20 °C freezer into the −18 °C cutting room. For an EDC B-cut, cut two ~18 cm pieces using the band saw. Shave away the outer 5 mm from each surface of the two ice pieces to minimize surface contamination. Similarly, remove at least 5 mm of ice around any visible crack. Depending on how much ice had to be removed, an additional piece of ice needs to be prepared in the same way. In total, the decontaminated sample pieces should weigh about 600 g for EDC.
- Place the sample pieces in the extraction vessel, together with the magnetic stirring bar. While still in the cutting room, seal the vessel using a regular wrench and a torque

wrench set to 20 Nm. For transport to the extraction system, place the sealed extraction vessel inside an insulated box, surrounded by eutectics. Bring the vessel and the dewar to the laboratory.

A.1.2. Ice sample gas extraction

Having prepared the ice sample, the next step is to melt the ice and extract the ancient air contained therein.

- Attach the extraction vessel to C_6. Then place the extraction vessel inside the cooled dewar and wrap it in aluminium foil to keep the ice as cold as possible while the extraction vessel and the connecting line are being evacuated. Open V_{20}, V_{21}, and V_{22}, evacuating the extraction vessel first using the membrane pump for 3 min and subsequently switching to the turbo pump for 45 min. Make sure the water trap protecting the turbo pump is filled with LN_2.
- Monitor the ice temperature 5 min and 20 min into evacuating the sample vessel, and at the end of the 45 min. To do so, briefly close V_{20} and read out the vapour pressure at P_1, from which the ice temperature can then be inferred. If the extraction vessel has been well insulated, the ice temperature should not surpass −15 °C (~1.7 mbar) at the end of the 45 min.
- After evacuating the sample vessel, check the connection to the sample vessel for leaks by reading out the pressure gauge at the turbo pump (after the water trap). The turbo pump should reach a vacuum of about $1 \cdot 10^{-6}$ mbar or lower. Additionally, close V_{20} and make sure the pressure at P_1 stays stable over 10 s.
- Before starting the melting process, check the temperature readings of WT_1 and WT_2. Desired values are −90 °C for WT_1, and −95 °C for WT_2. Then open V_{18}, V_{17}, V_{13}, and V_{11}, linking the sample vessel to the evacuated finger connected to C_1 which had been placed to cool in the 10 K cryostat beforehand. Open the finger Nupro valve.
- Start the melting process: Remove the aluminium foil and add water at 40–50 °C to the dewar, i.e., water that was boiled in the kettle some 45 min ago. If there is still plenty of ice 20 min into the melting, increase the melting speed by adding hot water.
- Once the ice has fully melted (after around 15–20 min), remove the sample vessel from the water bath and place it onto the stirring plate. Ideally, the last few pieces of ice only melt when the vessel is already out of the water bath. This ensures the water temperature and thus the vapour pressure do not get too high and thereby prevents potential clogging of the water traps.

- Start the stirring plate. The whirl created should not quite reach the bottom of the vessel. Keep stirring until 90 min have passed since the start of the melting process. Regularly monitor P_1 and P_2. P_2 should reach a stable pressure of about $1.5\cdot10^{-3}$ mbar, P_1 is typically around 15 mbar by the end of the 90 min.
- After 90 min, close the finger Nupro valve and V_{11}, remove the finger from the cryostat and detach it from C_1.

Having thus frozen the sample air into a finger, the next step is to let the air reach temperature equilibrium before splitting it into a small (2 cm^3) and a large aliquot (50 cm^3). The smaller aliquot in the split air volume is later analysed on the Delta V. The larger aliquot, i.e., the noble gas aliquot, will be analysed on the MAT 253. From here on, ice sample, BOA sample and AL sample are all treated identically.

- Attach the finger with the sample gas to C_4. For this, the small and large equilibration volume are already connected to C_3.
- Next, open V_2, V_8, V_7, and all valves leading from the turbo pump to the equilibration volumes and evacuate the lines for 30 min.
- Check for leak-tightness, especially for connections C_3 and C_4. This is done by checking that P_2 reaches its minimum value (usually on the order of 10^{-4} mbar) and stays stable at that value for at least 30 sec when isolated from the turbo pump. Once leak-tightness is guaranteed, close V_2 and open the finger Nupro valve to let the sample gas expand into the two equilibration volumes. Lower the ventilated temperature equilibration box such that it encases the two volumes and the finger connected to them.
- Having done so, the gas is left to thermally equilibrate overnight and for a minimum of 12 hours. This minimises any fractionation due to thermal gradients.
- Empty the water traps overnight by pumping the water into the LN_2 trap in front of the turbo pump. This step is skipped for BOA and AL samples.
- In the next morning, split the sample air into two aliquots by closing V_8. Start the cryostat. Attach two fingers to C_1 and C_2 and evacuate fingers and lines.
- Once the cryostat has reached 15 K, fill the dewar surrounding LN_2 trap with liquid nitrogen required to freeze out CO_2 and potential drilling fluid from the Delta V aliquot.
- With the LN_2 trap operational, open V_2, V_{10} and V_9, allowing the smaller aliquot to flow through the trap into the finger connected to C_1 and placed in the 15 K cryostat.

Freeze the aliquot into the finger for 35 min and then close the finger Nupro valve and V_9.

- Close V_2, then detach the two equilibration volumes and the finger attached to C_4. Connect them to C_5 instead. Simultaneously unfreeze the CO_2 from the LN_2 trap by exchanging the LN_2 in the dewar for water. P_2 may serve as a first indication for drilling fluid contamination of the sample. P_2 of samples not contaminated by drilling fluid typically reads between $2–3 \cdot 10^{-2}$ mbar.
- Prepare the gettering process: Add four 5 cm strips of the Zr/Al alloy to the quartz glass tube; Connect the tube to the system via a ConFlat-flange sealed by a copper gasket; and place the getter oven such that it envelopes but does not touch the glass tube.
- Next, open V_4, V_5, V_6, and V_{19} and evacuate the getter tube and connections thereto. For this, first use the membrane pump for one minute, before switching to the turbo pump and pump for 10 min.
- Check connections for leaks, making sure P_2 is on the order of $1 \cdot 10^{-3}$ mbar (no perfect vacuum can be achieved due to the Zr/Al strips). Then heat the getter oven for 35 min until the thermometer placed right outside the getter oven reads 608 °C. The temperature within the oven is significantly higher, around 800–900 °C. Throughout these 35 min, the system is further evacuated by the turbo pump.
- After these 35 min, close V_4 and expand the large aliquot connected to C_5 into the getter vessel by opening V_8. The gettering process takes 45 min, during which the Zr/Al alloy absorbs all reactive gases of the sample air, leaving behind only noble gases and hydrogen.
- To remove the hydrogen, the getter oven needs to be cooled to approximately 300 °C, at which point most hydrogen is absorbed by the Zr/Al strips. To do so, lower the oven and place it below the glass tube for another 10 min after having turned the oven off.
- Finally, freeze the gettered sample gas into the finger connected to C_2 by opening V_4, V_3, V_9, and V_{10}.
- Remove both fingers from cryostat and attach them to the mass spectrometers. Let the fingers thermally equilibrate for at least 3 hours before IRMS analysis.

A.1.3. Mass spectrometer sample measurement

- Connect the WS I cylinder to the standard (right) side and the finger with sample gas to the sample (left) side of the mass spectrometer. When measuring WS I against WS II instead, connect WS II on the sample side.
- After connecting, only open the valves from the inlets to the membrane pump, thus making sure that the lab air does not get into the bellows or the source but into the membrane pump only. Once the pressure gauge in front of the membrane pump reads a pressure in the order of 10^{-1} mbar, switch to the turbo pump.
- Pump the two bellows and all lines connecting the gas inlets, bellows, and changeover valve using the turbo pump for at least 5 min. Make sure both bellows are fully expanded.
- Note down the current date, type of measurement (e.g., WS I vs. EDC #xxxx), the number of the finger the sample is contained in, and the box/trap ratio in the respective Excel summary file. Each mass spectrometer has its own Excel file.
- Fill an aliquot of WS I into the pipette volume between the two Nupro valves of the WS I cylinder. To do this, close the Nupro valve that is further away from the cylinder before opening the Nupro valve closer to the cylinder, thus letting the working standard expand from the cylinder into the pipette volume. Avoid skin contact with any part of the inlet to minimize thermal fractionation. Let the air between cylinder and pipette volume equilibrate for 5 min.
    - When measuring WS I vs. WS II: Do the same for the sample side.
    - When measuring WS I vs. finger: Nothing to be done for the sample side yet.
- Before the 5 min are up, close the six valves that separate the bellows and the inlets from the rest of the system, three each on standard side and sample side.
- When the 5 min are up, close the Nupro valve closer to the cylinder before you open the one further away, thus isolating the WS aliquot and then expanding the aliquot into the mass spectrometer bellow. Let equilibrate again for 5 min.
    - When measuring WS I vs. WS II: Do the same for the sample side.
    - When measuring WS I vs. finger: Expand sample air from finger into sample side bellow. Let equilibrate for 5 min.
- When the 5 min are up, close all valves around the bellows. Next, open the bellows to the changeover valve. Compress bellows to roughly match signal intensities at the preset signal intensities (see Tables 2.3. and 2.4.).

- Start the acquisition in the Acquisition ISODAT software. Make sure to select the correct measurement sequence, that is, the sequence of blocks the mass spectrometer runs. Give your file a recognizable name (e.g., yyyymmdd_WS I vs. xxxx).

A.2. Outside air and Atemluft protocols

The gas extraction for BOA and AL samples is very similar to that of an ice sample. Differences only exist in the beginning, as no ice needs to be melted and hence no water traps are required. The second part of the protocol is identical with the ice sample gas extraction protocol.

A.2.1. Bern Outside Air extraction

- Start the cryostat and attach a finger to C_1. Make sure to use one of the shorter fingers such that it fits under the equilibration box. Attach the equilibration volumes to C_3 and connect the outside air container to the large volume via C_4. Evacuate finger and lines. Pump lines for at least 30 min, including the outside air connection line.
- Once the cryostat has reached 15 K and all lines and the finger are evacuated, place the finger in the cryostat to cool down.
- Close V_2 and open the outside air Nupro valve for 3 s and close again.
- Subsequently, freeze the BOA sample into the finger placed in the cryostat. After 35 min, close the finger Nupro valve and V_{11}, remove finger from cryostat and detach the finger from C_1.
- Detach the outside air volume from C_4 and instead connect the finger with the sample air to C_4.
- The following steps are identical to those of the ice sample extraction process described in Annex A.1.2.

A.2.2. Atemluft extraction

- Open the AL bottle and adjust the flowrate to about 1 mL/min. Flush the AL line for a few hours or overnight before starting the extraction with the SGE valve open towards the fused silica capillary that vents into the lab. Before starting the extraction, check flowrate again. Attach the equilibration volumes to C_3 and connect the capillary going away from the other side of the SGE valve to the large volume via C_4. This last step may also be done while flushing the line.

- Start the cryostat and attach a finger to C_1. Make sure to use one of the shorter fingers such that it fits under the equilibration box. Evacuate finger and lines. Pump lines for at least 30 min, including the capillary connection. Check for leaks at C_3 and C_4 by making sure P_2 has reached its minimum value (usually on the order of 10^{-4} mbar) and stays stable at that value for at least 30 sec when isolated from the turbo pump.
- Close V_{11} and V_9, then open the SGE valve to the extraction system and admit AL to the turbo pump for 10 min. Close V_7 and pump the equilibration volumes for another 15 min. Check for potential leaks at C_3 again. Then close V_8, open V_7 and fill large equilibration volume with AL for about 45 min, i.e., such that the resulting AL sample is about 60 mL STP. In the meantime, evacuate the finger connected to C_1.
- After sampling AL for 60 min, close V_7 and switch the SGE valve to the lab position. Subsequently, freeze the AL sample to the finger placed in the 15 K cryostat. After 35 min, close the finger Nupro valve and V_{11} and detach the finger from C_1.
- Detach the AL capillary from C_4.
- The following steps are identical to those of the ice sample extraction process described in Annex A.1.2.

A.3. Sampling protocols

The 1-gallon volume used as a container for our outside air yields between 13 and 15 BOA samples. Thus, BOA needs to be replenished quite frequently, typically two to three times per measurement period. The working standards on the other hand deplete only very slowly over time. They have only been replenished once so far for both the MAT 253 and the Delta V, in June of 2021. A step-by-step description of how to replenish BOA and working standards cylinders be found in the following two subsections.

A.3.1. Bern Outside Air sampling

- Make sure BOA is sampled in the morning when the sun has not hit the facade yet to avoid thermal fractionation.
- Build up sampling line in room B82 as shown in the schematic in Figure 2.16. All material needed can be found in B82, except for the ethanol dewar and the stirring bar, which are in room 016, and the air pump, the flow meter, and the air buffer tank, which are currently stored in B79 and 0924, respectively.

- Make sure connections are properly tightened, but do not overdo the Ultra-Torr connections as not to break the glass water traps.
- Cool down the ethanol by mixing in liquid nitrogen until very viscous, roughly −90 °C. Ideally, the dewar containing the ethanol is kept in the −50 °C freezer to cool down for a day before sampling.
- Push the long black tubing through the blinds outside the window.
- Open Nupro valves of BOA volume and start the pump. Check the airflow at the flow meter, adjust the in-line Nupro valve until a flowrate of about 4 L/min has been reached.
- Once a stable airflow of 4 L/min has been established, flush the BOA volume at least ten times, i.e., for our volume of close to 4 L, pump for at least 10 min.
- After these 10 min, stop the pump, wait for three seconds to let the airflow cease, and simultaneously close the two Nupro valves at both ends of the BOA volume.
- Heat out the water traps for the next BOA sampling.

A.3.2. Replenishment of working standards

To mix working standards for both MAT 253 and Delta V, we use the setup shown in Figure A.1. This setup involves a crosspiece, which needs to be connected to the MAT 253. A pressure gauge is installed at the connection opposite to the mass spectrometer. At the other two ends of the crosspiece, the 2 L stainless-steel cylinder of working standard that should be replenished and the industrial gas mixture to replenish it with are connected. A Nupro valve on the left-hand side controls airflow from the industrial gas mixture. For the MAT 253 working standards, this industrial gas mixture consists of pure Ar, to which 123.8 ppm Kr and 9.5 ppm Xe were added to mimic the atmospheric mixing ratio. Additionally, a flask of pure Ar is needed. For the Delta V working standards, we use Atemluft, that is, compressed atmospheric air. To remove CO_2 from the Atemluft, an intermediate piece filled with Ascarite (NaOH) is placed in line with the industrial gas mixture. The crosspiece, the pressure gauge and the Ascarite intermediate piece are all stored in B82.

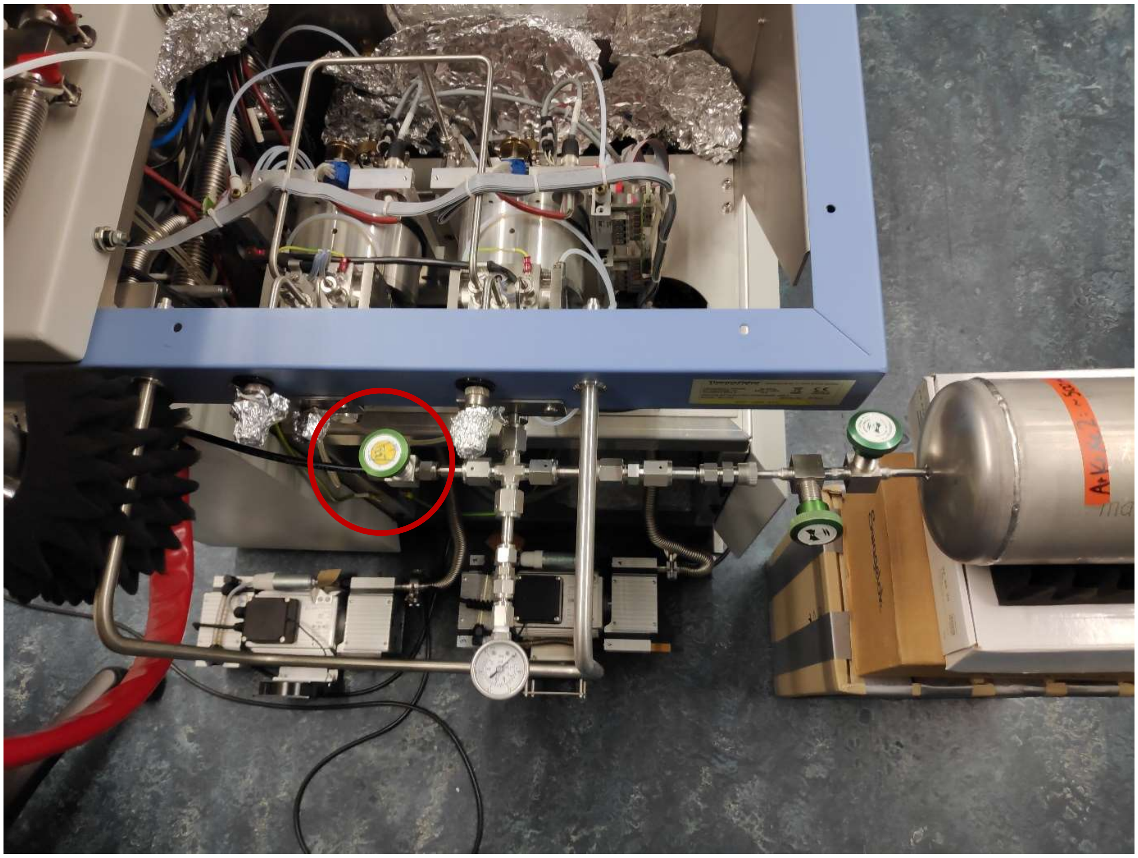

Figure A.1.: Setup used to replenish MAT 253 working standards. A crosspiece is attached to one of the MAT 253 inlets, to which a pressure gauge, the working standard cylinder, and the industrial gas mixture are connected. To replenish Delta V working standards, an intermediate piece filled with Ascarite is placed on the left side of the circled Nupro valve to remove CO_2.

A.3.2.a. MAT 253

- To mix MAT 253 WS I, connect the working standard cylinder to the crosspiece and empty the cylinder using the turbo pump of the mass spectrometer. If the cylinder used to contain working standard for the same mass spectrometer, 10–15 min of evacuation time are enough. Otherwise, evacuate the cylinder overnight.
- Next, connect the Ar flask to the setup and flush the connection line multiple times with Ar. Then pump the setup for another few minutes. Next, admit roughly 17.5 mbar Ar to the mass spectrometer bellow and the WS I cylinder, using the pressure gauge of the mass spectrometer bellow. The Ar flow speed can be controlled using the Nupro valve at the end of the Ar connection line. This addition of Ar makes the MAT 253 WS I composition more closely resemble that of an ice sample.

- Close all valves and connect the industrial noble gas mixture in place of the Ar flask. Pump the line again for a few minutes, then close the valve towards the mass spectrometer.
- Slowly admit the industrial noble gas mixture to the setup with the Nupro valves of the WS I cylinder still closed. Open the WS I Nupro valves only after a few seconds. This is done to ensure a positive pressure gradient towards the working standard cylinder.
- Fill the working standard cylinder with industrial noble gas mixture until the external pressure gauge that is part of the setup reads about 500 mbar STP. Once this pressure is achieved, close all valves.
- To mix MAT 253 WS II, repeat the above steps, omitting the initial filling of pure Ar.

A.3.2.b. Delta V

- To mix Delta V working standards, connect and evacuate a working standard cylinder as described above for the MAT 253 WS I.
- Connect the Atemluft flask together with the Ascarite filter piece to the setup and disconnect the evacuated working standard cylinder. **Since we want to prevent NaOH contamination of the mass spectrometer from the Ascarite at all costs, the Atemluft connecting line must not be pumped.** Instead, flush the setup for several minutes with Atemluft, keeping the valve towards the mass spectrometer closed.
- Close the Nupro valve at the end of the Atemluft connection line. Reconnect the evacuated working standard cylinder, then pump the crosspiece using the turbo pump of the mass spectrometer for several minutes. Close the valve towards the mass spectrometer.
- Slightly open the Nupro valve at the end of the Atemluft connection line, thus slowly letting Atemluft into the working standard cylinder. The slow gas flow guarantees optimal removal of CO_2 by the Ascarite. Fill the working standard cylinder with Atemluft until the external pressure gauge reads about 1.2 bar STP. Then close all valves.
- Both Delta V working standards are mixed in the same way.

A.4. Mass spectrometer protocols

Both IRMS use electron impact to ionise the input gas. The ionising electrons are produced in the mass spectrometer source by a thin tungsten wire, the filament. Over many months of use, the filament slowly degrades and eventually either does not achieve the necessary linearity, cannot produce a sufficiently strong signal intensity, or breaks. Although filament longevity can be extended somewhat by timely removal of the sample air after completion of the measurement routine, the filament will thus eventually need to be replaced. In any case, the filament should be replaced at the start of a measurement period to heighten the chances for measuring all ice samples and BOA samples with the same filament and source parameter settings. The following subsection gives a step-by-step procedure of how to replace the MAT 253 and the Delta V filaments. The procedure is similar for both mass spectrometers. In the second subsection, some indications for avoiding mass spectrometer instabilities and the tuning of source parameter settings are given.

A.4.1. Exchanging filaments

- Turn down emission current to 0 A, then turn off the source current, first on the computer **and then by switching the HV-switch on the mass spectrometer electronic board to "off".**
- Isolate the analyser housing to prevent it being flushed by lab air by switching the four-way SGE valve to the "0"-position.
- Shut down the pumps of the source and analyser housing. **This is the ideal time to for a pump overhaul.**
- Remove source housing screws. For the Delta V, disconnect the three HV plugs.
- Put on rubber gloves; **The source interior must not be touched with bare hands!**
- Carefully remove the source from its housing and place it in its fixture, i.e., a Styrofoam mould for the MAT 253 and on top of four copper blocks for the Delta V. Cover the source housing opening with aluminium foil.
- To replace the filament, remove the two fixating screws at the top of the filament's ceramic plate and loosen the screws of the two connecting wires. The old filament can now be taken out and replaced by a new one. If required, shorten the connecting wires of the new filament.
    - The positioning of the filament is critical for the MAT 253 to achieve sufficiently high signal intensities. The filament should align with the bottom of the trap opening. To check filament alignment, detach the trap by removing the magnet in front of it and its two fixating screws. Once the filament is positioned properly, tighten the filament screws, again check the filament positioning, and put trap back in place.

  - For the Delta V, filament positioning is not as critical.
- Before remounting the source, check source parts for signs of strong discolouring, in particular the ceramic rods and quartz-glass spacers. Check the gasket sealing the source housing for potential damage such as scratches. Make sure the source connecting wires do not touch under light compression of the source. Check that box and trap are not making contact.
- Remount the source. Before putting back on the HV connectors, check for potential short circuits of the source connecting wires using a multimeter between all lines. Restart the pumps and evacuate source housing until source pressure is on the order of 10^{-8} mbar, i.e., for at least 24 hours. Switch SGE valve back to "HV"-position to start pumping on the analyser housing again. Start tuning of source parameter settings.

A.4.2. Tuning of source parameter settings

- Before properly tuning the source parameter settings, make sure that the filament can produce sufficiently high signal strength and creates an ion beam with desirable peak shape, i.e., steep flanks and flat plateau in between. The flatness of the peaks is best seen when looking at ratios of ion currents. In case other source parts were exchanged, make sure the new parts have fully outgassed by making sure isotopic ratios are according to natural abundances.
- Test for potential step changes in the signal intensity. This is done by setting all source parameter settings to middle positions and then recording intensity-vs-source parameter curves for all source parameters. If step changes occur, avoid vicinity to associated voltages as best as possible during tuning.
- Perform a linearity tuning for all gas configurations the signal intensity allows to. Typically, linearity tuning is possible for all gas configurations except for the one used for Xe isotopes. Start tuning with all potentiometers in their middle position. Next, record the signal intensity as a function of the extraction voltage. Two peaks should be visible. When performing an intensity tuning, set the extraction voltage to the voltage of the main peak. When tuning for maximal linearity instead, use the smaller peak. If this smaller peak cannot be made out, opt for a high extraction voltage as this tends to lead to better linearity by reducing gas residence time in the ionisation housing.
- Optimize all other source parameter settings to maximize intensity, keeping the extraction voltage constant. Start with the potentiometers controlling the voltages of lenses closest to the ionization housing, i.e., the trap voltage and the electron energy,

followed by the x- and y-focus parameters and the singular lenses. Do multiple iterations, now including the extraction voltage, to maximize the signal intensity. Be sure not to change the extraction voltage by more than a few V to not move away from the linearity optimum.

- Once no more improvements in signal intensity can be achieved, again make sure there is no step change in the signal intensity in the vicinity of the source parameters.
- Repeat the above two steps multiple times to find multiple sets of potential source parameters for each gas configuration. Perform pressure imbalance runs for all settings, then choose the setting with the lowest pressure imbalance sensitivity.
- Perform a 4-hour (or longer) intensity-vs.-time run for each chosen source parameter setting, ensuring long-term signal stability.

A.4.3. A period of signal instability

In June of 2021, just before the start of the first measurement campaign, we encountered signal instability on our MAT 253. The signal went back and forth in rapid succession between two levels. These fluctuations occurred only in a certain pressure range and originally only for the Xe tuning. A typical oscillation pattern can be found in Figure A.2. For the filament in use at that time, Xe was the only element that was measured with an intensity tuning, i.e., with low extraction voltage. We thus decided to somewhat increase the extraction efficiency at the expense of a small decrease in beam intensity. The instability indeed disappeared temporarily, but the success was not permanent. When similar fluctuations appeared again in September 2021 and a filament change was also not resolving the issue, an in-depth analysis of the instability was undertaken. The following characteristics of the instability were found:

- When instable, the signal rapidly oscillated between two signal levels.
- The instability occurred independent of the magnet setting, the cup, and the filament, making it improbable that either magnet, analyser, or filament were the cause.
- The instability only occurred in a certain source pressure range.
- The instability only occurred at extraction voltages lower than approximately 45%.

These findings led us to the conclusion that either some part of the electronics or a potential leakage current in the source might be the instability's cause. In consequence, we exchanged the high voltage potential module of the x-focus source plate, which indicated that it was not able to hold the pre-set voltage stable. Also, the isolating ceramics rods, quartz glass spacers and deflection plates in the MAT 253 source that showed signs of discolouration were replaced. However, neither of these measures had any visible effect on the instability.

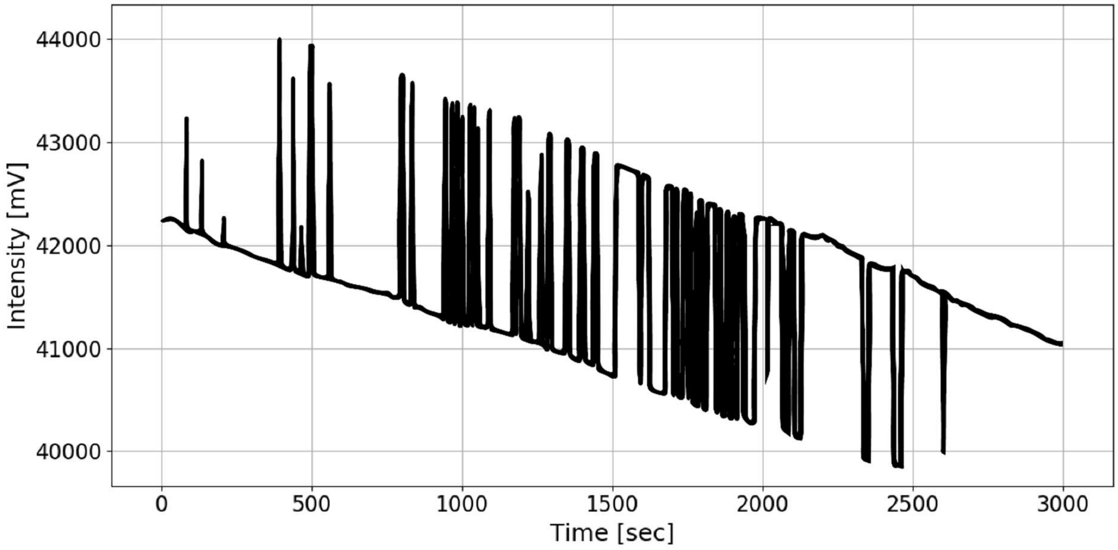

Figure A.2.: A typical oscillation pattern of signal instability as observed between June 2021 and December 2021, shown here for $\delta^{40/36}Ar$*.*

A hint from Ross Beaudette from Scripps eventually guided us to the source of the issue. When plotting the beam intensity over the voltage range of the trap source parameter, a step change in the otherwise smooth intensity curve can be detected for certain source parameter settings (see Figure A.3.). For the source parameters in use during that time, the step had a similar amplitude as the observed oscillations and was positioned close to the trap voltage used in tunings with instable signal. Furthermore, the trap voltage at which this step occurs, as well as to a lesser extent its amplitude, are dependent on both the extraction voltage and the source pressure. A higher extraction voltage and lower source pressure make the step occur at higher trap voltages, as well as to have a somewhat smaller amplitude. The opposite is found for a lower extraction voltage and higher source pressure. Thus, if the trap voltage is chosen close to the step change and the bellow pressure is set sufficiently high, the signal eventually starts to oscillate as the source pressure decreases over time.

It remains unclear what caused the mass spectrometer to start oscillating after having run smoothly for more than ten years. We can think of two scenarios: (i) the step in the trap voltage-intensity curve has recently appeared, or (ii) the step has always been there and a source parameter, most likely the extraction voltage, suddenly cannot be held at a stable potential anymore. If (i) were correct, we would expect that a gradual or sudden change in a hardware component in the source or trap had occurred at some point. As the source isolating parts had already been replaced before, the only other measure we could think of was replacing the trap connecting line. This line is re-bent whenever the filament is exchanged or repositioned and might thus have been damaged at some point. However, exchanging this line had no effect on the step. To test option (ii), we exchanged the high voltage potential module of the extraction plate. Indeed, minor improvements in extraction voltage stability were observed. This was to be expected as the newer modules come with an additional capacitor that helps to generate a more stable high voltage. This led to a narrowing of the pressure range affected by oscillations but was not sufficient to fully get rid of them. A possible step forward would be to equip all other HV potential modules with such capacitors in the hope to further improve signal stability. For now, the problem is circumvented by choosing the trap voltage sufficiently far away from where the step change occurs. Also, the position of the step is now monitored on a weekly basis by recording signal intensity-vs.-trap voltage (Figure A.3.). This is necessary as the step can substantially change its position as the filament degrades over time.

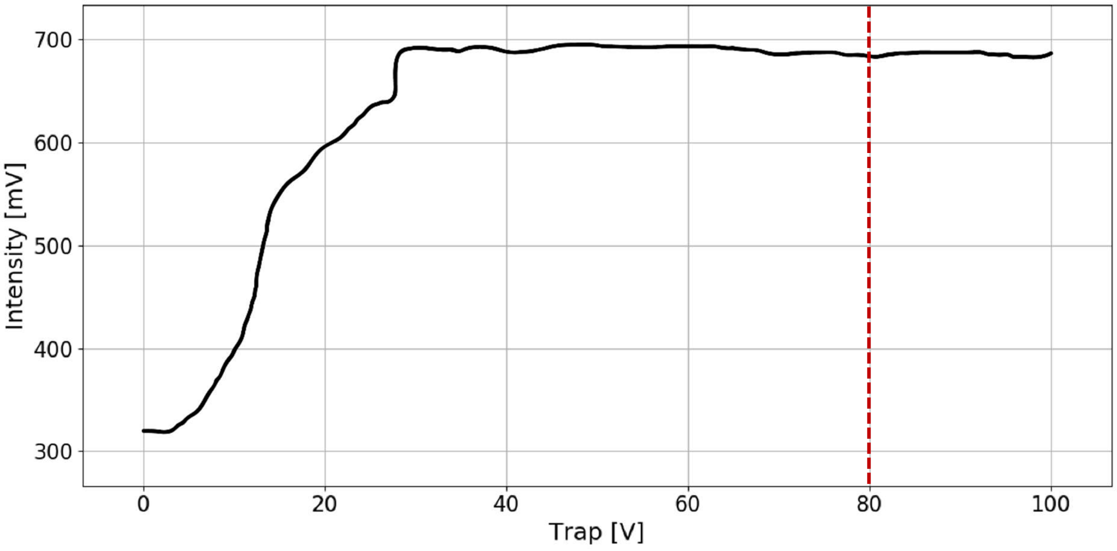

Figure A.3.: The culprit of the signal instability: a sharp step in the measured signal intensity as a function of the trap voltage, here at around 30 V. The position of this step and its amplitude were found to be dependent on both the extraction voltage and the source pressure. Consequently, we chose our trap current far away from the step, as indicated by the red line.

A.5. Mixing precise amounts of different gases

Equipped with the two pressure gauges P_1 and P_2, the extraction system can be used to measure out small amounts of gas to a precision of roughly 5%. The gauged gas amounts can then be frozen into a finger, allowing us to mix amounts of different gases with the following procedure:

- The two pressure gauges are swapped, such that the less sensitive pressure gauge P_1 is placed next to V_{13}.
- The gas container of choice is connected to the Ultra-Torr vacuum fitting C_7. Usually, this is a Working Standard II cylinder.
- If gas from a pressurized bottle should be mixed, connect the bottle via the VCR connection C_8.
- N_3 isolates the rest of the extraction line from these connections. N_4 controls the gas inlet from C_8.
- The pipette volume at the exit of the cylinder serves to gauge an aliquot of working standard. For gas from a pressurized bottle, the volume between N_3, N_4, and C_7 is used instead.
- Next, this aliquot is expanded into the extraction system, either to the line between V_2, V_3, V_9, V_{11}, V_{12}, and V_{13}. If higher precision is needed, the aliquot can be expanded to additional volumes connected to C_3, i.e., the small and large equilibration volumes and a finger connected to C_4.
- The gas amount in the line is then gradually decreased by isolating and then pumping away small gas aliquots, before re-expanding the rest of the gas. Always using the same volume for the expansion ensures a controlled stepwise reduction of gas pressure.
- If the desired pressure is reached, the gas is frozen into a finger connected to C_1 or C_2.

A.6. Overview of measured EDC ice samples

The following Tables A.1.–A.3. contain all ratios obtained from the EDC ice samples measured during this PhD project. Depth is given in units of meters; all isotopic and elemental ratios are in units of permille; ΔN_2 and ΔCO_2 are the difference between sample and standard side N_2 and CO_2, respectively, in units of mV. $\Delta N_2 < 200$ mV and $\Delta CO_2 < 0.5$ mV are indication of successful removal of reactive gases from the MAT 253 aliquot and successful removal of CO_2 from the Delta V aliquot, respectively. The tables are 6 pages long, with only acknowledgements, list of publications, declaration of consent, and curriculum vitae following.

Date	Bag Nr.	Depth	$\delta^{136/129}$Xe	$\delta^{134/129}$Xe	$\delta^{132/129}$Xe	$\delta^{86/82}$Kr	$\delta^{86/84}$Kr	$\delta^{40/36}$Ar$_{MAT}$	$\delta^{40/38}$Ar
04.10.22	EDC 2835	1558.975	3.254	2.247	1.354	1.925	0.962	2.012	0.989
03.26.22	EDC 2915	1602.975	3.322	2.319	1.382	1.962	1.001	2.010	0.988
03.25.22	EDC 3008	1654.125	3.295	2.334	1.393	1.948	0.962	1.997	0.989
03.24.22	EDC 3054	1679.425	3.379	2.251	1.414	1.966	0.979	2.017	1.010
04.11.22	EDC 3077	1692.075	3.352	2.466	1.427	2.007	0.997	2.071	1.016
05.03.22	EDC 3102	1705.825	3.614	2.476	1.520	2.094	1.064	2.149	1.066
03.29.22	EDC 3117	1714.075	3.515	2.493	1.547	2.098	1.055	2.143	1.065
04.13.22	EDC 3130	1721.225	3.494	2.544	1.520	2.096	1.051	2.179	1.068
05.04.22	EDC 3143	1728.375	3.592	2.436	1.515	2.051	1.029	2.157	1.063
04.28.22	EDC 3155	1734.975	3.353	2.361	1.398	2.002	1.004	2.120	1.051
05.08.22	EDC 3164	1739.925	3.425	2.507	1.428	2.008	1.009	2.120	1.042
04.29.22	EDC 3180	1748.725	3.276	2.345	1.360	1.925	0.961	2.046	1.006
05.10.22	EDC 3190	1754.225	3.277	2.415	1.318	1.908	0.956	2.012	0.989
05.11.22	EDC 3199	1759.175	3.165	2.357	1.327	1.826	0.936	1.979	0.978
05.13.22	EDC 3207	1763.575	3.009	2.129	1.241	1.774	0.884	1.904	0.942
04.14.22	EDC 3217	1769.075	2.903	2.073	1.242	1.722	0.859	1.877	0.919
04.19.22	EDC 3228	1775.125	2.812	1.994	1.205	1.684	0.838	1.836	0.901
05.12.22	EDC 3240	1781.725	2.712	1.856	1.113	1.618	0.825	1.804	0.885
05.17.22	EDC 3250	1787.225	2.481	1.726	0.999	1.453	0.724	1.651	0.818
05.18.22	EDC 3260	1792.725	2.380	1.702	1.002	1.443	0.720	1.596	0.783
04.20.22	EDC 3278	1802.625	2.416	1.807	1.085	1.468	0.747	1.606	0.795
04.05.22	EDC 3290	1809.225	2.341	1.662	1.005	1.435	0.711	1.584	0.787
03.30.22	EDC 3308	1819.125	2.457	1.695	1.068	1.465	0.748	1.574	0.775
05.05.22	EDC 3324	1827.925	2.625	1.778	1.085	1.530	0.766	1.623	0.797
04.15.22	EDC 3343	1838.375	2.728	1.908	1.157	1.596	0.787	1.705	0.842
04.06.22	EDC 3364	1849.925	2.781	1.890	1.190	1.635	0.819	1.734	0.849
03.23.22	EDC 3383	1860.375	2.820	1.884	1.219	1.649	0.822	1.727	0.846
04.21.22	EDC 3393	1865.875	2.807	1.932	1.188	1.605	0.807	1.727	0.855
03.17.22	EDC 3410	1875.225	2.792	1.964	1.169	1.637	0.830	1.731	0.857
03.31.22	EDC 3418	1879.625	2.712	1.836	1.162	1.661	0.827	1.759	0.868
04.07.22	EDC 3427	1884.575	2.759	2.039	1.199	1.656	0.825	1.763	0.868
04.08.22	EDC 3443	1893.375	2.604	1.842	1.108	1.556	0.787	1.695	0.838
04.09.22	EDC 3450	1897.225	2.538	1.830	1.099	1.475	0.743	1.650	0.809
04.01.22	EDC 3458	1901.625	2.481	1.662	1.107	1.498	0.753	1.628	0.803
05.06.22	EDC 3464	1904.925	2.460	1.880	1.033	1.500	0.757	1.627	0.804
03.22.22	EDC 3474	1910.425	2.614	1.815	1.091	1.575	0.781	1.720	0.851
04.22.22	EDC 3483	1915.375	2.395	1.625	1.058	1.447	0.720	1.596	0.791
04.02.22	EDC 3490	1919.225	2.391	1.588	0.975	1.422	0.730	1.573	0.771
06.28.22	EDC 4140	2276.725	3.143	2.219	1.313	1.849	0.915	1.907	0.935
06.21.22	EDC 4146	2280.025	3.319	2.277	1.393	1.911	0.963	1.914	0.939
06.22.22	EDC 4156	2285.525	3.335	2.385	1.395	1.942	0.973	1.953	0.957
06.23.22	EDC 4164	2289.925	3.368	2.356	1.424	1.969	0.993	1.962	0.970
06.29.22	EDC 4174	2295.425	3.532	2.482	1.469	2.032	1.016	2.054	1.021
06.24.22	EDC 4186	2302.025	3.456	2.481	1.476	2.048	1.035	2.075	1.023
07.08.22	EDC 4196	2307.525	3.464	2.474	1.433	2.048	1.012	2.122	1.045
06.30.22	EDC 4204	2311.925	3.445	2.486	1.427	2.028	1.023	2.095	1.037
07.09.22	EDC 4212	2316.325	3.289	2.312	1.368	1.958	0.978	2.034	0.995
07.01.22	EDC 4216	2318.525	3.213	2.304	1.349	1.893	0.955	1.977	0.966
07.10.22	EDC 4222	2321.825	3.113	2.244	1.301	1.868	0.942	1.957	0.968
07.02.22	EDC 4224	2322.925	3.115	2.148	1.317	1.871	0.941	1.951	0.958
07.05.22	EDC 4236	2329.525	2.659	1.881	1.101	1.612	0.809	1.729	0.852
07.11.22	EDC 4246	2335.025	2.595	1.780	1.053	1.555	0.767	1.712	0.839

Date	**Bag Nr.**	**Depth**	$\delta^{136/129}$**Xe**	$\delta^{134/129}$**Xe**	$\delta^{132/129}$**Xe**	$\delta^{86/82}$**Kr**	$\delta^{86/84}$**Kr**	$\delta^{40/36}$**Ar**$_{\text{MAT}}$	$\delta^{40/38}$**Ar**
07.06.22	EDC 4252	2338.325	2.538	1.817	1.072	1.539	0.780	1.699	0.831
07.07.22	EDC 4256	2340.525	2.474	1.717	1.016	1.503	0.752	1.650	0.802
06.15.22	EDC 4652	2558.325	3.284	2.208	1.340	1.866	0.943	1.962	0.966
06.09.22	EDC 4662	2563.825	3.233	2.289	1.328	1.914	0.946	1.959	0.963
06.04.22	EDC 4672	2569.325	3.277	2.248	1.357	1.959	0.981	1.973	0.976
06.10.22	EDC 4680	2573.725	3.323	2.260	1.396	1.980	0.981	1.972	0.961
05.19.22	EDC 4686	2577.025	3.454	2.416	1.428	1.972	0.983	2.031	0.998
05.20.22	EDC 4692	2580.325	3.573	2.449	1.473	2.078	1.038	2.117	1.029
06.11.22	EDC 4694	2581.425	3.385	2.446	1.437	1.988	0.987	2.077	1.020
06.14.22	EDC 4702	2585.825	3.578	2.450	1.487	2.058	1.030	2.143	1.055
05.31.22	EDC 4704	2586.925	3.541	2.508	1.501	2.047	1.020	2.119	1.048
06.20.22	EDC 4707	2588.575	3.523	2.359	1.453	2.024	1.021	2.123	1.039
05.24.22	EDC 4712	2591.325	3.391	2.351	1.423	1.350	0.973	2.090	1.027
06.05.22	EDC 4716	2593.525	3.338	2.329	1.358	1.870	0.979	2.060	1.006
06.01.22	EDC 4720	2595.725	3.211	2.220	1.324	1.845	0.939	1.941	0.953
05.25.22	EDC 4724	2597.925	3.087	2.093	1.331	1.819	0.907	1.904	0.935
06.06.22	EDC 4735	2603.975	2.723	1.847	1.131	1.669	0.833	1.762	0.861
06.02.22	EDC 4740	2606.725	2.798	1.932	1.201	1.596	0.808	1.731	0.851
06.07.22	EDC 4744	2608.925	2.563	1.845	1.058	1.534	0.775	1.657	0.815
06.03.22	EDC 4746	2610.025	2.474	1.762	1.088	1.367	0.737	1.618	0.790

Table A.1.: Isotopic ratios of Xe, Kr, and Ar obtained from the 72 EDC samples measured during this PhD-project. Depths are middle of the bag in units of meters. All ratios are in units of permille.

Date	**Bag Nr.**	**Depth**	**δ^{84}Kr/^{40}Ar**	**δ^{132}Xe/^{40}Ar**	**δ^{129}Xe/^{40}Ar**	**δ^{132}Xe/^{84}Kr**	**δ^{129}Xe/^{84}Kr**	**ΔN_2**
04.10.22	EDC 2835	1558.975	27.407	52.446	50.812	24.376	22.793	-16
03.26.22	EDC 2915	1602.975	28.795	53.387	51.984	23.904	22.637	-16
03.25.22	EDC 3008	1654.125	28.594	54.765	53.202	25.442	23.930	-16
03.24.22	EDC 3054	1679.425	28.200	55.166	53.553	26.212	24.642	-14
04.11.22	EDC 3077	1692.075	28.801	55.776	54.164	26.237	24.683	465
05.03.22	EDC 3102	1705.825	29.359	57.492	55.700	27.350	25.622	-16
03.29.22	EDC 3117	1714.075	31.022	60.231	58.534	28.329	26.691	-16
04.13.22	EDC 3130	1721.225	30.176	58.954	57.360	27.921	26.373	-16
05.04.22	EDC 3143	1728.375	30.236	58.469	56.854	27.410	25.849	-17
04.28.22	EDC 3155	1734.975	29.561	57.283	55.794	26.926	25.484	-16
05.08.22	EDC 3164	1739.925	29.510	57.048	55.490	26.749	25.241	-17
04.29.22	EDC 3180	1748.725	28.961	54.193	52.539	24.524	22.920	-16
05.10.22	EDC 3190	1754.225	28.702	53.403	51.882	24.012	22.537	-17
05.11.22	EDC 3199	1759.175	28.361	52.340	51.035	23.320	22.056	-16
05.13.22	EDC 3207	1763.575	28.567	51.558	50.037	22.345	20.867	-17
04.14.22	EDC 3217	1769.075	28.149	50.173	48.616	21.437	19.931	-15
04.19.22	EDC 3228	1775.125	27.333	47.325	46.228	19.443	18.372	-16
05.12.22	EDC 3240	1781.725	26.159	45.551	44.380	18.875	17.728	1921
05.17.22	EDC 3250	1787.225	24.684	41.154	39.925	16.068	14.871	-17
05.18.22	EDC 3260	1792.725	22.760	38.750	37.706	15.623	14.602	-16
04.20.22	EDC 3278	1802.625	23.285	39.427	38.229	15.787	14.621	-16
04.05.22	EDC 3290	1809.225	22.915	38.684	37.478	15.427	14.258	125
03.30.22	EDC 3308	1819.125	22.574	38.307	37.278	15.379	14.374	-16
05.05.22	EDC 3324	1827.925	22.591	39.992	38.856	17.020	15.912	-16
04.15.22	EDC 3343	1838.375	23.705	41.780	40.583	17.667	16.503	4
04.06.22	EDC 3364	1849.925	24.286	42.762	41.565	18.046	16.885	-16
03.23.22	EDC 3383	1860.375	24.815	44.177	43.087	18.905	17.854	-16
04.21.22	EDC 3393	1865.875	24.678	44.401	43.204	19.214	18.035	-9
03.17.22	EDC 3410	1875.225	26.103	45.875	44.480	19.281	17.939	-13
03.31.22	EDC 3418	1879.625	25.852	45.498	44.248	19.152	17.939	-16
04.07.22	EDC 3427	1884.575	25.924	44.775	43.696	18.394	17.357	-16
04.08.22	EDC 3443	1893.375	25.229	42.472	41.373	16.832	15.770	6
04.09.22	EDC 3450	1897.225	25.125	41.885	40.785	16.355	15.287	-16
04.01.22	EDC 3458	1901.625	25.066	42.031	40.899	16.554	15.459	-15
05.06.22	EDC 3464	1904.925	23.646	39.751	38.695	15.733	14.703	197
03.22.22	EDC 3474	1910.425	26.000	43.712	42.742	17.248	16.301	110
04.22.22	EDC 3483	1915.375	24.754	41.426	40.224	16.279	15.112	-16
04.02.22	EDC 3490	1919.225	24.273	40.288	39.241	15.653	14.643	-4
06.28.22	EDC 4140	2276.725	26.266	48.855	47.352	22.019	20.563	1194
06.21.22	EDC 4146	2280.025	26.496	49.244	47.696	22.145	20.636	-17
06.22.22	EDC 4156	2285.525	26.623	50.094	48.671	22.855	21.474	91
06.23.22	EDC 4164	2289.925	27.067	51.462	50.065	23.727	22.361	-17
06.29.22	EDC 4174	2295.425	28.090	54.933	53.538	26.090	24.731	-17
06.24.22	EDC 4186	2302.025	28.872	57.343	55.545	27.677	25.941	-8
07.08.22	EDC 4196	2307.525	29.368	56.969	55.358	26.806	25.244	-18
06.30.22	EDC 4204	2311.925	29.175	56.784	55.252	26.830	25.351	-18
07.09.22	EDC 4212	2316.325	28.612	53.789	52.351	24.478	23.085	8
07.01.22	EDC 4216	2318.525	28.424	53.115	51.582	23.997	22.508	-19
07.10.22	EDC 4222	2321.825	27.934	50.995	49.647	22.429	21.119	-17
07.02.22	EDC 4224	2322.925	28.057	52.049	50.564	23.332	21.890	-18
07.05.22	EDC 4236	2329.525	26.043	44.856	43.781	18.315	17.263	-17
07.11.22	EDC 4246	2335.025	25.951	44.109	43.019	17.714	16.661	-17

Date	**Bag Nr.**	**Depth**	**δ^{84}Kr/^{40}Ar**	**δ^{132}Xe/^{40}Ar**	**δ^{129}Xe/^{40}Ar**	**δ^{132}Xe/^{84}Kr**	**δ^{129}Xe/^{84}Kr**	**ΔN_2**
07.06.22	EDC 4252	2338.325	26.050	44.665	43.564	18.140	17.069	34
07.07.22	EDC 4256	2340.525	25.044	42.231	41.185	16.774	15.760	-18
06.15.22	EDC 4652	2558.325	27.766	50.469	48.985	22.098	20.668	3
06.09.22	EDC 4662	2563.825	27.788	51.852	50.408	23.400	21.996	95
06.04.22	EDC 4672	2569.325	27.744	51.283	49.745	22.901	21.411	-15
06.10.22	EDC 4680	2573.725	28.395	53.759	52.262	24.670	23.229	259
05.19.22	EDC 4686	2577.025	28.850	56.478	54.952	26.857	25.381	1
05.20.22	EDC 4692	2580.325	29.786	57.896	56.366	27.272	25.781	353
06.11.22	EDC 4694	2581.425	29.427	55.597	54.168	25.416	24.033	-17
06.14.22	EDC 4702	2585.825	30.302	58.567	57.027	27.429	25.941	-14
05.31.22	EDC 4704	2586.925	29.737	58.880	57.281	28.283	26.730	80
06.20.22	EDC 4707	2588.575	29.886	59.108	57.606	28.352	26.891	307
05.24.22	EDC 4712	2591.325	30.823	62.067	60.537	30.301	28.820	60
06.05.22	EDC 4716	2593.525	28.870	55.376	53.979	25.743	24.384	12
06.01.22	EDC 4720	2595.725	27.595	51.079	49.774	22.846	21.580	-6
05.25.22	EDC 4724	2597.925	27.337	50.160	48.754	22.219	20.858	-17
06.06.22	EDC 4735	2603.975	25.823	45.856	44.603	19.527	18.312	289
06.02.22	EDC 4740	2606.725	25.586	43.987	42.595	17.939	16.587	-7
06.07.22	EDC 4744	2608.925	23.845	41.395	40.230	17.126	15.986	-14
06.03.22	EDC 4746	2610.025	23.189	40.168	38.895	16.591	15.352	-17

Table A.2.: Elemental ratios of Xe, Kr, and Ar obtained from the 72 EDC samples measured during this PhD-project on the MAT 253 IRMS. Depths are middle of the bag in units of meters. All ratios are in units of permille. Additionally, we show ΔN_2*, an indicator of how complete the gettering process worked. We consider* $\Delta N_2 < 200$ *mV an indication of a successful removal of reactive gases. However, samples with* $\Delta N_2 > 200$ *mV do not appear to be affected in any way and are kept in our analysis.*

Date	**Bag Nr.**	**Depth**	**$\delta^{15}N_2$**	**$\delta^{18}O_2$**	**$\delta^{17}O_2$**	**$\delta O_2/N_2$**	**$\delta Ar/N_2$**	**$\delta^{40/36}Ar_{Delta}$**	**ΔCO_2**
04.10.22	EDC 2835	1558.975	0.487	1.458	0.788	-9.739	0.461	1.916	0.11
03.26.22	EDC 2915	1602.975	0.488	0.870	0.482	-9.975	0.157	1.904	0.10
03.25.22	EDC 3008	1654.125	0.495	0.639	0.361	-10.002	0.205	1.902	0.15
03.24.22	EDC 3054	1679.425	0.494	0.859	0.473	-8.418	0.821	1.927	0.12
04.11.22	EDC 3077	1692.075	0.500	1.172	0.626	-9.382	0.808	1.954	0.01
05.03.22	EDC 3102	1705.825	0.521	1.559	0.838	-9.755	1.289	2.051	0.12
03.29.22	EDC 3117	1714.075	0.514	1.819	0.972	-11.147	0.618	2.019	0.11
04.13.22	EDC 3130	1721.225	0.531	2.013	1.062	-10.462	1.147	2.051	0.02
05.04.22	EDC 3143	1728.375	0.529	2.080	1.116	-10.926	1.333	2.041	0.18
04.28.22	EDC 3155	1734.975	0.511	2.102	1.127	-11.594	1.081	1.998	0.13
05.08.22	EDC 3164	1739.925	0.520	2.126	1.146	-11.436	0.821	1.824	0.04
04.29.22	EDC 3180	1748.725	0.508	2.184	1.194	-13.696	0.204	1.893	0.21
05.10.22	EDC 3190	1754.225	0.496	2.175	1.183	-13.054	-0.277	1.853	0.12
05.11.22	EDC 3199	1759.175	0.487	2.163	1.183	-13.485	-0.406	1.552	0.12
05.13.22	EDC 3207	1763.575	0.463	2.107	1.161	-13.797	-1.835	1.689	0.03
04.14.22	EDC 3217	1769.075	0.455	2.091	1.153	-14.491	-2.211	1.650	0.14
04.19.22	EDC 3228	1775.125	0.453	2.045	1.133	-15.234	-2.593	1.598	0.06
05.12.22	EDC 3240	1781.725	0.439	1.990	1.102	-14.052	-2.430	1.538	0.09
05.17.22	EDC 3250	1787.225	0.410	1.891	1.057	-13.983	-3.183	1.420	0.17
05.18.22	EDC 3260	1792.725	0.404	1.856	1.034	-12.285	-2.037	1.410	0.10
04.20.22	EDC 3278	1802.625	0.406	1.849	1.017	-11.909	-2.482	1.409	0.23
04.05.22	EDC 3290	1809.225	0.392	1.745	0.991	-11.782	-2.721	1.360	0.12
03.30.22	EDC 3308	1819.125	0.387	1.589	0.891	-10.892	-2.035	1.395	0.27
05.05.22	EDC 3324	1827.925	0.402	1.467	0.813	-8.786	-1.215	1.488	0.01
04.15.22	EDC 3343	1838.375	0.415	1.454	0.808	-8.947	-1.069	1.576	0.12
04.06.22	EDC 3364	1849.925	0.423	1.427	0.805	-10.053	-1.045	1.578	0.19
03.23.22	EDC 3383	1860.375	0.432	1.558	0.862	-10.716	-1.400	1.582	0.24
04.21.22	EDC 3393	1865.875	0.419	1.576	0.880	-9.708	-1.456	1.552	0.04
03.17.22	EDC 3410	1875.225	0.424	1.666	0.938	-12.768	-2.609	1.521	0.26
03.31.22	EDC 3418	1879.625	0.428	1.668	0.937	-11.717	-2.346	1.539	0.05
04.07.22	EDC 3427	1884.575	0.427	1.667	0.928	-12.797	-2.599	1.545	0.08
04.08.22	EDC 3443	1893.375	0.414	1.591	0.902	-14.166	-3.252	1.404	0.09
04.09.22	EDC 3450	1897.225	0.392	1.574	0.886	-14.754	-3.844	1.384	0.03
04.01.22	EDC 3458	1901.625	0.410	1.552	0.895	-14.345	-3.601	1.381	0.15
05.06.22	EDC 3464	1904.925	0.398	1.516	0.863	-12.937	-2.650	1.427	0.15
03.22.22	EDC 3474	1910.425	0.423	1.660	0.954	-14.769	-3.211	1.460	0.13
04.22.22	EDC 3483	1915.375	0.400	1.506	0.846	-13.811	-3.707	1.360	0.05
04.02.22	EDC 3490	1919.225	0.385	1.403	0.805	-14.036	-4.040	1.317	0.08
06.28.22	EDC 4140	2276.725	0.465	0.936	0.489	-5.340	-0.051	1.772	0.09
06.21.22	EDC 4146	2280.025	0.463	0.908	0.487	-4.784	0.204	1.824	0.03
06.22.22	EDC 4156	2285.525	0.481	0.934	0.497	-4.206	0.836	1.857	0.12
06.23.22	EDC 4164	2289.925	0.471	0.979	0.530	-4.958	0.570	1.884	-0.03
06.29.22	EDC 4174	2295.425	0.492	1.178	0.631	-6.088	1.104	1.964	0.04
06.24.22	EDC 4186	2302.025	0.499	1.509	0.804	-6.205	1.094	1.912	-0.03
07.08.22	EDC 4196	2307.525	0.525	1.807	0.976	-6.716	1.208	2.029	0.00
06.30.22	EDC 4204	2311.925	0.506	1.780	0.949	-7.606	0.771	2.033	0.00
07.09.22	EDC 4212	2316.325	0.503	1.727	0.921	-8.135	0.443	1.912	-0.03
07.01.22	EDC 4216	2318.525	0.484	1.677	0.919	-9.203	-0.281	1.848	-0.01
07.10.22	EDC 4222	2321.825	0.468	1.631	0.889	-9.599	-0.547	1.810	-0.04
07.02.22	EDC 4224	2322.925	0.479	1.621	0.899	-10.069	-0.716	1.802	0.03
07.05.22	EDC 4236	2329.525	0.421	1.474	0.827	-12.818	-3.082	1.525	0.03
07.11.22	EDC 4246	2335.025	0.429	1.650	0.921	-12.583	-3.288	1.484	-0.04

Date	**Bag Nr.**	**Depth**	**$\delta^{15}N_2$**	**$\delta^{18}O_2$**	**$\delta^{17}O_2$**	**$\delta O_2/N_2$**	**$\delta Ar/N_2$**	**$\delta^{40/36}Ar_{Delta}$**	**ΔCO_2**
07.06.22	EDC 4252	2338.325	0.416	1.656	0.928	-12.916	-3.637	1.484	0.04
07.07.22	EDC 4256	2340.525	0.387	1.594	0.892	-12.706	-3.534	1.460	-0.01
06.15.22	EDC 4652	2558.325	0.487	0.839	0.451	-7.034	-0.430	1.830	-0.03
06.09.22	EDC 4662	2563.825	0.480	0.760	0.400	-6.857	-0.208	1.857	0.06
06.04.22	EDC 4672	2569.325	0.482	0.768	0.416	-6.284	-0.155	1.887	0.02
06.10.22	EDC 4680	2573.725	0.479	0.907	0.467	-7.140	-0.364	1.838	-0.01
05.19.22	EDC 4686	2577.025	0.502	1.135	0.604	-6.999	0.286	1.913	0.12
05.20.22	EDC 4692	2580.325	0.525	1.421	0.754	-6.611	0.875	2.004	0.02
06.11.22	EDC 4694	2581.425	0.508	1.543	0.826	-7.003	0.673	1.990	0.02
06.14.22	EDC 4702	2585.825	0.532	1.943	1.022	-7.040	0.949	2.035	0.13
05.31.22	EDC 4704	2586.925	0.529	1.956	1.037	-7.112	1.053	1.966	0.17
06.20.22	EDC 4707	2588.575	0.523	1.973	1.040	-7.644	0.905	2.003	0.10
05.24.22	EDC 4712	2591.325	0.546	2.018	1.478	-9.415	0.532	-11.408	0.45
06.05.22	EDC 4716	2593.525	0.511	2.017	1.114	-8.182	0.509	0.657	0.07
06.01.22	EDC 4720	2595.725	0.479	2.020	1.094	-8.871	-0.254	1.770	0.10
05.25.22	EDC 4724	2597.925	0.474	2.077	1.130	-9.622	-0.680	1.718	0.04
06.06.22	EDC 4735	2603.975	0.441	2.088	1.141	-9.448	-1.804	1.556	0.05
06.02.22	EDC 4740	2606.725	0.436	2.072	1.131	-9.626	-2.171	1.522	0.05
06.07.22	EDC 4744	2608.925	0.415	1.985	1.084	-8.551	-2.293	1.453	0.02
06.03.22	EDC 4746	2610.025	0.412	1.984	1.143	-9.853	-2.360	-0.083	0.13

Table A.3.: Elemental and isotopic ratios of N_2*,* O_2*, and Ar obtained from the 72 EDC samples measured during this PhD-project on the Delta V IRMS. Depths are middle of the bag in units of meters. All ratios are in units of permille. Additionally, we show* ΔCO_2*, an indicator of how complete the* CO_2 *removal by the* LN_2 *trap was. We consider* $\Delta CO_2 < 0.5$ *mV an indication of a successful removal of* CO_2*.*

Acknowledgements

Throughout the past four years, I was fortunate to have received help, advice, and support from family and peers. Without them, this document would not exist in its current form, and the time in Bern would not have been half as enjoyable. I would like to thank...:

... **Hubertus Fischer** for taking on a former history student with at least 1.5 left hands to work in a physics laboratory. Thank you for the liberty of making mistakes, the hints and guidance for how to resolve them, and the scrutiny during long meetings required to properly understand them; and for giving me the chance to experience the frozen continent in person.

... **Daniel Baggenstos** for his unparalleled mentorship on working in science in general and in the laboratory in particular, as well as in scaling a boulder and safely redescending.

... **Jeffrey Severinghaus** for examining this thesis.

... **Thomas Stocker** for chairing the defence and his advice of what to bring and what not to bring when going to Antarctica.

... **Jochen Schmitt** for hinting at all the pandora's boxes that so many seemingly small problems in the lab happen to be, his many ideas of how to close them, and for making sure that they indeed are closed.

... **Sarah Shackleton** for all the inspiring MOT conversations and the shared sympathy when it comes to firn fractionation corrections.

... **Marcel Häberli** for introducing me to the world of MOT and to the experimental work in general as a tutor of my very first physics lab course.

... **Thomas Kellerhals** for setting up the extraction system and mass spectrometers.

... **Christoph Reinhard** for making things communicate with one another like they are supposed to and teaching me quite a few things about electronics in the meantime.

... **Kurt Grossenbacher**, **Samuel Marending**, and **Remo Walther** for fixing things faster than I can break them thanks to their great expertise and hands-on approach.

... **Doris Rätz**, **Bettina Schüpbach**, **Savio Villaverde**, and **Claudia Maschke** for solving many logistical problems without me even realising their existence.

... **Gunnar Jensen**, **Friedrich Burger**, and **Alexandre Emsenhuber** for their IT-support.

... **Peter Nyfeler** for curing all those small and smallish mass spectrometer illnesses.

... **Lars Mächler** for introducing me to the world of LabView.

... **Florian Krauß**, the other half of FloKus, for sharing an office, a laboratory, hotel rooms, beds, and probably the greatest adventure of our lives.

... **Henrique Traeger** for enduring a stressed office mate, keeping plants alive, and making sure break times are followed.

... **Chantal Zeppenfeld** for challenging me with bicycle tours, early morning runs, and scientific discussions; and for making lab-beer happen.

... **Michaela Muehl** for the shared frustration about machines that do not work as intended and the excitement when they finally do; and for an incredibly tidy cutting room.

... **Geunwoo Lee** for yet more sympathy about lab issues, for countless demonstrations of how to reach the top most gracefully, and for keeping Pizza-Monday alive.

... **Lison Soussaintjean** for looking after my ice and for a shared love for good French breakfasts.

... **Stephan Räss** for our shared love-hate relationship towards mass spectrometers.

... **Bärbel Seth** for making sure I did not freeze when in the cold room or in Antarctica.

... **Lucas Silva**, **Sarah Eggleston**, **Camilla Jensen**, **Stephanie Musy**, and **Evelien van Dijk** for many helpful, inspiring, and entertaining discussions about thesis writing or even more enjoyable science, teaching, bouldering, apple cake, and Tuesday jazz.

... **Sarah Jackson** for providing me with some great quotes for the introduction to this thesis. My favourite was one by Ernest Shackleton: "*Superhuman effort isn't worth a damn unless it achieves results*". A close second to an 8th grader's uninspired poem.

... **Jonas Beck** and **Sebastian Gross** for great entertainment during the coffee break and great support whenever the lab course equipment was misbehaving.

... **Melanie Salvisberg** for making me believe in my scientific abilities.

... **Antoine Thévanaz**, **Giulia Wienhues**, **Michael Keller**, **Juhyeong Han**, and many others from the Climate Sciences Master program for sharing my path since many years and for the close friendships that developed on the way.

... the entire **KUP-team**, for all the fruitful exchanges and fruit-full cakes during coffee breaks, and for keeping that wonderful KUP spirit high.

Very special thanks go to...

... **Ariane**, **Regula** and **Marc Grimmer** for their lifelong support, encouragement, and helpful advice, for making sure I am aware of birthdays and all those tax and insurance things, and for giving me the chance to follow whichever path I deemed good or at least interesting.

... **Imogen Gabriel** for all the laughter, love, and lasagna, which kept my spirits high throughout (most of) the writing process.

Last but not least, I would like to thank you, dear reader, for taking up the daunting task of opening this PhD-thesis – and be it just to read the acknowledgement section.

Publications

Grimmer, M.; Baggenstos, D.; Schmitt, J.; Shackleton, S.; Severinghaus, J.P.; Fischer, H.: Strong influence of millennial-scale variability on mean ocean temperature evolution across the last four glacial terminations, in prep.

Haeberli, M., Baggenstos, D., Schmitt, J., Grimmer, M., Michel, A., Kellerhals, T., Fischer, H., 2021. Snapshots of mean ocean temperature over the last 700 000 years using noble gases in the EPICA Dome C ice core. Clim. Past 17, 843–867. https://doi.org/10.5194/cp-17-843-2021.

Pöppelmeier, F., Baggenstos, D., Grimmer, M., Liu, Z., Schmitt, J., Fischer, H., Stocker, T.F., 2023. The Effect of Past Saturation Changes on Noble Gas Reconstructions of Mean Ocean Temperature. Geophys. Res. Lett. 50, e2022GL102055. https://doi.org/10.1029/2022GL102055.

Declaration of consent

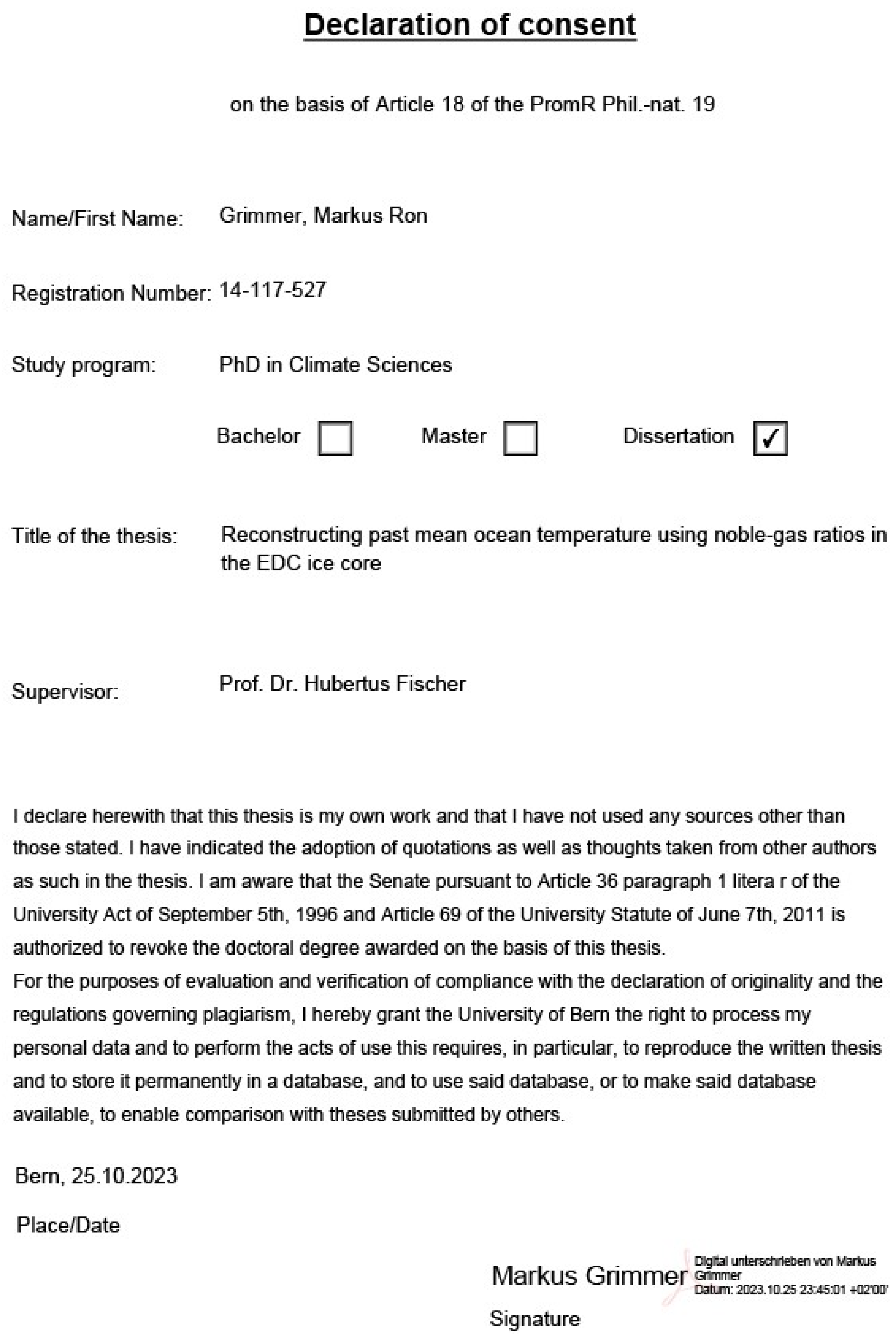

Declaration of consent

on the basis of Article 18 of the PromR Phil.-nat. 19

Name/First Name: Grimmer, Markus Ron

Registration Number: 14-117-527

Study program: PhD in Climate Sciences

Bachelor ☐ Master ☐ Dissertation ☑

Title of the thesis: Reconstructing past mean ocean temperature using noble-gas ratios in the EDC ice core

Supervisor: Prof. Dr. Hubertus Fischer

I declare herewith that this thesis is my own work and that I have not used any sources other than those stated. I have indicated the adoption of quotations as well as thoughts taken from other authors as such in the thesis. I am aware that the Senate pursuant to Article 36 paragraph 1 litera r of the University Act of September 5th, 1996 and Article 69 of the University Statute of June 7th, 2011 is authorized to revoke the doctoral degree awarded on the basis of this thesis.
For the purposes of evaluation and verification of compliance with the declaration of originality and the regulations governing plagiarism, I hereby grant the University of Bern the right to process my personal data and to perform the acts of use this requires, in particular, to reproduce the written thesis and to store it permanently in a database, and to use said database, or to make said database available, to enable comparison with theses submitted by others.

Bern, 25.10.2023

Place/Date

Markus Grimmer
Digital unterschrieben von Markus Grimmer
Datum: 2023.10.25 23:45:01 +02'00'

Signature